Formation, Characterization, and Oxidative Reactivity of Bio-inspired Peroxo- and Hydroxo-manganese(III) Complexes

By

Bogamuwe H. M. Gayan B. Wijeratne

Submitted to the graduate degree program in Chemistry and the Graduate Faculty of the University of Kansas in partial fulfillment of the requirements for the degree of Doctor of Philosophy

_____
Chairperson: Dr. Timothy A. Jackson

_____
Dr. Mikhail V. Barybin

_____
Dr. Jon A. Tunge

_____
Dr. David R. Benson

_____
Dr. Kevin C. Leonard

Date Defended: June 10, 2015

The Dissertation Committee for Bogamuwe H. M. Gayan B. Wijeratne certifies that this is the approved version of the following thesis:

Formation, Characterization, and Oxidative Reactivity of Bio-inspired Peroxo- and Hydroxo-manganese(III) Complexes

_____

Chairperson: Dr. Timothy A. Jackson

Date approved: June 12, 2015

Abstract

Manganese-dependent enzymes that react with dioxygen and its reduced derivatives are ubiquitous in nature, catalyzing pivotal processes such as the light-driven oxidation of water to dioxygen, generation of peroxidized fatty acids, and detoxification of reactive oxygen species such as superoxide and peroxide. Peroxo-, hydroxo-, and oxo-manganese intermediates are often invoked in the mechanisms of a majority of these enzymes. However, detailed understanding of the mechanisms involving Mn-containing enzymes is lacking, warranting further investigations in this area of study. Due to numerous restrictions involved with carrying out such mechanistic studies using the actual proteins of interest, utilization of synthetic bio-inspired model complexes has been a frequent practice. To this end, a series of peroxomanganese(III) complexes with varied steric and electronic properties have been synthesized, and characterized by low-temperature electronic absorption and magnetic circular dichroism (MCD) spectroscopies, as well as complementary density functional theory (DFT) and time-dependent DFT computations. This work resulted in the first report where steric properties of the supporting ligand were shown to play a predominant role in modulating the Mn-peroxo interactions in η^2-peroxomanganese(III) intermediates. This study provided intriguing insight into the significance of steric factors of enzymatic active sites in fine-tuning their reactivity properties.

Since a majority of peroxomanganese(III) model complexes display impaired thermal stabilities under ambient conditions, designing ligands that minimize their decay pathways is of great interest. This has motivated the design, synthesis, and characterization of such an oxidatively robust supporting ligand, L^7BQ (L^7BQ = 1,4-di(quinolin-8-yl)-1,4-diazepane), and the characterization of its Mn^{II} complex by X-ray diffraction techniques. The corresponding peroxomanganese(III) adduct has been generated and spectroscopically characterized. This

adduct exhibits interesting reaction patterns with strong acids and acyl chlorides. Activation of non-prophyrinoid peroxomanganese(III) complexes to generate high-valent oxidants is extremely rare, which makes the reactivity of this new Mn^{III}-O_2 adduct highly intriguing.

Apart from biological significance, dioxygen activation by Mn^{II} centers is of great importance both in environmentally benign synthetic approaches, as well as alternative energy applications such as fuel cells. Several such Mn^{II} complexes have been synthesized, and characterized by X-ray diffraction and other techniques. Mechanistic understanding of Mn^{II}-mediated dioxygen activation is still in its infancy, although such systems have been successfully utilized in a number of O_2-dependent oxidation reactions in generating synthetically desirable organic substrates. We have carried out mechanistic studies of dioxygen activation using electronic absorption, electronic paramagnetic resonance (EPR), and X-ray absorption spectroscopies, in conjugation with mass spectrometric and kinetic analysis. Based on the current evidence, a mechanistic proposal is presented, describing the O_2 activation reactivity of these new Mn^{II} systems.

Intriguingly, the O_2 activation reactions of these new Mn^{II} complexes yield a single metal product in excellent yields (>98%), which has been structurally-characterized as the corresponding Mn^{III}-OH complex. Monomeric hydroxomanganese(III) complexes are relatively rare, and those that can mediate substrate oxidation reactions are even more scarce. In biology, hydroxomanganese(III) adducts are known to mediate crucial proton-coupled electron transfer (PCET) processes, especially during the peroxidation of fatty acids by non-heme Mn-containing enzyme lipoxygenase, and the water oxidation pathway of the oxygen evolving center in photosystem II. In light of these biological examples, we have carried out a thorough kinetic investigation of the PCET reactivity of the monomeric Mn^{III}-OH complex,

[Mn^{III}(OH)(dpaq)](OTf), with a series of substituted phenols with variable bond dissociation free energies (BDFEs up to 79 kcal/mol in MeCN), and the weak O–H bond substrate TEMPOH (BDFE = 66 kcal/mol in MeCN). [Mn^{III}(OH)(dpaq)](OTf) is the first example of a Mn^{III}-OH adduct that has exhibited saturation kinetics during its PCET reactivity. This kinetic profile implies the presence of an accumulating intermediate during the phenol oxidation reactions. Our data suggest that this intermediate is a H-bonded precursor complex that forms between the oxidant and the substrate prior to the rate-limiting transfer of the hydrogen atom. Stepwise electron and proton transfer processes have been discounted based on our Polanyi analysis of the kinetic data, as well as kinetic isotope studies, among other evidence. Interestingly, the related Mn^{III}-OMe complex, [Mn^{III}(OMe)(dpaq)](OTf), reacts with the same series of phenolic substrates, and does not exhibit the saturation kinetics displayed by the Mn^{III}-OH species. [Mn^{III}(OMe)(dpaq)](OTf) is the only example of a Mn^{III}-OMe complex that mediates PCET with phenolic substrates.

Both [Mn^{III}(OH)(dpaq)](OTf) and [Mn^{III}(OMe)(dpaq)](OTf) were found to oxidize TEMPOH to produce TEMPO and the corresponding Mn^{II} species as observed by electronic absorption and EPR spectroscopies. Eyring analysis of these reactions has provided insight into the activation parameters dictating these reactions. Furthermore, catalytic dioxygen reduction by [Mn^{III}(OH)(dpaq)](OTf) was also demonstrated, which revealed a turnover number of 1050, with the presence of TEMPOH as the H-atom donor substrate. Extending similar reactivity to other substrates may provide significantly greener, inexpensive oxidation protocols for the dioxygen-dependent generation of desirable synthetic targets.

Acknowledgements

First, and most importantly, I would like to pay my utmost gratitude to Professor Jackson, my research adviser and mentor. None of this would have been a possibility if it was not for your enlightening guidance and support, which had always brought out my very best, and nothing less. Your supreme methods of teaching and mentoring have truly inspired me over the years, and I have no doubt that I will always think of you as I mentor my students in future. I have greatly enjoyed the time in your group, and I wish you and the group a successful research journey for many more years ahead.

Misha, you have always been a great support throughout my time here at KU, and I will always remember you for your helpful advice and wonderful sense of humor. Jon, thank you for your edifying guidance during my post-doc search, and I must admit that I absolutely loved your organometallics class. I would also like to thank Dr. Benson and Dr. Leonard for agreeing to serve in my defense committee. To Dr. Victor W. Day, for solving my numerous crystal structures, and providing me with valuable advice on how to regrow my crystals whenever they did not look the best. (Also, for being so mysterious during the time of refining the structures, which always made me wonder if I was on the verge of a breakthrough!). Also, I would like to thank Dr. Justin Douglas for support with the EPR, and Dr. Erik Farquhar for his unfailing support during X-ray absorption experiments at the Brookhaven National Laboratory.

Robert, I would like to thank you for all the techniques you taught me in lab doing my early days in Jackson group, and it has always been a lot of fun to work with you. I have never met anyone that's quite like you, and I can never forget how you always had to say something about me… James and Amanda, and to all my past and present colleagues from the Barybin group, thanks for your support in lab, as well as for the fun times and laughter we often shared. It had been great working with you guys!

Thanks to all present Jackson group members, you guys are the best! Hannah, can't believe we have worked together for four years. Feels like yesterday when you first joined the lab. Derek and Allyssa, thanks for you guys' support throughout my "reign (and rain) of terror" period. It had been great sharing the lab with you guys. Josh, my buddy, I'm so glad you joined our lab. I just wish we had more time to work together, sharing "they're ok…" music. Andrew and Briana, I have greatly enjoyed mentoring you guys in lab. You have certainly been excellent undergraduates to work with. I wish all of you guys the very best in future, and really wish our paths would cross at some point in our careers. Domenick, you have always been an impressive example and a close friend to me. You always set the bar high, and it had really motivated me to work hard. The long hours at the NSLS beamline would never have been the same without you, and our late night road trips in New York will always remain memorable.

I would also like to extend my gratitude to my parents, who had always been there for me, no matter what I went through. Thank you amma and appachchi for believing in me, and being the most wonderful teachers I ever had in life. Your passion for teaching and enthusiasm to do your best for your students had deeply inspired me over the years. Thanks to my awesome cousins, Panduka, Indika, and Saleeka. Also to my wonderful in-laws, especially Hiranya and Laksheen… thanks for being the crazy sisters I always wanted. I must also thank my awesome teachers (especially Ms. S. Abeykoon, and late Mrs. C. Weerakoon), and undergrad professors (especially Prof. D. De Silva and Prof. S. Hewage), without whom, I would not be here today.

Beyond everything, my heartfelt thanks go out to my lovely wife, Shehani. We have come a long way since we first met in the sophomore year. It is your love, encouragement, and hard work that have motivated me to come this far. Thank you for always being my partner and friend in everything, and for constantly believing in my talents. I love you immensely, and eagerly look forward to sharing all of life's challenges together with you, in the loving assurance of the Almighty Father.

TABLE OF CONTENTS page

Abbreviations and Acronyms

BDE	bond-dissociation enthalpy
BDFE	bond-dissociation free energy
CCA	cyclohexanecarboxaldehyde
CPET	concerted proton-electron transfer
CT	charge-transfer
CV	cyclic voltammetry
DCM	dichloromethane
DFT	density functional theory
DHA	9,10-dihydroanthracene
EPR	electron paramagnetic resonance
ESI-MS	electrospray ionization mass spectrometry
EXAFS	extended X-ray absorption fine-structure
FWHM	full-width at half-maximum
H/D KIE	hydrogen/ deuterium kinetic isotope effect
HAT	hydrogen atom transfer
H_2O_2	hydrogen peroxide
HPCA	homoprotocatechuate
LO	lipoxygenase
MCD	magnetic circular dichroism
MeCN	acetonitrile
MLCT	metal-to-ligand charge-transfer
Mn-HPCD	manganese homoprotocatechuate 2,3-dioxygenase

Mn-RNR	manganese ribonucleotide reductases
Mn-SOD	manganese superoxide dismutase
NMR	nuclear magnetic resonance
NSLS	National Synchrotron Light Source
OAT	oxygen atom transfer
OEC	oxygen evolving complex
PCET	proton-coupled electron transfer
PhIO	iodosobenzene
PSII	photosystem II
TD-DFT	time-dependent density functional theory
TEMPOH	2,2′-6,6′-tetramethylpiperidine-1-ol
UV	ultraviolet
VTVH	variable temperature, variable field
XANES	X-ray absorption near-edge structure
XAS	X-ray absorption spectroscopy
XRD	X-ray diffraction
ZFS	zero-field splitting

CHAPTER 1

Bio-inspired Peroxo- and Hydroxo-manganese(III) Complexes: An Overview

1.1 Introduction

Manganese-dependent catalysts that react with dioxygen and all its reduced derivatives (superoxide, peroxide and oxide) contribute numerous biologically and industrially pivotal processes.[1-17] Detoxification of reactive oxygen species, such as superoxide or hydrogen peroxide,[1-3] biosynthesis of deoxyribonucleotides,[18] peroxidation of fatty acids,[5-8] and water oxidation to dioxygen within biological systems,[19-21] as well as industrially relevant olefin epoxidation,[15] and alcohol oxidation[13,14,22] processes, are several of such examples. Although detailed mechanistic insights into most of the biological processes are currently lacking, small molecule mimics of these systems have long been used to model their chemistries.[19,23,24] In most instances, manganese centers act as redox-active catalysts, as they shuttle between multiple oxidation states within the catalytic process, and facilitate electron and/or atom (or group) transfer steps.[25-28] Irrespective of the structure of the active site, or the catalytic conversion, the majority of these enzymes are proposed to feature mid-valent oxidants such as peroxo- and/or hydroxomanganese(III) intermediates.[9,11,27-31]

1.1.1. Peroxomanganese(III) Intermediates in Biology. For most manganese enzymes, peroxo level intermediates are inferred on the basis of their reactivity and/or as supported by spectroscopic and computational evidence. To this end, for manganese superoxide dismutase (Mn-SOD), and manganese homoprotocatechuate 2,3-dioxygenase (Mn-HPCD), strong spectroscopic evidence suggest the presence of peroxomanganese(III) intermediates within their mechanisms of action. The active site of Mn-SOD contains a manganese center within a trigonal bipyramidal geometry, coordinated to three histidines, an aspartate, and a solvent ligand (Figure 1.1).[24] This manganese center shuttles between Mn^{II} and Mn^{III} as it disproportionates superoxide to O_2 and H_2O_2.[25,26] The reduction of superoxide to peroxide can

take place via two pathways involving Mn-SOD: prompt protonation and inner sphere pathways. Prompt protonation pathway generates H_2O_2 by manganese-catalyzed superoxide reduction and protonation potentially by an outer sphere pathway. The latter pathway involves a product-inhibited complex, which is presumed to involve a peroxomanganese(III) adduct resulting from superoxide binding to the manganese center.[32] The actual structure of this product-inhibited intermediate is not known to-date.[9] However in a different study, crystals of *E.coli* Mn-SOD formed a side-on bound peroxomanganese(III) intermediate when soaked with peroxide at low temperatures. This adduct was characterized by X-ray diffraction techniques with 1.55 Å resolution.[33] The structure revealed Mn–O distances that ranged from 2.09 to 2.58 Å, which is exceptionally longer than those of other peroxomanganese(III) complexes (1.83 to 1.91 Å). The peroxo ligand occupied an axial position, typically occupied by a solvent molecule. Irrespective of whether this species corresponds to the product-inhibited species formed in Mn-SOD, this provides the only structurally characterized peroxomanganese(III) intermediate within an enzyme active site.

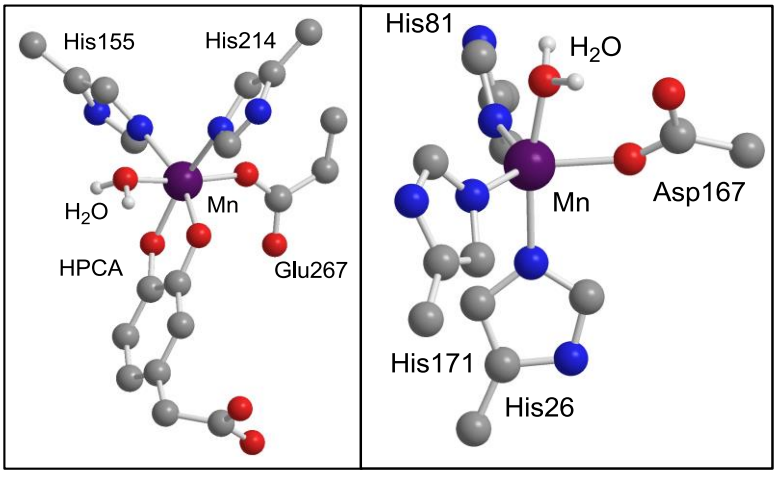

Figure 1.1. Left: Active site of Mn-HPCD with the substrate and one water ligand bound to the metal center. Right: Mn-SOD active site structure with the axial water ligation.

Mn-HPCD consists of a manganese active site with a pseudo-octahedral geometry, ligated by two histidines, one glutamate and three water molecules in its primary coordination sphere (Figure 1.1).[34] This coordination environment is commonly observed for a number of dioxygen activating non-heme iron enzymes in biology.[34] Rapid-freeze-quench EPR analysis of Mn-HPCD from *Brevibacterium fuscum* reported by Que, Lipscomb, and Hendrich and coworkers provided evidence of two distinct intermediates as Mn-HPCD-HPCA complex was exposed to O_2 saturated buffer at pH = 7.4.[11] The first intermediate (I1) maximized to 5% of total Mn at 15 ms, and, based on the EPR data, was best described as comprising a high-spin Mn^{III} center ferromagnetically coupled to an axially coordinated superoxo ligand. The second intermediate (I2), which maximized at 75% of total Mn at 34 ms, was formulated as a Mn^{II}-alkylperoxo species that decays to produce the dioxygenated substrate.

1.1.2 Hydroxomanganese(III) Species in Biology. Hydroxomanganese(III) adducts have been characterized or proposed as key intermediates in a small, yet diverse set of manganese-containing enzymes.[1,3,5-8,19] Mn-SOD is known to feature a Mn^{III}-OH unit in its oxidized resting state, where the hydroxo ligand plays the crucial role of redox tuning of the Mn center.[35-37] This form of the enzyme undergoes a proton-coupled electron transfer (PCET) reaction to generate the reduced Mn^{II}-OH_2 adduct, which then binds to superoxide.

The non-heme iron-dependent enzyme lipoxygenase (LO), which is present in plants and mammals is known to catalyze the regio- and stereospecific dioxygenation of *cis,cis*-1,4-pentadiene-containing fatty acids to alkyl hydroperoxides using dioxygen.[38-42] These oxidized fatty acids provide starting compounds for the biosynthesis of jasmonic acid ((*1R,2R*)-3-oxo-2-(*2Z*)-2-pentenyl-cyclopentaneacetic acid) and traumatic acid (dodec-2-enedioic acid), which are vital for growth-regulation and wound-healing, respectively.[43] Human LO activity has been

implicated in certain cancers and inflammatory conditions.[43] The resting state of the plant LOs has been characterized by X-ray diffraction methods to contain an Fe^{II} center ligated to three histidines, one asparagine, and one isoleucine residue, where a solvent molecule completes the pseudo-octahedral geometry around the metal center (Figure 1.2).[38,39] Mammalian LOs contain a similar active site, where the asparagine residue has been replaced by a fourth histidine residue.[40-42] Unlike most non-heme Fe enzymes, the ferrous form of LO is inactive, and the active form contains a ferric center. Spectroscopic analysis of this active form by Extended X-ray Absorption Fine Structure (EXAFS) has revealed a ferric center with the same amino acid ligation, as the crystallographically-characterized ferrous form, with the coordinated solvent formulated as a hydroxide ligand with a short Fe–O distance of 1.88 Å.[44]

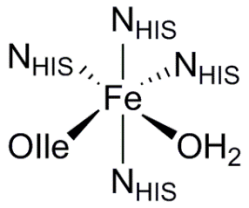

Figure 1.2. Schematic diagram of the non-heme Fe active site of rabbit 15-lipoxygenase.

Recently, Oliw and coworkers discovered a Mn-dependent LO (Mn-LO) enzyme secreted by the pathogenic fungus *Gaeumannomyces graminis*.[5-8] Gene sequence analysis of Mn-LO has revealed its homology to plant Fe-LOs; thus, the primary coordination sphere of Mn-LO likely resembles that of plant Fe-LOs.[45] Mn-LO peroxidizes linoleic acid with a temperature-dependent hydrogen/ deuterium kinetic isotope effect (H/D KIE) of ≈ 21,[6] which is in contrast to the larger, temperature-independent H/D KIE of Fe-LOs (≈ 56).[46,47] The basis for these differences is

currently unknown. It is also unclear if Mn-LO is exclusive to fungal species, with higher forms of life only containing Fe-LOs.

In the mechanism of LO-mediated oxidation reactions, a PCET from the fatty acid substrate to the M^{III}-OH (M = Fe or Mn) unit of the catalyst has been proposed to initiate the catalytic cycle (Figure 1.3).[48] This generates a substrate based radical, which resonates to produce a more stable radical-based intermediate. This intermediate then binds to dioxygen, producing a substrate-bound superoxo radical. The superoxo radical abstracts a hydrogen atom from the metal-bound water molecule to give rise to the peroxidized fatty acid product, as well as the active M^{III}-OH form of the enzyme. This mechanism is unique as dioxygen is reduced by the activated substrate, but not by the catalytic metal center, as observed for numerous other metal mediated dioxygen activation pathways.[49]

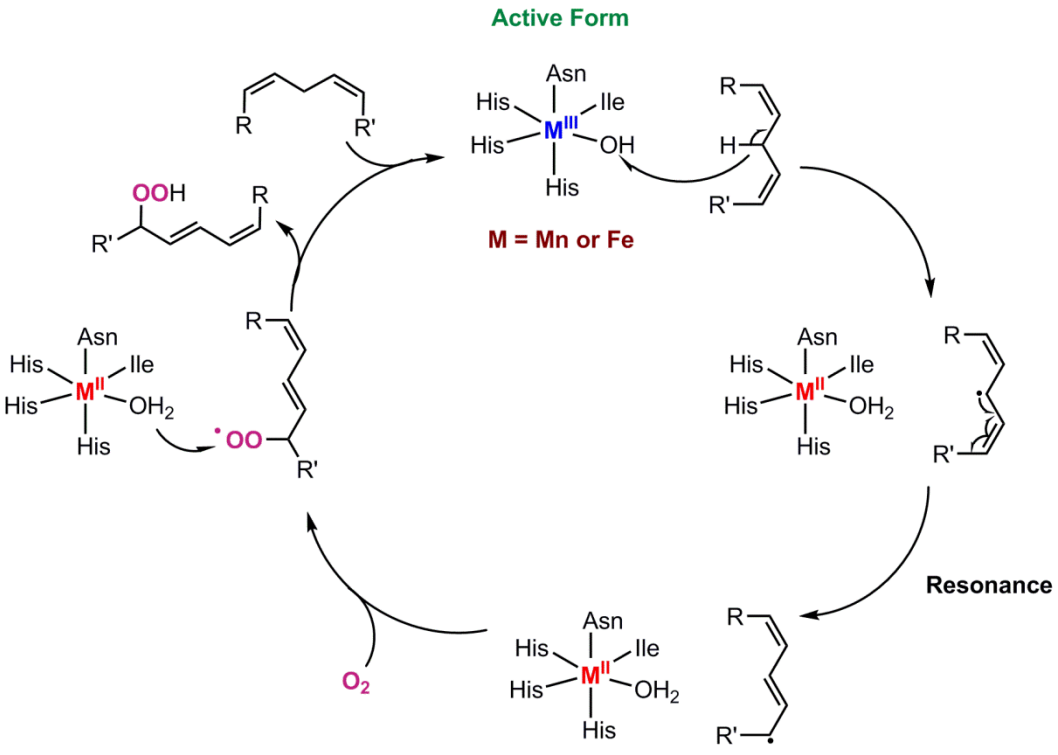

Figure 1.3. Proposed catalytic cycle for fatty acid peroxidation by lipoxygenase enzymes.

Another biological example where intermediates with Mn–OH adducts are proposed is the water oxidation process catalyzed by the oxygen evolving complex (OEC) of photosystem II (PSII) in cyanobacteria, algae, and green plants.[19-21,27-30,50] This catalytic process has drawn significant attention due to its vitality for aerobic life, and the high efficiency oxidation of water to dioxygen. Generating analogs of OEC with high stability and catalytic efficiency had been an outstanding challenge to synthetic chemists. The structure of the active site of OEC has been under much debate until Umena and coworkers reported its crystal structure at a resolution of 1.9 Å in 2011 (Figure 1.4).[51] This structure revealed a Mn_4CaO_5 active site cluster consisting of a Mn_3CaO_4 cubane, which binds to the fourth Mn center (often referred to as the "dangler Mn") via a bridging oxo ligand. A more recent crystal structure resolved using femtosecond X-ray laser revealed the presence of a water molecule between the dangler Mn center and the cubane.[52] The catalytic cluster of OEC consists of multiple water ligands, some of which presumably undergo stepwise oxidation to produce dioxygen (*vide infra*). The multinuclear active site is held in place by three glutamic acid residues, two aspartic acid residues, two histidine residues, and one alanine residue. All Mn centers are six coordinated, while the Ca center is seven coordinated within the Mn_4CaO_5 cluster.[51]

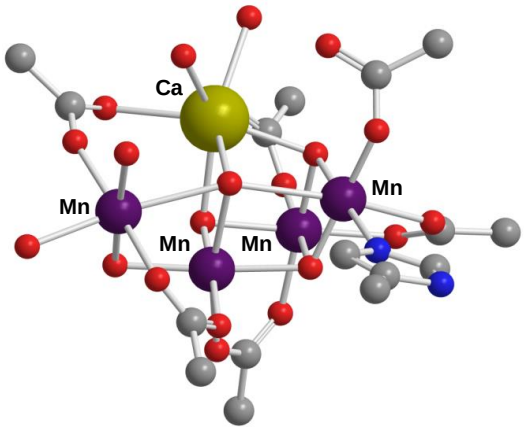

Figure 1.4. The active site of the oxygen evolving complex of photosystem II consisting of the Mn_4CaO_5 cluster resolved at 1.9 Å resolution.

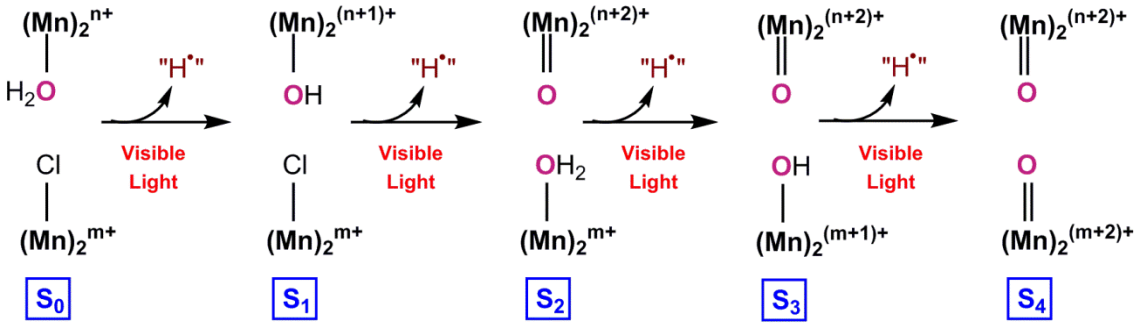

Scheme 1.1. Mechanism for water oxidation at the OEC as proposed by Babcock and coworkers.[28]

The mechanism of water oxidation at the OEC has been a subject of large controversy;[21] thus, the proposal of the involvement of Mn–OH intermediates within the catalytic cycle of OEC is more tenuous. However, the mechanism described by Babcock and coworkers can be used to sufficiently describe the chemistry without disregarding the current experimental observations.[28] According to this proposed catalytic process, the cluster is thought to propagate from its least oxidized S_0 state to the highest oxidized S_4 state, during which, Mn-coordinated water molecules are proposed to undergo stepwise PCET (Scheme 1.1), where protons and electrons are shuttled away from the cluster in a series of steps, each driven by the absorption of a photon by the photosynthetic apparatus. Presumably, the oxidation of the Mn–OH_2 units generate Mn–OH (or Mn–O(H)–Mn) adducts, which undergo a second oxidation process to give rise to Mn=O (or Mn–O–Mn) units. When the cluster has reached its most-oxidized S_4 state with Mn-bound oxo ligands, it switches back to the S_0 state upon the liberation of dioxygen. A nearby tyrosyl radical has been proposed to be responsible for the abstraction of hydrogen atoms by Mn-bound water ligands or hydroxyl groups during this process.[27,28,53] In support to this proposal, the range of O–H bond dissociation enthalpies (BDE) of water ligands and bridging hydroxyl ligands of

dimanganese(III,III), dimanganese(III,IV), dimanganese(IV,IV) model systems (O–H BDE = 77 – 92 kcal/mol)[54-56] are thermodynamically compatible with transferring hydrogen atoms to a tyrosyl radical (tyrosine O–H BDE = 86 kcal/mol[57]).

1.2 Peroxomanganese(III) Model Complexes

Given the expected importance of Mn^{III}-O_2 species in biologically and industrially relevant chemical pathways, coordination chemists have sought to generate model systems, which are often less cumbersome to isolate in high yields, and carry out detailed investigations, compared to the actual enzymatic systems. Most peroxomanganese(III) model complexes are thermally unstable, and therefore, they are only generated at low temperatures (<0 ^{o}C), complicating their solid-state characterization.[32] In spite of their impaired thermal stability, eight crystal structures have been reported so far (Figure 1.5), including the first report of a peroxomanganese(III) complex by Valentine and coworkers in 1987.[58-64] Other examples where solid-state characterization is lacking, Mn^{III}-O_2 complexes are supported by spectroscopic investigations, mass spectrometric data, and/or computational work.[65-72]

The generation, characterization, and chemical reactivity of η^2-peroxomanganese(III), and η^1-alkylperoxomanganese(III) complexes have been summarized in a recent review.[32] The properties of peroxomanganese(III) adducts relevant to this dissertation will be summarized here. η^2-peroxomanganese(III) adducts have been synthesized by oxidizing the Mn^{II} parent complex with either potassium superoxide (KO_2),[58,68-70] H_2O_2,[61,62,68-70] or dioxygen.[71-73] Regardless of the method, these chemically generated peroxomanganese(III) intermediates often exhibit modest yields, which complicates their structural characterization with techniques such as X-ray absorption spectroscopy (XAS), especially when crystallographic characterization is not feasible.

A recent report by Anxolabéhère-Mallart and coworkers demonstrated that electrochemically generated superoxide can produce greater yields of peroxomanganese(III) compounds from Mn^{II} precursors supported by pentadentate ligands.[74] This methodology if extended to other systems, could potentially provide a fruitful method to generate high yields of peroxomanganese(III) compounds, which would aid in their structural characterization by XAS.

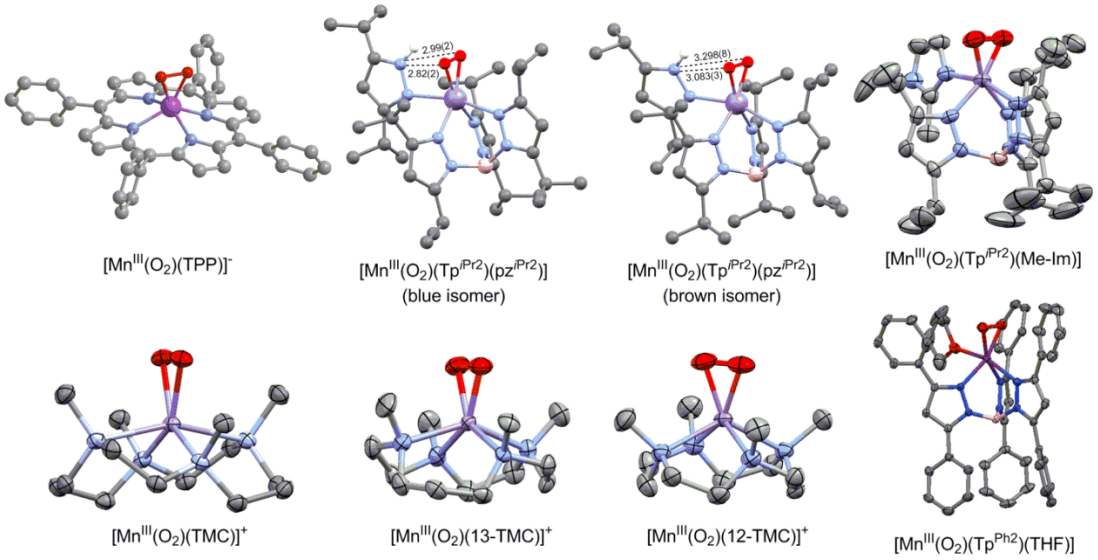

Figure 1.5. η^2-peroxomanganese(III) complexes characterized by X-ray crystallography.

All structurally characterized peroxomanganese(III) intermediates reveal hexacoordinated Mn^{III} centers with a η^2 (side-on-bound) peroxo ligand with Mn–O and O–O bond lengths ranging from 1.838 to 1.901 Å and 1.402 to 1.43 Å, respectively (Figure 1.5).[58-60,62,63,67,75] Spectroscopically characterized η^2-peroxomanganese(III) species commonly display weak (ε = 60 – 490 M^{-1} cm^{-1}) absorption features within the visible region (λ_{max} = 670 – 415 nm), that stem from the Mn^{III} ligand field, and peroxo-to-Mn^{III} charge transfer (CT) transitions.[70] In a recent study, detailed spectroscopic (electronic absorption and MCD) and computational investigations (TD-DFT) revealed the spectral assignments for the $[Mn^{III}(O_2)(L^7py_2{}^H)]^+$ complex, shown in

Figure 1.6.[70] The electronic absorption spectrum of $[Mn^{III}(O_2)(L^7py_2{}^H)]^+$ displayed two prominent features centered at 445 nm (22 472 cm^{-1}) and 590 nm (16 950 cm^{-1}). These features were attributed to the peroxo $\pi_{op}^* \rightarrow Mn^{III}$ d_{yz} CT transition, and Mn^{III} $d_z{}^2 \rightarrow d_{xy}$ ligand-field one-electron excitation, respectively. The latter transition is typically observed around 10 000 cm^{-1} for a six-coordinated Mn^{III} complex.[70] In the case of $[Mn^{III}(O_2)(L^7py_2{}^H)]^+$, this feature is blue-shifted due to the significant covalency between the peroxo ligand and manganese center, which results in significant destabilization of the $3d_{xy}$ acceptor orbital.

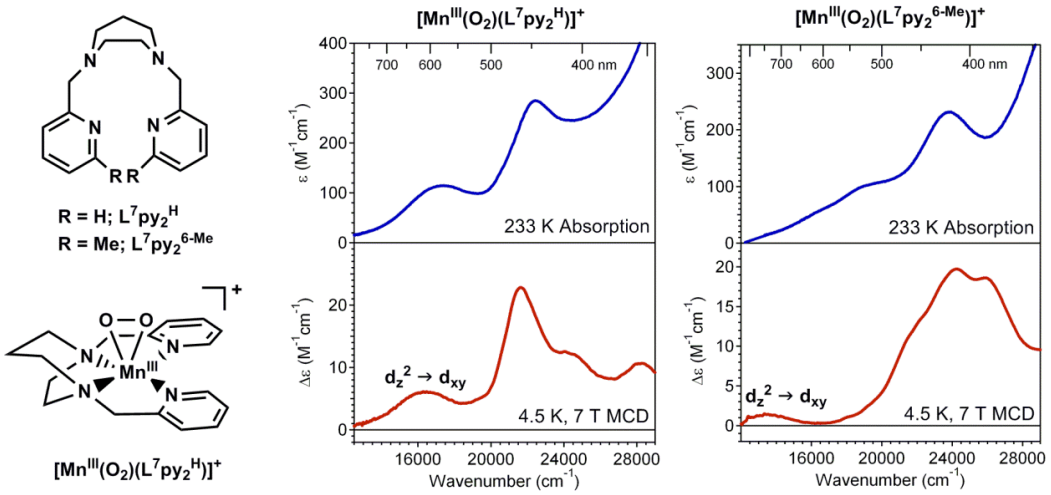

Figure 1.6. Schematic structures of the $L^7py_2{}^R$ ligand platform and $[Mn^{III}(O_2)(L^7py_2{}^H)]^+$ (left), and electronic absorption and MCD spectra of $[Mn^{III}(O_2)(L^7py_2{}^H)]^+$ (middle) and $[Mn^{III}(O_2)(L^7py_2{}^{6\text{-}Me})]^+$ (right). The $d_z{}^2 \rightarrow d_{xy}$ transition of $[Mn^{III}(O_2)(L^7py_2{}^{6\text{-}Me})]^+$ is ~3000 cm^{-1} blue-shifted in comparison with that of $[Mn^{III}(O_2)(L^7py_2{}^H)]^+$.

The most common type of reactions that peroxomanganese(III) complexes mediate are aldehyde deformylation reactions, where they generate alkenes and ketones (depending on the extent of oxidation) from aldehydes. This reveals the nucleophilic nature of the peroxo moiety of η^2-peroxomanganese(III) complexes. Furthermore, the conversion of these Mn^{III}-O_2 complexes to dimanganese(III,IV) species, and Mn^{III}-oxo/hydroxo hybrid species have also been

reported.[71,76] More intriguingly, the porphyrin-based peroxomanganese(III) complex, $[Mn^{III}(O_2)(TMP)]^-$ (TMP = tetramesitylporphyrin) has been observed to react with benzoyl chloride to generate high-valent Mn^V-oxo species, which performed olefin epoxidation. This reactivity is of great interest, as the conversion of mid-valent peroxo-type intermediates to high-valent intermediates have been proposed for numerous biological pathways.[49,77] In spite of those proposals, and the porphyrinoid complex mentioned above, examples of activation of peroxomanganese(III) species to generate high-valent oxidants are extremely scarce.

More recently, Nam and coworkers have reported the conversion of the η^2-peroxomanganese(III) complex, $[Mn^{III}(O_2)(TMC)]^+$ (TMC = 1,4,8,11-tetramethyl-1,4,8,11-tetraazacyclotetradecane), to the corresponding η^1-hydroperoxomanganese(III) adduct, upon reaction with 3 equiv. of $HClO_4$ at -40 ^oC. Furthermore, $[Mn^{III}(OOH)(TMC)]^{2+}$ reverted to $[Mn^{III}(O_2)(TMC)]^+$ upon the addition of 3 equiv. of triethylamine. Although it has been previously proposed that Mn^{III}-O_2 adducts can be converted to Mn^{III}-OOH species upon protonation,[65] this work provides evidence for the first η^1-hydroperoxomanganese(III) complex with detailed spectroscopic and computational characterization. In addition, $[Mn^{III}(OOH)(TMC)]^{2+}$ displayed oxo-atom transfer (OAT) reactivity with sulfides, revealing its electrophilic nature in contrast to the nucleophilic reactivity of η^2-peroxomanganese(III) complexes. The mechanistic details of the sulfide oxidation reaction are still unclear, although the homolytic O–O bond cleavage could potentially give rise to a high-valent Mn^{IV}-oxo oxidant, which could be mediating the observed OAT reactivity. It was also observed, in another recent study, that an electrochemically generated η^2-peroxomanganese(III) complex reacts with acids in the presence of reducing equivalents, where either the cleavage of Mn–O or O–O bond was observed depending on the strength of the acid.[78] In the presence of a strong acid ($HClO_4$), the

metal-bound peroxo moiety is protonated, cleaving the Mn–O bond, leading to the formation of H_2O_2. In contrast, when a weak acid is present, it was observed that the peroxo ligand is reduced further, causing the O–O bond cleavage. The resulting dioxo adduct is then protonated by the weak acid producing the final dihydroxo species.

1.3 Hydroxomanganese(III) Model Complexes

Although there are numerous synthetic examples of multinuclear manganese complexes with bridging hydroxide ligands,[23,55,56,79-85] monomeric manganese complexes with terminal hydroxyl ligands are relatively rare. In 1992, Armstrong and coworkers reported the first monomeric Mn^{III}-OH complex, [Mn^{III}(OH)(**L**^{1})], supported by a tetradentate dianionic phenolate-containing ligand (Figure 1.7).[86] This new compound was highly stable, which allowed its solid state characterization using X-ray diffraction methods. Since this first report, there have been eight reports of such complexes, where structural characterization has revealed Mn–OH distances in the range of 1.81 – 1.86 Å.[87-93] In this section, the methods utilized in the generation of monomeric Mn^{III}-OH compounds from Mn^{II} precursors, their characteristic structural properties, and oxidative reactivity is described in detail.

1.3.1 Generation of Hydroxomanganese(III) Complexes. The most commonly used oxidant in generating monomeric Mn^{III}-OH adducts from their Mn^{II} precursors is dioxygen. Although mechanistic details for these processes are still unclear, current proposals for these pathways involve dimeric manganese intermediates, and high-valent manganese species with terminal oxo ligands, as described in detail below. The yields of hydroxomanganese(III) complexes derived from dioxygen has been reported as moderate (~60%),[89,93] until the recent report by Kovacs and coworkers describing the generation of the O_2-derived

$[Mn^{III}(OH)(S^{Me2}N_4(tren))]^+$ complex in >98% yield.[91] This result is significant as such a high yield suggests the absence of a radical-based pathway, which would likely generate multiple products, rather than one major product by O_2 activation. Furthermore, another unique feature of these O_2-dependent syntheses is that the generation of Mn^{III}-OH adducts were also feasible with air oxidation of the Mn^{II} precursor complex in solution.[91,93] Thus, if these systems can be further developed to perform catalytic turnovers, they could provide highly desirable greener, less expensive aerobic oxidation catalysts that could in principle replace precious metal catalysts that are currently in use.

The two-electron oxidant and oxo-group transferring agent iodosobenzene (PhIO) has been used for the generation of the $[Mn^{III}(OH)(PY5)]^{2+}$ complex reported by Stack and coworkers (Figure 1.7).[87] While mechanistic details have not been described, PhIO could be responsible for the generation of a high-valent Mn^{IV}-oxo species in solution, as observed elsewhere.[94,95] Then this highly reactive Mn^{IV}-oxo complex could abstract a hydrogen atom to produce the Mn^{III}-OH end product. Finally, two of the reported Mn^{III}-OH species have been generated from Mn^{III} precursors, where a ligand exchange reaction generates the final Mn^{III}-OH species.[86,92]

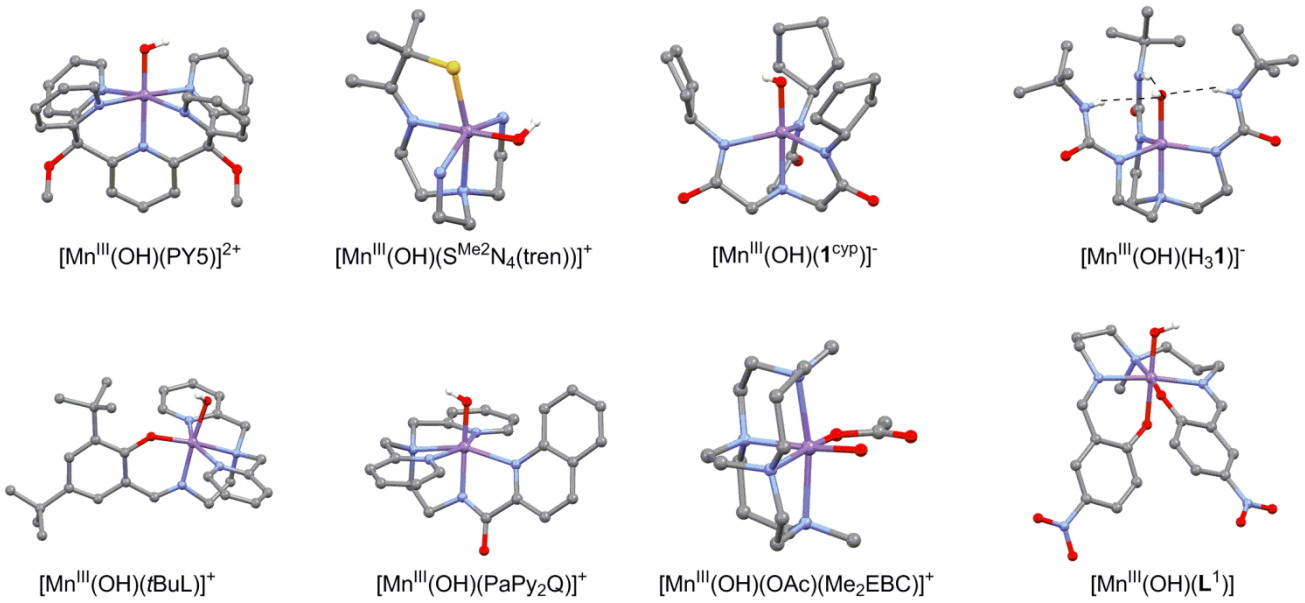

Figure 1.7. Crystallographically characterized monomeric Mn^{III}-OH complexes. Hydrogen atoms (other than the Mn–OH group), and non-coordinating counter anions and/ or solvent molecules have been excluded for clarity. See Table 1.1 for references.

Table 1.1. Crystallographic Mn–OH distances, experimental $\nu_{O\text{-}H}$ Frequencies; Solution Magnetic Susceptibility; Reduction Potentials for the Mn^{III}/Mn^{II} couple (vs. SCE); and Electronic Absorption Maxima and Extinction Coefficients for Hydroxomanganese(III) Complexes.

Complex	Mn–OH (Å)	$\nu_{O\text{-}H}$ ($\Delta^{18}O$) (cm^{-1})	μ_{eff} (μ_B)	E (Mn^{III}/Mn^{II}) (V)	λ_{max} (ε) (nm; $M^{-1}\,cm^{-1}$)	Ref.
$[Mn^{III}(OH)(PY5)]^{2+}$	1.807(3)	ND[a]	4.7(3)	+0.33	445 (500)	87
$[Mn^{III}(OH)(S^{Me2}N_4(tren))]^{+}$	1.854(8)	3367 (ND[a])	4.9	-0.44	299 (2221), 411 (260), 500 (320), 803 (40)	91
$[Mn^{III}(OH)(\mathbf{1}^{cyp})]^{-}$	1.816(4)	3643 (13)	5.0	ND[a]	NR[b]	89
$[Mn^{III}(OH)(H_3\mathbf{1})]^{-}$	1.872(2)	3613 (ND[a])	4.9	-1.35	[c]420 (325), 710 (600)	88,96
$[Mn^{III}(OH)(t\text{BuL})]^{+}$	1.86(3)	ND[a]	ND[a]	-0.36	405 (4112), 500 (670)	90,97
$[Mn^{III}(OH)(PaPy_2Q)]^{+}$	1.818(2)	3382 (ND[a])	4.9	ND[a]	485 (280), 740 (120)	92
$[Mn^{III}(OH)(OAc)(Me_2EBC)]^{+}$	1.812(4)	ND[a]	ND[a]	-1.17	231 (9640), 409 (110), 478 (80)	93
$[Mn^{III}(OH)(\mathbf{L}^1)]$	1.827(3)	ND[a]	5.1	ND[a]	[d]363 (23 000)	86

All measurements are reported at 25 °C in acetonitrile unless stated otherwise. [a]Not determined. [b]Not reported. [c]in DMSO. [d]in dichloromethane.

1.3.2 Characterization of Hydroxomanganese(III) Complexes. The X-ray crystal structures of monomeric Mn^{III}-OH complexes reveal Mn–OH distances that vary within the range of 1.81 – 1.86 Å. Longer Mn–OH bond lengths are observed when the hydroxyl group is involved in intramolecular and/ or intermolecular hydrogen-bonding interactions.[89,90] In fact, the longest Mn–OH distance (1.86 Å) was reported for a Mn^{III}-OH adduct where the Mn-bound hydroxyl unit is involved in a hydrogen bonding network that includes six aqua ligands, as evidenced in its solid-state structure.[90] In almost every other crystal structure (with the exception of $[Mn^{III}(OH)(S^{Me2}N_4(tren))]^+$), the Mn^{III}-OH unit is buried in a sterically crowded pocket, especially in the case of $[Mn^{III}(OH)(\mathbf{1}^{cyp})]^-$ and $[Mn^{III}(OH)(H_3\mathbf{1})]^-$. In the latter complex, both hydrogen-bonding and ligand steric interactions have facilitated the stabilization of the monomeric Mn^{III}-OH complex (Figure 1.7). Thus, in spite of the high tendency of hydroxyl ligands to bridge between two metal centers, monomeric Mn^{III}-OH complexes enhance their stabilities utilizing steric and/ or hydrogen bonding interactions under ambient conditions. Vibrational frequencies for the O–H stretches of the Mn^{III}-OH units have also been reported for four complexes, which range within 3367 – 3643 cm^{-1} (Table 1.1). The solution magnetic susceptibilities for most of these complexes are reported, which are always consistent with the presence of a monomeric high-spin Mn^{III} center in solution.[86,87,91,92] Electronic absorption spectroscopic signatures exhibited by some of these Mn^{III}-OH complexes have been reported, and are summarized in Table 1.1. These features vary significantly depending on the supporting ligand properties, which could be either neutral,[87,93] monoanionic,[90-92] dianionic,[86] or trianionic.[88,89] The overall charges of the Mn^{III}-OH complexes are reflected in their Mn^{III}/Mn^{II} reduction potentials, where more positively charged complexes have a higher reduction potential[98] (Table 1.1). Thus, the series of Mn^{III}-OH complexes reported to date consist of a

broad range (1.7 V) of Mn^{III}/Mn^{II} reduction potentials. The $[Mn^{III}(OH)(OAc)(Me_2EBC)]^+$ complex is a clear outlier having a low reduction potential of -1.17 V despite being monocationic. This could be due to the preferential stabilization of Mn^{III} within the rigid cavity of the Me_2EBC macrocyclic supporting ligand.

1.4 Oxidative Reactivity of Hydroxomanganese(III) Complexes

The most common type of oxidative reactivity in which mid-valent manganese oxidants engages is proton-coupled electron transfer (PCET) reactions.[28,48] These reactions are very common in biology, especially where the independent transfer of a proton or an electron is energetically uphill.[99] In fact, all biological examples of hydroxomanganese adducts take part in PCET at some stage of the mechanism in which they are involved. The M^{III}-OH (M = Fe or Mn) moiety of lipoxygenase undergoes initial PCET, which has been identified as the rate-determining step for peroxidation of fatty acids (Figure 1.3).[6,46-48] The oxidation of water molecules within the OEC involve Mn–OH intermediates that take part in PCET as the active site cluster reaches its most oxidized S_4 state.[27] Finally, the Mn^{III}-OH adduct of Mn-SOD undergoes PCET during its catalytic reactivity.[37] The ubiquitous nature of PCET in biology has motivated research in the development of bio-inspired metal complexes, which are capable of carrying out these reactions.[87,91,94,98,100-102] To date, numerous such oxidants have been reported, and the thermodynamic and kinetic properties of their reactivities have been studied in substantial detail.[56,79,87,91,100,103-118] Most importantly, high-valent Mn^{IV} and Mn^{V}-oxo complexes have been of great interest in this regard, which have displayed highly active PCET reactivities.[16,94,95,119] However, mid-valent hydroxomanganese(III) oxidants that are capable of mediating PCET are less common. In fact, there have been only two reports of such monomeric

M^{III}-OH complexes by Stack[87] and Kovacs,[91] where the respective oxidation of C–H and O–H bond substrates have been described (*vide infra*).

1.4.1 Proton-coupled Electron Transfer Reactions. These reactions are generally defined as the unidirectional transfer of a proton and an electron (or a hydrogen atom; $H^{\bullet} = H^{+} + e^{-}$) in a single or multiple kinetic steps.[102] Thus in these processes, a donor and an acceptor can be identified for the transfer of the $H^{\bullet}$. Classic organic PCET reactions involved a p-block radical as the $H^{\bullet}$ acceptor, and the proton and the electron share the same acceptor orbital following the transfer.[102,108] These reactions are often referred to as hydrogen atom transfer (HAT) reactions. Organic reactions that are driven by HAT processes are common in vitamin B-12 activity, detoxification of reactive oxygen species by antioxidants, and industrially relevant partial oxidation and combustion methodologies.[120]

In many examples of metal oxidants that mediate PCET, the proton and the electron are separated from each other during the transfer process. That is, the electron is generally accepted by the metal center, while the proton ends up at a basic ligand which could be a significant distance away from the metal center. In some examples, the metal center and the basic proton accepting ligand are separated as much as 11 Å, with very small electronic coupling between these sites.[111] In addition, for metal-mediated processes, the proton and the electron transfer processes could occur in single or multiple kinetic steps. Thus, PCET reactions involving metal oxidants are further categorized into concerted proton-electron transfer (CPET), proton transfer followed by electron transfer (PT/ET), and electron transfer followed by proton transfer (ET/PT).[102] Regardless of the distance between the proton and electron accepting sites, and the kinetic details, all PCET reactions are fundamentally similar to each other, and also to organic HAT reactions.[120] The thermodynamic description of these reactions will aid in better

understanding the feasibility and selectivity of these oxidative processes, which is important in designing novel metal oxidants with well-tuned PCET properties.

The thermodynamic feasibility of a PCET reaction has long been described in terms of the enthalpies (ΔH^o) of the reaction, until the elegant work by Mayer and coworkers that revealed that free energies (ΔG^o) are the most appropriate parameters for comparison, especially for PCET involving metals.[108] The differences between these terms arise from the change in entropy that occurs during the reaction. Although solvation entropies for both these forms of the oxidant are often identical for organic systems, metal complexes may have significantly different solvation entropies for their reduced and oxidized forms.[112,116,121,122] Thus herein, all energies are expressed in terms of ΔG^o unless otherwise stated. Similar to any chemical reaction, the thermodynamic feasibility of a PCET reaction is driven by the bond dissociation free energies of the reactants and the products. When the product is a transition metal complex, the bond dissociation free energy of the product can be calculated in terms of the reduction potential of the metal center (E^o), and the dissociation constant of the protonated ligand (pK_a) as described by Bordwell and coworkers (Scheme 1.2).[123] This expression provides a basic understand on how these physical properties can be modified in order to develop better oxidants/ catalysts for PCET. In principle, increasing both E^o and pK_a would lead to the design of more efficient PCET mediators, since it will increase the driving force of the reaction. Nevertheless, in practice, this is an impossible task since for the majority of transition metal complexes, E^o and pK_a are inversely related to each other.[100] However, one could attempt to increase both of these properties simultaneously, by using a strong oxidant and a strong base in unison, instead of intending to utilize a single PCET mediator.[124] Recently, this phenomenon has been used in conjugation with

chiral phosphoric acid catalysis to drive enantioselective organometallic PCET transformations.[125]

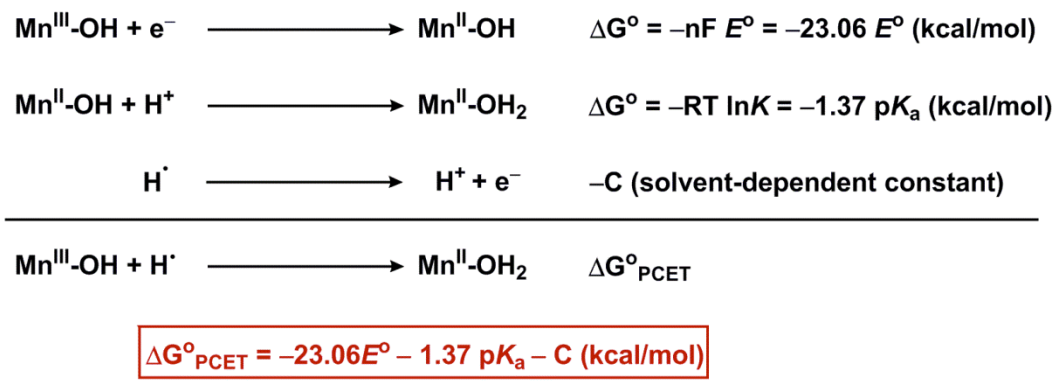

Scheme 1.2. Constituent thermodynamic processes that construct a PCET reaction, and the Bordwell expression that defines their free energy relationships.

In most metal-mediated PCET systems modifying E^o and pK_a can be challenging. As mentioned above, E^o often correlates well with the electronic properties of the supporting ligand, as it dictates the electrophilicity of the metal center (Table 1.1). Consequently, electron rich (anionic and/or soft base-containing) supporting ligands will generate less-reducing metal centers and *vice versa*. On the other hand, the pK_a of the oxidant is an intrinsic property of the proton accepting basic ligand, which can be tuned by the proximity of the proton acceptor to the cationic metal ion. Mid-valent M^{III}-OR type oxidants are very desirable in this case, as the pK_a is tunable by varying both the metal and the R group of the -OR ligand.[91,100] Such a tunability is absent for high-valent $M^{IV/V}$-oxo type oxidants. Thus, the identity of the -OR ligand can be utilized to control the oxidative reactivity of M^{III}-OR complexes. In a recent study by Kovacs and coworkers, the role of pK_a of a Mn^{III}-OR unit (R = H, CH_3, Ph, *p*-NO_2-Ph) on the PCET capabilities of a series of Mn^{III}-OR complexes was investigated.[91] It was concluded that a good

balance between E^o and pK_a is essential for metal oxidants to result in an adequate driving force for a given PCET process.[100]

Extensive thermodynamic studies reported by Mayer and coworkers have furthered the understanding of PCET reactions, and have shown that Marcus theory descriptions of electron transfer reactions do also hold well for PCET processes.[108,120] Consequently, the rate of a PCET process between a donor and an acceptor ($k_{AH/B^{\bullet}}$; cross transfer reaction) could be expressed in terms of their self-exchange rate constants ($k_{AH/A^{\bullet}}$ and $k_{BH/B^{\bullet}}$) as seen in Scheme 1.3. It has been shown that the experimentally measured cross-coupling rate constants correlate well with the calculated values based on the self-exchange rates of each reactant.[108] This phenomenon could also provide an explanation for the long observed differences in PCET rates of equally strong C–H and O–H bond substrates. Multiple PCET studies have exhibited that O–H bonds reacts faster (in some instances by several orders of magnitude[126-129]) than equally strong C–H bonds. Marcus theory cross-relations of PCET reactions reveal that this difference has its basis in the large differences in self-exchange rates of O–H and C–H bond substrates. For an example, Mayer has shown that the PCET rate between ^{t}BuOO$^{\bullet}$ radical and phenol is ~10^5 times greater than that rate with toluene, despite the similar driving forces of these reactions.[108] However, these rates correlated well with the calculated PCET rates using Marcus cross relations, where the ~10^8 difference in the self-exchange rates of phenol and toluene are taken into account. Thus, irrespective of the driving force of the PCET reaction, O–H bonds would react faster than equally strong C–H bond substrates. The reasoning behind these differences in self-exchange rates is still unclear, although several proposals have been made in relation to the differences in intermolecular and solvent interactions, and electronic structures of these functionalities.[130]

Scheme 1.3. PCET rate between an H• donor (HA) and an acceptor (B•) expressed in terms of their self-exchange rate constants ($k_{AH/A}$• and $k_{BH/B}$•). K_{eq} is the equilibrium constant for the cross-exchange reaction, and factor f is ≈1 for PCET reactions.

1.4.2 C–H Bond Oxidation Reactivity of $[Mn^{III}(OH)(PY5)]^{2+}$.

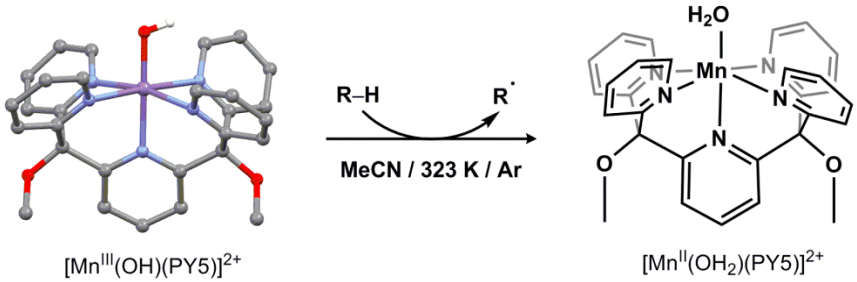

Figure 1.8. PCET reactivity of $[Mn^{III}(OH)(PY5)]^{2+}$ with weak C–H bond substrates (R–H) to generate $[Mn^{II}(OH_2)(PY5)]^{2+}$ and substrate radicals (R•).

In 2005, Stack and coworkers reported the $[Mn^{III}(OH)(PY5)]^{2+}$ (PY5 = 2,6-bis(bis(2-pyridyl)methoxymethane)pyridine) complex (Figure 1.8), which is capable of oxidizing weak C–H bond substrates by PCET, resembling the functionality of Mn-LOs.[87] $[Mn^{III}(OH)(PY5)]^{2+}$ was generated by treating the Mn^{II} precursor complex with PhIO in acetonitrile (90% yield). This complex is, by far, the most reactive Mn^{III}-OH oxidant reported to date, and the only oxidant

capable of oxidizing C–H bond substrates with bond dissociation enthalpies up to 88 kcal/mol. Kinetic studies of these PCET reactions were performed following the changes in electronic absorption in order to calculate second-order rate constants (k_2). $[Mn^{III}(OH)(PY5)]^{2+}$ oxidized DHA at a second order rate of 5.5(5) × 10^{-3} M^{-1} s^{-1} at 50 °C in MeCN, yielding > 80% anthracene as the organic product, which was characterized by GC-MS. This suggests that $[Mn^{III}(OH)(PY5)]^{2+}$ performs the expected stoichiometric PCET reactivity in solution, and generates the $[Mn^{II}(OH_2)(PY5)]^{2+}$ product complex and anthracene. The activation parameters for this PCET process were calculated following an Eyring analysis within the temperature range of 25 – 75 °C, revealing an enthalpy of activation ($\Delta H^{\ddagger}$) of 9.3(5) kcal/mol, and an entropy of activation ($\Delta S^{\ddagger}$) of -36(5) J K^{-1} mol^{-1}. This $\Delta S^{\ddagger}$ is significantly larger than that of the analogous Fe^{III}-OH complex,[131] which implies the presence of a highly ordered transition state for the Mn oxidant. All other organic substrates react with second order rate constants in the same order of magnitude as DHA, although product characterization and quantification for other substrates did not yield conclusive results. It is also important to note that the Polanyi plot (the plot of log k_2 versus the substrate BDE) displayed a slope of -0.1, which is significantly smaller than the expected -0.5 slope from Marcus theory.[120] In addition, the H/D KIE observed for DHA and toluene were 2.4 and 1.5 respectively, which are smaller than the commonly observed large H/D KIEs of high-valent PCET metal oxidants.[94,119,132] These unique differences of this mid-valent manganese oxidant provide important insights into the mechanistic details of its PCET reactivity, as described in detail in chapters 4 and 5. $[Mn^{III}(OH)(PY5)]^{2+}$ also oxidized 2,4,6-tri-tertbutylphenol ($^{4\text{-}t\text{-butyl}}$ArOH) to generate the corresponding phenoxyl radical ($^{4\text{-}t\text{-butyl}}ArO^{\bullet}$) in substoichiometric ratios.[87] The low product yield is suggestive of side reactions of the phenoxyl radical that prevented its full accumulation in solution.

A quasi-reversible reduction potential for the Mn^{III}/Mn^{II} couple of $[Mn^{III}(OH)(PY5)]^{2+}$ was observed at +0.810 V (ΔE_p = 150 mV) versus the standard hydrogen electrode (SHE) in MeCN at 25 °C. This is the largest reduction potential observed for a Mn^{III}-OH complex, which is attributed to the overall dicationic charge of the complex. A pK_a of 13.0(5) was determined for $[Mn^{II}(OH_2)(PY5)]^{2+}$ by optical titrations with singly deprotonated methyl orange and bromocresol green in MeCN at 25 °C. The independent determination of the E^o and pK_a enabled the calculation of a BDE of 82 kcal/mol for $[Mn^{II}(OH_2)(PY5)]^{2+}$ using the Bordwell relationship described in Scheme 1.2. Furthermore, using the calculated E^o and pK_a values, a stepwise PCET process was discounted, revealing a CPET mechanism for the substrate oxidation reactions of $[Mn^{III}(OH)(PY5)]^{2+}$.[87]

1.4.3 TEMPOH Oxidation by $[Mn^{III}(OH)(S^{Me2}N_4(tren))]^+$.

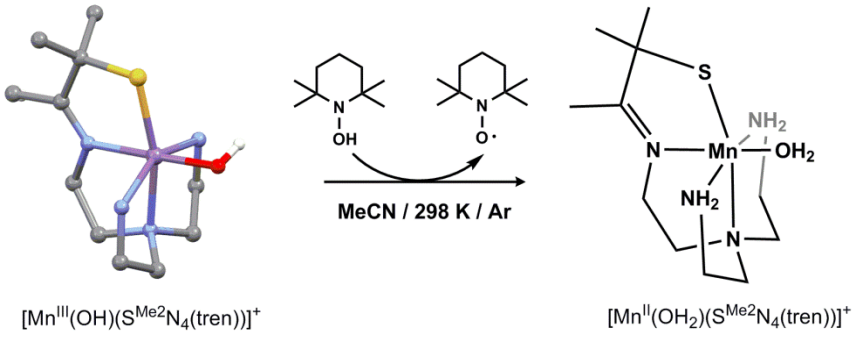

Figure 1.9. TEMPOH oxidation by $[Mn^{III}(OH)(S^{Me2}N_4(tren))]^+$ under ambient conditions to generate $[Mn^{II}(OH_2)(S^{Me2}N_4(tren))]^+$ and TEMPO.

Apart from $[Mn^{III}(OH)(PY5)]^{2+}$, the only other Mn^{III}-OH complex that is capable of mediating PCET is the $[Mn^{III}(OH)(S^{Me2}N_4(tren))]^+$ complex (Figure 1.9) reported by Kovacs and coworkers. This complex is supported by the thiolate-containing pentadentate monoanionic ligand $S^{Me2}N_4(tren)$ ($S^{Me2}N_4(tren)$ = 3-((2-(bis(2-aminoethyl)amino)ethyl)imino)-2-

methylbutane-2-thiolate). $[Mn^{III}(OH)(S^{Me2}N_4(tren))]^+$ is generated by the hydrolysis of the corresponding monooxo-bridged $Mn^{III}Mn^{III}$ dimer, which is derived from dioxygen reduction by $[Mn^{II}(S^{Me2}N_4(tren))]^+$.[91] $[Mn^{III}(OH)(S^{Me2}N_4(tren))]^+$ oxidized the weak O–H bond substrate TEMPOH (BDFE = 66.5 kcal/mol in MeCN[126]) at a second order rate constant of 2.1×10^3 M^{-1} s^{-1} at 25 °C in MeCN. TEMPOH is an ideal substrate to study CPET reactions, since both its deprotonation and one-electron oxidation are very much thermodynamically uphill, compared to the homolytic O–H bond cleavage to generate TEMPO.[126] For this reason, TEMPOH will always perform CPET unless met with a strong acid or a powerful one-electron oxidant. Therefore, the reactivity of $[Mn^{III}(OH)(S^{Me2}N_4(tren))]^+$ with TEMPOH exhibiting an H/D KIE of 3.1 is suggestive of a CPET mechanism with the O–H bond breaking step being the rate-determining step. Addition of 0.1 equiv. portions of TEMPOH to a solution of $[Mn^{III}(OH)(S^{Me2}N_4(tren))]^+$ suggested that the oxidation reaction is 1:1 with respect to the metal complex and the substrate, and the activation parameters were calculated to be $\Delta H^{\ddagger}$ = 8.2 kcal/mol and $\Delta S^{\ddagger}$ = -25.5 J K^{-1} mol^{-1}.

Most importantly, a variable pH electrochemical study (Pourbaix study) was performed on $[Mn^{III}(OH)(S^{Me2}N_4(tren))]^+$ in H_2O, which revealed a pH-dependent Mn^{III}/Mn^{II} reduction potential indicating the involvement of PCET. Consequently, using a modified Bordwell relationship (ΔG^{o}_{PCET} (BDFE) = 23.06 E_{pH} + 1.37 pH + 57.6 kcal/mol), it was shown that the BDFE of the MnO(H)–H unit in $[Mn^{II}(OH_2)(S^{Me2}N_4(tren))]^+$ is 74.0(5) kcal/mol in H_2O. This calculation provided insight into the feasibility of TEMPOH oxidation by $[Mn^{III}(OH)(S^{Me2}N_4(tren))]^+$, as well as its chemically inert behavior toward much stronger C–H bond substrates (1,4-cyclohexadiene (CHD) and DHA). Furthermore, although the direct determination of the BDFE of $[Mn^{II}(OH_2)(S^{Me2}N_4(tren))]^+$ in MeCN was not feasible due to

solvent exchange, an estimated BDFE of 70.1 kcal/mol was reported, based on the differences of solvation enthalpies of $H^{\bullet}$ in MeCN and H_2O. Consequently, $[Mn^{III}(OH)(S^{Me2}N_4(tren))]^+$ could only mediate PCET reactivity with the weak O–H bond substrate TEMPOH (BDFE = 66.5 kcal/mol in MeCN). Lastly, it was also demonstrated that $[Mn^{III}(OH)(S^{Me2}N_4(tren))]^+$ is capable of catalytically oxidizing TEMPOH, with at least 10 turnovers in a continuously oxygenated medium. It should also be noted that the current reports do not describe the optimization of this catalytic activity, in terms of substrate scope or supporting ligand variations.

1.5 Dioxygen Activation to Generate Mn^{III}-OH Complexes

Single or two-electron reduction of dioxygen by manganese(II) complexes is much less common than for their iron analogues, due to the high intrinsic reduction potential for the Mn^{III}/Mn^{II} redox couple.[133] Although numerous mechanistic proposals have been made for Mn-dependent O_2 activation, this process, or, most likely, these processes, remain(s) poorly understood.[134] Mn^{II} complexes that activate O_2 in order to generate Mn^{III}-OH adducts are even more scarce, warranting more work in this area. There have been two main proposed pathways for the formation of O_2-derived Mn^{III}-OH complexes by Borovik and Kovacs.[89,91,135,136] These mechanisms exhibit different Mn:O_2 stoichiometries, which should be distinguishable by manometry or $^{18}O_2$-labeling experiments. O_2-dependent kinetic measurements could also provide insight into the rate determining step of O_2 activation, which is important in elucidating the mechanism. Although not very common, such kinetic measurements have been performed via the addition of variable volumes of O_2 gas, or by the addition of O_2 saturated solvents.[71,135]

Borovik and coworkers proposed the initial formation of a peroxo-bridged $Mn^{III}Mn^{III}$ dimer for dioxygen activation by $[Mn^{II}(OAc)(\mathbf{1}^{cyp})]^{2-}$ (Scheme 1.4), which then undergoes

homolytic O–O bond cleavage to generate a monomeric high-valent Mn^{IV}=O adduct.[89] This highly reactive intermediate abstracts an $H^{\bullet}$ from the solvent (MeCN) to generate the final Mn^{III}-OH product. The evidence for the formation of the high-valent Mn^{IV}=O intermediate comes from the observation of triphenylphosphine oxide formation when the O_2 reaction was carried out in the presence of an excess of triphenylphosphine. Furthermore, when the reaction was carried out in d_3-MeCN, Mn^{III}-OD was observed as the major product, suggesting that the Mn^{IV}=O intermediate abstracts the final $H^{\bullet}$ or $D^{\bullet}$ from the solvent. Finally, the Mn:O stoichiometry was calculated as 2:1 from manometric measurements, which was confirmed by $^{18}O_2$-labeling experiments.

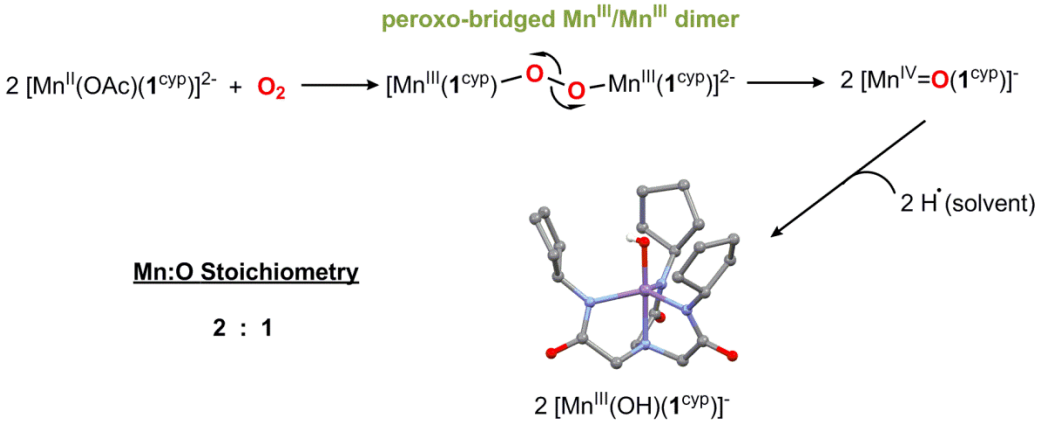

Scheme 1.4. Proposed mechanism for O_2 activation by $[Mn^{II}(OAc)(\mathbf{1}^{cyp})]^{2-}$.

More recently, Kovacs and coworkers reported dioxygen activation by the coordinatively unsaturated $[Mn^{II}(S^{Me2}N_4(6\text{-Me-DPEN}))]^{+}$ complex to form a monooxo-bridged $Mn^{III}Mn^{III}$ dimer ($\{[Mn^{III}(S^{Me2}N_4(6\text{-Me-DPEN}))]_2(\mu\text{-O})\}^{2+}$), with a crystallographically-characterized trans-μ-1,2-peroxo-bridged $Mn^{III}Mn^{III}$ intermediate ($\{[Mn^{III}(S^{Me2}N_4(6\text{-Me-DPEN}))]_2(\textit{trans}\text{-}\mu\text{-}1,2\text{-}O_2)\}^{2+}$.[135,136] This mechanism is supported by spectroscopic, $^{18}O_2$-labeling, as well as O_2-

dependent kinetic investigations of the formation of $\{[Mn^{III}(S^{Me2}N_4(6\text{-Me-DPEN}))]_2(\mu\text{-O})\}^{2+}$.[135] Moreover, the product of the reaction between $[Mn^{II}(S^{Me2}N_4(6\text{-Me-DPEN}))]^+$ and PhIO, was also characterized as $\{[Mn^{III}(S^{Me2}N_4(6\text{-Me-DPEN}))]_2(\mu\text{-O})\}^{2+}$.[136] Together, these data suggest that the mechanism of formation of $\{[Mn^{III}(S^{Me2}N_4(6\text{-Me-DPEN}))]_2(\mu\text{-O})\}^{2+}$ involves homolytic O–O bond cleavage of the observed $\{[Mn^{III}(S^{Me2}N_4(6\text{-Me-DPEN}))]_2(\textit{trans}\text{-}\mu\text{-}1,2\text{-}O_2)\}^{2+}$ species to generate a high-valent Mn^{IV}=O intermediate, which then reacts with a second equivalent of $[Mn^{II}(S^{Me2}N_4(6\text{-Me-DPEN}))]^+$ complex to form $\{[Mn^{III}(S^{Me2}N_4(6\text{-Me-DPEN}))]_2(\mu\text{-O})\}^{2+}$ (Scheme 1.5). Interestingly, the O_2-derived Mn^{III}-OH complex, $[Mn^{III}(OH)(S^{Me2}N_4(tren))]^+$, is also generated by the hydrolysis of a structurally similar monooxo-bridged $Mn^{III}Mn^{III}$ dimer, although in that case, no intermediates have been observed for dioxygen activation (Scheme 1.5A).[91,137] Given the close structural resemblance of $[Mn^{II}(S^{Me2}N_4(6\text{-Me-DPEN}))]^+$ and $[Mn^{II}(S^{Me2}N_4(tren))]^+$, $[Mn^{II}(S^{Me2}N_4(tren))]^+$ presumably activates dioxygen in a similar mechanism. Thus, the mechanism of the formation of $[Mn^{III}(OH)(S^{Me2}N_4(tren))]^+$ from O_2 can be proposed as shown in Scheme 1.5B. In this case, the Mn:O stoichiometry would be 4:1, as 50% of oxygen in Mn^{III}-OH is H_2O-derived. Consequently, an $^{18}O_2$-labelled experiment would only yield 50% ^{18}O-labelled Mn^{III}-OH.

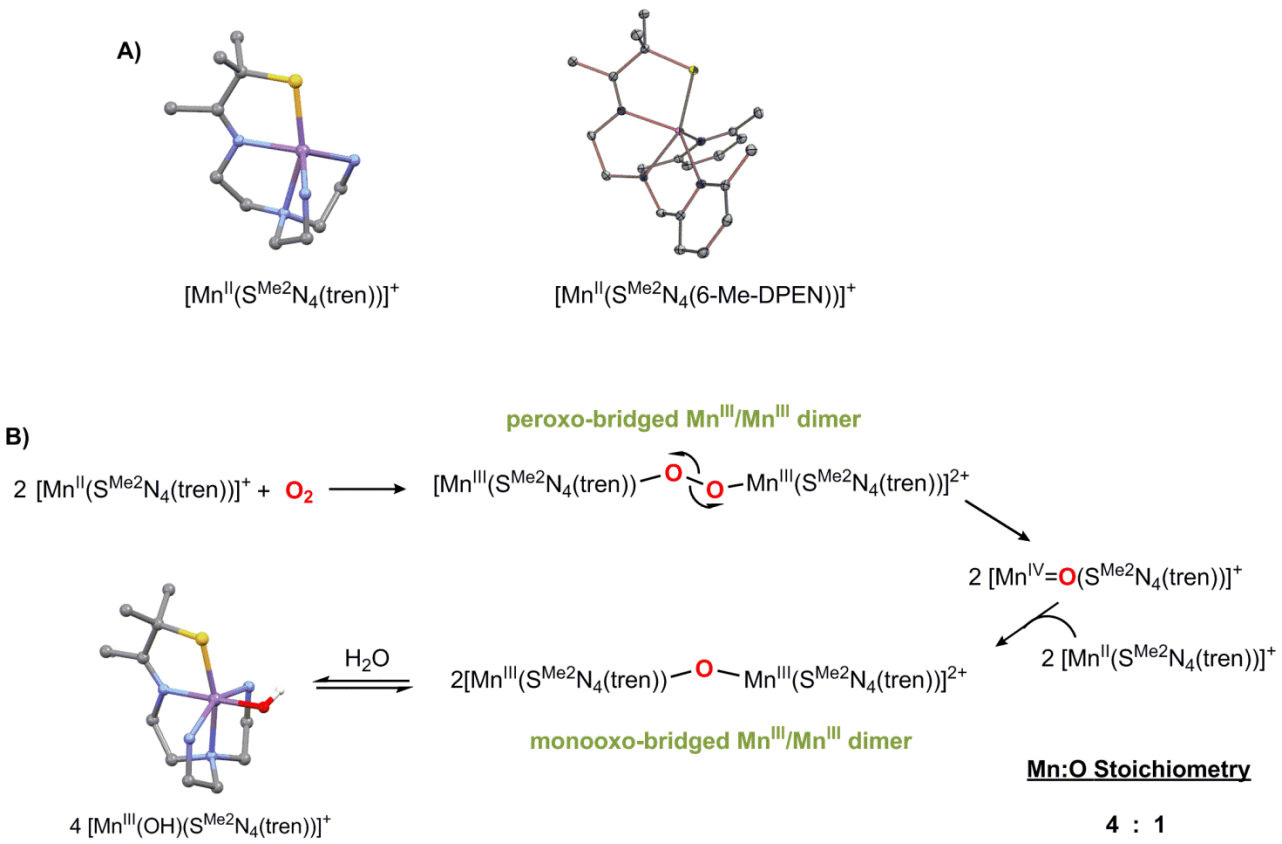

Scheme 1.5. A) X-ray crystal structures of $[Mn^{II}(S^{Me2}N_4(tren))]^+$ and $[Mn^{II}(S^{Me2}N_4(6\text{-Me-DPEN}))]^+$. B) Mechanistic proposal for dioxygen activation by $[Mn^{II}(S^{Me2}N_4(tren))]^+$ to form $[Mn^{III}(OH)(S^{Me2}N_4(tren))]^+$ based on the evidence on $[Mn^{II}(S^{Me2}N_4(6\text{-Me-DPEN}))]^+$.

The work herein describes the design, synthesis and characterization of novel peroxo- and hydroxo-manganese(III) adducts, along with kinetic analysis of the oxidative reactivities of the latter. Variations in geometric and electronic properties of peroxomanganese(III) complexes have revealed the importance of ligand-based steric and electronic properties in modulating the stabilities and reactivities of these often unstable reaction intermediates. Furthermore, novel dioxygen activating Mn^{II} complexes have been synthesized, and the dioxygen activation mechanistic studies are also reported. Moreover, kinetic investigations of the PCET reactivity of

hydroxomanganese(III) complexes have revealed unique reaction profiles unprecedented for such metal oxidants prior to this work.

1.6 References

1. Miller, A.-F., *Curr. Opin. Chem. Biol.* **2004,** *8*, 162-168.
2. Wu, A. J.; Penner-Hahn, J. E.; Pecoraro, V. L., *Chem. Rev.* **2004,** *104*, 903-938.
3. Grove, L. E.; Brunold, T. C., *Comments Inorg. Chem.* **2008,** *29*, 134-168.
4. Jackson, T. A.; Karapetian, A.; Miller, A.-F.; Brunold, T. C., *Biochemistry* **2005,** *44*, 1504-1520.
5. Wennman, A.; Karkehabadi, S.; Oliw, E. H., *Arch. Biochem. Biophys.* **2014,** *555–556*, 9-15.
6. Su, C.; Sahlin, M.; Oliw, E. H., *J. Biol. Chem.* **2000,** *275*, 18830-18835.
7. Su, C.; Oliw, E. H., *J. Biol. Chem.* **1998,** *273*, 13072-13079.
8. Hamberg, M.; Su, C.; Oliw, E., *J. Biol. Chem.* **1998,** *273*, 13080-13088.
9. Bull, C.; Niederhoffer, E. C.; Yoshida, T.; Fee, J. A., *J. Am. Chem. Soc.* **1991,** *113*, 4069-4076.
10. Hearn, A. S.; Tu, C. K.; Nick, H. S.; Silverman, D. N., *J. Biol. Chem.* **1999,** *274*, 24457-24460.
11. Gunderson, W. A.; Zatsman, A. I.; Emerson, J. P.; Farquhar, E. R.; Que, L.; Lipscomb, J. D.; Hendrich, M. P., *J. Am. Chem. Soc.* **2008,** *130*, 14465-14467.
12. Svedružic, D.; Jónsoon, S.; Toyota, C. G.; Reinhardt, L. A.; Ricagno, S.; Lindqvist, Y.; Richards, N. G. J., *Arch. Biochem. Biophys.* **2005,** *433*, 176-192.
13. Hage, R.; Lienke, A., *J. Mol. Catal. A: Chem.* **2006,** *251*, 150-158.
14. Hage, R.; Lienke, A., *Angew. Chem., Int. Ed.* **2006,** *45*, 206-222.
15. Lane, B. S.; Burgess, K., *Chem. Rev.* **2003,** *103*, 2457-2474.
16. Goldberg, D. P., *Acc. Chem. Res.* **2007,** *40*, 626-634.
17. Sibbons, K. F.; Shastri, K.; Watkinson, M., *Dalton Trans.* **2006**, 645-661.
18. Cotruvo, J. J. A.; Stubbe, J., *Metallomics* **2012,** *4*, 1020-1036.
19. McEvoy, J. P.; Brudvig, G. W., *Chem. Rev.* **2006,** *106*, 4455-4483.
20. Messinger, J.; Badger, M.; Wydrzynski, T., *Proc. Natl. Acad. Sci. U. S. A.* **1995,** *92*, 3209-3213.
21. Pecoraro, V. L.; Baldwin, M., J.; Caudle, M. T.; Hsieh, W.-Y.; Law, N., A., *Pure Appl. Chem.* **1998,** *70*, 925-929.
22. Roelfes, G.; Vrajmasu, V.; Chen, K.; Ho, R. Y. N.; Rohde, J.-U.; Zondervan, C.; la Crois, R. M.; Schudde, E. P.; Lutz, M.; Spek, A. L.; Hage, R.; Feringa, B. L.; Münck, E.; Que, L. J., *Inorg. Chem.* **2003,** *42*, 2639-2653.
23. Baldwin, M. J.; Stemmler, T. L.; Riggs-Gelasco, P. J.; Kirk, M. L.; Penner-Hahn, J. E.; Pecoraro, V. L., *J. Am. Chem. Soc.* **1994,** *116*, 11349-56.
24. Pecoraro, V. L.; Baldwin, M. J.; Gelasco, A., *Chem. Rev.* **1994,** *94*, 807-826.
25. Pick, M.; Rabani, J.; Yost, F.; Fridovich, I., *J. Am. Chem. Soc.* **1974,** *96*, 7329-7333.
26. Hsu, J. L.; Hsieh, Y. S.; Tu, C. K.; Oconnor, D.; Nick, H. S.; Silverman, D. N., *J. Biol. Chem.* **1996,** *271*, 17687-17691.

27. Hoganson, C.; Lydakis-Simantiris, N.; Tang, X.-S.; Tommos, C.; Warncke, K.; Babcock, G.; Diner, B.; McCracken, J.; Styring, S., *Photosynth. Res.* **1995,** *46*, 177-184.
28. Babcock, G. T. In *The oxygen-evolving complex in photosystem II as a metallo-radical enzyme*, 1995; Kluwer: 1995; pp 209-215.
29. Westphal, K. L.; Tommos, C.; Cukier, R. I.; Babcock, G. T., *Current Opinion in Plant Biology* **2000,** *3*, 236-242.
30. Tommos, C.; Babcock, G. T., *Acc. Chem. Res.* **1998,** *31*, 18-25.
31. Carrasco, R.; Morgenstern-Badarau, I.; Cano, J., *Inorg. Chim. Acta* **2007,** *360*, 91-101.
32. Leto, D.; Jackson, T., *J. Biol. Inorg. Chem.* **2014,** *19*, 1-15.
33. Porta, J.; Vahedi-Faridi, A.; Borgstahl, G. E. O., *J. Mol. Biol.* **2010,** *399*, 377-384.
34. Koehntop, K. D.; Emerson, J. P.; Que, L., Jr., *J. Biol. Inorg. Chem.* **2005,** *10*, 87-93.
35. Vance, C. K.; Miller, A. F., *Biochemistry* **2001,** *40*, 13079-13087.
36. Vance, C. K.; Miller, A.-F., *J. Am. Chem. Soc.* **1998,** *120*, 461-467.
37. Jackson, T. A.; Brunold, T. C., *Acc. Chem. Res.* **2004,** *37*, 461-470.
38. Minor, W.; Steczko, J.; Stec, B.; Otwinowski, Z.; Bolin, J. T.; Walter, R.; Axelrod, B., *Biochemistry* **1996,** *35*, 10687-10701.
39. Boyington, J.; Gaffney, B.; Amzel, L., *Science* **1993,** *260*, 1482-1486.
40. Fleming, J.; Thiele, B. J.; Chester, J.; O'Prey, J.; Janetzki, S.; Aitken, A.; Anton, I. A.; Rapoport, S. M.; Harrison, P. R., *Gene* **1989,** *79*, 181-188.
41. Gillmor, S. A.; Villasenor, A.; Fletterick, R.; Sigal, E.; Browner, M. F., *Nat. Struct. Mol. Biol.* **1997,** *4*, 1003-1009.
42. Sigal, E.; Craik, C. S.; Highland, E.; Grunberger, D.; Costello, L. L.; Dixon, R. A. F.; Nadel, J. A., *Biochem. Biophys. Res. Commun.* **1988,** *157*, 457-464.
43. Nelson, M. J. a. S. S. P., *Active Oxygen in Biochemistry*. Blackie Academic & Professional, London: 1995.
44. Scarrow, R. C.; Trimitsis, M. G.; Buck, C. P.; Grove, G. N.; Cowling, R. A.; Nelson, M. J., *Biochemistry* **1994,** *33*, 15023-15035.
45. Hörnsten, L.; Su, C.; Osbourn, A. E.; Hellman, U.; Oliw, E. H., *Eur. J. Biochem.* **2002,** *269*, 2690-2697.
46. Glickman, M. H.; Klinman, J. P., *Biochemistry* **1995,** *34*, 14077-14092.
47. Segraves, E. N.; Holman, T. R., *Biochemistry* **2003,** *42*, 5236-5243.
48. Que, L.; Ho, R. Y. N., *Chem. Rev.* **1996,** *96*, 2607-2624.
49. Meunier, B.; de Visser, S. P.; Shaik, S., *Chem. Rev.* **2004,** *104*, 3947-3980.
50. Pal, R.; Negre, C. F. A.; Vogt, L.; Pokhrel, R.; Ertem, M. Z.; Brudvig, G. W.; Batista, V. S., *Biochemistry* **2013,** *52*, 7703-7706.
51. Umena, Y.; Kawakami, K.; Shen, J.-R.; Kamiya, N., *Nature* **2011,** *473*, 55-60.
52. Kupitz, C.; Basu, S.; Grotjohann, I.; Fromme, R.; Zatsepin, N. A.; Rendek, K. N.; Hunter, M. S.; Shoeman, R. L.; White, T. A.; Wang, D.; James, D.; Yang, J.-H.; Cobb, D. E.; Reeder, B.; Sierra, R. G.; Liu, H.; Barty, A.; Aquila, A. L.; Deponte, D.; Kirian, R. A.; Bari, S.; Bergkamp, J. J.; Beyerlein, K. R.; Bogan, M. J.; Caleman, C.; Chao, T.-C.; Conrad, C. E.; Davis, K. M.; Fleckenstein, H.; Galli, L.; Hau-Riege, S. P.; Kassemeyer, S.; Laksmono, H.; Liang, M.; Lomb, L.; Marchesini, S.; Martin, A. V.; Messerschmidt, M.; Milathianaki, D.; Nass, K.; Ros, A.; Roy-Chowdhury, S.; Schmidt, K.; Seibert, M.; Steinbrener, J.; Stellato, F.; Yan, L.; Yoon, C.; Moore, T. A.; Moore, A. L.; Pushkar, Y.; Williams, G. J.; Boutet, S.; Doak, R. B.; Weierstall, U.; Frank, M.; Chapman, H. N.; Spence, J. C. H.; Fromme, P., *Nature* **2014,** *513*, 261-265.

53. Gilchrist, M. L.; Ball, J. A.; Randall, D. W.; Britt, R. D., *Proc. Natl. Acad. Sci. U. S. A.* **1995,** *92*, 9545-9549.
54. Caudle, M. T.; Pecoraro, V. L., *J. Am. Chem. Soc.* **1997,** *119*, 3415-3416.
55. Baldwin, M. J.; Pecoraro, V. L., *J. Am. Chem. Soc.* **1996,** *118*, 11325-11326.
56. Wang, K.; Mayer, J. M., *J. Am. Chem. Soc.* **1997,** *119*, 1470-1471.
57. Bordwell, F. G.; Cheng, J.; Ji, G. Z.; Satish, A. V.; Zhang, X., *J. Am. Chem. Soc.* **1991,** *113*, 9790-9795.
58. VanAtta, R. B.; Strouse, C. E.; Hanson, L. K.; Valentine, J. S., *J. Am. Chem. Soc.* **1987,** *109*, 1425-1434.
59. Kitajima, N.; Komatsuzaki, H.; Hikichi, S.; Osawa, M.; Moro-oka, Y., *J. Am. Chem. Soc.* **1994,** *116*, 11596-11597.
60. Singh, U. P.; Sharma, A. K.; Hikichi, S.; Komatsuzaki, H.; Moro-oka, Y.; Akita, M., *Inorg. Chim. Acta* **2006,** *359*, 4407-4411.
61. Seo, M. S.; Kim, J. Y.; Annaraj, J.; Kim, Y.; Lee, Y.-M.; Kim, S.-J.; Kim, J.; Nam, W., *Angew. Chem., Int. Ed.* **2007,** *46*, 377-380.
62. Annaraj, J.; Cho, J.; Lee, Y.-M.; Kim, S. Y.; Latifi, R.; de Visser, S. P.; Nam, W., *Angew. Chem. Int. Ed.* **2009,** *48*, 4150-4153.
63. Kang, H.; Cho, J.; Cho, K.-B.; Nomura, T.; Ogura, T.; Nam, W., *Chem.--Eur. J.* **2013**, 14119-14125.
64. Cho, J.; Sarangi, R.; Kang, H. Y.; Lee, J. Y.; Kubo, M.; Ogura, T.; Solomon, E. I.; Nam, W., *J. Am. Chem. Soc.* **2010,** *132*, 16977-16986.
65. Groni, S.; Dorlet, P.; Blain, G.; Bourcier, S.; Guillot, R.; Anxolabéhère-Mallart, E., *Inorg. Chem.* **2008,** *47*, 3166-3172.
66. Groni, S.; Blain, G.; Guillot, R.; Policar, C.; Anxolabéhère-Mallart, E., *Inorg. Chem.* **2007,** *46*, 1951-1953.
67. Colmer, H. E.; Geiger, R. A.; Leto, D. F.; Wijeratne, G. B.; Day, V. W.; Jackson, T. A., *Dalton Trans.* **2014,** *43*, 17949-17963.
68. Geiger, R. A.; Wijeratne, G.; Day, V. W.; Jackson, T. A., *Eur. J. Inorg. Chem.* **2012**, 1598-1608.
69. Geiger, R. A.; Chattopadhyay, S.; Day, V. W.; Jackson, T. A., *Dalton Trans.* **2011,** *40*, 1707-1715.
70. Geiger, R. A.; Chattopadhyay, S.; Day, V. W.; Jackson, T. A., *J. Am. Chem. Soc.* **2010,** *132*, 2821-2831.
71. Shook, R. L.; Peterson, S. M.; Greaves, J.; Moore, C.; Rheingold, A. L.; Borovik, A. S., *J. Am. Chem. Soc.* **2011,** *133*, 5810-5817.
72. Shook, R. L.; Gunderson, W. A.; Greaves, J.; Ziller, J. W.; Hendrich, M. P.; Borovik, A. S., *J. Am. Chem. Soc.* **2008,** *130*, 8888-8889.
73. Shook, R. L.; Borovik, A. S., *Inorg. Chem.* **2010,** *49*, 3646-3660.
74. El Ghachtouli, S.; Vincent Ching, H. Y.; Lassalle-Kaiser, B.; Guillot, R.; Leto, D. F.; Chattopadhyay, S.; Jackson, T. A.; Dorlet, P.; Anxolabehere-Mallart, E., *Chem. Commun.* **2013,** *49*, 5696-5698.
75. Seo, M. S.; Kim, J. Y.; Annaraj, J.; Kim, Y.; Lee, Y.-M.; Kim, S.-J.; Kim, J.; Nam, W., *Angew. Chem., Int. Ed.* **2007,** *46*, 377-380.
76. Leto, D. F.; Chattopadhyay, S.; Day, V. W.; Jackson, T. A., *Dalton Trans.* **2013,** *42*, 13014-13025.
77. Creager, S. E.; Raybuck, S. A.; Murray, R. W., *J. Am. Chem. Soc.* **1986,** *108*, 4225-4227.

78. Ching, H. Y. V.; Anxolabehere-Mallart, E.; Colmer, H. E.; Costentin, C.; Dorlet, P.; Jackson, T. A.; Policar, C.; Robert, M., *Chem. Sci.* **2014,** *5*, 2304-2310.
79. Larsen, A. S.; Wang, K.; Lockwood, M. A.; Rice, G. L.; Won, T.-J.; Lovell, S.; Sadílek, M.; Tureček, F.; Mayer, J. M., *J. Am. Chem. Soc.* **2002,** *124*, 10112-10123.
80. Mukhopadhyay, S.; Mandal, S. K.; Bhaduri, S.; Armstrong, W. H., *Chem. Rev.* **2004,** *104*, 3981-4026.
81. Sano, Y.; Weitz, A. C.; Ziller, J. W.; Hendrich, M. P.; Borovik, A. S., *Inorg. Chem.* **2013,** *52*, 10229-10231.
82. Baldwin, M. J.; Law, N. A.; Stemmler, T. L.; Kampf, J. W.; Penner-Hahn, J. E.; Pecoraro, V. L., *Inorg. Chem.* **1999,** *38*, 4801-4809.
83. Zhou, H.-B.; Wang, H.-S.; Chen, Y.; Xu, Y.-L.; Song, X.-J.; Song, Y.; Zhang, Y.-Q.; You, X.-Z., *Dalton Trans.* **2011,** *40*, 5999-6006.
84. Park, Y. J.; Ziller, J. W.; Borovik, A. S., *J. Am. Chem. Soc.* **2011,** *133*, 9258-9261.
85. Cheng, B.; Fries, P. H.; Marchon, J.-C.; Scheidt, W. R., *Inorg. Chem.* **1996,** *35*, 1024-1032.
86. Eichhorn, D. M.; Armstrong, W. H., *J. Chem. Soc., Chem. Commun.* **1992**, 85-87.
87. Goldsmith, C. R.; Cole, A. P.; Stack, T. D. P., *J. Am. Chem. Soc.* **2005,** *127*, 9904-9912.
88. Shirin, Z.; Hammes, B. S.; Young, V. G.; Borovik, A. S., *J. Am. Chem. Soc.* **2000,** *122*, 1836-1837.
89. Shirin, Z.; S. Borovik, A.; G. Young Jr, V., *Chem. Commun.* **1997**, 1967-1968.
90. El Ghachtouli, S.; Lassalle-Kaiser, B.; Dorlet, P.; Guillot, R.; Anxolabehere-Mallart, E.; Costentin, C.; Aukauloo, A., *Energy Environ. Sci.* **2011,** *4*, 2041-2044.
91. Coggins, M. K.; Brines, L. M.; Kovacs, J. A., *Inorg. Chem.* **2013,** *52*, 12383-12393.
92. Eroy-Reveles, A. A.; Leung, Y.; Beavers, C. M.; Olmstead, M. M.; Mascharak, P. K., *J. Am. Chem. Soc.* **2008,** *130*, 4447-4458.
93. Hubin, T. J.; McCormick, J. M.; Alcock, N. W.; Busch, D. H., *Inorg. Chem.* **2001,** *40*, 435-444.
94. Leto, D. F.; Ingram, R.; Day, V. W.; Jackson, T. A., *Chem. Commun.* **2013,** *49*, 5378-5380.
95. Wu, X.; Seo, M. S.; Davis, K. M.; Lee, Y.-M.; Chen, J.; Cho, K.-B.; Pushkar, Y. N.; Nam, W., *J. Am. Chem. Soc.* **2011,** *133*, 20088-20091.
96. Gupta, R.; Borovik, A. S., *J. Am. Chem. Soc.* **2003,** *125*, 13234-13242.
97. Ghachtouli, S. E.; Guillot, R.; Aukauloo, A.; Dorlet, P.; Anxolabéhère-Mallart, E.; Costentin, C., *Inorg. Chem.* **2012,** *51*, 3603-3612.
98. Wijeratne, G. B.; Corzine, B.; Day, V. W.; Jackson, T. A., *Inorg. Chem.* **2014,** *53*, 7622-7634.
99. Reece, S. Y.; Hodgkiss, J. M.; Stubbe, J.; Nocera, D. G., *Proton-coupled electron transfer: the mechanistic underpinning for radical transport and catalysis in biology*. 2006; Vol. 361, p 1351-1364.
100. Wijeratne, G. B.; Day, V. W.; Jackson, T. A., *Dalton Trans.* **2015,** *44*, 3295-3306.
101. Weinberg, D. R.; Gagliardi, C. J.; Hull, J. F.; Murphy, C. F.; Kent, C. A.; Westlake, B. C.; Paul, A.; Ess, D. H.; McCafferty, D. G.; Meyer, T. J., *Chem. Rev. (Washington, DC, U. S.)* **2012,** *112*, 4016-4093.
102. Layfield, J. P.; Hammes-Schiffer, S., *Chem. Rev.* **2013,** *114*, 3466-3494.
103. Porter, T. R.; Mayer, J. M., *Chem. Sci.* **2014,** *5*, 372-380.

104. Warren, J. J.; Menzeleev, A. R.; Kretchmer, J. S.; Miller, T. F.; Gray, H. B.; Mayer, J. M., *J. Phys. Chem. Lett.* **2013,** *4*, 519-523.
105. Manner, V. W.; Lindsay, A. D.; Mader, E. A.; Harvey, J. N.; Mayer, J. M., *Chem. Sci.* **2012,** *3*, 230-243.
106. Saouma, C. T.; Kaminsky, W.; Mayer, J. M., *J. Am. Chem. Soc.* **2012,** *134*, 7293-7296.
107. Warren, J. J.; Mayer, J. M., *J. Am. Chem. Soc.* **2011,** *133*, 8544-8551.
108. Mayer, J. M., *Acc. Chem. Res.* **2010,** *44*, 36-46.
109. Mader, E. A.; Mayer, J. M., *Inorg. Chem.* **2010,** *49*, 3685-3687.
110. Waidmann, C. R.; Zhou, X.; Tsai, E. A.; Kaminsky, W.; Hrovat, D. A.; Borden, W. T.; Mayer, J. M., *J. Am. Chem. Soc.* **2009,** *131*, 4729-4743.
111. Manner, V. W.; Mayer, J. M., *J. Am. Chem. Soc.* **2009,** *131*, 9874-9875.
112. Mader, E. A.; Manner, V. W.; Markle, T. F.; Wu, A.; Franz, J. A.; Mayer, J. M., *J. Am. Chem. Soc.* **2009,** *131*, 4335-4345.
113. Wu, A.; Mader, E. A.; Datta, A.; Hrovat, D. A.; Borden, W. T.; Mayer, J. M., *J. Am. Chem. Soc.* **2009,** *131*, 11985-11997.
114. Manner, V. W.; DiPasquale, A. G.; Mayer, J. M., *J. Am. Chem. Soc.* **2008,** *130*, 7210-7211.
115. Warren, J. J.; Mayer, J. M., *J. Am. Chem. Soc.* **2008,** *130*, 2774-2776.
116. Mader, E. A.; Davidson, E. R.; Mayer, J. M., *J. Am. Chem. Soc.* **2007,** *129*, 5153-5166.
117. Matsuo, T.; Mayer, J. M., *Inorg. Chem.* **2005,** *44*, 2150-2158.
118. Mayer, J. M.; Rhile, I. J., *Biochim. Biophys. Acta, Bioenerg.* **2004,** *1655*, 51-58.
119. Lansky, D. E.; Goldberg, D. P., *Inorg. Chem.* **2006,** *45*, 5119-5125.
120. Mayer, J. M., Thermodynamic Influences on C-H Bond Oxidation. In *Biomimetic Oxidations Catalyzed by Transition Metal Complexes* Meunier, B., Ed. Imperial College Press, London: 2000; pp 1-43.
121. Mader, E. A.; Larsen, A. S.; Mayer, J. M., *J. Am. Chem. Soc.* **2004,** *126*, 8066-8067.
122. Marcus, R. A.; Sutin, N., *Inorg. Chem.* **1975,** *14*, 213-216.
123. Bordwell, F. G.; Cheng, J., *J. Am. Chem. Soc.* **1991,** *113*, 1736-1743.
124. Tarantino, K. T.; Liu, P.; Knowles, R. R., *J. Am. Chem. Soc.* **2013,** *135*, 10022-10025.
125. Rono, L. J.; Yayla, H. G.; Wang, D. Y.; Armstrong, M. F.; Knowles, R. R., *J. Am. Chem. Soc.* **2013,** *135*, 17735-17738.
126. Warren, J. J.; Tronic, T. A.; Mayer, J. M., *Chem. Rev.* **2010,** *110*, 6961-7001.
127. Mayer, J. M.; Mader, E. A.; Roth, J. P.; Bryant, J. R.; Matsuo, T.; Dehestani, A.; Bales, B. C.; Watson, E. J.; Osako, T.; Valliant-Saunders, K.; Lam, W. H.; Hrovat, D. A.; Borden, W. T.; Davidson, E. R., *J. Mol. Catal. A: Chem.* **2006,** *251*, 24-33.
128. Roth, J. P.; Yoder, J. C.; Won, T.-J.; Mayer, J. M., *Science* **2001,** *294*, 2524-2526.
129. Tedder, J. M., *Angew. Chem., Int. Ed. Engl.* **1982,** *21*, 401-410.
130. Litwinienko, G.; Ingold, K. U., *Acc. Chem. Res.* **2007,** *40*, 222-230.
131. Goldsmith, C. R.; Stack, T. D. P., *Inorg. Chem.* **2006,** *45*, 6048-6055.
132. Sastri, C. V.; Lee, J.; Oh, K.; Lee, Y. J.; Lee, J.; Jackson, T. A.; Hirao, H.; Que, L., Jr.; Shaik, S.; Nam, W., *Proc. Natl. Acad. Sci. U. S. A.* **2007,** *104*, 19181-19186.
133. Rybak-Akimova, E. V., In *Mechanisms of Oxygen Binding and Activation at Transition Metal Centers. In Physical Inorganic Chemistry*, Bakac, A., Ed. John Wiley & Sons, Inc.: Hoboken, NJ: 2010; pp 109-188.
134. Horwitz, C. P.; Dailey, G. C., *Comments Inorg. Chem.* **1993,** *14*, 283-319.

135. Coggins, M. K.; Sun, X.; Kwak, Y.; Solomon, E. I.; Rybak-Akimova, E.; Kovacs, J. A., *J. Am. Chem. Soc.* **2013,** *135*, 5631-5640.
136. Coggins, M. K.; Toledo, S.; Shaffer, E.; Kaminsky, W.; Shearer, J.; Kovacs, J. A., *Inorg. Chem.* **2012,** *51*, 6633-6644.
137. Brines, L. M.; Shearer, J.; Fender, J. K.; Schweitzer, D.; Shoner, S. C.; Barnhart, D.; Kaminsky, W.; Lovell, S.; Kovacs, J. A., *Inorg. Chem.* **2007,** *46*, 9267-9277.

CHAPTER 2

Steric and Electronic Influences on the Structures of Peroxomanganese(III) Complexes Supported by Tetradentate Ligands

This work has been reproduced from: Geiger, R. A.; Wijeratne, G. B.; Day, V. W.; Jackson, T. A., *Eur. J. Inorg. Chem.*, **2012**, 1598-1608, with permission from John Wiley & Sons, Inc. The synthetic, spectroscopic, and computational work related to $L^7py_2^H$, $L^7py_2^{6\text{-}Me}$, $L^7py_2^{4\text{-}Me}$, L^7q_2 systems were carried out by Robert A. Geiger.

2.1. Introduction

Mono- and dinuclear manganese-based catalysts that react with dioxygen and its reduced forms have been shown to play crucial roles in both biological and synthetic catalytic pathways.[1-9] With regards to the biological systems, manganese superoxide dismutase (Mn-SOD), which catalyzes the disproportionation of superoxide to hydrogen peroxide and molecular oxygen,[1-5] and manganese ribonucleotide reductase, which facilitates the generation of deoxyribonucleotides from ribonucleotides, serve as important examples.[6-8] Synthetic manganese catalysts are used in a broad range of applications, including textile and fabric bleaching,[9,10] and olefin epoxidation,[11] among others.[12,13] Although detailed catalytic cycles for both the biological and synthetic systems are still being investigated, peroxomanganese(III) species are often proposed as key intermediates.[1,2,14-16] Therefore, descriptive studies on steric and electronic factors that govern the bonding of these peroxomanganese intermediates are of great interest.

A number of biomimetic, mononuclear peroxomanganese(III) complexes (referred to here as $[Mn^{III}(O_2)(L)]^+$) have been reported,[17-27] several of which have been characterized by X-ray crystallography. All structurally characterized $[Mn^{III}(O_2)(L)]^+$ adducts contain side-on peroxo (η^2-O_2) ligands with fairly symmetric $Mn-O_{peroxo}$ bonds that fall within the range of 1.85 to 1.90 Å.[17,22,23,26,27] Alkylperoxomanganese(III) compounds recently reported by Coggins and Kovacs show end-on peroxo binding.[28] There is only indirect, spectroscopic evidence for hydroperoxomanganese(III) species,[21] which stands in contrast to that observed for analogous iron systems, where both peroxo- and hydroperoxoiron(III) adducts have been characterized.[29-31] In addition, while resonance Raman spectroscopy has played a central role in the characterization of peroxoiron species,[29] similar studies of peroxomanganese(III) adducts have been complicated by sample degradation upon irradiation.[20,23] There is significant current interest in understanding

factors that control Mn−O_{peroxo} bond lengths in attempt to stabilize hydroperoxomanganese(III) adducts. Nam and co-workers reported that the binding of anions *trans* to the peroxo unit of the $[Mn^{III}(O_2)(13\text{-TMC})]^+$ complex (13-TMC = 1,4,7,10-tetramethyl-1,4,7,10-tetraazacyclotridecane) results in a shift in the peroxo from a side-on to a more end-on binding mode, as evidenced by an increased nucleophilicity of the peroxo ligand upon anion binding.[17]

We previously reported that $[Mn^{III}(O_2)(L)]^+$ adducts supported by the $L^7py_2^H$ and $L^7py_2^{6\text{-}Me}$ ligands (Figure 2.1; $L^7py_2^H$ = 1,4-bis(2-pyridylmethyl)-1,4-diazepane; $L^7py_2^{6\text{-}Me}$ = 1,4-bis(6-methyl-2-pyridylmethyl)-1,4-diazepane) have different magnetic circular dichroism (MCD) profiles that correlate to differences in Mn-O_2 bonding.[18] Specifically, for $[Mn^{III}(O_2)(L^7py_2^{6\text{-}Me})]^+$ there is a red-shift in the lowest-energy Mn^{III} $d_z^2 \rightarrow d_{xy}$ transition (band 1 or the HOMO-to-LUMO transition; see Scheme 2.1) by ~3 000 cm^{-1} relative to $[Mn^{III}(O_2)(L^7py_2^H)]^+$. With the aid of DFT computations, this red-shift was attributed to a change from a side-on-bound peroxo ligand with symmetric Mn−O_{peroxo} distances of 1.87 Å in $[Mn^{III}(O_2)(L^7py_2^H)]^+$ to a more asymmetrically bound peroxo ligand with Mn−O_{peroxo} distances of 1.87 and 1.91 Å for $[Mn^{III}(O_2)(L^7py_2^{6\text{-}Me})]^+$.[18] The acceptor orbital involved in this electronic transition is the Mn d_{xy} molecular orbital (MO), which is strongly Mn−O_{peroxo} σ-antibonding, and thus stabilized by this modest lengthening of the Mn−O_{peroxo} bond (Scheme 2.1). The Mn−O_{peroxo} bond elongation for the 6-Me-substituted complex was attributed to a reduction in the Lewis acidity of the Mn^{III} center due to the presence of the electron-donating 6-Me groups. However, in a subsequent study we reported that electronic absorption data for $[Mn^{III}(O_2)(L^7py_2^{4\text{-}Me})]^+$, which contains 4-Me-substituted pyridines (Figure 2.1), are essentially identical to those of $[Mn^{III}(O_2)(L^7py_2^H)]^+$.[19] This leads to the alternative proposal that steric clash between the 6-Me substituents and the peroxo ligand in $[Mn^{III}(O_2)(L^7py_2^{6\text{-}Me})]^+$ is the dominant contributor to the elongated Mn−O_{peroxo}

bond. Indeed, structural models developed using density functional theory (DFT) computations showed that steric bulk in the 6-position of $[Mn^{III}(O_2)(L^7py_2^{6\text{-}Me})]^+$ causes the pyridine rings to cant above and below the equatorial plane, which leads to crowding of the peroxide binding pocket by the 6-Me substituents and the pyridine rings. This conclusion was reinforced by the observation that the electronic absorption spectrum of the quinoline-containing analogue $[Mn^{III}(O_2)(L^7q_2)]^+$ (Figure 2.1), in which the quinolinylmethyl arms must cant significantly to ease steric crowding in the equational plane, is essentially identical to that of $[Mn^{III}(O_2)(L^7py_2^{6\text{-}Me})]^+$.[19] However, this proposal was made on the basis of electronic absorption data alone, and it is well-established from previous work that MCD spectroscopy offers a far more sensitive probe of Mn^{III} *d-d* transition energies. In addition, electronic variations in this ligand family have been comparatively unexplored, leaving it unclear how changes in the pyridine donor properties influence the Mn^{III}-O_2 unit.

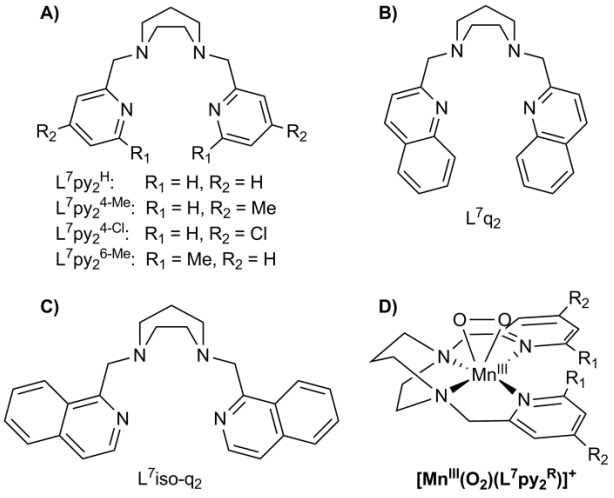

Figure 2.1. Structures of A) $L^7py_2^R$, B) L^7q_2, and C) L^7iso-q_2 ligands, and D) schematic representation of a $[Mn^{III}(O_2)(L^7py_2^R)]^+$ complex.

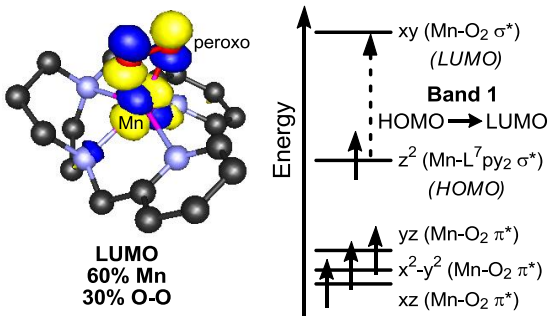

Scheme 2.1. DFT-computed structure of $[Mn^{III}(O_2)(L^7py_2{}^H)]^+$ with overlay contour plot of the LUMO (left) and Mn^{III} d orbital splitting diagram (right).

To more fully define the origin of spectral perturbations for the $[Mn^{III}(O_2)(L^7py_2{}^R)]^+$ series, and thereby explore steric and electronic influences on Mn^{III}-O_2 bonding, we herein report MCD and variable-temperature, variable-field (VTVH) MCD experiments for $[Mn^{III}(O_2)(L)]^+$ adducts supported by the previously reported $L^7py_2{}^{4\text{-Me}}$ and L^7q_2 ligands[19] as well as the new $L^7py_2{}^{4\text{-Cl}}$ and L^7iso-q_2 ligands that contain 4-chloropyridinylmethyl and isoquinolinylmethyl pendant arms, respectively (Figure 2.1). Peroxomanganese(III) complexes supported by the $L^7py_2{}^{4\text{-Me}}$, $L^7py_2{}^H$, and $L^7py_2{}^{4\text{-Cl}}$ ligand series permit comparison of electronic effects, as these ligands differ only in the nature of the pyridine substituent in the four-position, where steric effects on the peroxo ligand are minimized. The L^7iso-q_2 ligand offers an electronic complement to L^7q_2 that lacks the intra-ligand steric effects between the quinoline rings that are present when the latter ligand coordinates a metal. Along with supporting DFT computations, the MCD data firmly establish that steric clash between six-appended pyridines or quinoline groups leads to the formation of more asymmetrically bound peroxo ligands for the $L^7py_2{}^{6\text{-Me}}$ and L^7q_2 systems. Only a small spectral perturbation is observed when the electronic properties of the supporting ligand are altered, showing that either changes in the electronic properties of the supporting ligand do not greatly affect Mn^{III}-O_2 bonding or that the variation in the electronic properties are too conservative to appreciably perturb the peroxomanganese(III) unit.

2.2. Experimental Section

2.2.1. Materials. All chemicals were obtained from commercial vendors at ACS reagent-grade or better and were used without further purification. Acetonitrile and ether were dried using a PureSolv Micro system (Innovative Technologies) and degassed using standard techniques.[47] Butyronitrile and acetone were used as received. Manipulations of Mn^{II} complexes were carried out under argon using a glovebox or Schlenk techniques.

2.2.2. Instrumentation. ^{1}H NMR spectra were obtained on a Bruker DRX 400 MHz NMR spectrometer. Electronic absorption spectra were recorded on a Cary 50 Bio spectrophotometer (Varian) interfaced with a Unisoku cryostat (USP-203-A). ESI-mass spectrometry experiments were performed using an LCT Primers MicroMass electrospray-ionization time-of-flight instrument. Magnetic circular dichroism (MCD) spectra were collected on a spectropolarimeter (Jasco J-815) interfaced with a magnetocryostat (Oxford Instruments SM-4000-8).

2.2.3. Ligand Synthesis. 1,4-bis(2-pyridylmethyl)-1,4-diazepane ($L^7py_2^H$), 1,4-bis(6-methyl-2-pyridylmethyl)-1,4-diazepane ($L^7py_2^{6\text{-}Me}$), 1,4-bis(4-methyl-2-pyridylmethyl)-1,4-diazepane ($L^7py_2^{4\text{-}Me}$), and 1,4-bis(2-quinolinylmethyl)-1,4-diazepane (L^7q_2) were prepared as previously described.[18,19,48] Using a similar procedure, 1,4-bis(4-chloro-2-pyridylmethyl)-1,4-diazepane ($L^7py_2^{4\text{-}Cl}$) was prepared by reacting homopiperazine with 4-chloropicolinaldehyde (70% yield) and 1,4-bis(2-isoquinolinylmethyl)-1,4-diazepane (L^7iso-q_2) was prepared by reacting homopiperazine with 1-(bromomethyl)isoquinoline hydrobromide (65% yield). ^{1}H NMR data (400 MHz) for $L^7py_2^{4\text{-}Cl}$ and L^7iso-q_2 are as follows: $L^7py_2^{4\text{-}Cl}$ ($CDCl_3$; δ) 8.43 (d, 2H J_{HH} = 4.28), 7.54 (d, 2H, J_{HH} = 1.52), 7.17 (dd, 2H, J_{HH} = 2.64), 3.82 (s, 4H), 2.82 (t, 4H, J_{HH} = 3.44), 2.78 (s, 4H), 1.86 (p, 2H, J_{HH} = 4.8) and L^7iso-q_2 ($CDCl_3$; δ) 8.56 (d, 2H, J_{HH} = 8.4), 8.41

(d, 2H, J_{HH} = 5.72), 7.81 – 7.55 (m, 8H), 4.19 (s, 4H), 2.85 (t, 4H, J_{HH} = 5.92), 2.74 (s, 4H), 1.81 (p, 2H, J_{HH} = 5.96).

2.2.4. Preparation of Mn^{II} Complexes. The $[Mn^{II}(L^7py_2^R)(OTf)_2]$ (R = H, 4-Me, 6-Me) and $[Mn^{II}(L^7q_2)(OTf)_2]$ complexes were prepared by a previously reported metalation reaction.[18,19] The $[Mn^{II}(L^7iso\text{-}q_2)(OTf)_2]$ and $[Mn^{II}(L^7py_2^{4\text{-}Cl})(OTf)_2]$ complexes were synthesized with excellent yields (>85%) by reacting the $L^7py_2^{4\text{-}Cl}$ or $L^7iso\text{-}q_2$ ligands with $Mn(OTf)_2$ in MeCN solution in a 1:1 molar ratio. $Mn(OTf)_2$ was prepared by a previously reported procedure by reacting equimolar amounts of $(CH_3)_3Si(OTf)$ and anhydrous $MnCl_2$.[23] Details of a representative preparation for a metal complex are as followed. To a stirred solution of 757.45 mg (2.145 mmol) of $Mn(OTf)_2$ in 10 mL of MeCN was added $L^7iso\text{-}q_2$ (821 mg, 2.145 mmol) in 10 mL of MeCN. The yellow solution was stirred overnight and evaporated under reduced pressure. The solid thus obtained was dried in vacuum. Recrystallization of the crude solid from MeCN/diethyl ether afforded nearly colorless crystals of $[Mn(L^7iso\text{-}q_2)](OTf)_2$ (1.42 g, 90%). Crystals suitable for X-ray diffraction experiments were grown from subsequent recrystallization using acetone/diethyl ether. ESI-MS data is as follows: found M^+ $\{[Mn(L^7iso\text{-}q_2)](Cl)\}^+$: 472.1, $\{[Mn(L^7iso\text{-}q_2)](Cl)\}^+$ requires M^+ 472.1; and found M^+ $\{[Mn(L^7py_2^{4\text{-}Cl})](Cl)\}^+$: 440.0, $\{[Mn(L^7py_2^{4\text{-}Cl})](Cl)\}^+$ requires M^+, 440.0, where in each case the triflate ions were replaced by a chloride ion in the mass spectrometer. Magnetic moments for $[Mn(L^7iso\text{-}q_2)(OTf)_2]$ and $[Mn(L^7py_2^{4\text{-}Cl})(OTf)_2]$ were determined using the ^1H NMR method of Evans in CD_3CN at 298 K.[41] Elemental analysis $[Mn^{II}(L^7iso\text{-}q_2)(OTf)_2]\cdot 0.6C_6H_{15}N\cdot 1.5H_2O$: $MnC_{30.6}H_{38}N_{4.6}O_{7.5}F_6S_2$ calcd (%): C 44.59, H 4.66, N 7.82; found (%): C 44.66, H 4.7, N 7.75; and $[Mn^{II}(L^7py_2^{4\text{-}Cl})(OTf)_2]\cdot 0.3C_4H_8O\cdot 0.75H_2O$: $MnC_{20.2}H_{23.9}N_4O_{7.05}F_6S_2$ calcd (%): C 32.81, H 3.26, N 7.58; found (%): C 32.50, H 3.66, N 7.98.

2.2.5. X-ray Crystallography. Single crystals of $[Mn(L^7iso\text{-}q_2)(OTf)_2]$ were grown by vapor diffusion of ether into an acetone solution of the complex. Single crystals of $[Mn(L^7py_2{}^{4\text{-}Cl})(OTf)_2]$ were grown by vapor diffusion of ether in to an acetonitrile solution of the complex at room temperature. Complete sets of unique diffracted intensities were measured for specimens of $[Mn(L^7iso\text{-}q_2)(OTf)_2]$ and $[Mn(L^7py_2{}^{4\text{-}Cl})(OTf)_2]$ using monochromated CuKα radiation (λ= 1.54178 Å) on a Bruker Single Crystal Diffraction System equipped with Helios multilayer x-ray optics, an APEX II CCD detector and a Bruker MicroSTAR microfocus rotating anode x-ray source operated at 45 kV and 60 mA. Lattice constants for each sample were determined with the Bruker SAINT software package. The Bruker software package SHELXTL was used to solve both structures using "direct methods" techniques. All stages of weighted full-matrix least-squares refinement were conducted using F_o^2 data with the SHELXTL Version 6.10 software package.[46] Details concerning X-ray diffraction experiments and data analysis are provided in the Appendix (A1). CCDC-854444 and CCDC-854443 contain the supplementary crystallographic data for $[Mn(L^7iso\text{-}q_2)(OTf)_2]$ and $[Mn(L^7py_2{}^{4\text{-}Cl})(OTf)_2]$, respectively. These data can be obtained free of charge from The Cambridge Crystallographic Data Centre via www.cccdc.cam.ac/data_request/cif.

2.2.6. In Situ Preparation of Peroxomanganese(III) Complexes. The peroxomanganese(III) intermediates were formed by treating 2.5 mM MeCN solutions of metal complexes with 5 equivalents H_2O_2 (30% in H_2O) and 0.5 equivalents triethylamine at -40 ^oC. The formation of the peroxomanganese(III) complexes was evident from the appearance of characteristic bands in the electronic absorption spectra and by ESI-mass spectrometry. Found M^+ $\{[Mn^{III}(O_2)(L^7py_2{}^{4\text{-}Cl})]\}^+$: 437.0, $\{[Mn^{III}(O_2)(L^7py_2{}^{4\text{-}Cl})]\}^+$ requires: M^+ 437.0; and found M^+ $\{[Mn^{III}(O_2)(L^7iso\text{-}q_2)]\}^+$: 469.1, $\{[Mn^{III}(O_2)(L^7iso\text{-}q_2)]\}^+$ requires: M^+ 469.1.

2.2.7. Magnetic Circular Dichroism Experiments. 15 mM frozen glass samples of $[Mn^{III}(O_2)(L^7py_2^{4\text{-}Me})]^+$, $[Mn^{III}(O_2)(L^7py_2^{4\text{-}Cl})]^+$, $[Mn^{III}(O_2)(L^7iso\text{-}q_2)]^+$ and $[Mn^{III}(O_2)(L^7q_2)]^+$ were prepared in butyronitrile at -40° C. Butyronitrile was used instead of MeCN, as the former produces an optical-quality glass upon freezing. The absorption spectra of these samples are essentially identical in acetonitrile and butyronitrile. Once formation of the peroxomanganese(III) species was complete (as monitored by UV-visible spectroscopy), the samples were cooled to -80° C, transferred to pre-cooled MCD cells, and flash-frozen in liquid N_2. The obtained MCD spectra were measured in mdeg (θ) and converted to Δε ($M^{-1}cm^{-1}$) using the standard conversion factor $\Delta\varepsilon = \theta/(32980 \cdot c \cdot d)$, where *c* is the concentration of the sample and *d* is the path length. Variable-temperature, variable-field MCD data were taken from full spectra collected at 2, 4, 8, and 15 K for positive and negative field strengths of 1 to 7 T in 1 T increments.

2.2.8. Density Functional Theory Calculations. The *ORCA* 2.8 software package was used for all DFT computations.[49] Initial models of $[Mn^{III}(O_2)(L^7py_2^{4\text{-}Cl})]^+$ and $[Mn^{III}(O_2)(L^7iso\text{-}q_2)]^+$ were built using the X-ray coordinates of the corresponding Mn^{II} complexes, then adding side-on peroxo ligands. The pyridyl and quinolinyl rings were rotated from a canted position to a planar position. All calculations were converged to the $S = 2$ spin state. Geometry optimizations employed the Becke-Perdew (BP86) functional[50,51] and the SVP (Ahlrichs split valence polarized)[52,53] basis set with the SV/J auxiliary basis set for all atoms except for manganese, nitrogen, and oxygen, where the larger TZVP (Ahlrichs triple-ζ valence polarized)[20] basis set in conjunction with the TZV/J auxiliary basis set were used. For these calculations, the resolution of identity (RI) approximation,[54] was used. Solvation effects associated with acetonitrile (dielectric constant ε = 36.6) were incorporated using COSMO, as implemented in *ORCA*.[55]

Vibrational frequency calculations performed for fully-optimized models revealed no negative frequencies. Optimized structures for other peroxomanganese(III) complexes are as described previously and used here for comparative purposes.[18,19] To determine the dependence of the optimized geometries on the choice of density functional, geometry optimizations were also performed for all peroxomanganese(III) complexes examined in this study using the hybrid B3LYP functional[56-58] and the same basis functions used in the BP86 calculations. Electronic transition energies and intensities were computed for all geometry optimized models using the time-dependent DFT (TD-DFT) method.[59-62] These calculations employed the same basis sets used for the geometry optimizations. Cartesian coordinates of all geometry-optimized models, as well as the corresponding TD-DFT-computed absorption spectra, are included in the Appendix (A1).

2.3. Results and Discussion

2.3.1. Structural properties of Mn^{II} complexes. Figure 2.2 displays ORTEP diagrams and space filling models for $[Mn^{II}(L^7iso\text{-}q_2)(OTf)_2]$ and $[Mn^{II}(L^7py_2{}^{4\text{-}Cl})(OTf)_2]$. Selected bond lengths and angles are given in Table 2.1. The X-ray structure of $[Mn^{II}(L^7iso\text{-}q_2)(OTf)_2]$ has a six-coordinate Mn^{II} center with the tetradentate $L^7iso\text{-}q_2$ ligand bound to the manganese center in a distorted *trans* conformation, where the four N atoms create a ruffled plane. The two axial coordination sites are occupied by triflate ions where the O(11)−Mn−O(21) bond angle is 145.17°. Thus, these ligands deviate substantially from idealized axial positions. An acetone molecule also present in the asymmetric unit does not interact with the Mn^{II} center (Mn^{II}−O distance of 6.649 Å). The Mn(II)−ligand bond lengths range from ~2.1 to 2.3 Å and are typical of a high-spin manganese(II) ion.[43,44]

The crystals of $[Mn^{II}(L^7py_2{}^{4\text{-Cl}})(OTf)_2]$, which are of the P2(1) space group (at 100 K), contain four independent molecules (referred to as A – D) in the asymmetric unit. The metric parameters for these four molecules are quite similar (Table A1.5), and in each case the Mn^{II} center is six-coordinate with a tetradentate $L^7py_2{}^{4\text{-Cl}}$ ligand and two triflate ligands. However, there are two key structural parameters that differentiate these molecules. First, the Mn−OTf bond length for the triflate on the ethyl face of the $L^7py_2{}^{4\text{-Cl}}$ ligand (Mn−O(11)) ranges from 2.042(11) to 2.286(14). Second, the angle between the O(11)−Mn−O(21) bonds is ~116º for molecules A and D and ~151º for molecules B and C (Table 2.1). These variations are likely related to one another and are tentatively attributed to greater steric crowding of the axial binding site on the ethyl face of the $L^7py_2{}^{4\text{-Cl}}$ ligand.

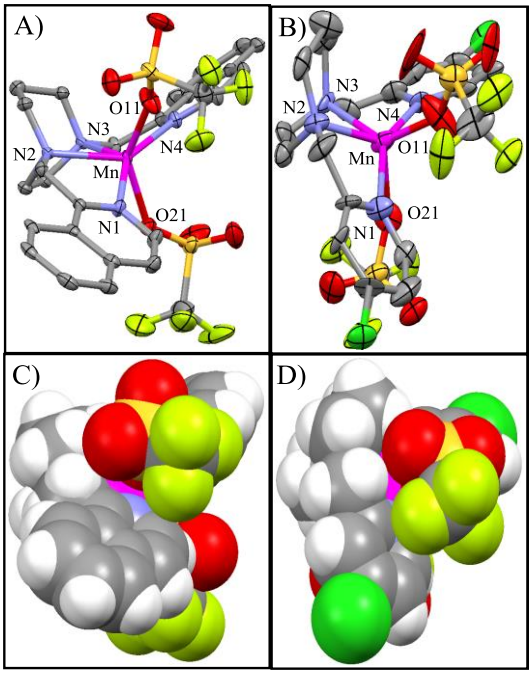

Figure 2.2. ORTEP diagrams of A) $[Mn^{II}(L^7iso\text{-}q_2)(OTf)_2]$ and B) $[Mn^{II}(L^7py_2{}^{4\text{-Cl}})(OTf)_2]$. Space filling models for C) $[Mn^{II}(L^7iso\text{-}q_2)(OTf)_2]$ and B) $[Mn^{II}(L^7py_2{}^{4\text{-Cl}})(OTf)_2]$. For ORTEP diagrams hydrogen atoms have been removed for clarity. Significant interatomic distances and angles are listed in Table 2.1.

Table 2.1. Selected Bond Lengths (Å) and Angles (°) for Mn(II) Complexes.

Complex	$[Mn(L^7iso\text{-}q_2)(OTf)_2]$	$[Mn(L^7py_2^{4\text{-}Cl})(OTf)_2]$[a]
Mn–N(1)	2.231(3)	2.250(26)[b]
Mn–N(2)	2.279(2)	2.317(17)[b]
Mn–N(3)	2.248(3)	2.302(77)[b]
Mn-–N(4)	2.246(3)	2.286(11)[b]
Mn–O(11)	2.149(3)	A: 2.151(7) B: 2.193(6) C: 2.286(14) D: 2.042(11)
Mn–O(21)	2.228(2)	2.235(39)[b]
N(1)–Mn–N(4)	148.49(9)	148.4(2.3)[b]
N(2)–Mn–N(3)	71.59(9)	70.2(7)[b]
O(11)–Mn–O(21)	145.17(11)	A: 116.4(3) B: 152.8(3) C: 151.2(4) D: 119.4(5)

[a] Metric parameters represent the average of four independent molecules (A – D) in the asymmetric unit, with the exception of the Mn-O(11) distance and O(11)-Mn-O(21) angle, for which individual values are listed. Metric parameters for individual molecules A - D are listed in the Appendix (A1). [b]For these parameters, the standard deviation refers to the variation over the four independent molecules in the asymmetric unit.

The properties of $[Mn^{II}(L^7iso\text{-}q_2)(OTf)_2]$ and $[Mn^{II}(L^7py_2^{4\text{-}Cl})(OTf)_2]$ in solution were probed using ESI-MS experiments and the ^1H NMR method of Evans.[32] ESI-MS data sets collected for $[Mn^{II}(L^7iso\text{-}q_2)(OTf)_2]$ and $[Mn^{II}(L^7py_2^{4\text{-}Cl})(OTf)_2]$ revealed major ion peaks at *m/z* = 472.1 and 440.0, consistent with $\{Mn^{II}(L^7iso\text{-}q_2)(Cl)\}^+$ and $\{Mn^{II}(L^7py_2^{4\text{-}Cl})(Cl)\}^+$ ions, respectively, where a Cl^- ion was substituted for the OTf^- ions in the mass spectrometer. The ^1H NMR experiments afforded effective magnetic moments of 6.3 (Diam. Corr. = 0.5) and 6.1 (Diam. Corr. = 0.6) μ_B for $[Mn(L^7iso\text{-}q_2)(OTf)_2]$ and $[Mn(L^7py_2^{4\text{-}Cl})(OTf)_2]$ in deuterated acetonitrile at room temperature. These values coincide well with the theoretical effective magnetic moment of 5.9 μ_B expected for mononuclear high-spin manganese(II) systems. On the basis of these experiments, we conclude the mononuclearity observed for $[Mn(L^7iso\text{-}q_2)(OTf)_2]$ and $[Mn(L^7py_2^{4\text{-}Cl})(OTf)_2]$ in the solid state is retained in MeCN solution.

2.3.2. Formation of Peroxomanganese(III) Complexes. The absorption spectra of acetonitrile solutions of $[Mn^{II}(L^7iso\text{-}q_2)(OTf)_2]$ and $[Mn^{II}(L^7py_2^{4\text{-}Cl})(OTf)_2]$ are featureless at

energies below 33 000 cm^{-1}, as expected for high spin Mn^{II} complexes. Treatment of these complexes with 5 equivalents H_2O_2 and 0.5 equivalents triethylamine at -40^o C results in the formation of new absorption features in the visible region (Figure 2.3, top). This behavior is reminiscent of that observed for Mn^{II} complexes supported by the closely related $L^7py_2^R$ (R = H, 6-Me, and 4-Me) and L^7q_2 ligands (Figure 2.3, center and bottom), where the formation of $[Mn^{III}(O_2)(L)]^+$ adducts accounts for the appearance of new absorption bands in the visible region.[18,19] Indeed, mass spectrometry experiments on solutions of $[Mn^{II}(L^7iso\text{-}q_2)(OTf)_2]$ and $[Mn^{II}(L^7py_2^{4\text{-}Cl})(OTf)_2]$ following treatment with H_2O_2 and base revealed major ion peaks consistent with $[Mn^{III}(O_2)(L^7iso\text{-}q_2)]^+$ and $[Mn^{III}(O_2)(L^7py_2^{4\text{-}Cl})]^+$, respectively, supporting the formulation of these new chromophores as peroxomanganese(III) adducts. Although these peroxomanganese(III) species are relatively stable at -40 ºC, they decay within minutes to hours at 0 ºC (Table 2.2). The $[Mn^{III}(O_2)(L^7iso\text{-}q_2)]^+$ intermediate is the most stable peroxomanganese(III) adduct supported by the L^7-family of ligands, exhibiting a half-life at 0 ºC of 30 minutes.

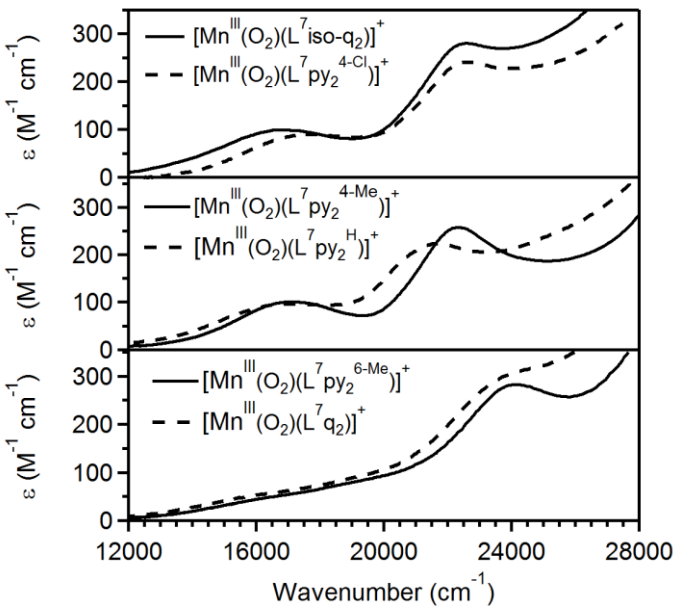

Figure 2.3. Electronic absorption spectra of $[Mn^{III}(O_2)(L^7iso\text{-}q_2)]^+$, $[Mn^{III}(O_2)(L^7py_2{}^{4\text{-}Cl})]^+$ (top), $[Mn^{III}(O_2)(L^7py_2{}^{4\text{-}Me})]^+$, $[Mn^{III}(O_2)(L^7py_2{}^{H})]^+$ (center), $[Mn^{III}(O_2)(L^7py_2{}^{6\text{-}Me})]^+$, and $[Mn^{III}(O_2)(L^7q_2)]^+$ (bottom) in acetonitrile at -40° C.

Table 2.2. Properties of Peroxomanganese(III) Complexes Supported by $L^7py_2{}^R$, L^7q_2 and $L^7iso\text{-}q_2$ Ligands.

complex	λ_{max} (cm^{-1}) (ε(M^{-1} cm^{-1}))	$t_{1/2}$ at 0 °C
$[Mn^{III}(O_2)(L^7iso\text{-}q_2)]^+$	22 420 (291)	30 min
	17 040 (112)	
$[Mn^{III}(O_2)(L^7py_2{}^{4\text{-}Cl})]^+$	22 620 (262)	10 min
	17 610 (102)	
$[M^{III}(O_2)(L^7q_2)]^{+\,b}$	24 050 (305)	4 min
	~16 500 (70)	
$[Mn^{III}(O_2)(L^7py_2{}^{H})]^{+\,a}$	21 690 (280)	15 min
	17 000 (120)	
$[Mn^{III}(O_2)(L^7py_2{}^{4\text{-}Me})]^{+\,b}$	22 470 (260)	6 min
	~17 000 (100)	
$[Mn^{III}(O_2)(L^7py_2{}^{6\text{-}Me})]^{+\,a}$	24 100 (280)	6 min
	~16 130 (80)	

[a] From reference 18. [b] From reference 19.

The absorption spectra of $[Mn^{III}(O_2)(L^7iso\text{-}q_2)]^+$ and $[Mn^{III}(O_2)(L^7py_2{}^{4\text{-}Cl})]^+$ are nearly identical to those previously reported for $[Mn^{III}(O_2)(L^7py_2{}^{H})]^+$ and $[Mn^{III}(O_2)(L^7py_2{}^{4\text{-}Me})]^+$,[18,19]

consisting of a weak, well-defined feature at ~17 500 cm^{-1} and a more intense band at ~22 000 cm^{-1} (Figure 2.3 and Table 2.2). This is in spite of the electronic differences between the supporting ligands. Moreover, these spectra are distinct from those previously reported for $[Mn^{III}(O_2)(L^7q_2)]^+$ and $[Mn^{III}(O_2)(L^7py_2{}^{6\text{-Me}})]^+$ that show a poorly-defined absorption band at ~15 500 cm^{-1} and a more intense feature at ~24 000 cm^{-1} (Figure 2.3, bottom).[19] Thus, the electronic absorption spectra of $[Mn^{III}(O_2)(L^7\text{iso-}q_2)]^+$ and $[Mn^{III}(O_2)(L^7py_2{}^{4\text{-Cl}})]^+$ further support the proposal that it is the presence or absence of intraligand steric clash between the pyridine or quinoline groups, and not electronic perturbations, that largely governs the electronic transition energies of these complexes. To permit a quantitative comparison of the excited state properties of these complexes on the basis of electronic transition energies instead of absorption maxima, MCD studies were performed for $[Mn^{III}(O_2)(L^7\text{iso-}q_2)]^+$ and $[Mn^{III}(O_2)(L^7py_2{}^{4\text{-Cl}})]^+$, as well as $[Mn^{III}(O_2)(L^7q_2)]^+$ and $[Mn^{III}(O_2)(L^7py_2{}^{4\text{-Me}})]^+$, for which only electronic absorption data had been previously reported.[19] The MCD spectra of the quinoline-containing $[Mn^{III}(O_2)(L^7\text{iso-}q_2)]^+$ and $[Mn^{III}(O_2)(L^7q_2)]^+$ complexes are discussed first.

2.3.3. MCD Data for $[Mn^{III}(O_2)(L^7\text{iso-}q_2)]^+$ and $[Mn^{III}(O_2)(L^7q_2)]^+$. The 2 K, 7 T MCD spectra of $[Mn^{III}(O_2)(L^7\text{iso-}q_2)]^+$ and $[Mn^{III}(O_2)(L^7q_2)]^+$ (Figure 2.4) each consist of a weak band at ~14 000 – 16 000 cm^{-1} and more intense features at higher energy. To provide a means of comparing the electronic transition energies of these complexes, Gaussian deconvolution of the MCD spectra were performed (Table 2.3 and Figure 2.4). This analysis reveals that the largest differences in transition energies occur for band 1, which is the only band to shift by >1 000 cm^{-1}. We note that bands 2 and 6 of $[Mn^{III}(O_2)(L^7q_2)]^+$ lack clear counterparts in the MCD spectrum of $[Mn^{III}(O_2)(L^7\text{iso-}q_2)]^+$. However, it is possible that for the latter complex these bands are simply too weak to observe and/or are obscured by more intense bands. Although the MCD

spectrum of $[Mn^{III}(O_2)(L^7iso\text{-}q_2)]^+$ can be fit by including additional bands at ~19 000 and 28 000 cm^{-1}, this does not significantly improve the goodness of fit. In any case, the presence or absence of these bands does not impact the major conclusions of this study.

By relation to our previous work,[18] band 1 is assigned as the Mn^{III} $d_z^2 \rightarrow d_{xy}$ transition (Scheme 2.1). Because the d_{xy} acceptor orbital is strongly Mn−O_{peroxo} σ-antibonding, the energy of this band largely reflects the Mn−O_{peroxo} bond strength. On this basis, the red-shift in band 1 for $[Mn^{III}(O_2)(L^7q_2)]^+$ is attributed to a weakening of the Mn−O_{peroxo} σ-interaction, likely through a slight bond elongation. When bound to a metal complex, the quinoline arms in the L^7q_2 ligand must cant above and below the equatorial plan to minimize steric interactions, which causes crowding of the axial binding sites. This is similar to that described previously for the $[Mn^{III}(O_2)(L^7py_2{}^{6\text{-}Me})]^+$ system.[18] In contrast, the isoquinoline arms in the $L^7iso\text{-}q_2$ ligand have modest steric interactions with one another and minimal canting is possible. The smaller red-shift for $[Mn^{III}(O_2)(L^7q_2)]^+$ and $[Mn^{III}(O_2)(L^7iso\text{-}q_2)]^+$ on the one hand, versus $[Mn^{III}(O_2)(L^7py_2{}^{6\text{-}Me})]^+$ and $[Mn^{III}(O_2)(L^7py_2{}^{H})]^+$ on the other (1000 and 3000 cm^{-1}, respectively; see Table 2.3), is attributed to a reduced steric clash between the flat quinoline arms in L^7q_2 as compared to the 6-methylpyridine groups in $L^7py_2{}^{6\text{-}Me}$.

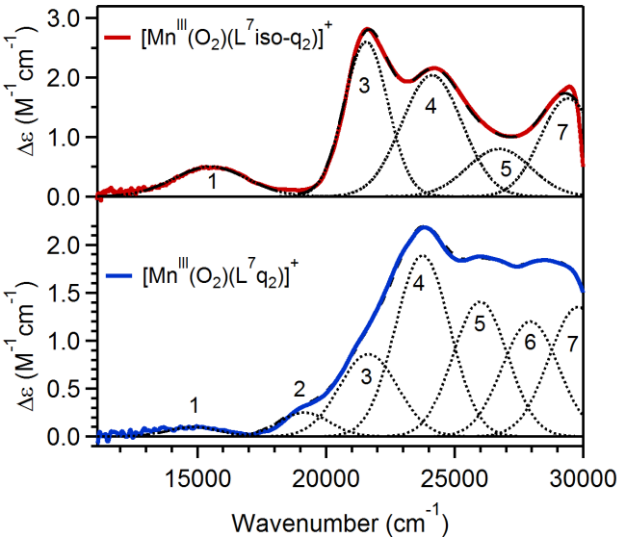

Figure 2.4. 2 K, 7 T MCD spectra of $[Mn^{III}(O_2)(L^7iso\text{-}q_2)]^+$ (top) and $[Mn^{III}(O_2)(L^7q_2)]^+$ (bottom). Individual Gaussian curves (dotted lines) and their sums (dashed lines) obtained from fits of these data sets are displayed on their respective spectra. Conditions: MCD data were collected for 15 mM frozen glass samples in butyronitrile.

Table 2.3. Electronic Transitions Energies for $[Mn^{III}(O_2)(L^7py_2{}^R)]^+$ (R = H, 6-Me, 4-Me, and 4-Cl), $[Mn^{III}(O_2)(q_2)]^+$, and $[Mn^{III}(O_2)(L^7iso\text{-}q_2)]^+$ Complexes Determined from Gaussian Deconvolutions of 2 K, 7 T MCD Data.[a]

	$[Mn^{III}(O_2)(L)]^+$					
L =	$L^7iso\text{-}q_2$	L^7q_2	$L^7py_2{}^{4\text{-Me}}$	$L^7py_2{}^{4\text{-Cl}}$	$L^7py_2{}^{H}$	$L^7py_2{}^{6\text{-Me}}$
Band 1	15 500	14 450	16 400	16 630	16 300	13 650
Band 2		19 150	19 090	19 180		18 800
Band 3	21 560	21 650	21 325	21 510	21 830	21 665
Band 4	24 120	23 760	23 000	23 340	24 430	24 000
Band 5	26 730	26 000	24 500	24 750	26 650	
Band 6		27 950	27 110	26 980	28 735	28 720
Band 7	29 400	29 800	30 300	29 940	30 100	30 860

[a] Values for L = $L^7py_2{}^H$ and $L^7py_2{}^{6\text{-Me}}$ are from reference 18.

While the shift in band 1 for $[Mn^{III}(O_2)(L^7iso\text{-}q_2)]^+$ and $[Mn^{III}(O_2)(L^7q_2)]^+$ can be related to Mn^{III}-O_2 σ-interactions, interpretation of the spectral changes at higher energies (bands 2 – 7) is less straightforward. Previously reported TD-DFT computations performed for the related $[Mn^{III}(O_2)(L^7py_2{}^H)]^+$ complex predicted both additional Mn *d-d* and weak peroxo-to-

manganese(III) charge-transfer (CT) transitions in this energy window.[18] The CT transitions involve excitation from the out-of-plane peroxo π-antibonding MOs (O_2 π_{op}*) to the low-lying, singly-occupied Mn d_{xz}, d_{yz}, and $d_{x^2-y^2}$ orbitals, all of which are weakly Mn−O_{peroxo} π-antibonding (Scheme 2.1). Thus, the energies of these orbitals will be, to varying degrees, dependent on Mn−O_{peroxo} π-interactions that are significantly less sensitive to modest changes in the Mn−O_{peroxo} bond length. However, the intensities of any peroxo-to-manganese(III) CT transitions in this spectral region will be modulated by the percentage of peroxo character in the Mn-based orbitals. Furthermore, the intensities of Mn *d*-*d* transitions will be affected by both the extent of mixing between Mn *d* and ligand orbitals and the proximity of Mn *d*-*d* and CT excited states. Given the very strong similarities between the majority of the transition energies for these two complexes (Table 2.3), the spectral perturbations at higher energy are attributed to changes in transition intensity.

2.3.4. MCD Data for $[Mn^{III}(O_2)(L^7py_2^{4\text{-}Me})]^+$ and $[Mn^{III}(O_2)(L^7py_2^{4\text{-}Cl})]^+$. Gaussian deconvolution of the 2 K, 7 T MCD spectra of $[Mn^{III}(O_2)(L^7py_2^{4\text{-}Me})]^+$ and $[Mn^{III}(O_2)(L^7py_2^{4\text{-}Cl})]^+$ reveal a total of seven electronic transitions from 11 000 to 31 000 cm^{-1}. The deconvoluted MCD spectra are shown in Figure 2.5, and the transition energies are collected in Table 2.3. Despite the differences in the expected electron-donating properties of pyridines in the $L^7py_2^{4\text{-}Me}$ and $L^7py_2^{4\text{-}Cl}$ ligands, the electronic transition energies of the corresponding $[Mn^{III}(O_2)(L)]^+$ complexes differ by no more than 400 cm^{-1}, indicating very similar geometric and electronic structures. When transition energies previously obtained for $[Mn^{III}(O_2)(L^7py_2^{H})]^+$ are also considered (Table 2.3), it is clear that electronic perturbations of the pyridine groups have a modest effect on the spectral properties of the Mn^{III}-O_2 unit. Indeed, among the $[Mn^{III}(O_2)(L^7py_2^{R})]^+$ (R = H, 4-Me, and 4-Cl) series, there is only a small (~300 cm^{-1}) blue-shift in band 1 as the pyridine group

becomes more electron withdrawing (Table 2.3). When the electronic transition energies of $[Mn^{III}(O_2)(L^7py_2{}^{6\text{-}Me})]^+$ are considered (Table 2.3), these data firmly establish that it is the position, and not the identity, of the pyridine substituent that has the largest influence on the spectroscopic properties of these complexes. Figure 2.6 shows an expanded view of the low-energy region of the MCD spectra of these complexes, which highlights the red-shift of band 1 for $[Mn^{III}(O_2)(L^7py_2{}^{6\text{-}Me})]^+$.

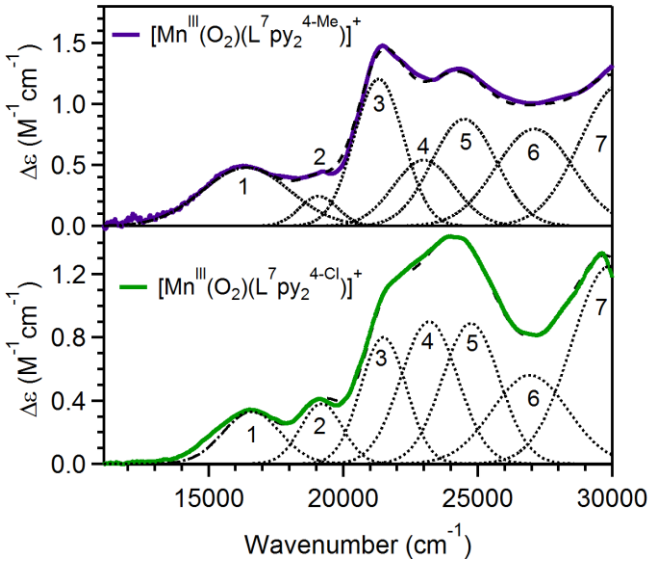

Figure 2.5. 2 K, 7 T MCD spectra of $[Mn^{III}(O_2)(L^7py_2{}^{4\text{-}Me})]^+$ (top) and $[Mn^{III}(O_2)(L^7py_2{}^{4\text{-}Cl})]^+$ (bottom). Individual Gaussian curves (dotted lines) and their sums (dashed lines) obtained from fits of these data sets are displayed on their respective spectra. Conditions: MCD data were collected for 15 mM frozen glass samples in butyronitrile.

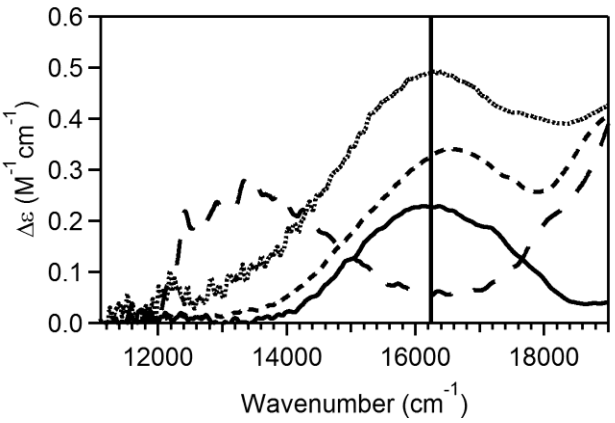

Figure 2.6. Expanded view of the low-energy region of the 2 K, 7 T MCD spectra of $[Mn^{III}(O_2)(L^7py_2^{4\text{-}Me})]^+$ (dotted curve), $[Mn^{III}(O_2)(L^7py_2^{4\text{-}Cl})]^+$ (short dashed curve), $[Mn^{III}(O_2)(L^7py_2^{H})]^+$ (solid curve), and $[Mn^{III}(O_2)(L^7py_2^{6\text{-}Me})]^+$ (long dashed curve). A black vertical line is shown at 16 300 cm^{-1} to highlight the small shifts apparent for the $[Mn^{III}(O_2)(L^7py_2^{R})]^+$ (R = 4-Me, H, and 4-Cl) series; see Table 2.3.

2.3.5. VTVH MCD Data. VTVH MCD curves collected for bands 3 of $[Mn^{III}(O_2)(L^7\text{iso-}q_2)]^+$, $[Mn^{III}(O_2)(L^7py_2^{4\text{-}Me})]^+$, and $[Mn^{III}(O_2)(L^7py_2^{4\text{-}Cl})]^+$ are shown in Figure 2.7. (Unfortunately, the low signal-to-noise ratio of the VTVH MCD signal for $[Mn^{III}(O_2)(L^7q_2)]^+$ at temperatures greater than 6 K yielded data unsuitable for detailed analysis.) These data were fit using the formalism of Neese and Solomon[33] to gain insights into the ground-state properties of these complexes. Figure 2.7 shows the best fits when both the zero-field splitting parameters (*D* and *E/D*) and the transition moment products (M_{xy}, M_{xz}, and M_{yz}) are optimized to fit the data. The sensitivity of the goodness-of-fit parameter χ^2 (where χ^2 is the sum of the squares of the difference between experimental and fit data sets) to variations in *D* and *E/D* was assessed by systematically fixing the ZFS parameters at different values and floating the transition moment products to minimize χ^2. As shown in the Appendix (Figures A1.1 – A1.3), all data sets are best fit with $|D| > 1$ cm^{-1}, but *E/D* is poorly defined. For $[Mn^{III}(O_2)(L^7\text{iso-}q_2)]^+$ and $[Mn^{III}(O_2)(L^7py_2^{4\text{-}Cl})]^+$ there is an upper-bound of $|D|$ at ~2.5 cm^{-1}. The observation that fits of VTVH MCD data

yield uncertainty in the magnitude and sign of *D* has been observed for other complexes and discussed in detail elsewhere.[34,35] We note here that the range of *D* values obtained from this procedure are consistent with those reported for other $[Mn^{III}(O_2)(L)]^+$ complexes (-2.0 to -2.9 cm^{-1}).[18,20,21,25] Because a $D < 0$ cm^{-1} was determined in all those cases, it is likely the peroxomanganese(III) complexes examined here have negative *D* values as well, although this cannot be determined from the VTVH MCD data alone. As a consequence of the insensitivity of fits of the VTVH MCD data of $[Mn^{III}(O_2)(L^7iso\text{-}q_2)]^+$, $[Mn^{III}(O_2)(L^7py_2{}^{4\text{-}Me})]^+$ and $[Mn^{III}(O_2)(L^7py_2{}^{4\text{-}Cl})]^+$ to changes in *D* and *E/D*, the polarizations for these electronic transitions cannot be accurately determined. This is in contrast to that observed for $[Mn^{III}(O_2)(L^7py_2{}^{H})]^+$ and $[Mn^{III}(O_2)(L^7py_2{}^{6\text{-}Me})]^+$, where the VTVH MCD data were quite sensitive to changes in *D* and *E/D*, permitting an accurate determination of both the ZFS parameters and transition polarizations for these complexes.[18]

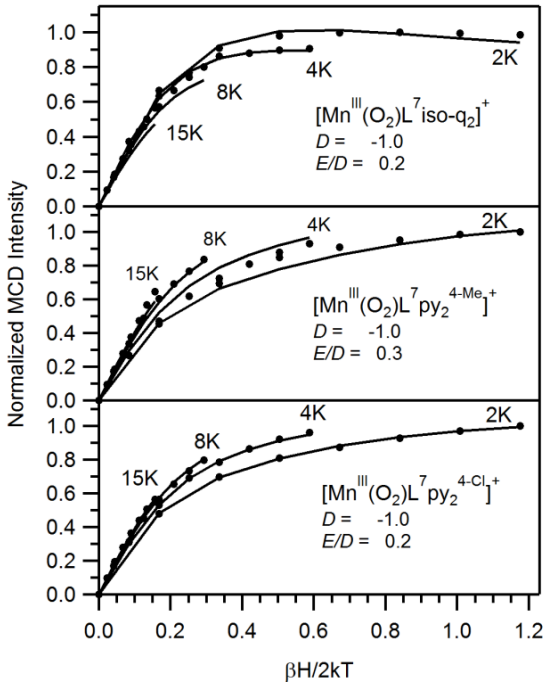

Figure 2.7. VTVH MCD data (circles) collected for $[Mn^{III}(O_2)(L^7iso\text{-}q_2)]^+$ (top; 21 598 cm^{-1}), $[Mn^{III}(O_2)(L^7py_2{}^{4\text{-}Me})]^+$ (center; 22 075 cm^{-1}), and $[Mn^{III}(O_2)(L^7py_2{}^{4\text{-}Cl})]^+$ (bottom; 24 096 cm^{-1}) at the temperatures indicated. Fits to the data (solid lines) using the ZFS parameters indicated and the following transition polarizations: $[Mn^{III}(O_2)(L^7iso\text{-}q_2)]^+$: 2% *x*, 3% *y* and 95% *z*; $[Mn^{III}(O_2)(L^7py_2{}^{4\text{-}Me})]^+$: 48% *x*, 8% *y*, and 44% *z*; $[Mn^{III}(O_2)(L^7py_2{}^{4\text{-}Cl})]^+$: 31% *x*, 8% *y*, and 61% *z*.

2.3.6. DFT Computations. DFT computations were performed to obtain optimized structures of $[Mn^{III}(O_2)(L^7iso\text{-}q_2)]^+$ and $[Mn^{III}(O_2)(L^7py_2{}^{4\text{-}Cl})]^+$ to compare with those previously obtained for the $[Mn^{III}(O_2)(L^7py_2{}^{R})]^+$ (R = H, 6-Me, and 4-Me) and $[Mn^{III}(O_2)(L^7q_2)]^+$ complexes. Important metric parameters of the DFT-optimized models are collected in Table 2.4, and the optimized structures of $[Mn^{III}(O_2)(L^7iso\text{-}q_2)]^+$ and $[Mn^{III}(O_2)(L^7py_2{}^{4\text{-}Cl})]^+$ are shown in Figure 2.8. We note that these geometry optimizations were performed using the pure BP86 functional; similar metric parameters are obtained using the hybrid B3LYP functional (Appendix A.1).

For all Mn^{III}-O_2 species examined in this work, the DFT-optimized structures consist of six-coordinate Mn^{III} centers with side-on peroxo ligands that sit above a distorted square plane created by the four nitrogen atoms of the supporting ligand. This is consistent with the relatively small shifts in electronic transition energies observed for these complexes (Table 2.3). In general, the Mn−O_{peroxo} bond lengths are ~1.87 Å, and quite symmetric, with differences of ≤ 0.004 Å for a given complex (Table 2.4). However, the $[Mn^{III}(O_2)(L^7py_2^{6\text{-}Me})]^+$ and $[Mn^{III}(O_2)(L^7q_2)]^+$ complexes provide exceptions, as both exhibit one long Mn−O_{peroxo} bond length of ~1.89 – 1.91 Å, which give rise to Mn−O_{peroxo} bond length differences of 0.041 and 0.021 Å, respectively. Although these variations in bond lengths are quite small, they are magnified in the Mn $d_z^2 \rightarrow d_{xy}$ transition energy because the Mn d_{xy} orbital is strongly Mn−O_{peroxo} σ-antibonding (Scheme 2.1). Specifically, TD-DFT computations were used previously to show that a 0.04 Å change in bond length is expected to give rise to a band shift of at least 1 000 cm^{-1}.[18] With the series of complexes reported in this study, we are able to demonstrate that there is a rough correlation between the experimental energy of the Mn $d_z^2 \rightarrow d_{xy}$ transition (band 1) and the DFT-computed Mn−O_{peroxo} bond length (Figure 2.9, top). The fact that a perfectly linear relationship is not observed is not surprising. While the energy of the acceptor orbital is tuned by Mn−O_{peroxo} interactions, the donor orbital for this transition (Mn d_z^2) is Mn-$L^7py_2^R$ σ-antibonding. Thus, changes in the electronic structure of the supporting ligand should modulate the transition energy. However, the observation of a correlation between one Mn−O_{peroxo} distance and the energy of band 1 underscores the greater covalency of the Mn−O_{peroxo} bonds compared to Mn−N bonds, which accounts for the peroxo perturbations having the greatest influence on the electronic transition energy.

Table 2.4. Metal-Ligand Bond Lengths (Å) for Peroxomanganese(III) Complexes Based on DFT Geometry Optimizations

	$[Mn^{III}(O_2)(L)]^+$					
L =	$L^7iso\text{-}q_2$	L^7q_2 [b]	$L^7py_2^{4\text{-}Me}$ [b]	$L^7py_2^{4\text{-}Cl}$	$L^7py_2^{H}$ [a]	$L^7py_2^{6\text{-}Me}$ [a]
Mn-O(1)	1.869	1.886	1.873	1.869	1.872	1.907
Mn-O(2)	1.865	1.865	1.869	1.866	1.868	1.866
O(1)-O(2)	1.445	1.439	1.444	1.442	1.444	1.452
Mn-N(1)	2.229	2.304	2.097	2.218	2.108	2.177
Mn-N(2)	2.206	2.201	2.288	2.207	2.283	2.279
Mn-N(3)	2.282	2.294	2.214	2.281	2.212	2.147
Mn-N(4)	2.169	2.136	2.215	2.107	2.215	2.296

[a] From reference 18, although a different atom numbering scheme is used here. [b] From reference 19.

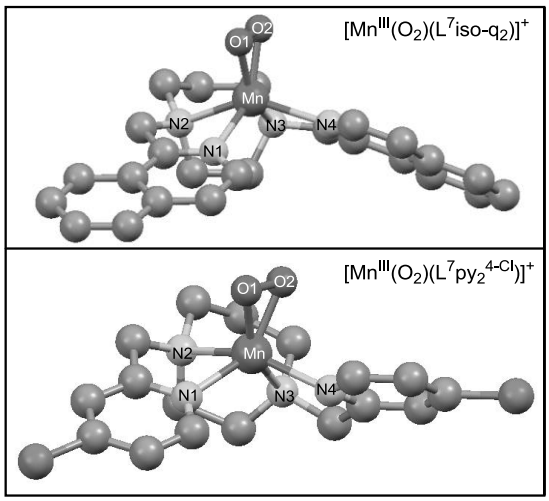

Figure 2.8. DFT-optimized structures of $[Mn^{III}(O_2)(L^7iso\text{-}q_2)]^+$ (top) and $[Mn^{III}(O_2)(L^7py_2^{4\text{-}Cl})]^+$ (bottom).

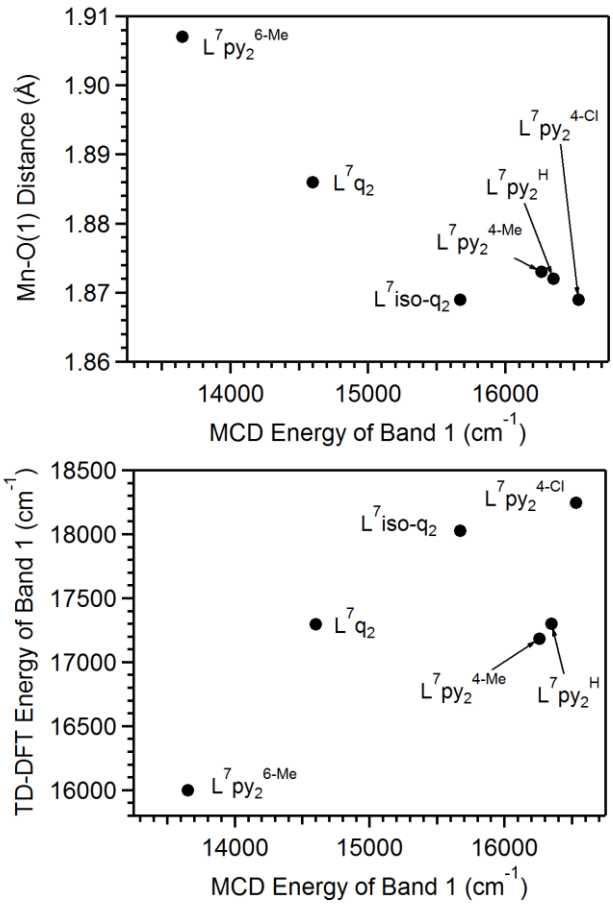

Figure 2.9. Top: Plot of the DFT-computed Mn−O(1) distance as a function of the energy of band 1 determined by MCD spectroscopy. Bottom: Comparison of experimental and TD-DFT computed energies of band 1.

Given that the optimized structures of the $[Mn^{III}(O_2)(L)]^+$ complexes are able to account for the major spectral perturbations, we performed time-dependent DFT (TD-DFT) computations for this series to determine if this theoretical method could reproduce the variation in the Mn $d_z^2 \rightarrow d_{xy}$ transition energy observed experimentally. Although the absolute error of electronic transition energies computed using the TD-DFT method are expected to be on the order of the observed bandshift (~3 000 cm^{-1}), and can in fact be much larger,[36] it is possible that the *trend* in energies could nonetheless be reproduced by this method due to cancellation of systematic error among this series. Figure 2.9 (bottom) shows the energy of the Mn $d_z^2 \rightarrow d_{xy}$ transition (band 1)

obtained from MCD spectroscopy and TD-DFT computations using the B3LYP functional. Similar results are obtained using the hybrid PBE0 functional (Appendix (A1)). These results show that the trend is reproduced in a very general fashion, which we consider to be quite acceptable in light of the well-documented limitations and failures of the TD-DFT method. For example, $[Mn^{III}(O_2)(L^7py_2{}^{4\text{-}Cl})]^+$ and $[Mn^{III}(O_2)(L^7py_2{}^{6\text{-}Me})]^+$ provide the respective high and low energy extremes for both the experimental and computed transitions (Figure 2.9, bottom). However, there are clear outliers. Most notably, the TD-DFT computations predict the $[Mn^{III}(O_2)(L^7py_2{}^{4\text{-}Cl})]^+$ and $[Mn^{III}(O_2)(L^7py_2{}^{6\text{-}Me})]^+$ complexes to have transition energies within ~200 cm^{-1}, in contrast to the experimental difference of ~2 000 cm^{-1}. Although there were variations in TD-DFT-computed electronic transition energies for other bands (figures A1.5. and A1.6.), given the very, very minor experimental bandshifts observed for these transitions (Table 2.3), we did not pursue a detailed analysis of these perturbations.

2.4. Conclusions

In this work we have described the generation and characterization of manganese(II) and peroxomanganese(III) complexes supported by the tetradentate, diazacycloalkane ligands L^7iso-q_2 and $L^7py_2{}^{4\text{-}Cl}$. MCD and VTVH MCD data collected for these Mn^{III}-O_2 complexes, and corresponding data collected for a series of previously reported peroxomanganese(III) adducts, were analyzed within the framework provided by DFT computations to determine how the properties of the supporting ligand affect the geometric and electronic structure of the Mn^{III}-O_2 unit. Collectively, the experimental data and computational results support the conclusion that all complexes feature six-coordinate Mn^{III} centers with side-on peroxo ligands. Specifically, among the six complexes described, the majority of electronic transition energies are within 1 000 cm^{-1},

and the zero-field splitting parameters are comparable. The largest spectroscopic variation is in the lowest-energy *d-d* band, which shifts by up to 3 000 cm^{-1} depending on the *steric* properties of the supporting ligand. This is rationalized by considering that the presence of bulky substituents in the 6-position gives rise to canting of the pyridylmethyl (or quinolinylmethyl) arms, creating a slightly smaller peroxo binding pocket that leads to elongation of one $Mn{-}O_{peroxo}$ bond. Increasing the steric bulk in the six-position of the pyridine ring not only leads to the largest spectral perturbations, but also impacts the overall stability of the peroxomanganese(III) species formed. For example, the previously reported $[Mn^{III}(O_2)(L^7py_2{}^{6\text{-}MeO})]^+$ complex exhibits a half-life of six minutes at -40 ºC, comparable to the half-lives of other peroxomanganese(III) complexes at 0 ºC (Table 2.2).[18] Nonetheless, the absorption spectrum of this complex is essentially identical to that of $[Mn^{III}(O_2)(L^7py_2{}^{6\text{-}Me})]^+$, supporting our model that intraligand sterics affect spectral properties. In contrast, only a very minor (~300 cm^{-1}) shift in the lowest-energy *d-d* band is observed when the electronic properties of the ligand are modulated in the $L^7py_2{}^{4\text{-}Me}$, $L^7py_2{}^{H}$, and $L^7py_2{}^{4\text{-}Cl}$ ligand series. The most cogent case for the influence of intraligand sterics is offered by the $[Mn^{III}(O_2)(L^7py_2{}^{6\text{-}Me})]^+$ and $[Mn^{III}(O_2)(L^7py_2{}^{4\text{-}Me})]^+$ species, which differ only in the position of the pyridine substituent, yet the former complex shows the lowest-energy *d-d* transition red-shifted by ~3 000 cm^{-1}.

These results should be considered in light of a proposal that the binding of anions, such as N_3^-, CN^-, and $CF_3CO_2^-$, *trans* to the peroxo ligand in the $[Mn^{III}(O_2)(13\text{-TMC})]^+$ complex causes a shift from side-on to end-on peroxo binding mode.[17] Intriguingly, the binding of these axial ligands did not appear to significantly alter the electronic absorption signals but did affect the reduction potential and reactivity with aldehydes. Our observation that electronic perturbations cause minimal changes in geometric and electronic structure should thus be viewed

in context. In the series of complexes described here, electronic perturbations occur roughly *cis* to the peroxo unit and are conservative compared to substitution of anionic ligands. Thus, for peroxomanganese(III) systems, electronic effects may be predominant if they occur *trans* to the peroxo ligand and/or involve anionic ligands with a range of properties. This would be similar to that observed for oxometal species, where substitutions *trans* to the oxo ligand have a more dramatic influence on reactivity and spectroscopic properties than *cis* subsitutions.[37-41]

Our proposal that the steric properties of the supporting ligand exert an influence over $Mn^{III}–O_{peroxo}$ bond lengths reinforces work from the groups of Riordan, Solomon, Brunold, and Nam that has elegantly shown how the interplay of steric and electronic factors contribute to the relative stabilities of side-on peroxometal and end-on superoxometal species in nickel and cobalt systems. For example, $[Ni^{II}(12\text{-TMC})]^{2+}$ forms a side-on peroxonickel(III) when treated with H_2O_2,[42,43] while $[Ni^{II}(TMC)]^{2+}$ forms an end-on superoxonickel(II) species upon the same reaction (12-TMC = 1,4,7,10-tetramethyl-1,4,7,10-tetraazacyclododecane and TMC = 1,4,8,11-tetramethyl-1,4,8,11-tetraazacyclotetradecane).[44] In contrast, both the $[Co^{II}(12\text{-TMC})]^{2+}$ and $[Co^{II}(TMC)]^{2+}$ compounds react with H_2O_2 to form side-on peroxocobalt(III) complexes.[45,46] The difference in reactivity between the Ni and Co species is due to the high thermodynamic driving force for the oxidation of Co^{II} to Co^{III}, which overcomes the steric demands exerted by macrocyclic ligand.[46] Thus, because of the intrinsic properties of the transition metal center, different metals may form distinct intermediates using the same oxidant and supporting ligand. This has implications for metalloenzymes that can accommodate different metal ions in their active sites.

In conclusion, when considering the structures and reactivities of peroxomanganese(III) intermediates, whether formed in manganese enzymes or synthetic catalysts, it should be

recognized that the steric properties of the local coordination environment may very well exert a larger effect than electronic perturbations. This in turn, supports the argument of biological systems utilizing steric bulk of local coordination environment rather than, or in concert with, electronic effects in bringing about variations in $M-O_{peroxo}$ bond strengths to tune reactivity.

2.5. References

1. Bull, C.; Niederhoffer, E. C.; Yoshida, T.; Fee, J. A., *J. Am. Chem. Soc.* **1991,** *113*, 4069-4076.
2. Hearn, A. S.; Tu, C. K.; Nick, H. S.; Silverman, D. N., *J. Biol. Chem.* **1999,** *274*, 24457-24460.
3. Grove, L. E.; Brunold, T. C., *Comments Inorg. Chem.* **2008,** *29*, 134-168.
4. Miller, A.-F., Superoxide processing. In *Comprehensive Coordination Chemistry II*, McCleverty, J. A.; Meyer, T. J., Eds. Elsevier Ltd.: Oxford, UK, 2004; Vol. 8, pp 479-506.
5. Miller, A.-F., *Curr. Opin. Chem. Biol.* **2004,** *8*, 162-168.
6. Cotruvo, J. A.; Stubbe, J., *Proc. Natl. Acad. Sci. U.S.A.* **2008,** *105*, 14383-14388.
7. Cotruvo, J. A.; Stubbe, J., *Biochemistry* **2010,** *49*, 1297-1309.
8. Zhang, Y.; Stubbe, J., *Biochemistry* **2011,** *50*, 5615-5623.
9. Hage, R.; Lienke, A., *J. Mol. Catal. A: Chem.* **2006,** *251*, 150-158.
10. Hage, R.; Lienke, A., *Angew. Chem. Int. Ed.* **2006,** *45*, 206-222.
11. Lane, B. S.; Burgess, K., *Chem. Rev.* **2003,** *103*, 2457-2473.
12. Goldberg, D. P., *Acc. Chem. Res.* **2007,** *40*, 626-634.
13. Sibbons, K.; Shastri, K.; Watkinson, M., *Dalton Trans.* **2006,** *2006*, 645-661.
14. Hayden, J.; Hendrich, M., *J. Biol. Inorg. Chem.* **2010,** *15*, 729-736.
15. Cox, N.; Ogata, H.; Stolle, P.; Reijerse, E.; Auling, G.; Lubitz, W., *J. Am. Chem. Soc.* **2010,** *132*, 11197-11213.
16. Shook, R. L.; Peterson, S. M.; Greaves, J.; Moore, C.; Rheingold, A. L.; Borovik, A. S., *J. Am. Chem. Soc.* **2011,** *133*, 5810-5817.
17. Annaraj, J.; Cho, J.; Lee, Y.-M.; Kim, S. Y.; Latifi, R.; de Visser, S. P.; Nam, W., *Angew. Chem. Int. Ed.* **2009,** *48*, 4150-4153.
18. Geiger, R. A.; Chattopadhyay, S.; Day, V. W.; Jackson, T. A., *J. Am. Chem. Soc.* **2010,** *132*, 2821-2831.
19. Geiger, R. A.; Chattopadhyay, S.; Day, V. W.; Jackson, T. A., *Dalton Trans.* **2011,** *40*, 1707-1715.
20. Groni, S.; Blain, G.; Guillot, R.; Policar, C.; Anxolabéhère-Mallart, E., *Inorg. Chem.* **2007,** *46*, 1951-1953.
21. Groni, S.; Dorlet, P.; Blain, G.; Bourcier, S.; Guillot, R.; Anxolabéhère-Mallart, E., *Inorg. Chem.* **2008,** *47*, 3166-3172.
22. Kitajima, N.; Komatsuzaki, H.; Hikichi, S.; Osawa, M.; Moro-oka, Y., *J. Am. Chem. Soc.* **1994,** *116*, 11596-11597.

23. Seo, M. S.; Kim, J. Y.; Annaraj, J.; Kim, Y.; Lee, Y.-M.; Kim, S.-J.; Kim, J.; Nam, W., *Angew. Chem. Int. Ed.* **2007,** *46*, 377-380.
24. Shook, R. L.; Borovik, A. S., *Inorg. Chem.* **2010,** *49*, 3646-3660.
25. Shook, R. L.; Gunderson, W. A.; Greaves, J.; Ziller, J. W.; Hendrich, M. P.; Borovik, A. S., *J. Am. Chem. Soc.* **2008,** *130*, 8888-8889.
26. Singh, U. P.; Sharma, A. K.; Hikichi, S.; Komatsuzaki, H.; Moro-oka, Y.; Akita, M., *Inorg. Chim. Acta* **2006,** *359*, 4407-4411.
27. VanAtta, R. B.; Strouse, C. E.; Hanson, L. K.; Valentine, J. S., *J. Am. Chem. Soc.* **1987,** *109*, 1425-1434.
28. Coggins, M. K.; Kovacs, J. A., *J. Am. Chem. Soc.* **2011,** *133*, 12470-12473.
29. Costas, M.; Mehn, M. P.; Jensen, M. P.; Que, L., Jr., *Chem. Rev.* **2004,** *104*, 939-986.
30. Simaan, A. J.; Banse, F.; Mialane, P.; Boussac, A.; Un, S.; Kargar-Grisel, T.; Bouchoux, G.; Girerd, J.-J., *Eur. J. Inorg. Chem.* **1999**, 993-996.
31. Simaan, A. J.; Döpner, S.; Banse, F.; Bourcier, S.; Bouchoux, G.; Boussac, A.; Hildebrandt, P.; Girerd, J.-J., *Eur. J. Inorg. Chem.* **2000**, 1627-1633.
32. Evans, D. F.; Jakubovic, D. A., *J. Chem. Soc., Dalton Trans.* **1988**, 2927-2933.
33. Neese, F.; Solomon, E. I., *Inorg. Chem.* **1999,** *38*, 1847-1865.
34. Krzystek, J.; Fiedler, A. T.; Sokol, J. J.; Ozarowski, A.; Zvyagin, S. A.; Brunold, T. C.; Long, J. R.; Brunel, L.-C.; Telser, J., *Inorg. Chem.* **2004,** *43*, 5645-5658.
35. Krzystek, J.; Zvyagin, S. A.; Ozarowski, A.; Fiedler, A. T.; Brunold, T. C.; Telser, J., *J. Am. Chem. Soc.* **2004,** *126*, 2148-2155.
36. Neese, F., *J. Biol. Inorg. Chem.* **2006,** *11*, 702-711.
37. Jackson, T. A.; Rohde, J.-U.; Seo, M. S.; Sastri, C. V.; DeHont, R.; Ohta, T.; Stubna, A.; Kitagawa, T.; Münck, E.; Nam, W.; Que, L., Jr., *J. Am. Chem. Soc.* **2008,** *130*, 12394-12407.
38. Rohde, J.-U.; Que, L., Jr., *Angew. Chem. Int. Ed.* **2005,** *44*, 2255-2258.
39. Rohde, J.-U.; Stubna, A.; Bominaar, E. L.; Münck, E.; Nam, W.; Que, L., Jr., *Inorg. Chem.* **2006,** *45*, 6435-6445.
40. Zhou, Y.; Shan, X.; Mas-Ballesté, R.; Bukowski, M.; Stubna, A.; Chakrabarti, M.; Slominski, L.; Halfen, J. A.; Münck, E.; Que, L., Jr., *Angewandte Chemie International Edition* **2008,** *47*, 1896-1899.
41. Sastri, C. V.; Lee, J.; Oh, K.; Lee, Y. J.; Lee, J.; Jackson, T. A.; Hirao, H.; Que, L., Jr.; Shaik, S.; Nam, W., *Proc. Natl. Acad. Sci. USA* **2007,** *104*, 19181-19186.
42. Kieber-Emmons, M. T.; Annaraj, J.; Seo, M. S.; Van Heuvelen, K. M.; Tosha, T.; Kitagawa, T.; Brunold, T. C.; Nam, W.; Riordan, C. G., *J. Am. Chem. Soc.* **2006,** *128*, 14230-14231.
43. Kieber-Emmons, M. T.; Riordan, C. G., *Acc. Chem. Res.* **2007,** *40*, 618-625.
44. Cho, J.; Sarangi, R.; Annaraj, J.; Kim, S. Y.; Kubo, M.; Ogura, T.; Solomon, E. I.; Nam, W., *Nat Chem* **2009,** *1*, 568-572.
45. Cho, J.; Sarangi, R.; Kang, H. Y.; Lee, J. Y.; Kubo, M.; Ogura, T.; Solomon, E. I.; Nam, W., *J. Am. Chem. Soc.* **2010,** *132*, 16977-16986.
46. Sarangi, R.; Cho, J.; Nam, W.; Solomon, E. I., *Inorg. Chem.* **2010,** *50*, 614-620.
47. Armarego, W. L. F.; Perrin, D. D., *Purification of Laboratory Chemicals*. Butterworth-Heinemann: Oxford, U.K., 1997.
48. Mayilmurugan, R.; Stoeckli-Evans, H.; Palaniandavar, M., *Inorg. Chem.* **2008,** *47*, 6645-6658.

49. Neese, F., *ORCA - an ab initio, Density Functional and Semiempirical Program Package, Version 2.8*, University of Bonn, 2009. *ORCA - an ab initio, Density Functional and Semiempirical Program Package, Version 2.8, University of Bonn, 2009.*
50. Becke, A. D., *J. Chem. Phys.* **1986,** *84*, 4524-4529.
51. Perdew, J. P., *Physical Review B* **1986,** *33*, 8822-8824.
52. Schäfer, A.; Horn, H.; Ahlrichs, R., *J. Chem. Phys.* **1992,** *97*, 2571-2577.
53. Schäfer, G.; Huber, C.; Ahlrichs, R., *J. Chem. Phys.* **1994,** *100*, 5829-5835.
54. Neese, F., *J. Comput. Chem.* **2003,** *24*, 1740-1747.
55. Sinnecker, S.; Rajendran, A.; Klamt, A.; Diedenhofen, M.; Neese, F., *J. Phys. Chem. A* **2006,** *110*, 2235-2245.
56. Becke, A. D., *J. Chem. Phys.* **1993,** *98*, 1372-1377.
57. Becke, A. D., *J. Chem. Phys.* **1993,** *98*, 5648-5652.
58. Lee, C.; Yang, W.; Parr, R. G., *Phys. Rev. B* **1988,** *37*, 785-789.
59. Bauernschmitt, R.; Ahlrichs, R., *Chem. Phys. Lett.* **1996,** *256*, 454-464.
60. Casida, E. M.; Jamorski, C.; Casida, K. C.; Salahub, D. R., *J. Chem. Phys.* **1998,** *108*, 4439-4449.
61. Stratman, R. E.; Scuseria, G. E.; Frisch, M. J., *J. Chem. Phys.* **1998,** *109*, 8218-8224.
62. Neese, F.; Olbrich, G., *Chem. Phys. Lett.* **2002,** *362*, 170-178.

CHAPTER 3

Targeting Oxidatively Robust Ligands in Stabilizing Manganese-dependent Reactive Intermediates

X-ray diffraction data collection and analysis were carried out by Dr. Victor W. Day.

3.1. Introduction

Peroxomanganese(III) intermediates have been proposed for numerous manganese-dependent enzymes that are crucial in biology, including Mn-SOD,[1,2] Mn-HPCD,[3,4] Mn-oxalate oxidase[5,6] and oxalate decarboxylase.[7,8] Furthermore, peroxo-level intermediates have also been proposed for the enzymatic processes involving dinuclear enzymes such as Mn-catalase[9] and ribonucleotide reductase (Mn-RNR).[10,11] Mechanistic details related to a majority of these manganese-dependent enzymes are currently unclear, warranting detailed studies on model systems. Small molecule model complexes have long served as useful tools in understanding the mechanisms of metalloenzymes,[12-18] not only because they are less cumbersome to handle in laboratory, but are also often isolable in high yields. To this end, peroxomanganese(III) model complexes have provided useful insights into numerous biological systems, including Mn-SOD,[18] Mn-HPCD[19,20] and Mn-RNR.[14,21] In addition to these enzymatic examples, furthering the understanding of the structure and reactivity of these Mn^{III}-peroxo intermediates will broaden the potential for the design of high-efficiency synthetic manganese catalysts,[22,23] which are highly desirable in industrial applications over precious metal catalysts that are currently in use.

The two most prominent challenges for investigating the chemistry of peroxomanganese(III) complexes originate from their generally low chemical yields, and their impaired thermal stability.[18] Although most chemically synthesized Mn^{III}-peroxo complexes exhibit low to moderate yields, a recent study by Anxolabéhère-Mallart and coworkers revealed that electrochemically generated superoxide can produce high yielding peroxomanganese(III) adducts supported by pentadentate ligands.[24] Whether or not this method can be successfully extended to a majority of Mn^{III}-peroxo compounds has yet to be determined. Substoichiometric

yields of these complexes have severely limited their structural characterization, especially using techniques such as X-ray absorption spectroscopy.

Despite the impaired thermal stability of peroxomanganese(III) intermediates, several solid state structures have been reported, including both side-on η^2-peroxomanganese(III),[25-31] and end-on η^1-alkylperoxomanganese(III) adducts.[19,20] Apart from these, all other peroxomanganese(III) species have been observed under cryogenic conditions, and have been routinely characterized using a combination of spectroscopic and computational methods, in conjugation with studies of their reactivity properties.[13,14,24,32-39] The highly unstable nature of a majority of these complexes has created interest in the investigation of their decay pathways, which could serve immensely in designing supporting ligands that may aid in enhancing their lifetimes. Detailed kinetic studies have revealed that the decay of η^1-alkylperoxomanganese(III) complexes occur with a rate-limiting O–O bond cleavage step.[19,20] This observation is also supported by the products observed in their thermal decay. Intriguingly, the O–O bond breaking step of the alkylperoxomanganese(III) intermediate of Mn-HPCD has been proposed as the overall rate determining step for its catechol dioxygenation mechanism.[4]

Detailed studies on potential decay pathways for η^2-peroxomanganese(III) complexes are more scarce. In a recent study, the peroxomanganese(III) complex, $[Mn^{III}(O_2)(N4py)]^+$, when generated with stoichiometric amounts of superoxide (30% yield of $[Mn^{III}(O_2)(N4py)]^+$), was observed to decay forming a bis(μ-oxo)dimanganese(III,IV) complex.[14] However, when excess superoxide was used to generate higher yields of $[Mn^{III}(O_2)(N4py)]^+$ (60% yield), the major decay product was found to be Mn^{II} species. Thus, it was proposed that in the former case, $[Mn^{III}(O_2)(N4py)]^+$ reacts with the excess Mn^{II} precursor in solution to generate the dimeric bis(μ-oxo)dimanganese(III,IV) species. This was further supported by the formation of ~90% of

the bis(μ-oxo)dimanganese(III,IV) species by the addition of $[Mn^{II}(N4py)]^{2+}$ into a solution of $[Mn^{III}(O_2)(N4py)]^{+}$ at low temperatures. The mechanism of the conversion of $[Mn^{III}(O_2)(N4py)]^{+}$ to the dimeric species by reacting with $[Mn^{II}(N4py)]^{2+}$ mimics the activity of Mn-RNR.[10,11] Thus, one potential decay mechanism for Mn^{III}-O_2 involves trapping by unreacted Mn^{II} complex.

In another study by Anxolabéhère-Mallart and coworkers, the reactivity of a Mn^{II} complex supported by L (Scheme 3.1) with excess H_2O_2 was studied using electronic absorption and electron paramagnetic resonance (EPR) spectroscopies in conjunction with ESI-MS.[39] When the starting $[Mn^{II}(L)(H_2O)]^{2+}$ complex was reacted with excess (1000 equiv.) H_2O_2, a blue-green solution resulted with prominent absorption features at 436 nm and 611 nm. This solution had a prominent mass peak corresponding to the respective peroxomanganese(III) species, $[Mn^{III}(O_2)(L)]^{+}$. However, the parallel-mode X-band EPR spectra collected for this resultant solution exhibited multiple features centered at g = 8.1, g = 5.1, and g = 2.0. It has been previously observed that the EPR feature at g = 8.1 corresponds to $[Mn^{III}(O_2)(L)]^{+}$, and thus, the multiple EPR features were suggestive of a mixture of species in solution. Therefore, this chemistry was studied further under acidic and basic conditions. When 2 equiv. of trimethylamine were added to the blue-green solution, it immediately changed color to turquoise blue with the disappearance of the absorption feature at 436 nm. The turquoise blue solution exhibits only one of the previously observed EPR features at g = 8.1, which is characteristic of the η^2-peroxomanganese(III) species. In addition, the mass spectrum showed a prominent ion peak corresponding to that of $[Mn^{III}(O_2)(L)]^{+}$. This Mn^{III}-O_2 complex decays over time to generate the corresponding bis(μ-oxo)dimanganese(III,IV) dimer (brown), with the intermediacy of the peroxo-bridged dimanganese(III,III) dimer (Scheme 3.1). The EPR features for these dimeric species compare well with previously reported data.[38] In contrast, when 1 equiv. of

$HClO_4$ was added into the blue-green solution, the solution color changed to green, which only displays the EPR features at g = 5.1, and g = 2.0. Thus, it was proposed that the initial reactivity between the Mn^{II} starting complex and excess H_2O_2 generates a mixture of species, which are in acid-base equilibrium. Furthermore, the addition of excess base favors the formation of the η^2-peroxomanganese(III) species, which decays to the bis(μ-oxo)dimanganese(III,IV) dimeric species. In contrast, acid addition generates the proposed η^1-hydroperoxomanganese(III) species, $[Mn^{III}(OOH)(L)]^+$. Interestingly, the decay of this species does not generate the dimeric species, but EPR evidence suggested the formation of Mn^{II} in solution. Thus, it was proposed that the peroxo-bridged dimanganese(III,III) dimer undergoes proton-assisted O–O bond cleavage in the presence of acid, generating $[Mn^{III}(OOH)(L)]^+$ (Scheme 3.1), which prevents the formation of the bis(μ-oxo)dimanganese(III,IV) dimer. The final Mn^{II} decay product in acidic medium was crystallized, and was characterized by XRD as the Mn^{II} complex supported by a ligand oxidation product, L' (Scheme 3.1). This provided solid evidence of the major decay product of Mn^{III}-O_2 and Mn^{III}-OOH species in the presence of acid, revealing the possibility of ligand oxidation. Accordingly, in this case, the oxidation of the weak benzylic –CH_2 linker groups to carboxylate groups was observed.

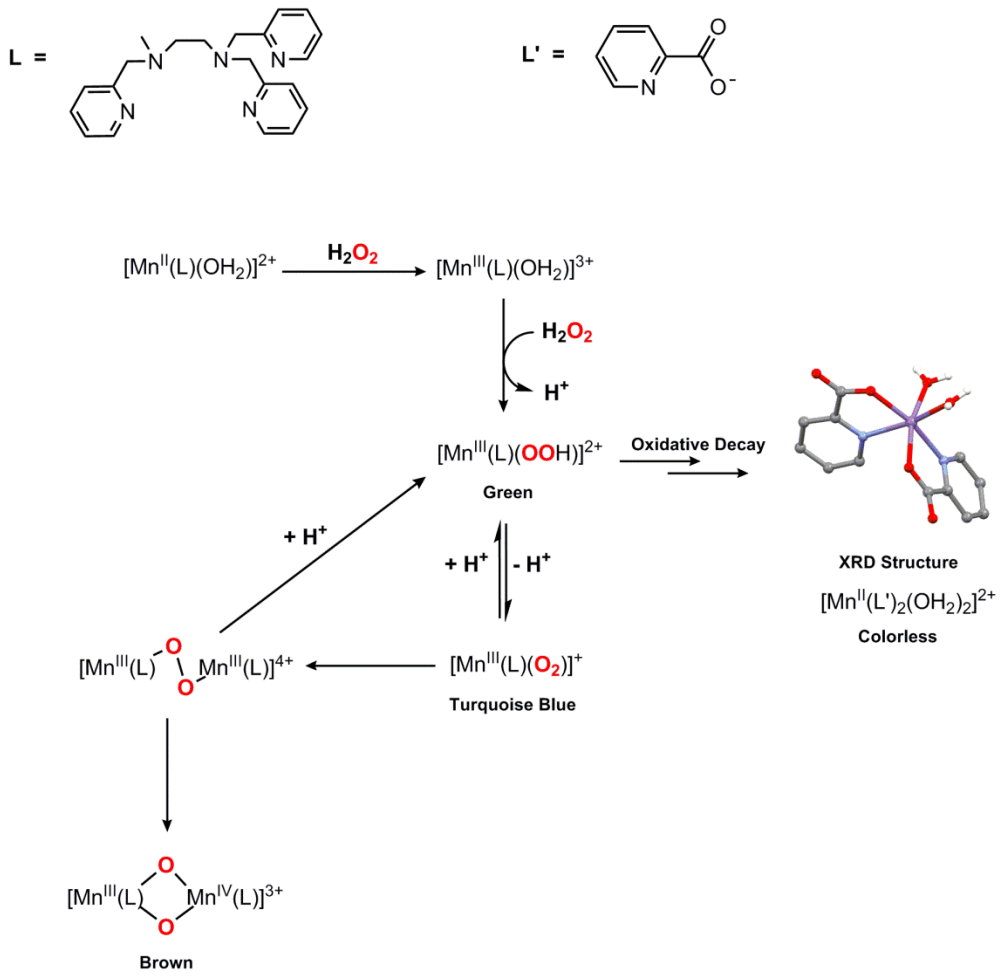

Scheme 3.1. The proposed formation and decay pathways of a peroxomanganese(III) species that provide evidence for ligand oxidation during its decay. The XRD structure shows the final manganese decay product, where the metal center is coordinated to two pyridine carboxylate molecules that resulted from ligand oxidation.

We have previously observed that the addition of 1 equiv. of strong acid to the spectroscopically characterized peroxomanganese(III) species, $[Mn^{III}(O_2)(L^7py_2^{6\text{-}Me})]^+$ (Figure 3.1), generates a new intermediate with a predominant absorption feature at 530 nm (Figure A2.7).[40] This species is highly unstable, and decays rapidly within the course of a few seconds at -40 ^oC. Similar to what has been previously observed by Anxolabéhère-Mallart[39] and Nam,[41] this new species could be the corresponding Mn^{III}-OOH complex, $[Mn^{III}(OOH)(L^7py_2^{6\text{-}Me})]^{2+}$. Accordingly, the decay of $[Mn^{III}(OOH)(L^7py_2^{6\text{-}Me})]^{2+}$ could be facilitated by oxidation of the

benzylic –CH_2 bridging groups of the supporting ligand, that link the homopiperazine backbone with the pyridyl groups, or the 6-methyl substituents on the pyridine rings. The isolation and stabilization of Mn^{III}-OOH species is of extreme interest, as very little is known about the structure and function of those reactive intermediates. This stands in contrast to analogous iron systems where the formation of fairly stable Fe^{III}-OOH adducts has been observed by protonation of corresponding Fe^{III}-O_2 species.[42-44] In addition, these linker –CH_2 groups could also facilitate the oxidative decay of $[Mn^{III}(O_2)(L^7py_2^{6\text{-}Me})]^+$, given their weak C–H bond strengths (BDE ≈ 90 kcal/mol).

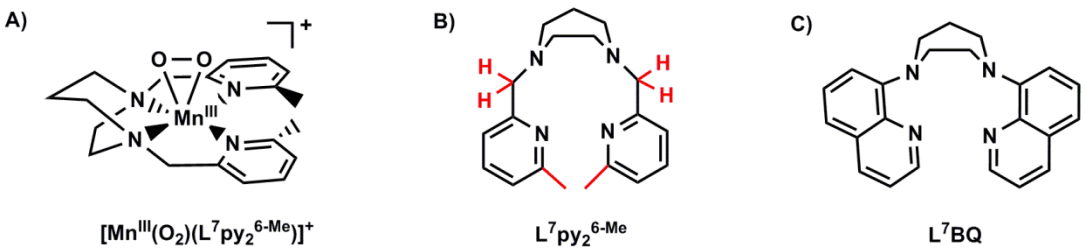

Figure 3.1. The schematic structures of A) $[Mn^{III}(O_2)(L^7py_2^{6\text{-}Me})]^+$ B) $L^7py_2^{6\text{-}Me}$ ligand highlighting the potentially oxidizable groups in red, and C) the proposed L^7BQ ligand.

In light of this insight, design and synthesis of a novel ligand platform excluding the linker –CH_2 group of the $L^7py_2^R$ ligand system (L^7BQ) was of interest (Figure 3.1), as this could potentially enhance the stability of reactive intermediates. We were successful in synthesizing the proposed L^7BQ ligand in moderate yield, and the corresponding Mn^{II} complex, $[Mn^{II}(L^7BQ)]^{2+}$, which has been characterized by X-ray diffraction techniques. $[Mn^{II}(L^7BQ)]^{2+}$ reacts with H_2O_2 and Et_3N to generate the expected peroxomanganese(III) complex, $[Mn^{III}(O_2)(L^7BQ)]^+$. Although its detailed spectroscopic characterization is still underway,

reactivity properties of $[Mn^{III}(O_2)(L^7BQ)]^+$ are quite intriguing, which are described in this chapter, along with other reactivities of $[Mn^{II}(L^7BQ)]^{2+}$.

3.2. Experimental Methods

3.2.1. Materials and Instrumentation. All chemicals and solvents were obtained from commercial vendors at ACS grade or better, and were used without further purification. Acetonitrile, methanol, and ether were dried and degassed using a Pure Solv (2010) solvent purification system. Extra dry toluene (99% purity), and other dry solvents, were purchased from Acros Organics and degassed by four freeze-pump-thaw cycles using Schlenk techniques. All dried, degassed solvents were immediately taken into an argon-filled glove box, and were stored in tightly-sealed Schlenk glassware. Synthesis of L^7BQ ligand, and $[Mn^{II}(L^7BQ)]^{2+}$ was carried out under inert conditions as described below. All ^1H NMR spectra were collected on a Bruker DRZ 400 MHz spectrometer and a Bruker DPX 300 MHz spectrometer with an ONP probe. All ^1H NMR experiments were performed at room temperature in $CDCl_3$ (δ = 7.24 ppm) unless stated otherwise. Mass spectrometry experiments were performed using an LCT Primers MicroMass electrospray time-of-flight instrument. Electronic absorption spectra were obtained on a Varian Cary 50 Bio spectrophotometer interfaced with a Unisoku cryostat (USP-203-A) capable of maintaining temperatures between 150 and 373 K.

3.2.2. Synthesis of L^7BQ Ligand. 8-bromoquinoline (832.2 mg, 4.0 mmol), homopiperazine (300.48 mg, 3.0 mmol), and NaO^tBu (324 mg, 3.4 mmol) were combined in a Schlenk tube in dry, degassed toluene (40 mL), along with 4 mol% of $Pd_2(dba)_3$ (110.0 mg, 0.12 mmol), and 10 mol% of BINAP (168 mg, 0.27 mmol) within an argon-filled glove box. The tube was sealed with an air-tight septum, and stirred at 110 ^oC for 18 hrs. The reaction mixture was

then cooled to room temperature, and was diluted with excess (~100 mL) diethyl ether. This mixture was filtered through celite, and was evaporated to dryness under reduced pressure. The crude product was purified by flash chromatography over silica gel using ethyl acetate and hexane (1 : 20) as the eluent. The clean ligand was isolated as a yellow oil in 60% yield (420 mg), and was characterized by ^{1}H NMR and ESI-MS.

3.2.3. Synthesis of [$Mn^{II}(L^7BQ)(OTf)_2$]. An equimolar mixture of L^7BQ and $Mn^{II}(OTf)_2$ produced high yields (>90%) of [$Mn^{II}(L^7BQ)(OTf)_2$] when stirred overnight in an inert atmosphere at room temperature. $Mn^{II}(OTf)_2$ was synthesized according to literature procedures.[28] A detailed procedure for the metalation of L^7BQ is as follows. To a stirred acetonitrile solution (5 mL) of L^7BQ (100 mg, 0.282 mmol), an equimolar quantity of $Mn^{II}(OTf)_2$ (99 mg, 0.282 mmol) was added in the same solvent (5 mL), and was stirred overnight under an inert atmosphere. The mixture was then filtered using a syringe filter, and dried under reduced pressure. The solid product was recrystallized with MeCN and Et_2O by vapor diffusion. Light yellow crystals suitable for X-ray diffraction analysis were obtained by subsequent recrystallization with the same solvent system. [$Mn^{II}(L^7BQ)(OTf)_2$] was further characterized by the effective magnetic moment analysis by the ^{1}H NMR method of Evans[45] in CD_3CN at 25 ^oC, and by ESI-MS and EPR (Figures A2.3 and A2.4). The effective magnetic moment at 25 ^oC was found to be 6.3 (Diam. Corr. = 0.5) μ_B in CD_3CN, which agrees with the expected value (5.9 μ_B) for a monomeric high-spin Mn^{II} center. ESI-MS: {[$Mn^{II}(L^7BQ)(OTf)]^+$} *m/z* = 558.0777 (calc. = 558.0745). The perpendicular-mode X-band EPR spectrum of a frozen acetonitrile solution of [$Mn^{II}(L^7BQ)(OTf)_2$], exhibits features at 230 mT and 350 mT at 5 K, which are characteristic of monomeric Mn^{II} species.[14]

3.2.4. X-ray diffraction data collection and analysis for $[Mn^{II}(L^7BQ)](OTf)$. A light-yellow single-domain crystal of $[Mn^{II}(L^7BQ)](OTf)$ was suspended with Paratone N oil on a MiteGen MicroMount and placed on a goniometer head in a cold nitrogen stream at 100 K for a single-crystal X-ray structure determination. Monochromatic X-rays were provided by a Bruker diffractometer equipped with Helios multilayer optics, an APEX II CCD detector and a Bruker MicroStar microfocus rotating anode X-ray source operating at 45 kV and 60 mA. Intensity data (5238 0.5°-wide ω- or φ-scan frames with counting times of 2-3 seconds each) were collected with the Bruker program SMART[46] and diffracted intensities were measured with the Bruker program SAINT.[47] The space group[48] and crystallographic data are summarized in Table A2.1. The Bruker software package SHELXTL was used to solve the structure and locate all nonhydrogen atoms with "direct methods" techniques. Hydrogen atoms were located from a difference Fourier and included in the structural model as independent isotropic atoms whose parameters were allowed to vary in least-squares refinement cycles. All stages of weighted full-matrix least-squares refinement were conducted using F_o^2 data with the SHELXTL Version 2010.3-0 software package.[49] The final structural model incorporated anisotropic thermal parameters for all non-hydrogen atoms and isotropic thermal parameters for all hydrogen atoms.

3.2.5. Generation of $[Mn^{III}(O_2)(L^7BQ)]^+$. The peroxomanganese(III) complex, $[Mn^{III}(O_2)(L^7BQ)]^+$ was generated by treating a 2.5 mM acetonitrile solution of $[Mn^{II}(L^7BQ)(OTf)_2]$ with 5 equiv. of H_2O_2 and 1.5 equiv. of Et_3N at -40 ^oC. Characteristic changes in the electronic absorption spectrum were evident of the formation of $[Mn^{III}(O_2)(L^7BQ)]^+$, where two bands rapidly grew in at 450 nm and 660 nm. These features compare well with the electronic spectroscopic signatures of other closely related peroxomanganese(III) complexes.[13,32,33] Furthermore, ESI-MS also provided evidence for the

formation of $[Mn^{III}(O_2)(L^7BQ)]^+$ (Figures A2. 5 and A2. 6). ESI-MS $\{[Mn^{III}(O_2)(L^7BQ)]^+\}$ *m/z* = 441.1106 (calc. = 441.1123); $\{[Mn^{III}(^{18}O_2)(L^7BQ)]^+\}$ *m/z* = 445.1156 (calc. = 445.1208). EPR samples of $[Mn^{III}(O_2)(L^7BQ)]^+$ were prepared at -40 ^oC in acetonitrile following cryogenic techniques, and were analyzed at 5 K.

3.2.5.1. Reactivity of $[Mn^{III}(O_2)(L^7BQ)]^+$ with $HClO_4$. The $[Mn^{III}(O_2)(L^7BQ)]^+$ adduct was generated as described above, and 0.5 equiv. of $HClO_4$ was added in MeCN at -40 ^oC. $[Mn^{III}(O_2)(L^7BQ)]^+$ reacted immediately, forming new absorption features at 500 nm and 900 nm. This new product is highly unstable under the given conditions, and decayed rapidly as observed by electronic absorption spectroscopy.

3.2.5.2. Reactivity of $[Mn^{III}(O_2)(L^7BQ)]^+$ with Acetyl Chloride. $[Mn^{III}(O_2)(L^7BQ)]^+$ reacted rapidly when 0.5 equiv. of acetyl chloride was introduced in MeCN at -40 ^oC. New absorption features grew in at 460 nm, 670 nm, and 800 nm. Although mass spectrometric analysis to determine the identity of this new species was not conclusive, EPR analysis provided useful insights. EPR samples of this new intermediate were prepared at -40 ^oC in acetonitrile, using cryogenic techniques. Warming up to room temperature caused the rapid decay of this new intermediate.

3.2.6. Reactivity of $[Mn^{II}(L^7BQ)]^{2+}$ with Iodosobenzene. Treating a 2.5 mM acetonitrile solution of $[Mn^{II}(L^7BQ)(OTf)_2]$ with 2.5 equiv. of iodosobenzene (PhIO), generates a new species with an intense absorption feature (ϵ = 1000 M^{-1} cm^{-1}) centered at 485 nm. This species is indefinitely stable in solution under ambient conditions.

3.3. Results and Analysis

3.3.1. Design and synthesis of L^7BQ ligand. Given the potential ligand oxidative decay pathways of the $[Mn^{III}(O_2)(L^7py_2^R)]^+$ series of peroxomanganese(III) complexes, the L^7BQ ligand was designed in order to support new intermediates with higher thermal stability. The synthesis of this ligand would involve the coupling of two quinolinyl moieties with each secondary amine functionality of homopiperazine. Coupling of secondary amines with aryl halides can be attained via Pd-catalyzed Buchwald-Hartwig cross-coupling reactions.[50,51] In this case, 8-bromoquinoline and homopiperazine would be coupled to generate the desired aminoquinolinyl L^7BQ ligand (L^7BQ = 1,4-di(quinolin-8-yl)-1,4-diazepane; Scheme 3.2). Although Buchwald-Hartwig cross-coupling reactions that involve two nucleophilic centers are less common, we were successful in optimizing the reaction conditions for the synthesis of L^7BQ ligand in moderate yields (~60%). ^{1}H NMR data (400 MHz) for L^7BQ ($CDCl_3$, δ) = 8.86 (dd, *J* = 4.1, 1.9 Hz, 2H), 8.09 (dd, *J* = 8.3, 1.9 Hz, 2H), 7.40 (t, *J* = 7.8 Hz, 2H), 7.35 (dd, *J* = 8.2, 4.1 Hz, 2H), 7.31 (dd, *J* = 8.2, 1.3 Hz, 2H), 7.21 (dd, *J* = 7.6, 1.4 Hz, 2H), 4.09 (s, 4H), 3.96 – 3.76 (m, 4H), 2.38 (p, *J* = 5.7 Hz, 2H). ESI-MS: {$[L^7BQ + H]^+$} *m/z* = 355.1902 (calc. = 355.1923). For ^{1}H NMR and ESI-MS spectra, see Figures A2.1 and A2.2, respectively.

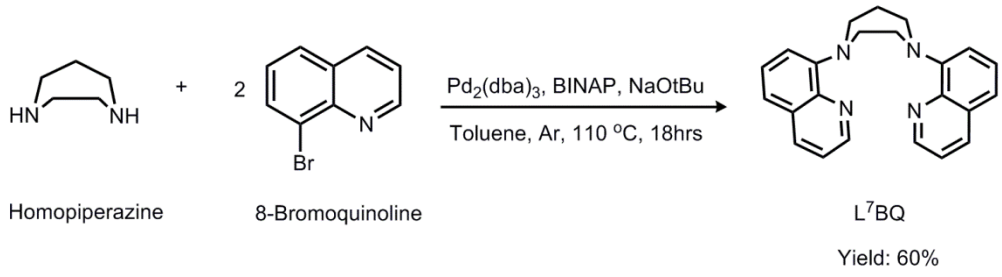

Scheme 3.2. Synthetic scheme for the L^7BQ ligand.

3.3.2. Structural Properties of $[Mn^{II}(L^7BQ)(OTf)_2]$. The XRD structure of $[Mn^{II}(L^7BQ)(OTf)_2]$ contains a six-coordinate manganese center in a pseudo-octahedral geometry (Figure 3.2). Significant bond lengths and angles of $[Mn^{II}(L^7BQ)(OTf)_2]$ are summarized in Table 3.1. In this structure, the L^7BQ ligand is coordinated in a tetradentate fashion occupying the equatorial plane (N1–N4), with the Mn^{II} ion showing no displacement from the equatorial plane. The angles between the equatorial ligands vary between 72^o - 137^o, revealing clear deviations from idealized octahedral symmetry. The axial sites are occupied by the two triflate ions with an O11–Mn–O21 bond angle of 155.06^o. The Mn–N distances vary between 2.2 – 2.3 Å and Mn–O distances are ~2.2 Å (Table 3.1), which are typical for high-spin Mn^{II} centers (Figure 3.2).[13,32,52] An acetonitrile solvent molecule is also present in the asymmetric unit (not shown in Figure 3.2), which does not interact with the metal center (Mn–N distance of 6.729 Å).

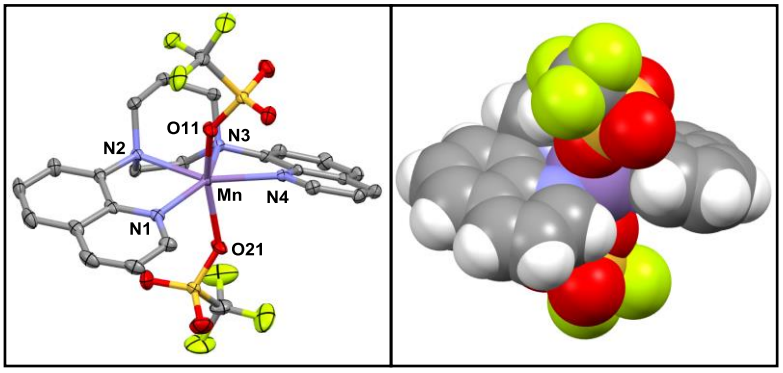

Figure 3.2. ORTEP diagram (left) and the space-filling model (right) for $[Mn^{II}(L^7BQ)(OTf)_2]$. ORTEP diagram shows 50% thermal probability. Hydrogen atoms and the non-coordinating solvent molecule have been removed for clarity. Significant interatomic distances and angles are listed in Table 3.1.

Table 3.1. Selected Bond Lengths (Å) and Angles (deg) for $[Mn^{II}(L^7BQ)(OTf)_2]$.

Atom pair	Distance (Å)	Angle	Value (^{o})
Mn–N1	2.1846(14)	O11–Mn–O21	155.05(5)
Mn–N2	2.3011(15)	N1–Mn–N2	76.73(5)
Mn–N3	2.2841(14)	N2–Mn–N3	71.47(5)
Mn–N4	2.2109(14)	N3–Mn–N4	75.84(5)
Mn–O11	2.1869(12)	N4–Mn–N1	137.04(5)
Mn–O21	2.2152(13)	N1–Mn–O11	85.22(5)

3.3.3. Oxidation of $[Mn^{II}(L^7BQ)(OTf)_2]$ with H_2O_2. The reaction of a 2.5 mM solution of $[Mn^{II}(L^7BQ)(OTf)_2]$ with 5 equiv. H_2O_2 and 1.5 equiv. of Et_3N in acetonitrile, gives rise to a new intermediate species at -40 ^{o}C. This new complex displays two prominent absorption features centered at 450 nm (ϵ = 295 M^{-1} cm^{-1}) and 660 nm (ϵ = 80 M^{-1} cm^{-1}; Figure 3.3 (left)), which are strikingly similar to those of other structurally similar η^2-peroxomanganese(III) complexes that are prepared under similar reaction conditions.[13,32,33] This new species is only stable for ~5 min at -40 ^{o}C in acetonitrile, and decays rapidly as the solution temperature is elevated. Furthermore, when higher equivalents of the base were used for the formation of this intermediate, it was observed to decay even more rapidly. The mass spectrum of this solution displays an ion peak at 441.1135 *m/z*, which compares well with that expected for $[Mn^{III}(O_2)(L^7BQ)]^+$ (calc. = 441.1123 *m/z*). When $H_2{}^{18}O_2$ was used to generate this intermediate, the corresponding ion peak shifted to 445.1156 *m/z*, providing further evidence for the presence of a peroxo ligand derived from H_2O_2. It should be noted that these peaks corresponding to Mn^{III}-O_2 intermediates are of low intensity in their mass spectrometric data collected at room temperature. This is anticipated, given the impaired thermal stability of this species at temperatures higher than -40 ^{o}C. Furthermore, the parallel mode X-band EPR spectrum of $[Mn^{III}(O_2)(L^7BQ)]^+$ shows no features at 5 K, which is typical of Mn^{III} compounds with large zero-field splitting.[53] The perpendicular mode X-band EPR spectra of $[Mn^{III}(O_2)(L^7BQ)]^+$

collected at 5 K (the green trace in Figure 3.3 (right)), reveals a low-intensity derivative shaped signal at 350 mT, with a multi-line hyperfine pattern which is indicative of dimeric manganese species. This is potentially a product of thermal decay of $[Mn^{III}(O_2)(L^7BQ)]^+$. However, this spectrum does not exhibit any features corresponding to $[Mn^{II}(L^7BQ)(OTf)_2]$ (compare with the red trace in Figure 3.3 (right)), suggesting that most of the $[Mn^{II}(L^7BQ)(OTf)_2]$ is consumed during the formation of $[Mn^{III}(O_2)(L^7BQ)]^+$.

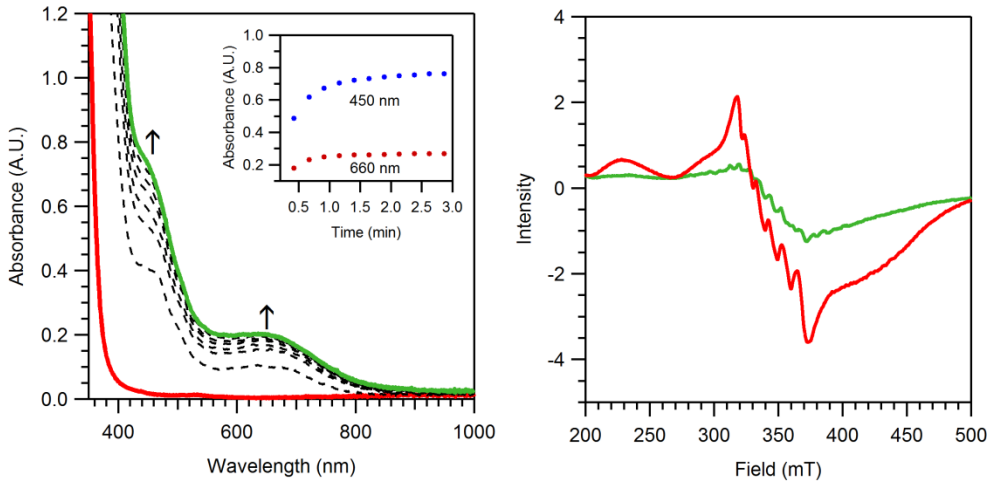

Figure 3.3. Left: Electronic absorption spectral changes of $[Mn^{II}(L^7BQ)(OTf)_2]$ (solid red trace) upon the addition of 5 equiv. H_2O_2 and 1.5 equiv. Et_3N in acetonitrile at -40 ^oC. Inset: Time evolution of absorption features at 450 nm and 660 nm. Right: Perpendicular mode X-band EPR spectra corresponding to 2 mM frozen acetonitrile solutions of $[Mn^{II}(L^7BQ)(OTf)_2]$ (solid red trace) and $[Mn^{III}(O_2)(L^7BQ)]^+$ (solid green trace) collected at 5 K.

Since the impaired thermal stability of $[Mn^{III}(O_2)(L^7BQ)]^+$ severely limits its further characterization, its formation in different solvents with lower freezing points (acetone, methanol, butyronitrile, ethanol, dichloromethane, tetrahydrofuran, and 2-methyltetrahydrofuran) was attempted. Unfortunately, $[Mn^{III}(O_2)(L^7BQ)]^+$ could not be generated in any of these solvents, even at a lower yield than in acetonitrile. The limited variability of the solvent and

temperature for $[Mn^{III}(O_2)(L^7BQ)]^+$ formation has prevented its solid state characterization or further spectroscopic characterization. For example, MCD characterization of $[Mn^{III}(O_2)(L^7BQ)]^+$ is not feasible, due to the poor glassing capabilities of acetonitrile. We have previously shown that MCD spectroscopy can provide useful insights into understanding the geometric and electronic structures of peroxomanganese(III) species.[13,31,32] Furthermore, unlike the closely related $[Mn^{III}(O_2)(L^7py_2^R)]^+$ series of peroxo compounds,[13,32] $[Mn^{III}(O_2)(L^7BQ)]^+$ could not be generated using KO_2 as the oxidant. Thus, the generation of $[Mn^{III}(O_2)(L^7BQ)]^+$ is strictly limited to the conditions described here (*vide supra*). Future work will involve studies using solvent mixtures with different compositions (for example, acetonitrile/ toluene mixtures), and/ or other oxidants for the generation and stabilization of $[Mn^{III}(O_2)(L^7BQ)]^+$. However, $[Mn^{III}(O_2)(L^7BQ)]^+$ exhibits intriguing reactivity patterns with acids and acid halides (*vide infra*), which are unprecedented for non-porphyrinoid η^2-peroxomanganese(III) complexes.

3.3.4. Reactivity of $[Mn^{III}(O_2)(L^7BQ)]^+$ with $HClO_4$. $[Mn^{III}(O_2)(L^7BQ)]^+$ reacts rapidly with 0.5 equiv. of $HClO_4$ in acetonitrile at -40 ^oC giving rise to new absorption features centered at 500 nm (ϵ = 225 M^{-1} cm^{-1}), 900 nm (ϵ = 85 M^{-1} cm^{-1}; Figure 3.4). This new species (**1**) is highly unstable under these conditions ($t_{1/2}$ = ~5 min) at -40 ^oC, which has prevented its detailed characterization to date. However, the absorption signatures of **1** are highly reminiscent of those of monomeric Mn^{IV}=O species, especially the low-energy absorption feature at ~900 nm.[52,54,55] Activation of η^2-peroxomanganese(III) complexes supported by non-porphyrin based ligands to generate high-valent oxidants are very rare,[18] which makes the conversion of $[Mn^{III}(O_2)(L^7BQ)]^+$ to **1** of great interest. As previously observed for Mn^{III}-peroxo compounds, $[Mn^{III}(O_2)(L^7BQ)]^+$ may react with $HClO_4$ to generate $[Mn^{III}(OOH)(L^7BQ)]^{2+}$ by the protonation of the peroxo ligand (Scheme 3.3).[39,41] A subsequent homolytic O–O bond cleavage would give rise to the

proposed $[Mn^{IV}(O)(L^7BQ)]^{2+}$ species. Even though a single example of spectroscopically characterized Mn^{III}-OOH species has been reported,[41] there is only indirect evidence for its conversion to high-valent oxidants. Thus, this chemistry is of high significance, not only in understanding the interaction of peroxomanganese(III) complexes with strong acids, but also in gaining insight into the structure and reactivity of Mn^{III}-OOH intermediates. Furthermore, the reactivity properties of **1** with organic substrates, and the product distribution of those reactions will also provide useful information that will aid in elucidating its identity. The decay product (blue trace in Figure 3.4) of **1** resembles **2** (*vide infra*), the identity of which is proposed as a monooxo-bridged dimanganese(III,IV) species based on the present data. The yield of **2** in this case (assuming its 100% yield in the reactivity between $[Mn^{III}(O_2)(L^7BQ)]^+$ and acetyl chloride (*vide infra*)) is ~15%, which could either imply that the conversion of $[Mn^{III}(O_2)(L^7BQ)]^+$ to **1** is not high-yielding, or that **1** decays via multiple pathways. The optimization of the generation of **1** by the observed pathway, and other potential pathways will be the subject of future studies.

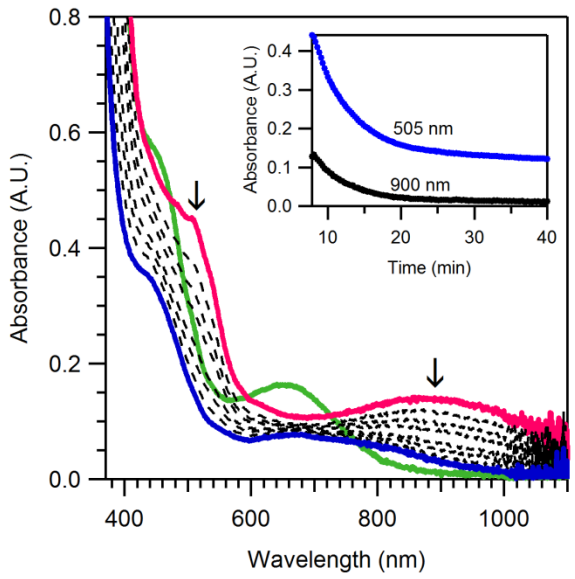

Figure 3.4. Electronic absorption spectroscopic changes exhibited as $[Mn^{III}(O_2)(L^7BQ)]^+$ (solid green trace) reacts with 0.5 equiv. $HClO_4$ to generate **1** (solid pink trace) in acetonitrile at -40 ^oC, and its decay under the same conditions. Inset: Time evolution of the absorption signals at 505 nm and 900 nm immediately following the addition of acid.

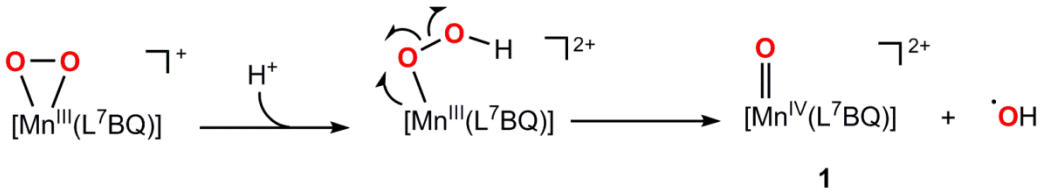

Scheme 3.3. Proposed reaction scheme for the formation of **1** upon the reaction between $[Mn^{III}(O_2)(L^7BQ)]^+$ and 0.5 equiv. $HClO_4$ in acetonitrile at -40 ^oC.

3.3.5. Reactivity of $[Mn^{III}(O_2)(L^7BQ)]^+$ with Acetyl Chloride (CH_3COCl). η^2-peroxomanganese(III) complexes supported by electron-rich porphyrin ligands have exhibited reactivity with benzoyl chloride to generate the corresponding η^1-acylperoxomanganese(III) species, which undergoes heterolytic O–O bond cleavage to generate high-valent Mn^V-oxo species.[56-58] Treating $[Mn^{III}(O_2)(L^7BQ)]^+$ with 0.5 equiv. of acetyl chloride generates a new

species (**2**) in acetonitrile at -40 ^{o}C, with characteristic absorption features at 460 nm (ϵ = 760 M^{-1} cm^{-1}), 670 nm (ϵ = 205 M^{-1} cm^{-1}), and 800 nm (ϵ = 165 M^{-1} cm^{-1}; Figure 3.5 (left)). These absorption features are comparable to those of bis(μ-oxo)dimanganese(III,IV) species as previously observed by us[14] and others.[59-61] The perpendicular mode X-band EPR spectrum of **2** displays a 16-line signal at 350 mT at 5 K, which is also characteristic of bis(μ-oxo)dimanganese(III,IV) complexes (Figure 3.5 (right)).[14] The reactivity of $[Mn^{III}(O_2)(L^7BQ)]^+$ with acetyl chloride could also involve an acylperoxomanganese(III) intermediate, but such intermediates have not been observed for non-porphyrinoid complexes to date. In fact, non-porphyrinoid peroxomanganese(III) complexes that react with acid chlorides to generate a single product in high yields are uncommon. Although the mechanistic details of this reactivity are still unclear, we propose that $[Mn^{III}(O_2)(L^7BQ)]^+$ reacts with acetyl chloride to generate the corresponding acetylperoxomanganese(III) species as seen in the porphyrin systems (Scheme 3.4). This intermediate could then undergo heterolytic O–O bond cleavage to generate the $Mn^{V}{\equiv}O$ species, which could dimerize with unreacted $[Mn^{II}(L^7BQ)(OTf)_2]$ to result in formation of the spectroscopically observable dimanganese(III,IV) species. Thus, our proposal suggests that **2** is a monooxo-bridged dimanganese(III,IV) species, which are also known to result in 16-line EPR features.[62] The decay of **2** is slow, exhibiting a half-life of ~50 min in acetonitrile at -40 ^{o}C. Future work will focus on obtaining solid state characterization of **2**, and further structural investigations using techniques such as X-ray absorption spectroscopy. Furthermore, reactivity studies with organic substrates will also aid in understanding the structural and reactivity properties of **2**.

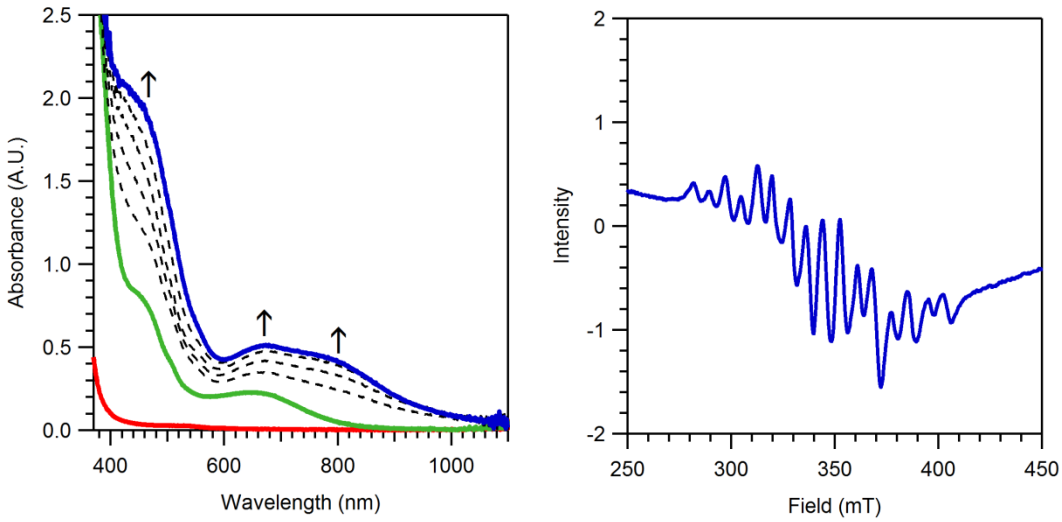

Figure 3.5. Left: Formation of **2** (solid blue trace) upon reacting $[Mn^{III}(O_2)(L^7BQ)]^+$ (solid green trace) with 0.5 equiv. of acetyl chloride in acetonitrile at -40 °C. Right: X-band EPR spectrum of **2** in frozen acetonitrile at 5 K.

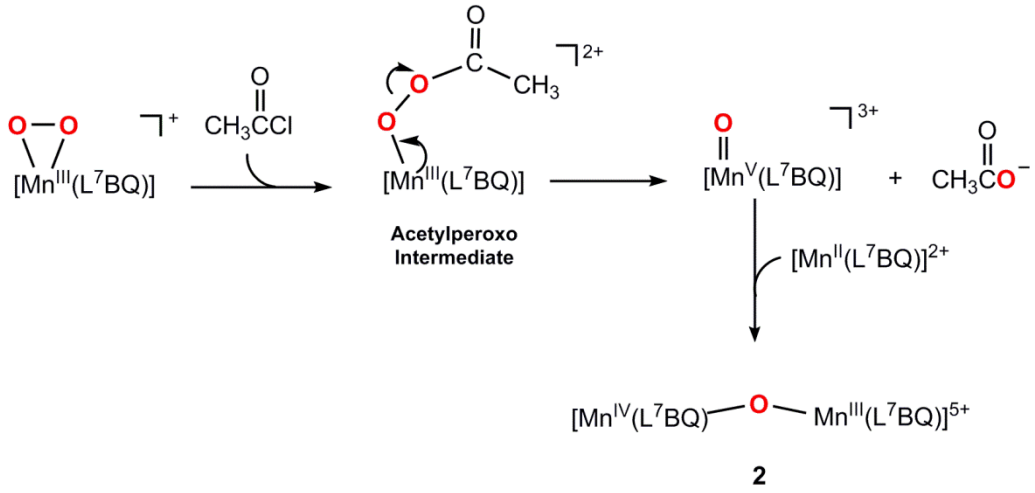

Scheme 3.5. Proposed mechanism for the formation of **2** when $[Mn^{III}(O_2)(L^7BQ)]^+$ is reacted with 0.5 equiv. of acetyl chloride at -40 °C in MeCN.

3.3.6. Reactivity of $[Mn^{II}(L^7BQ)]^{2+}$ with Iodosobenzene (PhIO). The reactivity with PhIO is of interest as it is a commonly used two-electron oxidant that also behaves as an oxo-atom transferring agent. Accordingly, it has been frequently used in the generation of monomeric M^{IV}=O complexes from their M^{II} precursors where M = Mn or Fe.[52,54,63] Addition of 2.5 equiv. of PhIO to a 2.5 mM acetonitrile solution of $[Mn^{II}(L^7BQ)]^{2+}$ generates a new species (**3**), with an intense absorption feature at 485 nm (ϵ = 1000 M^{-1} cm^{-1}; Figure 3.6). **3** is highly stable under ambient conditions. Unfortunately, further characterization of **3** by techniques such as EPR, XAS and ESI-MS has proved unsuccessful to date. The EPR spectrum of **3** does not exhibit any prominent features that are comparable to other known Mn spectra, which could suggest that **3** is predominantly Mn^{III}, which is often EPR silent. ESI-MS data of **3** is not clean, making the results inconclusive. However, unlike $[Mn^{III}(O_2)(L^7BQ)]^+$, **3** can be generated in multiple solvents (acetonitrile, 2,2,2-trifluoroethanol, dichloromethane, and methanol), which should facilitate its characterization by techniques such as X-ray diffraction and MCD spectroscopy. Furthermore, the reactivity properties of **3** have yet to be investigated. Such studies should provide additional insight into the identity of **3**.

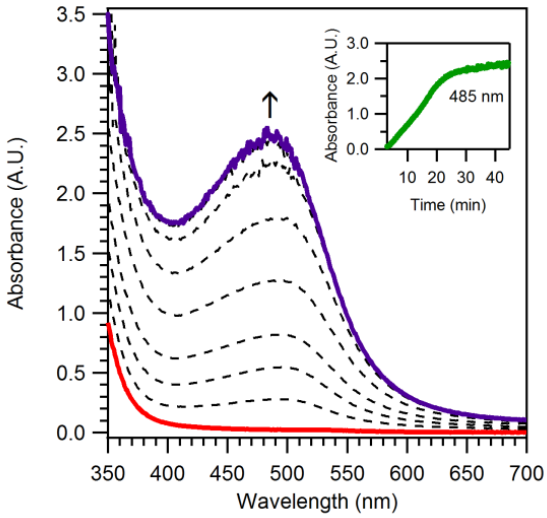

Figure 3.6. Electronic absorption changes observed during the reaction between $[Mn^{II}(L^{7}BQ)]^{2+}$ and 2.5 equiv. of PhIO. Inset: Time evolution of the absorption feature at 485 nm.

3.4. Discussion and Outlook

Peroxomanganese(III) adducts have been proposed as key intermediates for a number of enzymatic conversions as well as some synthetic catalytic pathways involving manganese centers.[1-6,22,23,64] Compared to analogous iron systems, mechanistic knowledge of manganese-dependent biological processes is still rather limited. Furthermore, due to numerous challenges involved in enzymatic studies, small molecule model complexes of such systems have been widely used to understand the properties of these pathways.[12-18] The most common type of peroxomanganese(III) complexes reported in the literature is η^2-peroxomanganese(III) complexes with a side-on peroxo ligand bound to a manganese(III) center.[13,14,24-39] Although less common, η^1-alkylperoxomanganese(III) and *trans*-μ-1,2-peroxo-bridged dimanganese(III,III) dimeric species have also been structurally characterized.[19,20,65] The common limitations in the characterization and reactivity studies of these intermediates often stem from their low chemical yields and impaired thermal stability. To this end, this work has focused on the design and

synthesis of a more oxidatively robust ligand to support reactive intermediates, which could presumably enhance the lifetime of peroxomanganese(III) complexes. In addition, due to the highly tolerant nature of the supporting ligand, these complexes are expected to display unique, unprecedented reactivities with the formation of more stable reactive intermediates.

Although most peroxomanganese(III) species reported in current literature are unstable under ambient conditions, detailed studies on the decay pathways of these intermediates are rare. η^1-alkylperoxomanganese(III) complexes have been observed to decay with a rate-limiting homolytic O–O bond cleavage process.[19,20] In contrast, a detailed spectroscopic study of the decay of an η^2-peroxomanganese(III) complex supported by a pentadentate ligand[39] provided important insights into a possible ligand oxidative decay pathway for the $[Mn^{III}(O_2)(L^7py_2{}^R)]^+$ series (*vide supra*). Thus, as a modification to the $L^7py_2{}^R$ platform, the L^7BQ ligand system was designed.

The L^7BQ ligand was synthesized in moderate yields (60 %) using a Pd-catalyzed cross coupling reaction between homopiperazine and 8-bromoquinoline (Scheme 3.2). The Mn^{II} complex of this system, $[Mn^{II}(L^7BQ)(OTf)_2]$, was synthesized by metalation of the L^7BQ ligand using standard procedures, and has been characterized by X-ray diffraction methods.

When treated with 5 equiv. of H_2O_2 and 1.5 equiv. of triethylamine, $[Mn^{II}(L^7BQ)(OTf)_2]$ produced a new intermediate in acetonitrile solution at -40 ^oC, which has been characterized as $[Mn^{III}(O_2)(L^7BQ)]^+$ by electronic absorption and EPR spectroscopies as well as mass spectrometry. Unfortunately, $[Mn^{III}(O_2)(L^7BQ)]^+$ does not exhibit enhanced thermal stability as anticipated. Furthermore, the highly limited solvent, temperature and oxidant variability in its generation have severely limited its further characterization. However, its formation in mixed solvent systems that are known to produce good quality glass upon freezing (such as MeCN/

toluene mixtures) has yet to be studied. In addition, electrochemically generated superoxide may aid in generating $[Mn^{III}(O_2)(L^7BQ)]^+$ in high yields, paving the way for other characteristic methods such as X-ray absorption spectroscopy. Nevertheless, $[Mn^{III}(O_2)(L^7BQ)]^+$ displays intriguing reactivity patterns (as summarized in Scheme 3.5), most of which are unprecedented for non-porphyrinoid peroxomanganese(III) complexes.

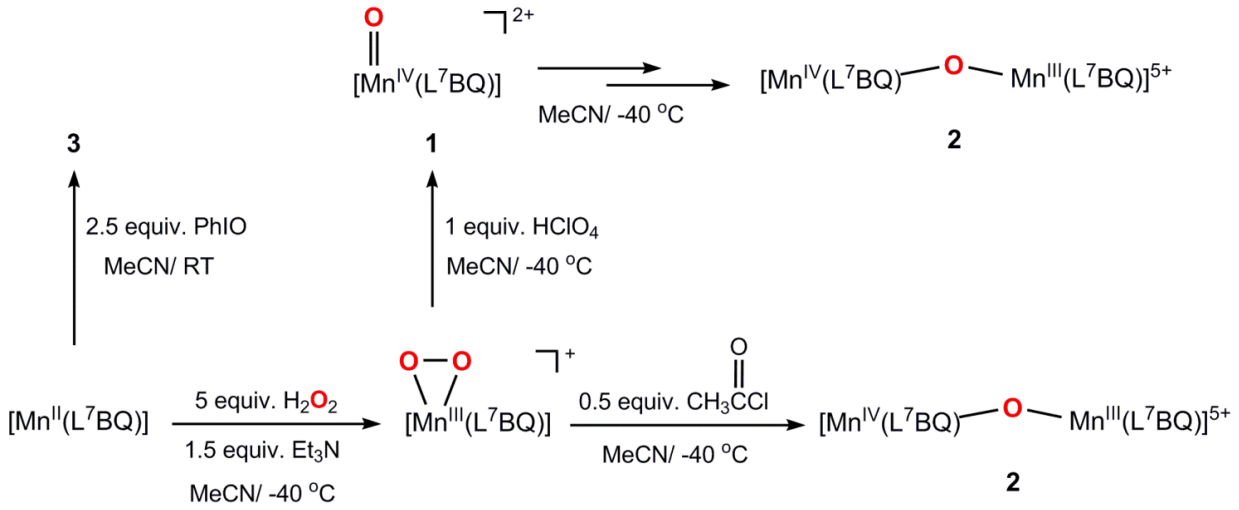

Scheme 3.5. Proposed reaction landscape for $[Mn^{II}(L^7BQ)(OTf)_2]$ and the corresponding η^2-peroxomanganese(III) species, $[Mn^{III}(O_2)(L^7BQ)]^+$.

$[Mn^{III}(O_2)(L^7BQ)]^+$ reacts with 0.5 equiv. of $HClO_4$ to generate the novel intermediate **1** at -40 °C. **1** has electronic absorption features that highly resemble those of monomeric Mn^{IV}=O complexes.[52,54,55] This observation is of great interest, as activation of non-porphyrinoid peroxomanganese(III) complexes to generate high-valent oxidants is unprecedented in current literature. In the case of $[Mn^{III}(O_2)(L^7BQ)]^+$, we propose the protonation of the peroxo ligand upon acid addition to generate $[Mn^{III}(OOH)(L^7BQ)]^{2+}$, which then undergoes homolytic O–O bond cleavage to generate the high-valent $[Mn^{IV}(O)(L^7BQ)]^{2+}$ species (Scheme 3.3). In support of this proposal, Nam and coworkers have recently reported the generation of

$[Mn^{III}(OOH)(TMC)]^{2+}$ by the protonation of $[Mn^{III}(O_2)(TMC)]^{+}$ complex using 3 equiv. of $HClO_4$ (TMC = 1,4,8,11-tetramethyl-1,4,8,11-tetraazacyclotetradecane).[41] Optimization of the reaction conditions for this observed chemistry is an important subject of future investigations. Specifically, analyzing the yield of **1** as a function of the number of equivalents of acid will provide important insights into the mechanistic details of the reaction involved. Furthermore, if **1** is a high-valent Mn^{IV}=O species, it is expected to oxidize substrates such as DHA and/or PPh_3.[52] DHA is known to react with Mn^{IV}=O species to form anthracene by a PCET pathway, while PPh_3 would generate $P(O)Ph_3$ by oxygen atom transfer (OAT). Thus, reacting $[Mn^{III}(O_2)(L^7BQ)]^{+}$ with acid in the presence of such substrates, and analysis of the final reaction mixtures by GC-MS for the presence of the expected organic products, will provide important insights into the identity of **1**. Furthermore, given the observed rapid decay of **1** under current conditions, investigation of its formation and decay in d_3-MeCN would produce useful information regarding the involvement of the solvent during its decay. Finally, perpendicular-mode X-band EPR experiments will also provide evidence for the presence of the proposed $[Mn^{IV}(O)(L^7BQ)]^{2+}$ species in solution. The *in situ* formation of **1** by reacting $[Mn^{III}(O_2)(L^7BQ)]^{+}$ with acid inside the EPR tube would presumably facilitate its isolation in high yields, minimizing the thermal decay.

Furthermore, $[Mn^{III}(O_2)(L^7BQ)]^{+}$ reacts with acetyl chloride in acetonitrile solution at -40 ^{o}C to generate **2**, of which, the absorption features and EPR spectrum are consistent with a dimanganese(III,IV) species.[14,59-61,66] The peroxomanganese(III) adduct supported by tetramesitylporphyrin (TMP) has been previously observed to react with benzoyl chloride to generate the corresponding acylperoxomanganese(III) species, which undergoes O–O bond heterolysis to generate the $[Mn^{V}(O)(TMP)]^{+}$ complex.[56-58] To the best of our knowledge,

$[Mn^{III}(O_2)(L^7BQ)]^+$ provides the only example of a non-porphyrinoid peroxomanganese(III) complex that displays any reactivity with acid chlorides. As suggested for **1**, generating **2** in the presence of organic substrates will also provide evidence of the proposed mechanism involved in this reaction pathway (*vide supra*). If a high-valent $Mn^V{\equiv}O$ species is involved in the mechanism as suggested, it can be expected to react rapidly with substrates such as DHA and PPh_3. Furthermore, $H_2{}^{18}O_2$-labeling experiments will also provide important insights into the mechanism, where cryogenic mass spectrometric analysis will aid in detecting the label distribution in thermally unstable intermediates. In addition, due to the reasonable half-life ($t_{1/2}$ = ~50 min) of **2** at -40 ^oC, its solid state analysis should be feasible by XRD. It should be noted that the generation of **2** in solvent other than MeCN has not been attempted, which could reveal other solvent systems where crystal growth can be carried out at much lower temperatures than -40 ^oC. Finally, since the solution composition of **2** appears to be clean by EPR, its X-ray absorption spectroscopic analysis could also provide useful insights into its structural identity.

The reactivity of $[Mn^{II}(L^7BQ)(OTf)_2]$ with oxidants other than H_2O_2 is yet to be investigated in detail. However, current results of its reactivity with 2.5 equiv. of PhIO in acetonitrile at 25 ^oC show formation of a new species, **3**, with an intense absorption feature at 485 nm. **3** has not been fully characterized yet, but its formation from Mn^{II} and PhIO is interesting, as the latter has been utilized in generating monomeric Mn^{IV}=O and Mn^{III}-OH adducts from their Mn^{II} precursors.[52,54,63] Potential solid state and spectroscopic characterization, in combination with reactivity studies would provide detailed insight into the properties of **3**.

In conclusion, this work describes the design and synthesis of a new ligand system and its Mn^{II} metal complex, that may act as an oxidatively robust system in minimizing the ligand oxidative decay pathways observed for peroxomanganese(III) intermediates. The new

peroxomanganese(III) species, $[Mn^{III}(O_2)(L^7BQ)]^+$, shows a unique reactivity profile which can potentially serve in furthering the current understanding of the chemistry of peroxomanganese(III) intermediates (Scheme 3.5). Future work will focus on optimizing reaction conditions in order to enhance the yields and stabilities of the observed intermediates, enabling their detailed structural and spectroscopic characterization, as well as reactivity investigations. Furthermore, modifying the steric and electronic properties of the L^7BQ supporting ligand may facilitate the fine-tuning of the metal center properties that dictate the stabilities of these transient intermediates.

6.5. References

1. Miller, A.-F., *Curr. Opin. Chem. Biol.* **2004,** *8*, 162-168.
2. Grove, L. E.; Brunold, T. C., *Comments Inorg. Chem.* **2008,** *29*, 134-168.
3. Koehntop, K. D.; Emerson, J. P.; Que, L., Jr., *J. Biol. Inorg. Chem.* **2005,** *10*, 87-93.
4. Gunderson, W. A.; Zatsman, A. I.; Emerson, J. P.; Farquhar, E. R.; Que, L.; Lipscomb, J. D.; Hendrich, M. P., *J. Am. Chem. Soc.* **2008,** *130*, 14465-14467.
5. Borowski, T.; Bassan, A.; Richards, N. G. J.; Siegbahn, P. E. M., *J. Chem. Theory Comput.* **2005,** *1*, 686-693.
6. Opaleye, O.; Rose, R.-S.; Whittaker, M. M.; Woo, E.-J.; Whittaker, J. W.; Pickersgill, R. W., *J. Biol. Chem.* **2006,** *281*, 6428-6433.
7. Tabares, L. C.; Gätjens, J.; Hureau, C.; Burrell, M. R.; Bowater, L.; Pecoraro, V. L.; Bornemann, S.; Un, S., *J. Phys. Chem. B* **2009,** *113*, 9016-9025.
8. Tanner, A.; Bowater, L.; Fairhurst, S. A.; Bornemann, S., *J. Biol. Chem.* **2001,** *276*, 43627-43634.
9. Wu, A. J.; Penner-Hahn, J. E.; Pecoraro, V. L., *Chem. Rev.* **2004,** *104*, 903-938.
10. Cotruvo, J. A.; Stich, T. A.; Britt, R. D.; Stubbe, J., *J. Am. Chem. Soc.* **2013**.
11. Cotruvo, J. J. A.; Stubbe, J., *Metallomics* **2012,** *4*, 1020-1036.
12. Pecoraro, V. L.; Baldwin, M. J.; Gelasco, A., *Chem. Rev.* **1994,** *94*, 807-826.
13. Geiger, R. A.; Wijeratne, G.; Day, V. W.; Jackson, T. A., *Eur. J. Inorg. Chem.* **2012**, 1598-1608.
14. Leto, D. F.; Chattopadhyay, S.; Day, V. W.; Jackson, T. A., *Dalton Trans.* **2013,** *42*, 13014-13025.
15. Goldsmith, C. R.; Cole, A. P.; Stack, T. D. P., *J. Am. Chem. Soc.* **2005,** *127*, 9904-9912.
16. Wijeratne, G. B.; Corzine, B.; Day, V. W.; Jackson, T. A., *Inorg. Chem.* **2014,** *53*, 7622-7634.
17. Wijeratne, G. B.; Day, V. W.; Jackson, T. A., *Dalton Trans.* **2015,** *44*, 3295-3306.
18. Leto, D.; Jackson, T., *J. Biol. Inorg. Chem.* **2014,** *19*, 1-15.

19. Coggins, M. K.; Kovacs, J. A., *J. Am. Chem. Soc.* **2011,** *133*, 12470-12473.
20. Coggins, M. K.; Martin-Diaconescu, V.; DeBeer, S.; Kovacs, J. A., *J. Am. Chem. Soc.* **2013,** *135*, 4260-4272.
21. Mullins, C. S.; Pecoraro, V. L., *Coord. Chem. Rev.* **2008,** *252*, 416-443.
22. Sibbons, K. F.; Shastri, K.; Watkinson, M., *Dalton Trans.* **2006**, 645-661.
23. Saisaha, P.; de Boer, J. W.; Browne, W. R., *Chem. Soc. Rev.* **2013,** *42*, 2059-2074.
24. El Ghachtouli, S.; Vincent Ching, H. Y.; Lassalle-Kaiser, B.; Guillot, R.; Leto, D. F.; Chattopadhyay, S.; Jackson, T. A.; Dorlet, P.; Anxolabehere-Mallart, E., *Chem. Commun.* **2013,** *49*, 5696-5698.
25. VanAtta, R. B.; Strouse, C. E.; Hanson, L. K.; Valentine, J. S., *J. Am. Chem. Soc.* **1987,** *109*, 1425-1434.
26. Kitajima, N.; Komatsuzaki, H.; Hikichi, S.; Osawa, M.; Moro-oka, Y., *J. Am. Chem. Soc.* **1994,** *116*, 11596-11597.
27. Singh, U. P.; Sharma, A. K.; Hikichi, S.; Komatsuzaki, H.; Moro-oka, Y.; Akita, M., *Inorg. Chim. Acta* **2006,** *359*, 4407-4411.
28. Seo, M. S.; Kim, J. Y.; Annaraj, J.; Kim, Y.; Lee, Y.-M.; Kim, S.-J.; Kim, J.; Nam, W., *Angew. Chem., Int. Ed.* **2007,** *46*, 377-380.
29. Annaraj, J.; Cho, J.; Lee, Y.-M.; Kim, S. Y.; Latifi, R.; de Visser, S. P.; Nam, W., *Angew. Chem. Int. Ed.* **2009,** *48*, 4150-4153.
30. Kang, H.; Cho, J.; Cho, K.-B.; Nomura, T.; Ogura, T.; Nam, W., *Chem.--Eur. J.* **2013**, 14119-14125.
31. Colmer, H. E.; Geiger, R. A.; Leto, D. F.; Wijeratne, G. B.; Day, V. W.; Jackson, T. A., *Dalton Trans.* **2014,** *43*, 17949-17963.
32. Geiger, R. A.; Chattopadhyay, S.; Day, V. W.; Jackson, T. A., *J. Am. Chem. Soc.* **2010,** *132*, 2821-2831.
33. Geiger, R. A.; Chattopadhyay, S.; Day, V. W.; Jackson, T. A., *Dalton Trans.* **2011,** *40*, 1707-1715.
34. Geiger, R. A.; Leto, D. F.; Chattopadhyay, S.; Dorlet, P.; Anxolabéhère-Mallart, E.; Jackson, T. A., *Inorg. Chem.* **2011,** *50*, 10190-10203.
35. Borovik, A. S., *Acc. Chem. Res.* **2004,** *38*, 54-61.
36. Shook, R. L.; Gunderson, W. A.; Greaves, J.; Ziller, J. W.; Hendrich, M. P.; Borovik, A. S., *J. Am. Chem. Soc.* **2008,** *130*, 8888-8889.
37. Shook, R. L.; Peterson, S. M.; Greaves, J.; Moore, C.; Rheingold, A. L.; Borovik, A. S., *J. Am. Chem. Soc.* **2011,** *133*, 5810-5817.
38. Groni, S.; Blain, G.; Guillot, R.; Policar, C.; Anxolabéhère-Mallart, E., *Inorg. Chem.* **2007,** *46*, 1951-1953.
39. Groni, S.; Dorlet, P.; Blain, G.; Bourcier, S.; Guillot, R.; Anxolabéhère-Mallart, E., *Inorg. Chem.* **2008,** *47*, 3166-3172.
40. Geiger, R. A. Spectroscopic and Computational Studies of the Physical Properties and Reactivities of Peroxomanganese(III) Complexes. University of Kansas, 2011.
41. So, H.; Park, Y. J.; Cho, K.-B.; Lee, Y.-M.; Seo, M. S.; Cho, J.; Sarangi, R.; Nam, W., *J. Am. Chem. Soc.* **2014,** *136*, 12229-12232.
42. Lubben, M.; Meetsma, A.; Wilkinson, E. C.; Feringa, B.; Que, L., *Angewandte Chemie International Edition in English* **1995,** *34*, 1512-1514.
43. He, Y.; Goldsmith, C. R., *Chem. Commun.* **2012,** *48*, 10532-10534.
44. Ho, R. Y. N.; Roelfes, G.; Feringa, B. L.; Que, L., *J. Am. Chem. Soc.* **1999,** *121*, 264-265.

45. Evans, D. F.; Jakubovic, D. A., *J. Chem. Soc., Dalton Trans.* **1988**, 2927-2933.
46. Data Collection: SMART Software in APEX2 v2010.3-0 Suite. Bruker-AXS, E. C. P., Madison, WI 53711-5373 USA.
47. Data Reduction: SAINT Software in APEX2 v2010.3-0 Suite. Bruker-AXS, E. C. P., Madison, WI 53711-5373 USA
48. International Tables for Crystallography, V. A., 4th ed., Kluwer: Boston (1996).
49. Refinement: SHELXTL v2010.3-0. Bruker-AXS, E. C. P., Madison, WI 53711-5373 USA.
50. Surry, D. S.; Buchwald, S. L., *Chem. Sci.* **2011,** *2*, 27-50.
51. Childers, W. E.; Havran, L. M.; Asselin, M.; Bicksler, J. J.; Chong, D. C.; Grosu, G. T.; Shen, Z.; Abou-Gharbia, M. A.; Bach, A. C.; Harrison, B. L.; Kagan, N.; Kleintop, T.; Magolda, R.; Marathias, V.; Robichaud, A. J.; Sabb, A. L.; Zhang, M.-Y.; Andree, T. H.; Aschmies, S. H.; Beyer, C.; Comery, T. A.; Day, M.; Grauer, S. M.; Hughes, Z. A.; Rosenzweig-Lipson, S.; Platt, B.; Pulicicchio, C.; Smith, D. E.; Sukoff-Rizzo, S. J.; Sullivan, K. M.; Adedoyin, A.; Huselton, C.; Hirst, W. D., *J. Med. Chem.* **2010,** *53*, 4066-4084.
52. Leto, D. F.; Ingram, R.; Day, V. W.; Jackson, T. A., *Chem. Commun.* **2013,** *49*, 5378-5380.
53. Bencini, A.; Gatteschi, D., Inorganic Electronic Structure and Spectroscopy. In *Inorganic Electronic Structure and Spectroscopy*, Solomon, E. I.; Lever, A. B. P., Eds. John Wiley & Sons, Inc.: 2006; Vol. Volume I: Methodology, pp 93-155.
54. Wu, X.; Seo, M. S.; Davis, K. M.; Lee, Y.-M.; Chen, J.; Cho, K.-B.; Pushkar, Y. N.; Nam, W., *J. Am. Chem. Soc.* **2011,** *133*, 20088-20091.
55. Chattopadhyay, S.; Geiger, R. A.; Yin, G.; Busch, D. H.; Jackson, T. A., *Inorg. Chem.* **2010,** *49*, 7530-7535.
56. Groves, J. T.; Watanabe, Y.; McMurry, T. J., *J. Am. Chem. Soc.* **1983,** *105*, 4489-4490.
57. Creager, S. E.; Murray, R. W., *Inorg. Chem.* **1987,** *26*, 2612-2618.
58. Creager, S. E.; Raybuck, S. A.; Murray, R. W., *J. Am. Chem. Soc.* **1986,** *108*, 4225-4227.
59. Goodson, P. A.; Glerup, J.; Hodgson, D. J.; Michelsen, K.; Weihe, H., *Inorg. Chem.* **1991,** *30*, 4909-4914.
60. Gamelin, D. R.; Kirk, M. L.; Stemmler, T. L.; Pal, S.; Armstrong, W. H.; Penner-Hahn, J. E.; Solomon, E. I., *J. Am. Chem. Soc.* **1994,** *116*, 2392-2399.
61. Brewer, K. J.; Calvin, M.; Lumpkin, R. S.; Otvos, J. W.; Spreer, L. O., *Inorg. Chem.* **1989,** *28*, 4446-4451.
62. Hureau, C.; Sabater, L.; Anxolabéhère-Mallart, E.; Nierlich, M.; Charlot, M.-F.; Gonnet, F.; Rivière, E.; Blondin, G., *Chem. Eur. J.* **2004,** *10*, 1998-2010.
63. Ray, K.; England, J.; Fiedler, A. T.; Martinho, M.; Münck, E.; Que, L., *Angewandte Chemie International Edition* **2008,** *47*, 8068-8071.
64. Babcock, G. T. In *The oxygen-evolving complex in photosystem II as a metallo-radical enzyme*, 1995; Kluwer: 1995; pp 209-215.
65. Coggins, M. K.; Sun, X.; Kwak, Y.; Solomon, E. I.; Rybak-Akimova, E.; Kovacs, J. A., *J. Am. Chem. Soc.* **2013,** *135*, 5631-5640.
66. Hureau, C.; Blondin, G.; Charlot, M.-F.; Philouze, C.; Nierlich, M.; Césario, M.; Anxolabéhère-Mallart, E., *Inorg. Chem.* **2005,** *44*, 3669-3683.

CHAPTER 4

Saturation Kinetics in Phenolic O–H Bond Oxidation by a Mononuclear Mn(III)–OH Complex Derived from Dioxygen

4.1. Introduction

Manganese-dependent enzymes play diverse biological roles, ranging from the generation of deoxynucleotides in pathogenic bacteria,[1] to the water splitting reaction of plants, algea, and cyanobacteria.[2] Hydroxo-manganese adducts have been proposed to play critical roles in the catalytic cycles of a small, yet diverse, set of these manganese-dependent enzymes.[2-6] For example, experimental[7] and computational[8,9] studies have provided strong support for a mononuclear hydroxomanganese(III), Mn^{III}-OH, adduct in the oxidized state of manganese-superoxide dismutase (MnSOD). This enzyme catalyzes the disproportionation of superoxide to dioxygen and hydrogen peroxide, thereby defending aerobic organisms from a reactive oxygen species.[3,4] The Mn^{III}-OH unit of oxidized MnSOD is involved in a hydrogen-bonding network with a nearby glutamine residue that plays a controlling role in the functionally important redox-tuning mechanism of the enzyme.[10-12]

There is also evidence for hydroxo-manganese species in the active sites of Mn-lipoxygenase[13] and the OEC.[14,15] These enzymes respectively catalyze the dioxygenation of polyunsaturated fatty acids[5,6] and water splitting.[2] For both Mn-lipoxygenase and the OEC, hydroxo-manganese species have been proposed to participate in proton-coupled electron-transfer (PCET) reactions.[16, 17] Support for a concerted proton-electron transfer (CPET) reaction in Mn-lipoxygenase comes from the fact that the conversion of α-linoleic acid to its hydroperoxy-derivative proceeds with a temperature-independent[18] kinetic isotope effect (KIE; k_H / k_D) of 20 - 24.[6] For the OEC, the proposition that a hydroxo-manganese species participates in catalytically relevant PCET is more tenuous, as there is substantial debate regarding the mechanistic details of this system.[2,19-23] Nonetheless, the abstraction of a hydrogen-atom from a hydroxo- or aqua-manganese moiety by a nearby tyrosyl radical, $Y_zO\cdot$, has been proposed as one

of several possible mechanisms for stepwise oxidation of the tetramanganese cluster during turnover.[24-26] Terminal water ligands and bridging hydroxide ligands in dimanganese(III,III), dimanganese(III,IV) and dimanganese(IV,IV) model complexes have O–H bond dissociation enthalpies (BDEs) of 77 - 92 kcal/mol,[27-29] a range which is thermodynamically compatible with the transfer of hydrogen atoms to $Y_zO\cdot$ (the O–H BDE of tyrosine is 86 kcal/mol).[30]

Although synthetic inorganic chemistry has provided numerous examples of multinuclear manganese complexes with bridging hydroxides,[27,29,31-38] mononuclear manganese complexes with terminal hydroxide ligands are comparatively less common. Indeed, to the best of our knowledge, crystal structures have been reported for only eight mononuclear Mn^{III}-OH complexes.[39-46] In these structures, the Mn–OH distances range from 1.81 to 1.86 Å, with the longer distances observed for complexes where the hydroxo ligand is involved in hydrogen-bonding.[40,41] In fact, inter- or intra-molecular hydrogen-bonding is observed in many of the solid-state structures.[39-41,46] In several structurally-characterized complexes, the hydroxo ligand is sterically shielded by the supporting ligand,[40,44,45] which presumably disfavors formation of hydroxo-bridged, multinuclear complexes. Notably, several mononuclear Mn^{III}-OH complexes were generated by treatment of the corresponding manganese(II) species with dioxygen.[44-47]

While the number of known synthetic Mn^{III}-OH complexes is small, the number of such species that participate in PCET reactions is even smaller. To the best of our knowledge, the only reported example of C–H bond oxidation by a synthetic Mn^{III}-OH adduct is found in the $[Mn^{III}(OH)(PY5)]^{2+}$ complex of Stack and co-workers (Figure 4.1, left; PY5 = 2,6-bis(bis(2-pyridyl)methoxymethane)pyridine).[39] This complex is capable of oxidizing hydrocarbon substrates with C–H BDEs ranging from approximately 75 - 88 kcal/mol by a CPET mechanism.

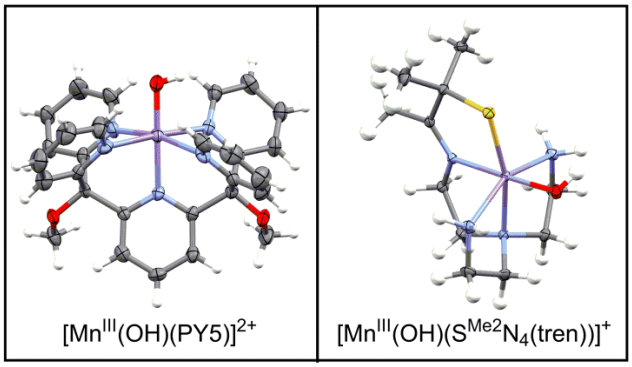

Figure 4.1. X-ray diffraction structures of the cationic fragments of $[Mn^{III}(OH)(PY5)](ClO_4)_2$[39] (left) and $[Mn^{III}(OH)(S^{Me2}N_4(tren))](PF_6)\cdot H_2O$[46] (right).

Kovacs and co-workers recently reported a Mn^{III}-OH adduct supported by the monoanionic N_4S ligand $S^{Me2}N_4(tren)$ (Figure 4.1, right), which is capable of O–H bond oxidation of TEMPOH (TEMPOH = 2,2'-6,6'-tetramethylpiperidine-1-ol)).[46] TEMPOH is an ideal substrate for investigating CPET reactivity because it has a relatively weak O–H bond (in MeCN, BDE = 70.6 kcal/mol; bond dissociation free energy, BDFE, = 66.5 kcal/mol), and, when occurring separately, both its deprotonation and one-electron oxidation are quite unfavorable thermodynamically (pK_a = 41 and E^o = 0.71 V vs. $FeCp_2^+/FeCp_2$ in MeCN).[48] Thus, TEMPOH oxidation proceeds by a CPET mechanism unless it is reacting with an exceptionally strong base or one-electron oxidant. The $[Mn^{III}(OH)(S^{Me2}N_4(tren))_2]^+$ complex quantitatively converted TEMPOH to TEMPO, with a second-order rate constant of 2.1×10^3 $M^{-1}s^{-1}$ at 25 ºC in MeCN.[46] A TEMPOH/TEMPOD KIE of 3.1 was observed, consistent with the expected CPET mechanism. Interestingly, the $[Mn^{III}(OH)(S^{Me2}N_4(tren))]^+$ complex was formed by hydrolysis of the oxo-bridged species $[Mn^{III}_2(\mu\text{-}O)(S^{Me2}N_4(tren))_2]^{2+}$, which itself was generated through O_2 oxidation of the $[Mn^{II}(S^{Me2}N_4(tren))]^+$ precursor complex.[46] Because the reaction of $[Mn^{III}(OH)(S^{Me2}N_4(tren))]^+$ with TEMPOH regenerates $[Mn^{II}(S^{Me2}N_4(tren))]^+$, this Mn system served as an aerobic oxidation catalyst for TEMPOH, with at least 10 turnovers.[46]

In this present work, we report a new Mn^{III}-OH complex, $[Mn^{III}(OH)(dpaq)]^+$, featuring the previously reported monoanionic N_5 ligand $dpaq^{49-51}$ (dpaq = 2-[bis(pyridin-2-ylmethyl)]amino-N-quinolin-8-yl-acetamidate). This complex is generated by treatment of the corresponding $[Mn^{II}(dpaq)](OTf)_2$ species with dioxygen in MeCN at room temperature and is remarkably stable, decaying by only 10% when stored in MeCN solution at 25 ºC for one week. $[Mn^{III}(OH)(dpaq)]^+$ is capable of oxidizing TEMPOH by a CPET mechanism. The oxidation of the hydrocarbon xanthene (BDFE = 73.3 kcal/mol in diemthysulfoxide) is also observed. In addition, this complex can oxidize phenolic substrates with BDFEs (in MeCN) up to 78.5 kcal/mol. Intriguingly, saturation behavior is observed in phenol oxidation by $[Mn^{III}(OH)(dpaq)]^+$ but not in TEMPOH oxidation. A plausible explanation for these unusual results and the relevance of this work within the broader context of transition-metal-mediated CPET reactions is discussed.

4.2. Materials and Methods

All procedures, including the generation of $[Mn^{II}(dpaq)](OTf)$ and organic substrates, as well as kinetic experiments, were carried out under an argon atmosphere, unless otherwise stated. Acetonitrile, methanol and ether were degassed and dried using a Pure Solv Micro (2010) solvent purification system. These solvents were degassed in air-tight solvent reservoirs (4 L), by bubbling Ar gas through the solvent for 20 min at room temperature. Acetonitrile and ether were dried using air-tight amlumina columns, and methanol was dried using a drierite column. Anhydrous dichloromethane was purchased from Acros Organics (99.9% purity), and was degassed by four freeze-pump-thaw cycles using Schlenk techniques. All solvents were taken into an argon filled glovebox immediately after dispensing from the solvent purification system

or following the freeze-pump-thaw cycles, and were stored in tightly-sealed Schlenk glassware. The purity of O_2 gas used was >99% and was further purified using by passage through a drierite and 5 Å molecular sieves prior to use. TEMPOH, TEMPOD and 2,4,6-tri-*t*-butylphenol-*d* ($^{4\text{-}t\text{-butyl}}$ArOD) were prepared according to literature procedures,[52,53] and >99% deuteration of TEMPOD and $^{4\text{-}t\text{-butyl}}$ArOD was confirmed by ^{1}H NMR experiments.

4.2.1. Preparation of [Mn^{II}(dpaq)](OTf). [Mn^{II}(dpaq)](OTf) was generated in high yield (>90%) by reacting the H-dpaq ligand with Mn^{II}(OTf)$_2$ in the presence of NaO^{t}Bu in MeOH under an inert atmosphere. The Mn^{II}(OTf)$_2$ salt was generated using a previously reported method.[54] The detailed metallation procedure is as follows. To a stirred solution of 100 mg (0.26 mmol) of H-dpaq in 2 ml of MeOH was added 92 mg (0.26 mmol) of Mn^{II}(OTf)$_2$ in 2 ml of MeOH, followed by 25 mg (0.26 mmol) of NaO^{t}Bu in 2 ml of MeOH under an inert atmosphere. The orange colored resultant solution was stirred overnight and then the solvent was evaporated to dryness under vacuum. The solid product was recrystallized using MeOH/ Et_2O to yield orange colored crystals of [Mn^{II}(dpaq)](OTf). Crystals for X-ray diffraction analysis were obtained by subsequent recrystallization of the final solid product in the MeOH/ Et_2O solvent system. [Mn^{II}(dpaq)](OTf) was further characterized by ESI-MS and effective magnetic moment analysis by the ^{1}H NMR method of Evans[55] in CD_3CN at 298 K. ESI-MS (Figure A3.1): {[Mn^{II}(dpaq)]$^+$} *m/z* = 437.0994 (calc. 437.1048). The effective magnetic moment (μ_{eff}) was found to be 6.3 (Diam. Corr. = 1.0) μ_B, which compares well with the expected value (μ_{eff} = 5.9 μ_B) for mononuclear high-spin Mn^{II} centers. Elemental analysis [Mn^{II}(dpaq)](OTf): $C_{24}H_{20}F_3MnN_5O_4S$ calc. (%): C 49.15, H 3.44, N 11.94; found (%): C 48.96, H 3.51, N 11.79.

4.2.2. X-ray diffraction data collection and analysis for [Mn^{II}(dpaq)](OTf). All X-ray diffraction experiments were performed on a Bruker Proteum Single Crystal Diffraction System

equipped with Helios multilayer optics, an APEX II CCD detector, and a Bruker MicroSTAR microfocus rotating anode x-ray source operating at 45 kV and 60 mA. The Bruker software package SHELXTL was used to solve the structures using "direct methods" techniques. All stages of weighted full-matrix least-squares refinement were conducted using F_o^2 data with the SHELXTL Version 2010.3-0 software package.[56]

Yellow single crystals of the triflate salt for the cationic polymer, $[Mn(C_{23}H_{19}N_5O)^+]_n$ are, at 100(2) K, monoclinic, space group Cc - C_s^4 (No. 9)[57] with a = 28.6094(9) Å, b = 9.2197(3) Å, c = 28.5260(9) Å, β = 100.550(1)°, V = 7397.1(4) $Å^3$ and Z = 4 ($[Mn(C_{23}H_{19}N_5O)]_3[CF_3SO_3]_3$) formula units {$d_{calcd}$ = 1.577 g/cm^3; μ_a(CuKα) = 5.729 mm^{-1}}. A full set of unique diffracted intensities [5241 frames with counting times of 2 to 4 seconds and an ω- or ϕ-scan width of 0.50°] was measured[58] for a single-domain specimen using monochromated CuKα radiation (λ = 1.54178 Å). Lattice constants were determined with the Bruker SAINT software package using peak centers for 9466 reflections. A total of 30828 integrated reflection intensities having 2θ(CuKα) < 139.58° were produced using the Bruker program SAINT;[59] 9683 of these were unique and gave R_{int} = 0.037. The data were corrected empirically for variable absorption effects using equivalent reflections; the relative transmission factors ranged from 0.836 to 1.000.

The final structural model incorporated anisotropic thermal parameters for all nonhydrogen atoms and isotropic thermal parameters for all hydrogen atoms. Hydrogen atoms were included in the structural model at idealized positions (sp^2- or sp^3-hybridized geometry and C–H bond lengths of 0.95 – 0.99 Å) with isotropic thermal parameters fixed at values 1.20 times the equivalent isotropic thermal parameter of the carbon atom to which they are covalently bonded.

A total of 1028 parameters were refined using 2 restraints, 9683 data and weights of w = 1/ [$\sigma^2(F^2)$ + (0.0563 P)^2 + (12.3197 P)], where P = [F_O^2 + 2F_C^2] / 3. Final agreement factors at convergence for $[Mn(C_{23}H_{19}N_5O)^+]_n$ are: R_1(unweighted, based on F) = 0.037 for 9583 independent absorption-corrected "observed" reflections having 2θ(CuKα) < 139.58° and I > 2σ(I); R_1(unweighted, based on F) = 0.037 and wR_2(weighted, based on F^2) = 0.096 for all 9683 independent absorption-corrected reflections having 2θ(CuKα) < 139.58°. The largest shift/s.u. was 0.001 in the final refinement cycle. The final difference map had maxima and minima of 1.30 and -0.52 $e^-/Å^3$, respectively.

4.2.3. Preparation of [Mn^{III}(OH)(dpaq)](OTf). [Mn^{III}(OH)(dpaq)](OTf) was formed by reacting a 2.5 mM [Mn^{II}(dpaq)](OTf) solution in MeCN with excess O_2 gas at room temperature. The formation of [Mn^{III}(OH)(dpaq)](OTf) was monitored by electronic absorption spectroscopy, as the Mn^{III} complex has characteristic features at 550 and 780 nm. A representative formation reaction is as follows. A 2.5 mM [Mn^{II}(dpaq)](OTf) solution (2.9 mg in 2ml of MeCN) was prepared under an inert atmosphere and transferred to a gas-tight cuvette sealed with a pierceable septum. An excess of O_2 gas was then delivered to the solution by means of a syringe, and the formation of [Mn^{III}(OH)(dpaq)](OTf) was monitored by electronic absorption spectroscopy. The formation was complete in ~40 min and the resulting dark gold solution was evaporated to dryness under reduced pressure. The solid residue was then recrystallized using MeCN/ Et_2O. (3.1 mg/ 98% yield). Synthesis of [Mn^{III}(OH)(dpaq)](OTf) on a larger scale was undertaken to obtain suitable material for X-ray crystallographic and kinetic experiments. In this procedure, O_2 gas was passed through an acetonitrile solution (20 mg in 5 ml) of [Mn^{II}(dpaq)](OTf), and the completion of the formation of [Mn^{III}(OH)(dpaq)](OTf) was confirmed by ESI-MS and electronic absorption spectroscopy. The resulting solution was evaporated to dryness under

reduced pressure, and the solid residue was recrystallized using MeCN/ Et_2O. Dark gold $[Mn^{III}(OH)(dpaq)](OTf)$ crystals of X-ray crystallographic quality were obtained by repetitive recrystallization, and were further characterized by ESI-MS and effective magnetic moment (μ_{eff}) analysis by the ^1H NMR method of Evans in CD_3CN at 298 K. ESI-MS (Figure A3.1): $\{[Mn^{III}(OH)(dpaq)]^+\}$ *m/z* = 454.1056 (calc. 454.1076). μ_{eff} found was 4.9 μ_B (at 298 K for 5 mM solution in CD_3CN; Diam. Corr. = 0.4) which compares well with the calculated value of 4.9 μ_B for a monomeric high-spin d^4 system. This value is also in close comparison with previously reported solution magnetic susceptibility values for mononuclear hydroxomanganese(III) complexes (μ_{eff} = 4.7 μ_B for $[Mn^{III}(OH)(PY5)]^+$ and μ_{eff} = 4.9 μ_B for $[Mn^{III}(OH)(S^{Me2}N_4(tren))_2]^+$).[39,46] Cyclic voltammetric studies of $[Mn^{III}(OH)(dpaq)](OTf)$ were conducted under an argon atmosphere in acetonitrile (12.89 mg in 10 ml) at 298 K. A 0.1 M acetonitrile solution of $Bu_4N(PF_6)$ was used as the supporting electrolyte, and a glassy carbon working electrode, a platinum auxiliary electrode, and a AgCl/Ag reference electrode were used. Elemental analysis $[Mn^{III}(OH)(dpaq)](OTf)$: $C_{24}H_{21}F_3MnN_5O_5S$ calc. (%): C 47.77, H 3.51, N 11.61; found (%): C 47.26, H 3.65, N 11.62.

4.2.4. X-ray diffraction data collection and analysis for $[Mn^{III}(OH)(dpaq)](OTf)$. Dark gold single crystals of the CH_3CN solvated salt, $[Mn(OH)(C_{23}H_{20}N_5O)][CF_3SO_3]$, are, at 100(2) K, monoclinic, space group $P2_1/n$ (an alternate setting of $P2_1/c$ - C_{2h}^5 (No. 14))[57] with a = 9.2406(3) Å, b = 24.7263(8) Å, c = 12.2658(4) Å, β = 97.257(1)°, V = 2780.1(2) $Å^3$ and Z = 4 formula units {d_{calcd} = 1.540 g/cm^3; $\mu_a(CuK\alpha)$ = 5.176 mm^{-1}}. A full set of unique diffracted intensities [5226 frames with counting times of 1 to 3 seconds and an ω- or ϕ-scan width of 0.50°] was measured[58] for a single-domain specimen using monochromated CuKα radiation (λ = 1.54178 Å). Lattice constants were determined with the Bruker SAINT software package using

peak centers for 9628 reflections. A total of 25663 integrated reflection intensities having $2\theta(CuK\alpha) < 139.63°$ were produced using the Bruker program SAINT;[59] 5017 of these were unique and gave $R_{int} = 0.039$. The data were corrected empirically for variable absorption effects using equivalent reflections; the relative transmission factors ranged from 0.689 to 1.000.

The triflate anion is 85/15 disordered between two closely spaced sites in the asymmetric unit. This disorder produces a slightly elongated anisotropic thermal ellipsoid for oxygen O(11) in the major-occupancy triflate anion. The bond lengths and angles for the minor-occupancy (15%) triflate were restrained to have values similar to those of the major-occupancy anion. The final structural model incorporated anisotropic thermal parameters for all nonhydrogen atoms of the metal cation, major-occupancy triflate anion and the CH_3CN solvent molecule. The nonhydrogen atoms for the minor-occupancy triflate anion were incorporated with isotropic thermal parameters. The hydrogen atoms were located from a difference Fourier and included in the structural model as individual isotropic atoms. The positional and thermal parameters for hydrogen atoms and the minor-occupancy triflate were allowed to vary in least-squares refinement cycles.

A total of 509 parameters were refined using 19 restraints, 5017 data and weights of $w = 1/ [\sigma^2(F^2) + (0.0291 P)^2 + (2.4398 P)]$, where $P = [F_o^2 + 2F_c^2] / 3$. Final agreement factors at convergence are: R_1(unweighted, based on F) = 0.031 for 4941 independent absorption-corrected "observed" reflections having $2\theta(CuK\alpha) < 139.63°$ and $I > 2\sigma(I)$; R_1(unweighted, based on F) = 0.031 and wR_2(weighted, based on F^2) = 0.079 for all 5017 independent absorption-corrected reflections having $2\theta(CuK\alpha) < 139.63°$. The largest shift/s.u. was 0.001 in the final refinement cycle. The final difference map had maxima and minima of 0.49 and -0.58 $e^-/Å^3$, respectively.

4.2.5. Kinetic studies of [Mn^{III}(OH)(dpaq)](OTf) with substituted phenols. For each kinetic experiment, a 1.25 mM $[Mn^{III}(OH)(dpaq)]^+$ (1.6 mg, $2.5x10^{-3}$ mmol) solution was prepared in acetonitrile (2 ml) within an argon-filled glovebox, transferred to a gas-tight cuvette sealed with a pierceable septum. A solution of the phenolic substrate was prepared in dichloromethane (300 μL) and sealed in a 4 mL glass vial with a pierceable septum. Then, the cuvette containing the $[Mn^{III}(OH)(dpaq)]^+$ solution was inserted into a temperature-controlled cryostat (Unisoku), held at 50 °C, coupled to an Agilent 8453 UV/Visible spectrophotometer. Upon achieving thermal equilibrium (10 min), data collection was started, and 100 μL of the substrate solution was injected into the cuvette using a gas-tight syringe. Data collection times ranged from 3000 to 6000 s. An aliquot of the final reaction mixture was analyzed by perpendicular-mode X-band electron paramagnetic resonance (EPR) spectroscopy at 5 K and revealed signals consistent with $[Mn^{II}(dpaq)]^+$ and a phenoxyl radical (Figure A3.2). The rates of the reactions were calculated by applying initial rate approximation (initial 20% of the disappearance of $[Mn^{III}(OH)(dpaq)]^+$ was monitored at 800 nm) in order to prevent any interference by side reactions at longer time scales. These initial rates (in absorbance units / time) were converted into s^{-1} units by using the absorption coefficient (ε_{800} = 130 M^{-1} cm^{-1}) and initial concentration (1.25 mM) of $[Mn^{III}(OH)(dpaq)]^+$. For reactions involving the 2,4,6-tri-*tert*-butylphenol, the kinetic data were collected to five half-lives and fit directly to obtain a pseudo-first-order rate constant. In these cases, the directly obtained pseudo-first-order rate constants were identical, within error, to those obtained using the initial rate method.

4.2.6. Kinetic studies of [Mn^{III}(OH)(dpaq)](OTf) with TEMPOH. Similar to the kinetic experiments with phenols, a 1.25 mM $[Mn^{III}(OH)(dpaq)]^+$ (1.6 mg, $2.5x10^{-3}$ mmol) solution was prepared in acetonitrile (2 ml) within an argon-filled glovebox, and was sealed in a

gas-tight cuvette with a pierceable septum. The TEMPOH solution was prepared in acetonitrile (100 μL) and sealed in a 300 μL glass vial with a pierceable septum. Data collection was started, and the TEMPOH solution was added into the $[Mn^{III}(OH)(dpaq)]^{+}$ solution using a gas-tight syringe. Data collection times ranged from 200 to 4000 s. A final reaction mixture analyzed by perpendicular-mode X-band EPR spectroscopy at 5 K revealed characteristic features consistent with the presence of the TEMPO radical (Figure A3.2). Kinetic experiments at variable temperatures (-15 to 45 ºC) were performed following the same procedure as described, allowing the cuvette to achieve thermal equilibrium (10 min) in the cryostat, prior to the addition of the substrate.

4.2.7. Kinetic studies of $[Mn^{III}(OH)(dpaq)](OTf)$ with xanthene. For each experiment, a 1.25 mM $[Mn^{III}(OH)(dpaq)]^{+}$ (1.6 mg, $2.5x10^{-3}$ mmol) solution was prepared in acetonitrile (2 ml) within an argon-filled glovebox. This solution was transferred to a gas-tight cuvette and sealed with a pierceable septum. The xanthene solution was prepared in dichloromethane (200 μL) and sealed in a 4 ml glass vial with a pierceable septum. Then, the cuvette containing the $[Mn^{III}(OH)(dpaq)]^{+}$ solution was inserted into a temperature-controlled cryostat held at 50 °C. Upon achieving thermal equilibrium, data collection was started, and 100 μL of the xanthene solution was injected into the cuvette using a gas-tight syringe. Data collection was carried out up to ~900 min. The rates of the reactions were calculated by applying initial rate approximation in order to exclude any interference by secondary reactions.

4.2.8. Catalytic oxidation of TEMPOH with $[Mn^{III}(OH)(dpaq)](OTf)$. For each experiment, $[Mn^{II}(dpaq)]^{+}$ (initial concentration = 0.031 mM) and TEMPOH (initial concentration = 125 mM) were measured into a 20 ml glass vial within an argon-filled glovebox and dissolved in acetonitrile (2 ml). This solution was sealed in a gas-tight cuvette with a

pierceable septum, and the electronic absorption spectrum was collected under ambient conditions. Then, an excess of dry dioxygen gas was bubbled through the solution, while electronic absorption spectra were collected every ~15 min. The solvent level of the reaction mixture was closely monitored confirming a negligible solvent evaporation during oxygenation.

4.3. Results and Analysis

4.3.1. Structural properties of [Mn^{II}(dpaq)](OTf). The X-ray diffraction structure of [Mn^{II}(dpaq)](OTf) shows three [Mn^{II}(dpaq)](OTf) molecules in the smallest asymmetric unit. Although these three molecules do show slight differences in bond lengths and angles, each consists of a Mn^{II} center in a highly distorted octahedral geometry (Figure 4.2), with two pyridine ligands (N4, N5), the quinoline ligand (N1) and the tertiary amine (N3) in the equatorial plane, and the amide nitrogen (N2) occupying an axial position. The other axial site is occupied by the amide oxygen atom (O1) of a second [Mn^{II}(dpaq)](OTf) molecule, forming an overall polymeric structure. Table 4.1 summarizes the structural properties for one of the $[Mn^{II}(dpaq)]^{+}$ cations in the asymmetric unit (cation B); corresponding metric parameters for the other cations can be found in Table A3.3. For the three cations, the angle between the axial ligands (O1–Mn–N2) is ~165 - 170° and the angles between the equatorial ligands vary from ~75° to ~105°, indicating large deviations from idealized octahedral geometry. Three triflate ions are also present in the crystal structure but do not interact with the Mn^{II} centers (Mn–O distances of ~6.4 Å). All Mn^{II}–ligand distances are in the range of 2.1 to 2.3 Å, which is typical for a high-spin Mn^{II} center. Notably, the C10–O1 distance of the amide ranges from 1.265(4) to 1.271(4) Å, which is typical of a C=O double bond. Thus, the Mn–O1 interaction is likely weak, and presumably the polymeric structure observed in the crystal structure reverts to separate

monomeric entities in solution. Overall, the structure of [Mn^{II}(dpaq)](OTf) compares well with that of a recently reported [Mn(dpaq)(NO)](ClO_4) complex, although the latter species showed shorter manganese-ligand bond lengths.[49] The shorter bond lengths in [Mn(dpaq)(NO)](ClO_4) are expected given the formulation of that complex as a low-spin Mn^{II} center antiferromagnetically coupled to an NO radical.

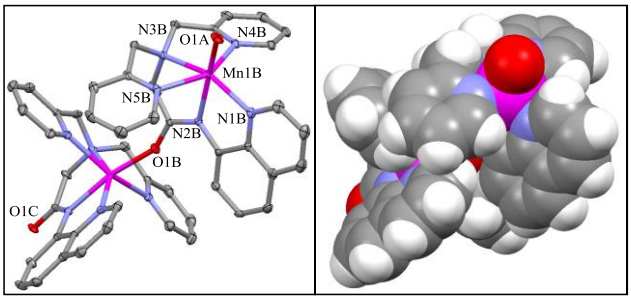

Figure 4.2. ORTEP (left) and space filling (right) diagrams showing two cations (B and C) in the asymmetric unit of the X-ray structure of [Mn^{II}(dpaq)](OTf). ORTEP diagram shows 50% probability thermal ellipsoids. Hydrogen atoms and noncoordinating triflate counteranions have been removed for clarity. Significant interatomic distances and angles are listed in Tables 4.1 and 3.S3.

Table 4.1. Selected Bond Lengths (Å) and Angles (deg) for [Mn^{II}(dpaq)](OTf) and [Mn^{III}(OH)(dpaq)](OTf).

[Mn^{II}(dpaq)]$^+$ (B) [a]			
Mn–O1A	2.079(2)	O1A–Mn–N2B	164.88(10)
Mn–N2B	2.191(3)	N4B–Mn–N5B	147.89(11)
Mn–N1B	2.214(3)	N1B–Mn–N3B	151.40(10)
Mn–N3B	2.314(3)	N4B–Mn–N2B	94.97(10)
Mn–N4B	2.244(3)	N1B–Mn–N2B	74.46(10)
Mn–N5B	2.286(3)	N3B–Mn–N2B	77.52(10)
[Mn^{III}(OH)(dpaq)](OTf)			
Mn–O2	1.806(13)	O2–Mn–N2	177.94(6)
Mn–N2	1.975(14)	N4–Mn–N5	152.53(5)
Mn–N1	2.072(14)	N1–Mn–N3	161.83(6)
Mn–N3	2.173(14)	N4–Mn–N2	85.22(5)
Mn–N4	2.260(14)	N1–Mn–N2	79.77(6)
Mn–N5	2.216(15)	N3–Mn–N2	82.51(6)

[a] Bond lengths and angles for one of the three [Mn^{II}(dpaq)]$^+$ cations in the asymmetric unit. Corresponding metric parameters for the other two cations are in Table A3.3.

4.3.2. Formation of [Mn^{III}(OH)(dpaq)](OTf). The absorption spectrum of [Mn^{II}(dpaq)](OTf) in acetonitrile shows a very weak band at 510 nm (ε = 24 M^{-1} cm^{-1}). When treated with excess O_2 gas at 25 ºC, the light orange colored [Mn^{II}(dpaq)](OTf) solution rapidly changed its color to dark gold, as new absorption features grew in at 550 (ε = 320 M^{-1} cm^{-1}) and 780 nm (ε = 130 M^{-1} cm^{-1}) (Figure 4.3; the extinction coefficients were obtained using recrystallized [Mn^{III}(OH)(dpaq)](OTf)). Formation of these new electronic absorption features is consistent with the oxidation of Mn^{II} upon reacting with O_2. Electronic absorption spectral signatures for other hydroxomanganese(III) species vary in terms of their energies,[43,45,46] although the closely related [Mn^{III}(OH)($PaPy_2Q$)]ClO_4 complex (where $PaPy_2Q$ is the amide-containing N_5 ligand N,N-bis(2-pyridylmethyl)-amine-N-ethyl-2-quinoline-2-carboxamide) has spectral features with striking similarities to those of [Mn^{III}(OH)(dpaq)](OTf).[42] The prominent absorption signatures for [Mn^{III}(OH)($PaPy_2Q$)]ClO_4 in acetonitrile are centered at 485 (ε = 280 M^{-1} cm^{-1}) and 740 (ε = 120 M^{-1} cm^{-1}) nm. These similarities between the electronic absorption features are anticipated given the closely related primary coordination spheres of [Mn^{III}(OH)($PaPy_2Q$)]ClO_4 and [Mn^{III}(OH)(dpaq)](OTf) (*vide infra*). The final product [Mn^{III}(OH)(dpaq)](OTf) was isolated in an essentially quantitative yield of greater than 98%. The half-life ($t_{1/2}$) of [Mn^{III}(OH)(dpaq)](OTf) was estimated by monitoring the electronic absorption spectrum of a 1.25 mM acetonitrile solution at 25 ºC. The concentration of [Mn^{III}(OH)(dpaq)]$^+$ decreased by ~10% after 6 days. Assuming a constant decay rate, the half-life of [Mn^{III}(OH)(dpaq)](OTf) under these conditions is estimated to be 26 days.

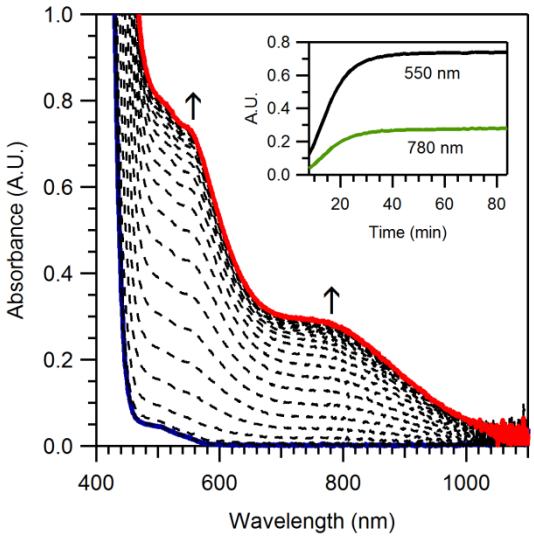

Figure 4.3. Electronic absorption spectra of 2.5 mM $[Mn^{II}(dpaq)]^{+}$ (solid blue trace) upon the addition of excess O_2 at 25 ºC in MeCN under argon. Inset: Time evolution of absorption signals at 550 and 780 nm.

4.3.3. Properties of $[Mn^{III}(OH)(dpaq)](OTf)$. The X-ray structure of $[Mn^{III}(OH)(dpaq)](OTf)$ contains a six-coordinate Mn^{III} center with a distorted octahedral geometry (Figure 4.4). Coordination of the dpaq ligand is the same as in $[Mn^{II}(dpaq)](OTf)$, with the exception that all Mn–N bonds, other than Mn–N4, are shorter in $[Mn^{III}(OH)(dpaq)](OTf)$ by 0.062 to 0.202 Å (Table 4.1). The hydroxide group in $[Mn^{III}(OH)(dpaq)](OTf)$ is trans to the amide nitrogen, with a Mn–O2 distance of 1.806(13) Å. Inspection of the extended structure of $[Mn^{III}(OH)(dpaq)]^{+}$ reveals that the hydrogen atom of the hydroxo ligand is involved in a hydrogen-bonding interaction with the amide oxygen of an adjacent $[Mn^{III}(OH)(dpaq)]^{+}$ molecule (O•••O and H•••O separations of 2.7308(18) and 1.95(3) Å, respectively). A free triflate ion and an acetonitrile molecule are observed within the asymmetric unit, but these are not associated with the metal center (Mn–O and Mn–N distances of ~6.2 and ~4.8 Å for triflate oxygen and acetonitrile nitrogen, respectively).

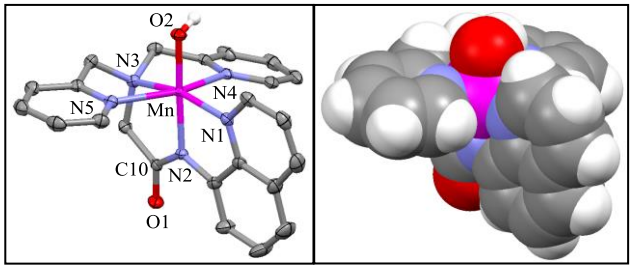

Figure 4.4. ORTEP (left) and space filling (right) diagrams of $[Mn^{III}(OH)(dpaq)](OTf)$. ORTEP diagram shows 50% probability thermal ellipsoids. Hydrogen atoms and noncoordinating triflate counteranion have been removed for clarity. Significant interatomic distances and angles are listed in Table 4.1.

There have been several X-ray structures of mononuclear Mn^{III}-OH complexes, and these have revealed Mn–O(H) distances within the range of 1.81 Å – 1.86 Å.[39-46] The longest distance of 1.86 Å is unusual, and represents hydrogen-bonding interactions with an ordered cluster of water molecules in the solid-state.[41] The $[Mn^{III}(OH)(dpaq)]^+$ complex has a Mn–O(H) distance of 1.806(13) Å, which is at the lower end of the range of previously reported distances for this class of compounds. The O2–Mn–N2 axis, which includes the hydroxide oxygen and amide nitrogen ligands, represents the compressed pseudo-Jahn-Teller axis. The observation of an intermolecular hydrogen-bond involving the hydroxo ligand in $[Mn^{III}(OH)(dpaq)]^+$ is not unusual. Four of the eight known X-ray structures of Mn^{III}-OH adducts show second-sphere hydrogen-bonding interactions in the solid-state structures.[39-41,46]

Cyclic voltammetric analysis of $[Mn^{III}(OH)(dpaq)](OTf)$ in acetonitrile revealed a partially reversible wave with an $E_{1/2}$ of -0.60 V vs Fc^+/Fc at a scan rate of 100 mV s^{-1} (ΔE_p = 120 mV; Figure A3.3), which we attribute to the Mn^{II}/Mn^{III} couple. This potential value is comparable to that reported for the reduction of $[Mn^{III}(OH)(S^{Me2}N_4(tren))_2]^+$ ($E_{p,c}$ = -0.6 V vs Fc^+/Fc in MeCN).[46] Previous studies have also described Mn^{II}/Mn^{III} reduction potentials for several other hydroxomanganese(III) complexes. Stack and coworkers reported that

$[Mn^{III}(OH)(PY5)]^{2+}$ (Figure 4.1, left) exhibited a quasi-reversible reduction wave at $E_{1/2}$ = +0.17 V vs Fc^{+}/Fc (reported as +0.81 V vs SHE; ΔE_p = 150 mV), which was attributed to the Mn^{II}/Mn^{III} couple.[39] The higher reduction potential for this dicationic complex compared to that of $[Mn^{III}(OH)(dpaq)]^{+}$ is anticipated given the difference in overall charge of the two complexes. Furthermore, a monoanionic hydroxomanganese(III) species supported by a trianionic ligand has a Mn^{II}/Mn^{III} couple at -1.51 V vs Fc^{+}/Fc (ΔE_p = 380 mV).[60] An outlier from this trend is $[Mn^{III}(OH)(OAc)(Me_2EBC)]^{+}$ (Me_2EBC = 4,11-dimethyl-1,4,8,11-tetraazabicyclo[6.6.2]hexadecane), for which $E_{1/2}$ = -1.33 V vs Fc^{+}/Fc (reported as -0.689 V vs SHE; ΔE_p = 132 mV). This deviation is presumably due to the preferential stabilization of Mn^{III} within the cavity of the macrocyclic supporting ligand.[45]

4.3.4. Reactivity of $[Mn^{III}(OH)(dpaq)]^{+}$ with TEMPOH. The isolation of $[Mn^{III}(OH)(dpaq)]^{+}$ allowed us to investigate the ability of this species to effect PCET reactions. Treatment of $[Mn^{III}(OH)(dpaq)]^{+}$ with 100 equiv. TEMPOH under an argon atmosphere in MeCN at 25 ºC lead to the rapid disappearance of the electronic absorption bands of $[Mn^{III}(OH)(dpaq)]^{+}$ (Figure 4.5). The final electronic absorption spectrum appears essentially identical to that of $[Mn^{II}(dpaq)]^{+}$ in MeCN, showing a very weak band at 510 nm. Using the intensity of this band, and the extinction coefficient for $[Mn^{II}(dpaq)]^{+}$ (*vide supra*), the Mn^{II} complex forms in 99% yield. The perpendicular-mode X-band EPR spectrum of the final reaction mixture at 5 K shows characteristic EPR features of the TEMPO radical centered at g = 2.04 (Figure A3.2A).[61] Together these data demonstrate that TEMPOH reacts with $[Mn^{III}(OH)(dpaq)]^{+}$ to generate TEMPO and $[Mn^{II}(OH_2)(dpaq)]$ quantitatively; *i.e.*, the PCET reaction goes to completion under these conditions.

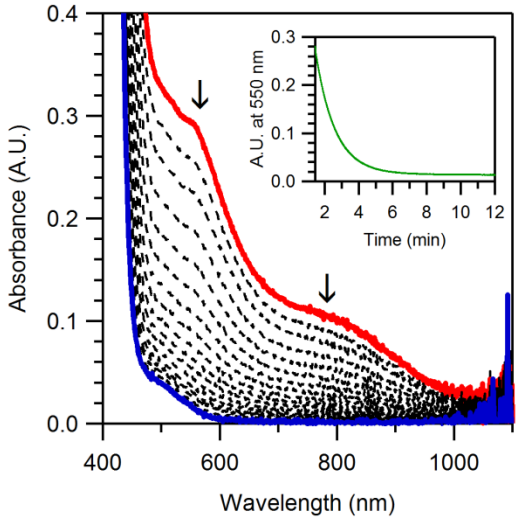

Figure 4.5. Electronic absorption spectra of 1.25 mM $[Mn^{III}(OH)(dpaq)]^+$ upon the addition of 100 equiv. TEMPOH at 25 ºC in MeCN under argon. Inset: Decay of the 550 nm absorption signal.

Kinetic parameters associated with this process were determined through a series of reactions between $[Mn^{III}(OH)(dpaq)]^+$ and 10 to 250 equiv. TEMPOH (pseudo-first-order conditions). In all cases, the decay of $[Mn^{III}(OH)(dpaq)]^+$ followed pseudo-first-order behavior to at least 5 half-lives (Figure 4.5, inset). The pseudo-first-order rate constants increase linearly as a function of TEMPOH concentration (Figure 4.6), giving a second-order rate constant of $1.3(1) \times 10^{-1}$ $M^{-1}s^{-1}$ at 25 ºC. Using deuterated TEMPOD, a kinetic isotope effect (KIE) of 1.8 was observed (Figure 4.6). The KIE value, although small, suggests that cleavage of the TEMPO–H/D bond occurs in the rate-determining step. Similar KIE values of less than 2.0 have been observed for O–H bond oxidation by other transition metal species in cases where rate-determining O–H/D bond cleavage has been proposed.[62] Given the exceptionally high pK_a of TEMPOH in MeCN (41),[48] the KIE is supportive of the expected CPET mechanism for this reaction. Moreover, the relatively low reduction potential of $[Mn^{III}(OH)(dpaq)]^+$ rules out a rapid electron transfer process. An Eyring analysis of the reaction of $[Mn^{III}(OH)(dpaq)]^+$ with

TEMPOH from -15 to 45 ºC (258 to 318 K), afforded activation parameters $\Delta H^{\neq}$ and $\Delta S^{\neq}$ of 9.9(9) kcal/mol and -35(3) cal/mol K, respectively (Figure 4.7). Thus, at 25 ºC, the entropic contribution to the free energy of activation ($T\Delta S^{\neq}$ = -10 kcal/mol) is equal to the enthalpic contribution.

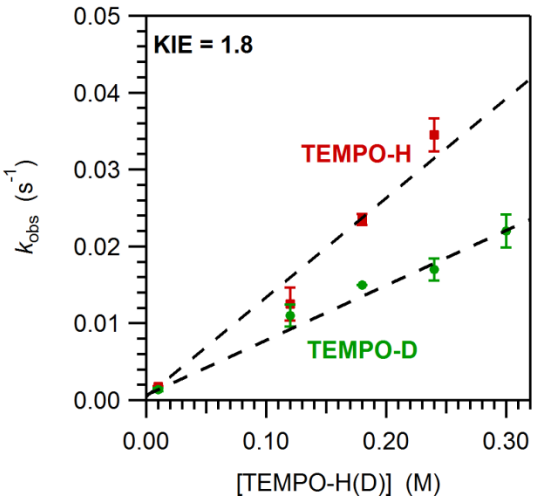

Figure 4.6. Pseudo-first order rate constants, k_{obs} (s^{-1}) versus TEMPOH and TEMPOD concentration for a 1.25 mM solution of $[Mn^{III}(OH)(dpaq)]^{+}$. The second-order rate constant, k_2 ($M^{-1}s^{-1}$), was calculated from the linear correlation of the observed rate constant and substrate concentration.

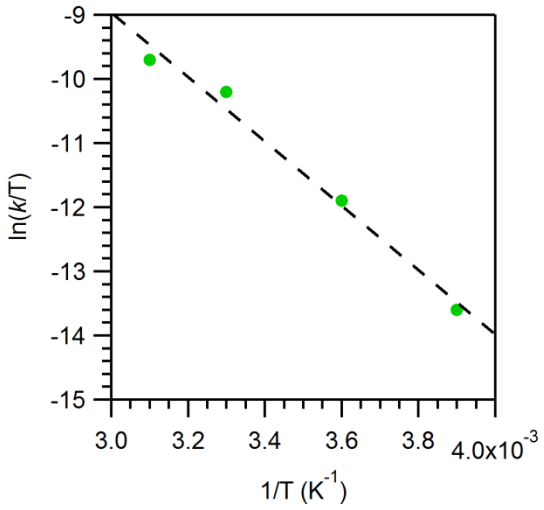

Figure 4.7. Eyring plot showing ln(k/T) versus 1/T (K^{-1}) for the reaction of 1.25 mM $[Mn^{III}(OH)(dpaq)]^{+}$ with TEMPOH from -15 to 45 ºC (258 to 318 K).

4.3.5. Reactivity of $[Mn^{III}(OH)(dpaq)]^+$ with xanthene. The addition of 250 equiv. of xanthene to a 1.25 mM solution of $[Mn^{III}(OH)(dpaq)]^+$ at 50 ºC led to the slow decay of the electronic absorption signals of the Mn^{III}-OH complex (Figure A3.4). Over the course of 15 hours after the addition of xanthene, 50% of $[Mn^{III}(OH)(dpaq)]^+$ was observed to disappear. Importantly, $[Mn^{III}(OH)(dpaq)]^+$ itself shows essentially no self-decay in the absence of xanthene in this time period. A pseudo-first order rate of 8×10^{-4} s^{-1} was determined for the reaction of $[Mn^{III}(OH)(dpaq)]^+$ with xanthene using the method of initial rates.

4.3.6. Reactivity of $[Mn^{III}(OH)(dpaq)]^+$ with phenols. $[Mn^{III}(OH)(dpaq)]^+$ also reacted with 2,4,6-tri-*t*-butylphenol ($^{4\text{-}t\text{-butyl}}$ArOH), which has an O–H bond nearly 11 kcal/mol stronger than that of TEMPOH (BDFE in MeCN of 77.1 and 66.5 kcal/mol, respectively). Monitoring the reaction of $[Mn^{III}(OH)(dpaq)]^+$ with $^{4\text{-}t\text{-butyl}}$ArOH by electronic absorption spectroscopy showed that the decay of the $[Mn^{III}(OH)(dpaq)]^+$ complex is concomitant with the formation of the corresponding phenoxyl radical, $^{4\text{-}t\text{-butyl}}$ArO· ($\lambda_{max}$ = 628 nm; ε = 400(10) M^{-1} cm^{-1} in MeCN at 25ºC; see Figure 4.8).[63] The phenoxyl radical was formed in 80% yield, relative to the initial $[Mn^{III}(OH)(dpaq)]^+$ concentration. A comparison of perpendicular-mode X-band EPR spectra of $[Mn^{II}(dpaq)]^+$, $[Mn^{III}(OH)(dpaq)]^+$, and the final products of $^{4\text{-}t\text{-butyl}}$ArOH oxidation provides evidence for the formation of $[Mn^{II}(dpaq)]^+$ and the phenoxyl radical following the phenol oxidation reaction (Figure A3.2B). The 80% yield of the phenoxyl radical was observed regardless of the initial $[Mn^{III}(OH)(dpaq)]^+$: $^{4\text{-}t\text{-butyl}}$ArOH ratio (Table A3.4). It is possible that the 80% yield is observed because the radical participates in side reactions that prevent its full accumulation. However, the clean isosbestic behavior observed in the reaction of $[Mn^{III}(OH)(dpaq)]^+$ with $^{4\text{-}t\text{-butyl}}$ArOH (Figure 4.8) is difficult to reconcile with the disappearance of 20% of the radical product during the timecourse of this reaction. The substoichiometric

formation of phenoxyl radical was also noted in the reaction of $[Mn^{III}(OH)(PY5)]^{+}$ (Figure 4.1, left) with $^{4\text{-}t\text{-butyl}}$ArOH.[39] For that system, the phenoxyl radical was formed after most of the Mn^{III}-OH complex was consumed, indicating a reaction between the metal complex and the phenoxyl radical. In this present work, the rate of formation of the radical is the same as the rate of disappearance of $[Mn^{III}(OH)(dpaq)]^{+}$; thus, we assume that no reaction occurs between the Mn^{III} complex and the phenoxyl radical. An alternative explanation for the 80% yield of the phenoxyl radical would be that the equilibrium for the reaction of $[Mn^{III}(OH)(dpaq)]^{+}$ and $^{4\text{-}t\text{-butyl}}$ArOH to give $[Mn^{II}(OH_2)(dpaq)]^{+}$ and $^{4\text{-}t\text{-butyl}}$ArO· does not lie very far to the right. This can be discounted by the nearly invariant yield of the phenoxyl radical over a range of initial $[Mn^{III}(OH)(dpaq)]^{+}$: $^{4\text{-}t\text{-butyl}}$ArOH concentrations (Table A3.4).

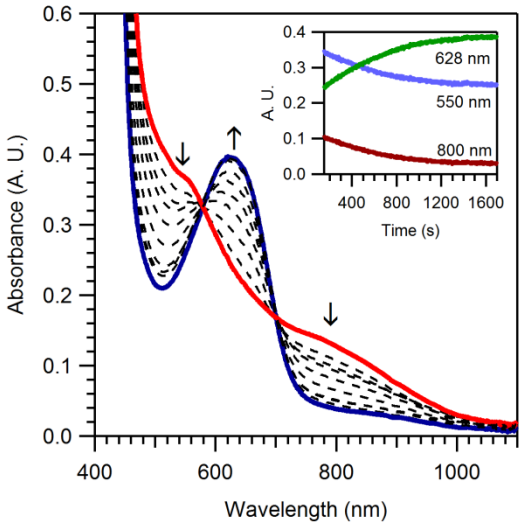

Figure 4.8. Electronic absorption spectra of 1.25 mM $[Mn^{III}(OH)(dpaq)]^{+}$ upon the addition of 100 equiv. 2,4,6-tri-*t*-butylphenol ($^{4\text{-}t\text{-butyl}}$ArOH) at 50 ºC in MeCN under argon. Inset: Time evolution of single-wavelength traces at 628, 550, and 800 nm.

When $[Mn^{III}(OH)(dpaq)]^{+}$ was treated with excess $^{4\text{-}t\text{-butyl}}$ArOH (10 - 125 equiv.), the decay of $[Mn^{III}(OH)(dpaq)]^{+}$ and formation of $^{4\text{-}t\text{-butyl}}$ArO· follow pseudo-first-order kinetics to at least 3 half-lives. Between 10 and 50 equiv. of added $^{4\text{-}t\text{-butyl}}$ArOH, the pseudo-first-order rate

constants (k_{obs}) show a nearly linear increase with respect to $^{4\text{-}t\text{-butyl}}$ArOH concentration. However, above 50 equiv. $^{4\text{-}t\text{-butyl}}$ArOH, saturation behavior was observed (Figure 4.9), indicating the formation of an intermediate prior to the rate-determining step (Scheme 4.1). Accordingly, the relationship between k_{obs} and the concentration of $^{4\text{-}t\text{-butyl}}$ArOH was fit using the following equation: $k_{obs} = k_1K_{eq}[^{4\text{-}t\text{-butyl}}\text{ArOH}] / 1 + K_{eq}[^{4\text{-}t\text{-butyl}}\text{ArOH}]$, where k_1 is the rate constant (in units of s^{-1}) for the rate-determining step and K_{eq} is the equilibrium constant describing the formation of the intermediate from $[Mn^{III}(OH)(dpaq)]^+$ and $^{4\text{-}t\text{-butyl}}$ArOH (Scheme 4.1). This analysis afforded a K_{eq} of 20(2) and a k_1 of 1.2(1) × 10^{-3} s^{-1} (Table 4.2).

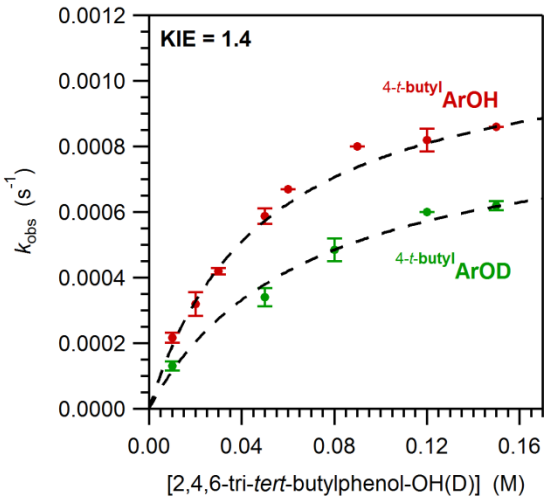

Figure 4.9. Observed pseudo-first-order rate constants (k_{obs}) as a function of $^{4\text{-}t\text{-butyl}}$ArOH and $^{4\text{-}t\text{-butyl}}$ArOD concentration for $[Mn^{III}(OH)(dpaq)]^+$.

Scheme 4.1. Reaction of $[Mn^{III}(OH)(dpaq)]^+$ with $^{4\text{-}t\text{-butyl}}$ArOH, where an initial equilibrium (K_{eq}) between $[Mn^{III}(OH)(dpaq)]^+$ and $^{4\text{-}t\text{-butyl}}$ArOH forms an intermediate, which converts to products by a rate-determining step (k_1).

Table 4.2. Equilibrium and Rate Constants from Kinetic Experiments between $[Mn^{III}(OH)(dpaq)]^+$ and Phenols at 50 ºC in MeCN, and Substrate $BDFE_{OH}$, pK_a, and Reduction Potential Values.

substrate	K_{eq}	k_1 (s^{-1})	$BDFE_{OH}$ [a]	pK_a [b]	E (V) [c]
$^{4\text{-MeO}}$ArOH	>700	$1.8(1) \times 10^{-3}$	73.9(1)	28	-0.806
$^{4\text{-Me}}$ArOH	18(1)	$1.5(1) \times 10^{-3}$	76(1)	27	-0.755
$^{4\text{-}t\text{-butyl}}$ArOH	20(2)	$1.2(1) \times 10^{-3}$	77.1(1)	28	-0.645
$^{4\text{-}t\text{-butyl}}$ArOD	15(2)	$8.9(1) \times 10^{-4}$			
$^{4\text{-H}}$ArOH	8(1)	$9.4(1) \times 10^{-4}$	78.5(1)	27	-0.619

[a] kcal/mol; from Warren *et al*. (ref. [48]) *or* determined following Waidman *et al.* (ref. [64]). [b] pK_a values in MeCN; see ref. [65]. [c] Potential for $PhO\cdot/PhO^-$ in DMSO vs. $Cp_2Fe^{0/+}$.

A similar analysis was performed for data collected using the deuterated phenol $^{4\text{-}t\text{-butyl}}$ArOD (Figure 4.9). The K_{eq} value for the reaction using $^{4\text{-}t\text{-butyl}}$ArOD is quite similar to that observed for $^{4\text{-}t\text{-butyl}}$ArOH (Table 4.2). Considering the standard deviations for the K_{eq} values, these parameters are almost overlapping. The k_1 values for the $^{4\text{-}t\text{-butyl}}$ArOD and $^{4\text{-}t\text{-butyl}}$ArOH substrates afford a KIE of 1.4.

To determine if the observed saturation behavior is a feature of the reaction of $[Mn^{III}(OH)(dpaq)]^+$ with phenolic substrates in general, we explored the reactivity of this complex with a series of phenols, including 4-methoxy-2,6-tri-*t*-butylphenol ($^{4\text{-MeO}}$ArOH), 4-methyl-2,6-tri-*t*-butylphenol ($^{4\text{-Me}}$ArOH), and 2,6-di-*t*-butylphenol ($^{4\text{-H}}$ArOH). This series encompasses a reasonable range of phenol O–H BDFEs (74 – 78.5 kcal/mol) and pK_a values (23 - 28), as summarized in Table 4.2. In reactions with phenols with BDFEs greater than 79 kcal/mol (3,5-di-tert-butyl-4-hydroxybenzonitrile ($^{4\text{-CN}}$ArOH) and 3,5-di-tert-butyl-4-hydroxybenzaldehyde ($^{4\text{-CHO}}$ArOH)), only a fraction of $[Mn^{III}(OH)(dpaq)]^+$ was consumed. This implies that the thermodynamic limit for the oxidative capability of this Mn^{III}-OH adduct is around 80 kcal/mol.

The reactions of $[Mn^{III}(OH)(dpaq)]^+$ with $^{4\text{-MeO}}$ArOH, $^{4\text{-Me}}$ArOH, and $^{4\text{-H}}$ArOH all showed saturation behavior, with the pseudo-first-order rate constants leveling at higher phenol

concentration (Figures 3.S5). Equilibrium and rate constants determined from fits to these data sets are collected in Table 4.2. In the case of $^{4\text{-MeO}}$ArOH, the observed rate was saturated even when using 10 equiv. of phenol (Figure A3.5, top right). Thus, only an estimate of the lower limit for K_{eq} (700) could be obtained for this substrate.

An Evans-Polanyi plot for the oxidation of phenolic substrates with $[Mn^{III}(OH)(dpaq)]^+$ shows a linear dependence of the rate-determining step (k_1) as a function of BDFE of the substrate (Figure 4.10). This relationship, along with the KIE value for the reaction of $[Mn^{III}(OH)(dpaq)]^+$ with $^{4\text{-}t\text{-butyl}}$ArOH, provides strong evidence that the rate-determining step in these reactions is a CPET between the phenol and the Mn^{III}–OH unit. Thus, the pre-equilibrium step shown in Scheme 4.1 potentially involves the formation of a hydrogen-bonded reactant complex.

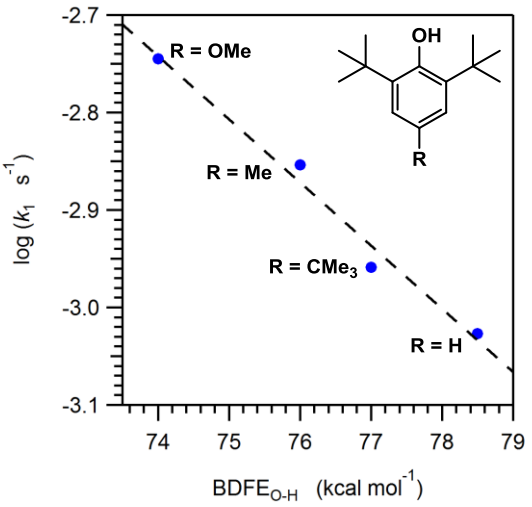

Figure 4.10. Evans-Polanyi plot of oxidation rate (k_1) of phenolic substrates versus the BDFE of the substrate.

To further probe the nature of the intermediate formed in the initial equilibrium reaction between $[Mn^{III}(OH)(dpaq)]^+$ and $^{4\text{-}t\text{-butyl}}$ArOH (Scheme 4.1), 400 equiv. of the phenol were added to a MeCN solution of $[Mn^{III}(OH)(dpaq)]^+$ at 50 °C. Under these conditions, the intermediate

species should initially be dominant in solution. Electronic absorption spectra collected 0.5 - 1.5 seconds after the addition of $^{4\text{-}t\text{-butyl}}$ArOH show very minor perturbations relative to the spectrum of pure $[Mn^{III}(OH)(dpaq)]^{+}$ (Figure A3.6). Specifically, the observed absorption maxima are not shifted upon $^{4\text{-}t\text{-butyl}}$ArOH addition, and the absorption intensity at 550 nm rises by only 12%. The observed increase in intensity is wavelength dependent and, thus, is potentially due to light scattering, which increases as a function of the fourth power of the light frequency. Under the reasonable assumption that the electronic absorption spectrum of $[Mn^{III}(OH_2)(dpaq)]^{2+}$ should be distinct from that of $[Mn^{III}(OH)(dpaq)]^{+}$, the similarities between the electronic absorption spectra before and after the addition of the $^{4\text{-}t\text{-butyl}}$ArOH suggest that the intermediate does not result from proton transfer between $^{4\text{-}t\text{-butyl}}$ArOH and $[Mn^{III}(OH)(dpaq)]^{+}$.

4.3.7. Catalytic oxidation of TEMPOH with $[Mn^{II}(dpaq)](OTf)$ and O_2. In the presence of a large excess of TEMPOH (4000 equiv.), $[Mn^{II}(dpaq)](OTf)$ catalytically converted TEMPOH into TEMPO in continuously oxygenated MeCN solution at 25 ºC. The catalytic process was followed over the course of 200 minutes by electronic absorption spectroscopy, monitoring the characteristic features of TEMPO and $[Mn^{II}(dpaq)](OTf)$ (Figure A3.7B). The direct oxidation of TEMPOH in the absence of the catalyst was investigated as a control (Figure A3.7A). Although oxidation of TEMPOH to TEMPO is observed in the control reactions, approximately 40% higher conversions are observed in the presence of $[Mn^{II}(dpaq)](OTf)$. Importantly, separate control experiments using catalytic amounts of $Mn^{II}(OTf)_2$ gave results within error of the control experiments lacking any Mn^{II} species. Thus, the increase in turnover numbers is attributed to catalytic activity of the $[Mn^{II}(dpaq)](OTf)$ complex. Correcting for the background oxidation of TEMPOH in the control reactions, a maximum of 1050 turnovers were observed using $[Mn^{II}(dpaq)](OTf)$ as an aerobic oxidation catalyst.

4.4. Discussion

Synthetic complexes with mononuclear hydroxomanganese(III) motifs are relatively rare,[39-46,66-69] as the hydroxo ligand is prone to bridge manganese centers.[27,29,31-38] Of the known mononuclear Mn^{III}-OH complexes, only two, $[Mn^{III}(OH)(PY5)]^{2+}$ and $[Mn^{III}(OH)(S^{Me2}N_4(tren))]^{+}$ (Figure 4.1), have been reported to perform substrate oxidation reactions,[39,46] and both these reactions proceed by a CPET process. Given these limited examples, relatively little is known concerning the factors affecting the CPET, or, more broadly, PCET, reactions of mononuclear hydroxomanganese(III) species. This is in spite of several biological examples where Mn^{III}-OH units are involved in important oxidation/ reduction reactions,[2,4,6,19] and stands in clear contrast to the abundance of studies focused on the PCET reactions of high-valent Mn-oxo and Mn-hydroxo species.[70,71] As noted by Mayer and co-workers, the oxidation reactions of lower valent M^{II}/M^{III} couples are overshadowed by studies of their high-valent counterparts.[72]

In this work, we have described a new mononuclear Mn^{III}-OH adduct, $[Mn^{III}(OH)(dpaq)]^{+}$, which is remarkably stable ($t_{1/2} \approx 26$ days at 25 ºC in MeCN) and is formed in essentially quantitative yields from reaction of $[Mn^{II}(dpaq)](OTf)$ with O_2. Because of the high intrinsic reduction potential of the Mn^{II}/Mn^{III} couple, reactivity with O_2 is less common for manganese(II) centers when compared to iron(II) analogous.[73] To the best of our knowledge, the formation of $[Mn^{III}(OH)(S^{Me2}N_4(tren))]^{+}$ from O_2 and the corresponding Mn^{II} complex $[Mn^{II}(S^{Me2}N_4(tren))]^{+}$ represents the only other example of the quantative formation of a Mn^{III}-OH adduct from a Mn^{II} center and O_2.[46] In that case, a mono-oxo bridged dimanganese(III,III) complex served as an intermediate. Other examples of mononuclear Mn^{III}-OH adducts generated by O_2 oxidation of a Mn^{II} complex include $[Mn^{III}(OH)(OAc)(Me_2EBC)]^{+}$,[45] and a set of

$[Mn^{III}(OH)(L)]^-$ species, where L is one of two trianionic tripodal ligands with a second-sphere cavity shielding the bound hydroxo ligand.[40,44] For one of the latter complexes, mechanistic studies provided evidence that the Mn^{III}-OH complex resulted from the initial formation of a peroxo-bridged-dimanganese(III,III) species that undergoes O–O bond homolysis to give two mononuclear Mn^{IV}=O intermediates.[44] The Mn^{IV}=O adducts convert to the observed Mn^{III}-OH species by a PCET reaction with solvent. More recently, Kovacs and co-workers have reported the first example of a peroxo-bridged-dimanganese(III,III) species, lending credence to this mechanism.[74] Investigations of the reaction of O_2 with the $[Mn^{II}(dpaq)](OTf)$ complex in MeCN using electronic absorption spectroscopy at low temperatures (-40 ºC) provide no evidence for the formation of any intermediates en route to $[Mn^{III}(OH)(dpaq)]^+$. In addition, attempts to detect transient Mn^{IV}=O species have led to only negative results. For example, when the oxygenation of $[Mn^{II}(dpaq)](OTf)$ is carried out in the presence of 10 equiv. PPh_3, the formation of $O=PPh_3$ is not observed and the yield of $[Mn^{III}(OH)(dpaq)]^+$ is unchanged. Nonetheless, the pathway for O_2-dependent formation of $[Mn^{III}(OH)(dpaq)]^+$ is currently under investigation utilizing different solvent systems that may favor the formation of reaction intermediates.

$[Mn^{III}(OH)(dpaq)]^+$ is capable of oxidizing substrates with O–H BDFEs less than 79 kcal/mol. Saturation behavior was observed in oxidation reactions with phenolic substrates. This is only the second report of a mononuclear Mn^{III}-OH adduct that is capable of performing a CPET reaction with phenols, and a relatively rare example of a Mn oxidant that shows saturation behavior in reaction with substrates.[75,76] Catalytic oxidation of organic substrates using O_2 as terminal oxidant is another attractive property of $[Mn^{III}(OH)(dpaq)]^+$, which is observed to perform over 1050 turnovers of TEMPOH in 3 hrs under the conditions employed. This turnover number is over two orders of magnitude larger than that observed for catalytic TEMPOH

oxidation by $[Mn^{III}(OH)(S^{Me2}N_4(tren))]^+$,[46] although the catalytic activity for that system was not optimized.

4.4.1. Nature of intermediate in phenol oxidation reactions of $[Mn^{III}(OH)(dpaq)]^+$. PCET reactions can occur via a sequential pathway (*i.e.*, initial proton transfer followed by electron transfer or *vice versa*) or a concerted pathway (CPET or HAT; see footnote 16). The previously reported $[Mn^{III}(OH)(PY5)]^{2+}$ and $[Mn^{III}(OH)(S^{Me2}N_4(tren))]^+$ complexes (Figure 4.1), perform C–H and/or O–H bond oxidations by a CPET process, where the proton and electron are transferred in a single kinetic step.[39,46] In contrast, a mononuclear Mn^{III}-oxo complex, $[Mn^{III}(O)(H_3buea)]^{2-}$ (H_3buea = tris[(*N*'-*tert*-butylureaylato)-*N*-ethyl]aminato), featuring a trianionic supporting ligand with a second-sphere hydrogen-bonding cavity around the oxo, performs C–H bond oxidation of dihydroanthracene through a sequential mechanism, with rate-limiting proton transfer prior to electron transfer.[66] This sequential pathway is favored for the Mn^{III}-oxo because of its high basicity (the pK_a of the corresponding Mn^{III}-hydroxo is 28.3 in DMSO[66]). In fact, treatment of $[Mn^{III}(O)(H_3buea)]^{2-}$ with $^{4\text{-}t\text{-butyl}}$ArOH in dimethylacetamide solvent resulted in a proton transfer reaction; oxidation of $^{4\text{-}t\text{-butyl}}$ArOH was not observed.[60]

The saturation behavior in the PCET reaction of $[Mn^{III}(OH)(dpaq)]^+$ with phenols could imply a sequential mechanism, as the kinetic behavior indicates an initial equilibration to an intermediate species prior to rate-determining formation of $[Mn^{II}(OH_2)(dpaq)]^+$ and the phenoxyl radical. In principle, there are several pathways consistent with saturation behavior, as outlined in Scheme 4.2. Pathway C, involving initial electron-transfer, can be excluded on the basis of the unfavorability of oxidizing the ArOH substrates in the absence of their deprotonation, as well as the low $E_{1/2}$ value for $[Mn^{III}(OH)(dpaq)]^+$ (*vide supra*).[48]

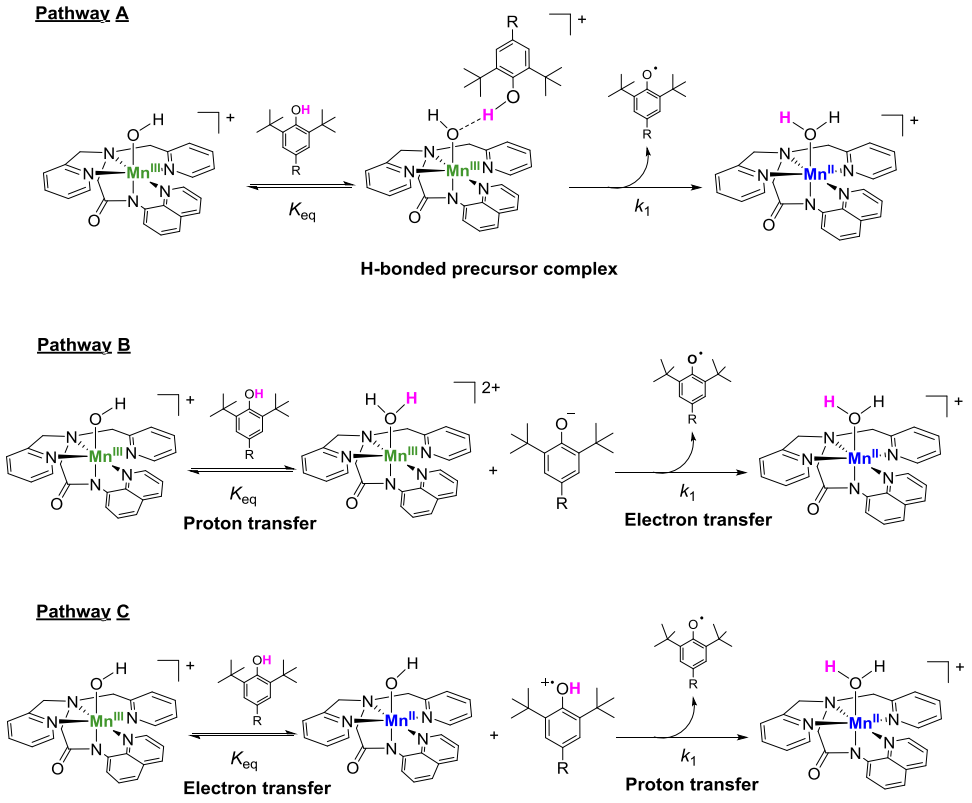

Scheme 4.2. Possible pathways for PCET reaction of $[Mn^{III}(OH)(dpaq)]^{+}$ with phenols.

There are several lines of evidence that the equilibrium step does not involve an initial proton transfer but potentially involves the formation of a hydrogen-bonded complex (pathways B and A, respectively; Scheme 4.2). First, there is no correlation between the observed K_{eq} values and the pK_a values of the phenols (Table 4.2). A correlation would be expected if the equilibrium were due to a proton transfer from the phenol to $[Mn^{III}(OH)(dpaq)]^{+}$.[77] Second, the electronic absorption spectrum of the intermediate, obtained within 0.5 seconds of adding a large excess of $^{4\text{-}t\text{-butyl}}$ArOH to a MeCN solution of $[Mn^{III}(OH)(dpaq)]^{+}$, is nearly identical to that of $[Mn^{III}(OH)(dpaq)]^{+}$ (Figure A3.6). Although the electronic absorption spectrum of a putative $[Mn^{III}(OH_2)(dpaq)]^{2+}$ species is not known, it is reasonable to assume that the change from hydroxo to aqua ligation would significantly perturb the ligand-field splitting of the Mn^{III} center

(potentially causing a re-orientation of the pseudo-Jahn-Teller axis[78]), resulting in noticeable shifts of the *d-d* transition energies. The minor changes observed experimentally are more consistent with a hydrogen-bonding interaction.[79] Third, the KIE of 1.4 for the rate-determining step in the reaction of $[Mn^{III}(OH)(dpaq)]^+$ with $^{4\text{-}t\text{-butyl}}$ArOH suggests that phenol O–H bond breaking be part of this step. Finally, k_1 is related to the BDFE values of the phenol O–H bonds, which is a hallmark of a CPET process. Given the above considerations, we conclude that the initial equilibrium step features the formation of a precursor complex, likely stabilized by hydrogen-bonding interactions, and that the rate-determining step is a CPET.

When CPET reactions are considered within the framework of Marcus theory, a precursor (or encounter) complex is expected to form prior to rate-determining proton-electron transfer.[80] While rare, precursor complexes have been observed for other CPET processes, and these are often,[75,81,82] but not always,[76] mediated by hydrogen-bonding interactions with an O–H group on the substrate. For example, a Mn^{IV}-hydroxo adduct supported by a bulky salen derivative also showed saturation behavior in reactions with substituted phenols.[75,76] For the reaction with $^{4\text{-H}}$ArOH, in particular, a K_{eq} of approximately 5000 was determined, and this equilibrium was attributed to the formation of a hydrogen-bonded complex. No initial equilibrium was observed in the reaction of the corresponding Mn^{IV}-oxo adduct with phenols.[75,76] In addition, Costas and co-workers observed the formation of a precursor complex in the reaction of hydrocarbons with an oxohydroxomanganese(IV) moeity supported by a neutral N_4 ligand, but the forces stabilizing the precursor complex remain unclear.[76] Saturation behavior was not observed in analogous reactions with the corresponding di(hydroxo)manganese(IV) complex. Taken together, these prior studies demonstrate that subtle

changes in properties of the metal-based oxidant can dramatically affect whether or not the formation of a precursor complex is observed.

It is, nonetheless, somewhat curious that saturation behavior should be observed in the reaction of $[Mn^{III}(OH)(dpaq)]^+$ with phenols, but not with TEMPOH, which likewise contains an O–H unit capable of hydrogen bonding. Indeed, TEMPOH has been shown to form a hydrogen-bond-mediated precursor complex, prior to rate-liming CPET, with $[Co^{III}(Hbim)(H_2bim)_2]^{2+}$ (H_2bim = 2,2'-biimidazoline).[79] However, given that the K_{eq} values observed for reaction of $[Mn^{III}(OH)(dpaq)]^+$ with phenols reflect small stabilizations in terms of free energy (-4.2 to -1.3 kcal/mol), seemingly minor differences in the hydrogen-bond donating (or accepting) ability of the phenol versus TEMOPH substrates, and/ or changes in solvent reorganization energies upon precursor complex formation, could lead to a precursor complex being less favorable in the case of TEMPOH substrate. Taken together, this and other work highlights our nascent understanding of the optimal conditions that must be achieved to observe formation of a precursor complex, and the impacts of precursor complexes on the overall CPET process.[75,76,81,82]

4.4.2. CPET reactivity of mononuclear Mn^{III}-OH complexes. To the best of our knowledge, $[Mn^{III}(OH)(dpaq)]^+$ is only the third hydroxomanganese(III) complex known to facilitate either O–H or C–H bond oxidations. As both $[Mn^{III}(OH)(dpaq)]^+$ and $[Mn^{III}(OH)(S^{Me2}N_4(tren))]^+$ (Figure 4.1, right) react with TEMPOH at 25 ºC in MeCN, a direct comparison can be made between these oxidants. On the basis of this kinetic data, $[Mn^{III}(OH)(S^{Me2}N_4(tren))]^+$ is a more rapid oxidant,[46] showing a second-order rate constant for TEMPOH oxidation 10^4-fold larger than that of $[Mn^{III}(OH)(dpaq)]^+$ (Table 4.3). The faster reaction for $[Mn^{III}(OH)(S^{Me2}N_4(tren))]^+$ is a consequence of a smaller enthalpy *and* entropy of activation compared to $[Mn^{III}(OH)(dpaq)]^+$ (Table 4.3). In both systems the negative $\Delta S^{\neq}$ values

mark an associative process; the substantially more negative $\Delta S^{\neq}$ for the reaction involving $[Mn^{III}(OH)(dpaq)]^+$ implies a more ordered transition state. The smaller $\Delta H^{\neq}$ for the reaction of $[Mn^{III}(OH)(S^{Me2}N_4(tren))]^+$ is tentatively attributed to an increased nucleophilicity caused by the electron-donating thiolate ligand. A similar effect has been observed in CPET reactions of a thiolate-ligated oxoiron(IV) complex.[83] Also of relevance in comparing TEMPOH reactivity with metal-hydroxo adducts is a recent study of the hydroxoiron(III) complex $Fe^{III}(OH)(TMP)$, which features a tetramesitylporphyrin supporting ligand.[72] In that case, a second-order rate constant of 76(5) $M^{-1}s^{-1}$ was observed for the oxidation of TEMPOH at 25 ºC in toluene (Table 4.3).

Table 4.3. Reaction Parameters for Oxidation of TEMPOH by Hydroxometal(III) Adducts.

complex	conc.[a]	k_2 ($M^{-1}s^{-1}$)	T (ºC)	solvent	$\Delta H^{\neq}$ [b]	$\Delta S^{\neq}$ [c]	$\Delta G^{\neq}$ [b]
$[Mn^{III}(OH)(dpaq)]^+$	1.25	$1.3(1) \times 10^{-1}$	25	MeCN	9.9(9)	-35(3)	20.3
$[Mn^{III}(OH)(S^{Me2}N_4(tren))]^+$ [d]	0.5	2.1×10^3	25	MeCN	8.2	-25.5	15.6
$Fe^{III}(OH)(TMP)$ [e]	0.08	$7.6(5) \times 10^1$	25	toluene	NR[f]	NR[f]	15.0(1)

[a] Concentration in mM. [b] kcal/mol. [c] cal / mol K. [d] Ref. 46. [e] Ref. 72. [f] Not reported.

Although both $[Mn^{III}(OH)(S^{Me2}N_4(tren))]^+$ and $Fe^{III}(OH)(TMP)$ react with TEMPOH much more rapidly than $[Mn^{III}(OH)(dpaq)]^+$, neither of those complexes is able to oxidize substrates with larger BDFEs. For example, $Fe^{III}(OH)(TMP)$ showed no reaction with $^{4\text{-}t\text{-}butyl}$ArOH over a period of 24 hours,[72] and the normal decay rate of $[Mn^{III}(OH)(S^{Me2}N_4(tren))]^+$ was unaffected by the presence of a large excess of 1,4-cyclohexadience, dihydroanthracene, or toluene.[46] In contrast, $[Mn^{III}(OH)(dpaq)]^+$ reacts with phenols with O–H BDFEs up to 79 kcal/mol, and can also activate the weak C–H bonds of xanthene (BDFE = 73.3 in dimethylsulfoxide). $[Mn^{III}(OH)(dpaq)]^+$ reacts with a large excess (250 equiv.) of xanthene with a pseudo-first-order rate constant of 8×10^{-4} s^{-1} at 50 ºC in MeCN, which is an order of

magnitude slower than that observed for $[Mn^{III}(OH)(PY5)]^{2+}$,[39] the only other Mn^{III}-OH complex known to oxidize C–H bonds.

For the reaction of $[Mn^{III}(OH)(dpaq)]^{+}$ with phenols, the rate of reaction is only weakly dependent on the phenol O–H BDFE (Figure 4.10). In particular, the observed slope of the log(*k*) versus BDFE correlation is only -0.07, which is significantly lower than the expected Marcus theory value of -0.5 for a reaction with a small thermodynamic driving force.[80] However, this slope should be viewed within the caveat that the linear-free energy relationship is only for a small range of substrate BDFEs. In any case, values between -0.5 and -0.3 have been reported for transition-metal oxidants,[80,84] including oxoruthenium(IV)[85] and oxomanganese(IV)[70,76] species, and are commonly interpreted as implying a symmetric transition state structure. Notably, a similarly weak correlation between rate and substrate BDE was observed for hydrocarbon oxidation by $[Mn^{III}(OH)(PY5)]^{2+}$ (slope = -0.1), and this was attributed to unusually large reorganizational energies of the oxidant ($\Delta S^{\neq}$ = -36(5) cal / mol K for the reaction of $[Mn^{III}(OH)(PY5)]^{2+}$ with dihydroanthracene).[39] This interpretation would be consistent with other instances were small slopes have been attributed to large entropies of reorganization, such that $T\Delta S^{\neq} > \Delta H^{\neq}$.[82]

It is tempting to speculate on whether the low dependence of the reaction rate on the substrate BDFE is a general feature of CPET reactions by manganese(III) centers that could be related to relatively large entropies of activation. This of course would have implications for the suitability of such oxidants in synthetic and biological oxidation reactions and/ or bear relevance to the mechanisms by which protein active sites tune the geometric and electronic structure to minimize reorganization during CPET. However, to the best of our knowledge, the set of reactions of $[Mn^{III}(OH)(dpaq)]^{+}$ and $[Mn^{III}(OH)(PY5)]^{2+}$ with phenols and hydrocarbons,

respectively, provide the only examples of linear-free energy relationships for CPET by manganese(III) centers. It is, therefore, ill-advised to draw far-reaching conclusions from this limited data set. Nonetheless, this work reveals complexities in identifying the geometric and electronic factors that contribute to the kinetic and thermodynamic behavior of PCET reactions and illustrates the importance of extending detailed studies of such reactions to mid- and even low-valent transition metal oxidants.

4.5. References.

1. Cotruvo, J. J. A.; Stubbe, J., *Metallomics* **2012,** *4*, 1020-1036.
2. McEvoy, J. P.; Brudvig, G. W., *Chem. Rev.* **2006,** *106*, 4455-4483.
3. Miller, A.-F., *Curr. Opin. Chem. Biol.* **2004,** *8*, 162-168.
4. Grove, L. E.; Brunold, T. C., *Comments Inorg. Chem.* **2008,** *29*, 134-168.
5. Su, C.; Oliw, E. H., *J. Biol. Chem.* **1998,** *273*, 13072-13079.
6. Su, C.; Sahlin, M.; Oliw, E. H., *J. Biol. Chem.* **2000,** *275*, 18830-18835.
7. Miller, A.-F.; Padmakumar, F.; Sorkin, D.; Karapetian, A.; Vance, C. K., *J. Inorg. Biochem.* **2003,** *93*, 71-83.
8. Han, W.-G.; Lovell, T.; Noodleman, L., *Inorg. Chem.* **2002,** *41*, 205-218.
9. Jackson, T. A.; Gutman, C. T.; Maliekal, J.; Miller, A.-F.; Brunold, T. C., *Inorg. Chem.* **2013,** *52*, 3356-3367.
10. Vance, C. K.; Miller, A.-F., *J. Am. Chem. Soc.* **1998,** *120*, 461-467.
11. Vance, C. K.; Miller, A. F., *Biochemistry* **2001,** *40*, 13079-13087.
12. Jackson, T. A.; Brunold, T. C., *Acc. Chem. Res.* **2004,** *37*, 461-470.
13. Although Mn-lipoxygenase has not been structurally characterized, the presence of a monuclear Mn^{III}-OH unit is inferred on the basis of analogy to the active site of Fe-lipoxygenase; see Boyington, J.; Gaffney, B.; Amzel, L., *Science* **1993**, *260*, 1482-1486, and Minor, W.; Steczko, J.; Stec, B.; Otwinowski, Z.; Bolin, J. T.; Walter, R.; Axelrod, B., *Biochemistry* **1996**, *35*, 10687-10701.
14. Umena, Y.; Kawakami, K.; Shen, J.-R.; Kamiya, N., *Nature* **2011,** *473*, 55-60.
15. Pal, R.; Negre, C. F. A.; Vogt, L.; Pokhrel, R.; Ertem, M. Z.; Brudvig, G. W.; Batista, V. S., *Biochemistry* **2013,** *52*, 7703-7706.
16. In this work, we use PCET to refer broadly to any reaction involving the overall transfer of a proton and an electron. Consequently, PCET reactions can occur in a sequential manner, where the electron and proton are transferred in separate kinetic steps, or can occur in a concerted process. Concerted processes can be further described as hydrogen-atom transfer (HAT) or concerted proton-electron transfer (CPET). HAT is often invoked when the proton and electron are transferred to the same orbital or bond, whereas CPET is used to describe cases where the electron and proton are transferred to separate orbitals and/or bonds. With this definition, CPET is common for transition metal-oxo or -hydroxo

species, where the electron is transferred to the metal and the proton is transferred to the oxo or hydroxo ligand. A more rigorous distinction between HAT and CPET has been offered by Hammes-Shiffer and co-workers (see reference 17), and depends on whether the proton transfer is electronically adiabatic (HAT) or nonadiabatic (CPET).

17. Layfield, J. P.; Hammes-Schiffer, S., *Chem. Rev.* **2013,** *114*, 3466-3494.
18. The k_H / k_D value was temperature-independent over the measured range of 5 - 45 ºC.
19. Mullins, C. S.; Pecoraro, V. L., *Coord. Chem. Rev.* **2008,** *252*, 416-443.
20. Tommos, C.; Babcock, G. T., *Acc. Chem. Res.* **1998,** *31*, 18-25.
21. Tang, X.-S.; Randall, D. W.; Force, D. A.; Diner, B. A.; Britt, R. D., *J. Am. Chem. Soc.* **1996,** *118*, 7638-7639.
22. Siegbahn, P. E. M., *Inorg. Chem.* **2000,** *39*, 2923-2935.
23. Zouni, A.; Witt, H.-T.; Kern, J.; Fromme, P.; Krauss, N.; Saenger, W.; Orth, P., *Nature* **2001,** *409*, 739-743.
24. Gilchrist, M. L.; Ball, J. A.; Randall, D. W.; Britt, R. D., *Proc. Natl. Acad. Sci. U. S. A.* **1995,** *92*, 9545-9549.
25. Hoganson, C.; Lydakis-Simantiris, N.; Tang, X.-S.; Tommos, C.; Warncke, K.; Babcock, G.; Diner, B.; McCracken, J.; Styring, S., *Photosynth. Res.* **1995,** *46*, 177-184.
26. Babcock, G. T. In *The oxygen-evolving complex in photosystem II as a metallo-radical enzyme*, 1995; Kluwer: 1995; pp 209-215.
27. Baldwin, M. J.; Pecoraro, V. L., *J. Am. Chem. Soc.* **1996,** *118*, 11325-11326.
28. Caudle, M. T.; Pecoraro, V. L., *J. Am. Chem. Soc.* **1997,** *119*, 3415-3416.
29. Wang, K.; Mayer, J. M., *J. Am. Chem. Soc.* **1997,** *119*, 1470-1471.
30. Bordwell, F. G.; Cheng, J., *J. Am. Chem. Soc.* **1991,** *113*, 1736-1743.
31. Larsen, A. S.; Wang, K.; Lockwood, M. A.; Rice, G. L.; Won, T.-J.; Lovell, S.; Sadílek, M.; Tureček, F.; Mayer, J. M., *J. Am. Chem. Soc.* **2002,** *124*, 10112-10123.
32. Mukhopadhyay, S.; Mandal, S. K.; Bhaduri, S.; Armstrong, W. H., *Chem. Rev.* **2004,** *104*, 3981-4026.
33. Sano, Y.; Weitz, A. C.; Ziller, J. W.; Hendrich, M. P.; Borovik, A. S., *Inorg. Chem.* **2013,** *52*, 10229-10231.
34. Baldwin, M. J.; Law, N. A.; Stemmler, T. L.; Kampf, J. W.; Penner-Hahn, J. E.; Pecoraro, V. L., *Inorg. Chem.* **1999,** *38*, 4801-4809.
35. Baldwin, M. J.; Stemmler, T. L.; Riggs-Gelasco, P. J.; Kirk, M. L.; Penner-Hahn, J. E.; Pecoraro, V. L., *J. Am. Chem. Soc.* **1994,** *116*, 11349-56.
36. Zhou, H.-B.; Wang, H.-S.; Chen, Y.; Xu, Y.-L.; Song, X.-J.; Song, Y.; Zhang, Y.-Q.; You, X.-Z., *Dalton Trans.* **2011,** *40*, 5999-6006.
37. Park, Y. J.; Ziller, J. W.; Borovik, A. S., *J. Am. Chem. Soc.* **2011,** *133*, 9258-9261.
38. Cheng, B.; Fries, P. H.; Marchon, J.-C.; Scheidt, W. R., *Inorg. Chem.* **1996,** *35*, 1024-1032.
39. Goldsmith, C. R.; Cole, A. P.; Stack, T. D. P., *J. Am. Chem. Soc.* **2005,** *127*, 9904-9912.
40. Shirin, Z.; Hammes, B. S.; Young, V. G.; Borovik, A. S., *J. Am. Chem. Soc.* **2000,** *122*, 1836-1837.
41. El Ghachtouli, S.; Lassalle-Kaiser, B.; Dorlet, P.; Guillot, R.; Anxolabehere-Mallart, E.; Costentin, C.; Aukauloo, A., *Energy Environ. Sci.* **2011,** *4*, 2041-2044.
42. Eroy-Reveles, A. A.; Leung, Y.; Beavers, C. M.; Olmstead, M. M.; Mascharak, P. K., *J. Am. Chem. Soc.* **2008,** *130*, 4447-4458.
43. Eichhorn, D. M.; Armstrong, W. H., *J. Chem. Soc., Chem. Commun.* **1992**, 85-87.

44. Shirin, Z.; S. Borovik, A.; G. Young Jr, V., *Chem. Commun.* **1997**, 1967-1968.
45. Hubin, T. J.; McCormick, J. M.; Alcock, N. W.; Busch, D. H., *Inorg. Chem.* **2001,** *40*, 435-444.
46. Coggins, M. K.; Brines, L. M.; Kovacs, J. A., *Inorg. Chem.* **2013,** *52*, 12383-12393.
47. Shook, R. L.; Peterson, S. M.; Greaves, J.; Moore, C.; Rheingold, A. L.; Borovik, A. S., *J. Am. Chem. Soc.* **2011,** *133*, 5810-5817.
48. Warren, J. J.; Tronic, T. A.; Mayer, J. M., *Chem. Rev.* **2010,** *110*, 6961-7001.
49. Hitomi, Y.; Iwamoto, Y.; Kodera, M., *Dalton Trans.* **2014,** *43*, 2161-2167.
50. Hitomi, Y.; Arakawa, K.; Funabiki, T.; Kodera, M., *Angew. Chem., Int. Ed.* **2012,** *51*, 3448-3452.
51. Coggins, M. K.; Zhang, M.-T.; Vannucci, A. K.; Dares, C. J.; Meyer, T. J., *J. Am. Chem. Soc.* **2014,** *136*, 5531-5534.
52. Wu, A.; Mader, E. A.; Datta, A.; Hrovat, D. A.; Borden, W. T.; Mayer, J. M., *J. Am. Chem. Soc.* **2009,** *131*, 11985-11997.
53. Lansky, D. E.; Goldberg, D. P., *Inorg. Chem.* **2006,** *45*, 5119-5125.
54. Seo, M. S.; Kim, J. Y.; Annaraj, J.; Kim, Y.; Lee, Y.-M.; Kim, S.-J.; Kim, J.; Nam, W., *Angew. Chem., Int. Ed.* **2007,** *46*, 377-380.
55. Evans, D. F.; Jakubovic, D. A., *J. Chem. Soc., Dalton Trans.* **1988**, 2927-2933.
56. Refinement: SHELXTL v2010.3-0. Bruker-AXS, E. C. P., Madison, WI 53711-5373 USA.
57. International Tables for Crystallography, V. A., 4th ed., Kluwer: Boston (1996).
58. Data Collection: SMART Software in APEX2 v2010.3-0 Suite. Bruker-AXS, E. C. P., Madison, WI 53711-5373 USA.
59. Data Reduction: SAINT Software in APEX2 v2010.3-0 Suite. Bruker-AXS, E. C. P., Madison, WI 53711-5373 USA
60. Gupta, R.; Borovik, A. S., *J. Am. Chem. Soc.* **2003,** *125*, 13234-13242.
61. Ottaviani, M. F.; Garcia-Garibay, M.; Turro, N. J., *Colloids and Surfaces A: Physicochemical and Engineering Aspects* **1993,** *72*, 321-332.
62. Manner, V. W.; Lindsay, A. D.; Mader, E. A.; Harvey, J. N.; Mayer, J. M., *Chem. Sci.* **2012,** *3*, 230-243.
63. Manner, V. W.; Markle, T. F.; Freudenthal, J. H.; Roth, J. P.; Mayer, J. M., *Chem. Commun.* **2008**, 256-258.
64. Waidmann, C. R.; Zhou, X.; Tsai, E. A.; Kaminsky, W.; Hrovat, D. A.; Borden, W. T.; Mayer, J. M., *J. Am. Chem. Soc.* **2009,** *131*, 4729-4743.
65. Kütt, A.; Leito, I.; Kaljurand, I.; Sooväli, L.; Vlasov, V. M.; Yagupolskii, L. M.; Koppel, I. A., *J. Org. Chem.* **2006,** *71*, 2829-2838.
66. Parsell, T. H.; Yang, M.-Y.; Borovik, A. S., *J. Am. Chem. Soc.* **2009,** *131*, 2762-2763.
67. Lassalle-Kaiser, B.; Hureau, C.; Pantazis, D. A.; Pushkar, Y.; Guillot, R.; Yachandra, V. K.; Yano, J.; Neese, F.; Anxolabehere-Mallart, E., *Energy & Environmental Science* **2010,** *3*, 924-938.
68. Gupta, R.; Taguchi, T.; Borovik, A. S.; Hendrich, M. P., *Inorg. Chem.* **2013,** *52*, 12568-12575.
69. Borovik, A. S., *Acc. Chem. Res.* **2004,** *38*, 54-61.
70. Leto, D. F.; Ingram, R.; Day, V. W.; Jackson, T. A., *Chem. Commun.* **2013,** *49*, 5378-5380.
71. Wang, Y.; Shi, S.; Wang, H.; Zhu, D.; Yin, G., *Chem. Commun.* **2012,** *48*, 7832-7834.

72. Porter, T. R.; Mayer, J. M., *Chem. Sci.* **2014,** *5*, 372-380.
73. Rybak-Akimova, E. V., In *Mechanisms of Oxygen Binding and Activation at Transition Metal Centers. In Physical Inorganic Chemistry*, Bakac, A., Ed. John Wiley & Sons, Inc.: Hoboken, NJ: 2010; pp 109-188.
74. Coggins, M. K.; Sun, X.; Kwak, Y.; Solomon, E. I.; Rybak-Akimova, E.; Kovacs, J. A., *J. Am. Chem. Soc.* **2013,** *135*, 5631-5640.
75. Kurahashi, T.; Kikuchi, A.; Shiro, Y.; Hada, M.; Fujii, H., *Inorg. Chem.* **2010,** *49*, 6664-6672.
76. Garcia-Bosch, I.; Company, A.; Cady, C. W.; Styring, S.; Browne, W. R.; Ribas, X.; Costas, M., *Angew. Chem., Int. Ed. Engl.* **2011,** *50*, 5648-5653.
77. It would also appear reasonable to anticipate a relationship between the pK_a of the phenol and the equilibrium constant for the formation of a hydrogen-bonded complex, when the phenol is the hydrogen-bond donor. In contrast, if the Mn-OH unit were to serve as a hydrogen-bond donor, then no correlation between pK_a and the K_{eq} values would be expected. In that scenario rapid hydrogen-bond rearrangement would be required prior to rate-limiting CPET.
78. Jackson, T. A.; Karapetian, A.; Miller, A.-F.; Brunold, T. C., *J. Am. Chem. Soc.* **2004,** *126*, 12477-12491.
79. Mader, E. A.; Mayer, J. M., *Inorg. Chem.* **2010,** *49*, 3685-3687.
80. Mayer, J. M., *Acc. Chem. Res.* **2010,** *44*, 36-46.
81. Kojima, T.; Hirai, Y.; Ishizuka, T.; Shiota, Y.; Yoshizawa, K.; Ikemura, K.; Ogura, T.; Fukuzumi, S., *Angew. Chem., Int. Ed. Engl.* **2010,** *49*, 8449-8453.
82. Ishizuka, T.; Ohzu, S.; Kotani, H.; Shiota, Y.; Yoshizawa, K.; Kojima, T., *Chemical Science* **2014,** *5*, 1429-1436.
83. Sastri, C. V.; Lee, J.; Oh, K.; Lee, Y. J.; Lee, J.; Jackson, T. A.; Hirao, H.; Que, L., Jr.; Shaik, S.; Nam, W., *Proc. Natl. Acad. Sci. U. S. A.* **2007,** *104*, 19181-19186.
84. Gardner, K. A.; Kuehnert, L. L.; Mayer, J. M., *Inorg. Chem.* **1997,** *36*, 2069-2078.
85. Matsuo, T.; Mayer, J. M., *Inorg. Chem.* **2005,** *44*, 2150-2158.

CHAPTER 5

O–H Bond Oxidation by a Monomeric Mn^{III}-OMe Complex

This work has been reproduced from: Wijeratne, G. B.; Day, V. W.; Jackson, T. A., *Dalton Trans.* **2015,** *44*, 3295-3306, by permission of The Royal Society of Chemistry.

5.1 Introduction

Manganese-dependent enzymes that mediate proton coupled electron transfer (PCET) reactions perform vital processes in humans and numerous other organisms.[1] PCET reactivity within the tetranuclear manganese active site of the oxygen evolving complex (OEC) of photosystem II represents a classic example. This active-site cluster consists of a Mn_3CaO_4 cubane with a dangler Mn atom linked to the cubane through bridging ligands.[2] In a more recent structure, a portion of the cluster is capped with four terminal water ligands.[2] During the oxidation of the OEC from its least oxidized S_0 state to the most oxidized S_4 state, coordinated water molecules within the cluster have been proposed to be deprotonated as a part of sequential PCET processes, producing reducing equivalents. [2-6] In light of this proposal, as well as numerous other biological examples of metal-mediated PCET,[7,8] model complexes that can facilitate PCET have been extensively studied to understand the thermodynamics and kinetics of these processes.[9-17]

In general, PCET reactions can be categorized as concerted or sequential, based on whether the proton and electron are being transferred in a single step or multiple steps, respectively.[18] Single-step processes where the proton and electron share the same orbital/bond following the reaction are often referred to as hydrogen atom ($H^{\bullet} = H^{+} + e^{-}$) transfer (HAT) reactions. This is a common reaction in organic chemistry, and has been the subject of numerous detailed studies over the past century.[13] On the other hand, when transition metal complexes are involved, most often the proton and electron are transferred to separate entities (*i.e.* a ligand and the metal), and no longer share the same bond. These metal-mediated PCET reactions can also occur either in a single (concerted proton-electron transfer; CPET) or multiple (proton transfer followed by electron transfer or *vice versa*; PT/ET or ET/PT) kinetic steps.[19] Synthetic transition

metal complexes that can facilitate PCET reactions are of great interest not only because they mimic metalloenzyme reactions, but also because PCET is central to many industrial processes.[1] Recently, more work has been focused on developing PCET mediators using greener, less expensive metals, such as high-valent and mid-valent manganese and iron complexes.[20-29] High-valent (M^{IV} or M^{V}; M = Mn or Fe) oxidants, typically containing terminal oxo ligands, have been the subject of a large number of studies, as these exhibit efficient reactivity with stronger, unactivated C–H or O–H bonds.[20-24] In contrast, only several examples of mid-valent metal (M^{III}) oxidants have been reported to-date,[25-29] although these compounds exhibit unique reactivity patterns that can be used to gain detailed understanding into the fundamental thermodynamic and kinetic parameters that govern PCET reactions. Among the mid-valent oxidants reported, M^{III}–OR (M = Mn or Fe; R = H, CH_3, Ph) species are the most common. In PCET reactions with M^{III}–OR species, M^{II}–O(H)R is generated as the final metal based product (Scheme 5.1).

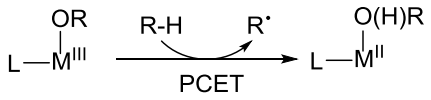

Scheme 5.1. PCET reactivity of a mid-valent oxidant (M^{III}–OR) with an $H^{\bullet}$ donor substrate (R–H, where R is C or O).

The principal thermodynamic parameters controlling PCET reactivity are the reduction potential of the oxidized metal center (E^{o}) and the acidity of the reduced product (*i.e.*, the pK_a of the M^{II}–O(H)R species).[13] The relationship between these values and the free energy change of the reaction (ΔG) is described by the Bordwell relationship ($\Delta G^{o} = -23.06E^{o} - 1.37pK_a - C$).[10,30] This relationship can, in principle, be applied to the design of better oxidants as both the reduction potential and pK_a parameters are tunable by the ligand framework. E^{o} can be controlled

through the electronic properties of the supporting and –OR ligands and the pK_a results from a combination of supporting ligand effects and intrinsic properties of the M^{II}–O(H)R group. In this regard, variation of the R group of mid-valent M–OR oxidants has the potential to tune PCET reactivity by a means unavailable for high-valent M=O species. However, given the limited examples of mid-valent M–OR oxidants with different R groups,[25,27,28] it is difficult to elaborate broadly on how ligand properties affect the thermodynamic and kinetic properties of the oxidant, and how these can be modified to design better PCET mediators.

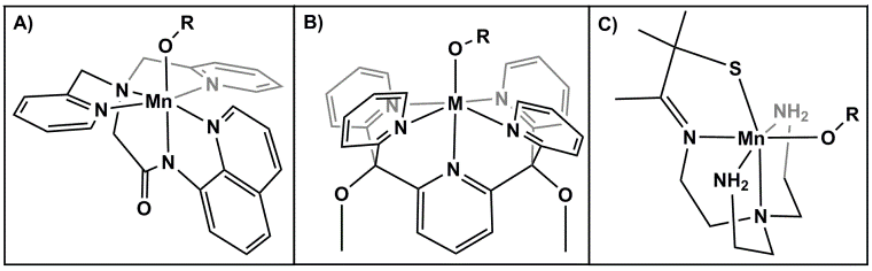

Figure 5.1. Representative Structures for PCET Mediating M^{III}–OR Adducts of A) $[Mn^{III}(OR)(dpaq)]^+$,[29] B) $[M^{III}(OR)(PY5)]^+$,[26] and C) $[Mn^{III}(OR)(S^{Me2}N_4(tren))]^+$ [25] series of complexes.

Current examples of PCET-mediating M^{III}–OR complexes with multiple R groups are found in the $[Mn^{III}(OH)(S^{Me2}N_4(tren))]^+$ and $[Mn^{III}(OMe)(S^{Me2}N_4(tren))]^+$ complexes of Kovacs and co-workers ($S^{Me2}N_4$(tren) = 3-((2-(bis(2-aminoethyl)amino)ethyl)imino)-2-methylbutane-2-thiolate),[25] and the $[M^{III}(OH)(PY5)]^{2+}$ and $[M^{III}(OMe)(PY5)]^{2+}$ complexes of Stack and Goldsmith (M = Mn and Fe; PY5 = 2,6-bis(bis(2-pyridyl)methoxymethane)pyridine) (Figure 5.1).[26-28] The change in thermodynamic properties as a function of the –OR group can be clearly seen in the experimental E^o values of the $[Mn^{III}(OR)(S^{Me2}N_4(tren))]^+$ series (Figure 5.1; R = H, –OMe, –OPh and $-OPh^{p\text{-}NO_2}$).[25] The $[Mn^{III}(OPh^{p\text{-}NO_2})(S^{Me2}N_4(tren))]^+$ complex, with the most electron-withdrawing $-OPh^{p\text{-}NO_2}$ ligand, displayed the highest E^o along with the lowest pK_a. In

contrast, $[Mn^{III}(OH)(S^{Me2}N_4(tren))]^+$, with one of the most electron-donating –OR ligands, showed the lowest E^o and highest pK_a.[25] Thus, in this series, E^o and pK_a display an inverse correlation. As a net result, only $[Mn^{III}(OH)(S^{Me2}N_4(tren))]^+$ and $[Mn^{III}(OMe)(S^{Me2}N_4(tren))]^+$ showed the ability to oxidize the weak O–H bond of TEMPOH, with similar second-order rate constants of 2.1×10^3 M^{-1} s^{-1} and 3.6×10^2 M^{-1} s^{-1}, respectively. The other two Mn^{III}–OR species with the most electron-withdrawing –OR ligands were inert toward TEMPOH. Therefore, it was concluded that under similar entropic factors, the more electron-withdrawing $[Mn^{III}(OPh^{p\text{-}NO_2})(S^{Me2}N_4(tren))]^+$ and $[Mn^{III}(OPh)(S^{Me2}N_4(tren))]^+$ did not have a sufficiently large E^o to overcome the substantially small pK_a to provide the requisite driving force for PCET.[25] In the Mn^{III} and Fe^{III} complexes of Stack and Goldsmith (Figure 5.1), interesting trends are evident when comparing the Mn versus Fe complexes, where $[Mn^{III}(OH)(PY5)]^{2+}$ was found to be the overall best oxidant of the series, with the highest E^o and pK_a.[28]

This present work describes the formation and PCET reactivity of the new complex $[Mn^{III}(OMe)(dpaq)]^+$, which is formed in quantitative yields when $[Mn^{II}(dpaq)]^+$ is reacted with dioxygen in methanol at 25 ^oC. The $[Mn^{III}(OMe)(dpaq)]^+$ complex reacts with TEMPOH and with phenolic substrates with O–H bond free energies up to 78.5 kcal/mol, and represents the only example of a monomeric Mn^{III}–OMe species that can activate phenolic O–H bonds. In contrast to that observed for the recently reported $[Mn^{III}(OH)(dpaq)]^+$ complex (Figure 5.1),[29] phenol oxidation by $[Mn^{III}(OMe)(dpaq)]^+$ does not show saturation behavior at high phenol concentrations, suggesting the absence of an accumulating intermediate. However, mechanistic studies suggest that $[Mn^{III}(OMe)(dpaq)]^+$ activates substrate O–H bonds by a CPET process. In light of the reactivity of $[Mn^{III}(OMe)(dpaq)]^+$ and other mid-valent Mn oxidants, a detailed discussion of thermodynamic and kinetic parameters dictating the feasibility of PCET is

presented, and we discuss characteristic differences in the oxidative reactivity of mid-valent versus high-valent oxidants.

5.2. Experimental

All procedures, including the generation of organic substrates and kinetic experiments, were carried out under an argon atmosphere, unless otherwise stated. Acetonitrile, methanol and ether were degassed and dried using a Pure Solv Micro (2010) solvent purification system. These solvents were degassed in air-tight solvent reservoirs (4 L) by bubbling Ar gas through the solvent for 20 min at room temperature. Acetonitrile and ether were dried using air-tight alumina columns, and methanol was dried using a drierite column. Anhydrous dichloromethane was purchased from Acros Organics (99.9% purity) and was degassed by four freeze-pump-thaw cycles using Schlenk techniques. All solvents were taken into an argon-filled glovebox immediately after dispensing from the solvent purification system, or following the freeze-pump-thaw cycles, and were stored in tightly-sealed Schlenk glassware. The purity of O_2 gas used was >99% and was further purified by passage through drierite and 5 Å molecular sieves prior to use. The amide-containing N_5 ligand H-dpaq, [Mn^{II}(dpaq)](OTf), and [Mn^{III}(OH)(dpaq)](OTf) were synthesized according to previously reported methods.[29,31] TEMPOH and TEMPOD were also prepared according to literature procedures,[9,32] and >99% deuteration of TEMPOD was confirmed by ^{1}H NMR experiments. All phenols, with >99% purity, were purchased from commercial sources.

5.2.1. Preparation of [Mn^{III}(OMe)(dpaq)](OTf) from [Mn^{II}(dpaq)](OTf) and Dioxygen. [Mn^{III}(OMe)(dpaq)](OTf) was generated by reacting a 2.5 mM [Mn^{II}(dpaq)](OTf) solution in MeOH with excess O_2 gas at room temperature. The formation of

[Mn^{III}(OMe)(dpaq)](OTf) was monitored by electronic absorption spectroscopy, as it has characteristic features at 510 and 760 nm. These features show no significant shifts in terms of their energies when compared to [Mn^{III}(OH)(dpaq)](OTf) but are more defined for [Mn^{III}(OMe)(dpaq)](OTf) in methanol. In addition, a solvent-dependent broadening of the absorption features of [Mn^{III}(OMe)(dpaq)](OTf) was observed for spectra collected in MeCN. A representative formation reaction is as follows. A 2.5 mM [Mn^{II}(dpaq)](OTf) solution (2.9 mg in 2 mL of MeOH) was prepared under an inert atmosphere and transferred to a gas-tight cuvette sealed with a pierceable septum. An excess of O_2 gas was then delivered to the solution by means of a syringe, and the formation of [Mn^{III}(OMe)(dpaq)](OTf) was monitored by electronic absorption spectroscopy. The formation was complete in ~4000 min and the resulting dark red solution was evaporated to dryness under reduced pressure. The solid residue was then recrystallized using MeOH/ Et_2O (3.0 mg/ 98% yield). [Mn^{III}(OMe)(dpaq)](OTf) was further characterized by ESI-MS and magnetic susceptibility. ESI-MS: {[Mn^{III}(OMe)(dpaq)]$^+$} *m/z* = 468.1219 (calc. 468.1232; Figure A4.1). The solution phase magnetic susceptibly found was 5.5 μ_B (at 25 °C in CD_3CN; Diam. Corr. = 0.8), which is comparable well with the expected μ_{eff} = 4.9 μ_B for a monomeric high-spin d^4 system.[25] Cyclic voltammetry of [Mn^{III}(OMe)(dpaq)](OTf) was recorded in MeCN (12.4 mg in 10 mL) at 25 °C under an argon atmosphere. A 0.1 M $Bu_4N(PF_6)$ solution was used as the supporting electrolyte along with a glassy carbon working electrode, platinum auxiliary electrode and a AgCl/Ag reference electrode. Elemental analysis [Mn^{III}(OMe)(dpaq)](OTf) • 0.3 H_2O : $C_{25}H_{23.6}F_3MnN_5O_{5.3}S$ calc. (%): C 48.21, H 3.82, N 11.24; found (%): C 47.78, H 3.38, N 11.25.

5.2.2. Preparation of [Mn^{III}(OMe)(dpaq)](OTf) from [Mn^{III}(OH)(dpaq)](OTf). A 2.5 mM solution of [Mn^{III}(OH)(dpaq)](OTf) (3.2 mg in 2 mL) was prepared as previously

described,[29] and the solvent was removed under reduced pressure. The solid residue was stirred in MeOH for 10 min. The final solution color was deep red. The electronic absorption spectrum and ESI-MS of this solution are identical to that of $[Mn^{III}(OMe)(dpaq)](OTf)$. This solution was then evaporated to dryness under reduced pressure and recrystallized using MeOH/ Et_2O. The final product was isolated as a solid in excellent yield (>98%). The resulting $[Mn^{III}(OMe)(dpaq)](OTf)$ complex is quantitatively converted back to $[Mn^{III}(OH)(dpaq)](OTf)$ (>98%) when dissolved in H_2O, as observed by ESI-MS experiments. Prominent ion peak in the mass spectrum of the resultant aqueous solution corresponds to *m/z* = 454.0902, as expected for $[Mn^{III}(OH)(dpaq)]^+$ (calc. *m/z* = 454.1076; Figure A4.1).

5.2.3. X-ray diffraction data collection and analysis for $[Mn^{III}(OMe)(dpaq)](OTf)$. Synthesis of $[Mn^{III}(OMe)(dpaq)](OTf)$ on a large scale to obtain suitable material for X-ray crystallographic and kinetic experiments was carried out starting from $[Mn^{III}(OH)(dpaq)](OTf)$. In this procedure, $[Mn^{III}(OH)(dpaq)](OTf)$ (20 mg in 5 mL) was dissolved in MeOH and was stirred for 10 min. The conversion of $[Mn^{III}(OH)(dpaq)](OTf)$ to $[Mn^{III}(OMe)(dpaq)](OTf)$ was monitored by ESI-MS and electronic absorption spectroscopy. Upon complete conversion, the resulting solution was evaporated to dryness under reduced pressure, and the solid residue was repeatedly recrystallized by vapor diffusion using MeOH and Et_2O under ambient conditions. Red racemically-twinned crystals of the partially hydrated salt, $[Mn(OCH_3)(C_{23}H_{20}N_5O)][CF_3SO_3]_2$, (1) are, at 100(2) K, orthorhombic, space group $Pna2_1 - C_{2v}^9$ (No. 33)[33] with a = 13.6388(4) Å, b = 26.1547(7) Å, c = 15.1412(4) Å, V = 5401.1(3) $Å^3$ and Z = 8 $[Mn(OCH_3)(C_{23}H_{20}N_5O)][CF_3SO_3] \bullet 0.37\ H_2O$ formula units (d_{calcd} = 1.533 g/cm^3; $\mu_a(CuK\alpha)$ = 5.306 mm^{-1}). A full set of unique diffracted intensities (5238 frames with counting times of 2 to 5 seconds and an ω- or ϕ-scan width of 0.50°) was measured[34] for a single-domain specimen

using monochromated CuKα radiation (λ= 1.54178 Å) on a Bruker Proteum Single Crystal Diffraction System equipped with Helios multilayer optics, an APEX II CCD detector and a Bruker MicroSTAR microfocus rotating anode X-ray source operating at 45 kV and 60 mA. Lattice constants were determined with the Bruker SAINT software package using peak centers for 9745 reflections. A total of 50470 integrated reflection intensities having 2θ(CuKα)< 140.02° were produced using the Bruker program SAINT;[35] 8511 of these were unique and gave R_{int} = 0.025. The data were corrected empirically for variable absorption effects using equivalent reflections; the relative transmission factors ranged from 0.715 to 1.000. The Bruker software package SHELXTL was used to solve the structure using "direct methods" techniques. All stages of weighted full-matrix least-squares refinement were conducted using F_o^2 data with the SHELXTL Version 2010.3-0 software package.[36]

The asymmetric unit contains two cationic metal complexes, two anions, and a water molecule of crystallization. A substantial portion of the structure is disordered. The quinoline ring for the second metal complex is 56%/44% disordered with two slightly different orientations in the crystal. Mild restraints were eventually applied to the anisotropic thermal parameters for 13 of the disordered quinoline nonhydrogen atoms. The nonhydrogen bond lengths and angles for both orientations were restrained to have values similar to those for the quinoline ring of the first metal complex. *This disorder produces slightly elongated or flattened anisotropic thermal ellipsoids for atoms in these quinoline ligands.* The second triflate anion is also disordered with two slightly different (58%/42%) orientations and the water solvent molecule of crystallization is present only 74% of the time. Both orientations for the second (disordered) triflate anion were restrained to have bond lengths and angles similar to the first (ordered) triflate.

The final structural model incorporated anisotropic thermal parameters for all nonhydrogen atoms of both metal complexes and the ordered triflate as well as the water oxygen atom and the sulfur atoms for both orientations of the disordered triflate. All other nonhydrogen atoms were incorporated into the structural model with isotropic thermal parameters. The hydrogen atoms for the metal complexes were included in the structural model at idealized positions (sp^2- or sp^3-hybridized geometry and C–H bond lengths of 0.95 – 0.99 Å). The methoxy methyl groups were incorporated in the structural model as rigid groups (using idealized sp^3-hybridized geometry and C–H bond lengths of 0.98 Å) with idealized "staggered" geometry. The hydrogen atoms were assigned fixed isotropic thermal parameters with values 1.20 (nonmethyl) and 1.50 (methyl) times the equivalent isotropic thermal parameter of the carbon atom to which they are bonded.

A total of 826 parameters were refined using 211 restraints, 8511 data and weights of $w = 1/ [\sigma^2(F^2) + (0.1429\ P)^2 + (13.9982\ P)]$, where $P = [F_O^2 + 2F_C^2] / 3$. Final agreement factors at convergence for $[Mn(OCH_3)(C_{23}H_{20}N_5O)][CF_3SO_3] \bullet 0.37\ H_2O$ are: R_1(unweighted, based on F) = 0.075 for 8385 independent absorption-corrected "observed" reflections having $2\theta(CuK\alpha) < 140.02°$ and $I > 2\sigma(I)$; R_1(unweighted, based on F) = 0.076 and wR_2(weighted, based on F^2) = 0.213 for all 8511 independent absorption-corrected reflections having $2\theta(CuK\alpha) < 140.02°$. The largest shift/s.u. was 0.004 in the final refinement cycle. The final difference map had maxima and minima of 1.18 and -0.77 $e^-/Å^3$, respectively.

5.2.4. Kinetic Studies of $[Mn^{III}(OMe)(dpaq)](OTf)$ with Substituted Phenols. For each kinetic experiment, a 1.25 mM $[Mn^{III}(OMe)(dpaq)]^+$ (1.5 mg, 2.5×10^{-3} mmol) solution was prepared in acetonitrile (2 mL) within an argon-filled glovebox, transferred to a gas-tight cuvette sealed with a pierceable septum. Solutions of phenolic substrate were prepared in

dichloromethane (300 μL) and sealed in a 4 mL glass vial with a pierceable septum. Then, the cuvette containing the $[Mn^{III}(OMe)(dpaq)]^+$ solution was inserted into a temperature-controlled cryostat (Unisoku), held at 50 °C, coupled to an Agilent 8453 UV/Visible spectrophotometer. Upon achieving thermal equilibrium (10 min), data collection was started, and 100 μL of the substrate solution was injected into the cuvette using a gas-tight syringe. Data collection times ranged from 300 to 6000 s. An aliquot of the final reaction mixture was analyzed by electron paramagnetic resonance (EPR) spectroscopy at 5 K. The rates of the reactions were calculated by applying the initial rate approximation in order to prevent any interference by side reactions at longer time scales. These initial rates (in absorbance units / time) were converted into s^{-1} units by using the extinction coefficient (ε_{800} = 130 M^{-1} cm^{-1}) and initial concentration (1.25 mM) of $[Mn^{III}(OMe)(dpaq)]^+$. For reactions involving the 2,4,6-tri-*t*-butylphenol, the kinetic data were collected to five half-lives and fit directly to obtain a pseudo-first-order rate constant. In these cases, the directly obtained pseudo-first-order rate constants were identical, within error, to those obtained using the initial rate method. The rates of reactions involving 4-methoxy-2,6-di-*t*-butylphenol as the substrate were directly fit to obtain pseudo-first-order rate constants as they were significantly faster (data collection times 300 – 3000 s), and the data exhibited pseudo-first-order behavior up to at least five half-lives.

5.2.5. Kinetic Studies of $[Mn^{III}(OMe)(dpaq)](OTf)$ with TEMPOH(D). Similar to the kinetic experiments with phenols, a 1.25 mM $[Mn^{III}(OMe)(dpaq)]^+$ (1.5 mg, 2.5 × 10^{-3} mmol) solution was prepared in acetonitrile (2 mL) within an argon-filled glovebox, and was sealed in a gas-tight cuvette with a pierceable septum. The TEMPOH (or TEMPOD) solution was prepared in acetonitrile (100 μL) and sealed in a 300 μL glass vial with a pierceable septum. Data collection was started, and the TEMPOH (or TEMPOD) solution was added into the

$[Mn^{III}(OMe)(dpaq)]^+$ solution using a gas-tight syringe. Data collection times ranged from 300 to 4000 s. Kinetic experiments at variable temperatures (-15 to 50 ºC) were performed following the same procedure as described, allowing the cuvette to achieve thermal equilibrium (10 min) in the cryostat, prior to the addition of the substrate. In order to confirm that substrate isotopic scrambling (*i.e.*, exchange of deuterium in TEMPOD with hydrogen due to trace H_2O) does not affect the H/D KIE, kinetic experiments were also performed where TEMPOD was dissolved in 1:1 MeCN:MeOD. The rates of reactions with added MeOD were identical, within error, to those without added MeOD (6.50(7) × 10^{-3} s^{-1} and 6.45(7) × 10^{-3} s^{-1}, respectively, for 100 equiv. of TEMPOD). All reactions involving TEMPOH (or TEMPOD) followed pseudo-first-order behaviour up to at least five half-lives.

5.3. Results and Analysis

5.3.1. Formation of $[Mn^{III}(OMe)(dpaq)](OTf)$ from Dioxygen. When treated with excess O_2 gas at 25 ºC, the light orange colored methanol solution of $[Mn^{II}(dpaq)](OTf)$ slowly changed its color to dark red, as new absorption features grew in at 510 (ε = 328 M^{-1} cm^{-1}) and 760 nm (ε = 130 M^{-1} cm^{-1}) (Figure 5.2; the extinction coefficients were obtained using recrystallized $[Mn^{III}(OMe)(dpaq)](OTf)$). These changes in the electronic absorption spectrum are consistent with the oxidation of the Mn^{II} center upon reacting with O_2. The final product of the oxygenation reaction, $[Mn^{III}(OMe)(dpaq)](OTf)$, was isolated in an essentially quantitative yield of greater than 98%. The formation of $[Mn^{III}(OMe)(dpaq)](OTf)$ from the oxygenation of a 2.5 mM $[Mn^{II}(dpaq)](OTf)$ solution in methanol took over 33 hours to approach completion (Figure 5.2), which is significantly longer than that of the same reaction in MeCN (~40 min; see reference 29). A half-life ($t_{1/2}$) of 26 days was estimated for $[Mn^{III}(OMe)(dpaq)](OTf)$ by

monitoring the electronic absorption spectrum of a 1.25 mM acetonitrile solution at 25 ºC. This is identical to the half-life observed previously for [Mn^{III}(OH)(dpaq)](OTf) under the same conditions.[29] At 50 ºC, the same concentration of [Mn^{III}(OMe)(dpaq)](OTf) in MeCN has an appreciable self-decay rate of 2.5(2) × 10^{-5} s^{-1} at 50 ºC, which corresponds to a half-life of 7.5(2) hours. [Mn^{III}(OH)(dpaq)](OTf) showed essentially no decay at 50 ºC in MeCN.

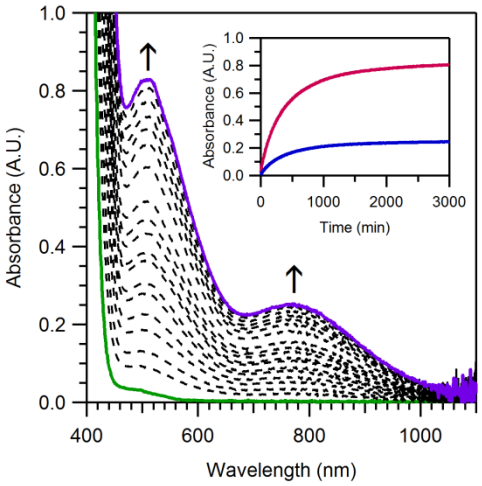

Figure 5.2. Electronic absorption spectra of 2.5 mM [Mn^{II}(dpaq)]$^+$ (solid green trace) upon the addition of excess O_2 at 25 ºC in MeOH under argon. Inset: Time evolution of absorption signals at 510 and 760 nm from data collected every 5 min.

5.3.2. Structural and Physical Properties of [Mn^{III}(OMe)(dpaq)](OTf). The X-ray structure of [Mn^{III}(OMe)(dpaq)](OTf) shows a six-coordinate Mn^{III} center with a distorted octahedral geometry (Figure 5.3), with the anionic amide ligand *trans* to the methoxide group. There are two molecules of [Mn^{III}(OMe)(dpaq)](OTf) within the asymmetric unit with very similar metric parameters; the metric parameters for the two cationic units are in Table 5.1 and A4.2. The structure of [Mn^{III}(OMe)(dpaq)](OTf) is virtually identical to that of the previously reported [Mn^{III}(OH)(dpaq)](OTf) complex.[29] Most Mn–N distances are statistically indistinguishable from those of [Mn^{III}(OH)(dpaq)](OTf), with the exception of the Mn–N4

distance, which is shorter in [Mn^{III}(OMe)(dpaq)](OTf) (2.203(6) and 2.154(7) Å in the two cations) than in [Mn^{III}(OH)(dpaq)](OTf) (2.260(14) Å). The methoxide group in [Mn^{III}(OMe)(dpaq)](OTf) has Mn–O2 distances of 1.825(4) and 1.814(5) Å (Tables 5.1 and A4.2), comparable to those of other Mn^{III}–OMe distances reported in literature (1.836(5) and 1.814(7)).[25,37] Two triflate ions and a water molecule are observed within the asymmetric unit as well but are not associated with the Mn centers (Mn–O(triflate) distances of 6.397 and 6.936 Å, and Mn–O(water) distances of 4.760 and 8.604 Å).

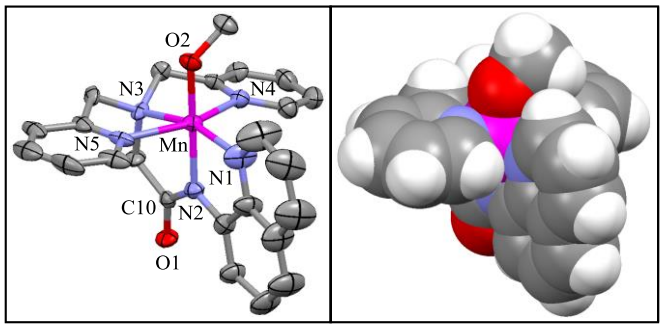

Figure 5.3. ORTEP (left) and space filling (right) diagrams of [Mn^{III}(OMe)(dpaq)](OTf). ORTEP diagram shows 50% probability thermal ellipsoids. Hydrogen atoms, non-coordinating triflate counteranions and the water molecule have been removed for clarity. Significant interatomic distances and angles are listed in Table 5.1.

Table 5.1. Bond Lengths and Angles for One of the Two [Mn^{III}(OMe)(dpaq)]$^{+}$ Cations in the Asymmetric Unit.[a]

[Mn^{III}(OMe)(dpaq)]$^{+}$ (A)			
Mn–O2	1.825(4)	O2–Mn–N2	177.9(3)
Mn–N2	1.979(5)	N4–Mn–N5	154.8(2)
Mn–N1	2.051(5)	N1–Mn–N3	161.7(2)
Mn–N3	2.175(5)	N4–Mn–N2	87.8(2)
Mn–N4	2.203(6)	N1–Mn–N2	80.0(2)
Mn–N5	2.212(6)	N3–Mn–N2	81.8(2)

[a] Corresponding Metric Parameters for the Other Cation are in Table A4.2.

Cyclic voltammetric studies of $[Mn^{III}(OMe)(dpaq)]^+$ were performed in MeCN, and revealed an irreversible Mn^{III}/Mn^{II} couple at a cathodic peak potential ($E_{p,c}$) of -0.88 V vs Fc^+/Fc at a scan rate of 100 mV s^{-1} at 25 °C (Figure A4.2). Although it is unwise to make strong comparisons of this irreversible reduction wave with the reversible or partially-reversible processes observed for the Mn^{III}/Mn^{II} couple of other mid-valent oxidants, including $[Mn^{III}(OH)(dpaq)]^+$, it is interesting that the $E_{p,c}$ of $[Mn^{III}(OMe)(dpaq)]^+$ is 0.22 V lower than the corresponding $E_{p,c}$ of $[Mn^{III}(OH)(dpaq)]^+$. The smaller reduction potential observed for $[Mn^{III}(OMe)(dpaq)]^+$ compared to $[Mn^{III}(OH)(dpaq)]^+$ is in contrast with the trend observed for several other M^{III}–OR oxidants,[25,27,28] but is consistent with the milder oxidizing ability of $[Mn^{III}(OMe)(dpaq)]^+$ (*vide infra*). In addition, in an electrochemical study of Mn^{III}–OR complexes supported by a phenolate-containing N_4O^- ligand reported by Anxolabéhère-Mallart and co-workers, a slightly lower irreversible reduction potential was observed for the Mn^{III}–OMe complex compared to the analogous Mn^{III}–OH species.[37]

Separate frozen samples of 2 mM $[Mn^{III}(OMe)(dpaq)]^+$ in MeCN and 1:1 ethanol:methanol (the latter of which is a glassing solvent) were analyzed by EPR spectroscopy at 5 K. Neither sample showed features in either perpendicular or parallel modes. This is consistent with a monomeric Mn^{III} complex with a moderate to large zero-field splitting.

5.3.3. Reactivity of $[Mn^{III}(OMe)(dpaq)]^+$ with TEMPOH.

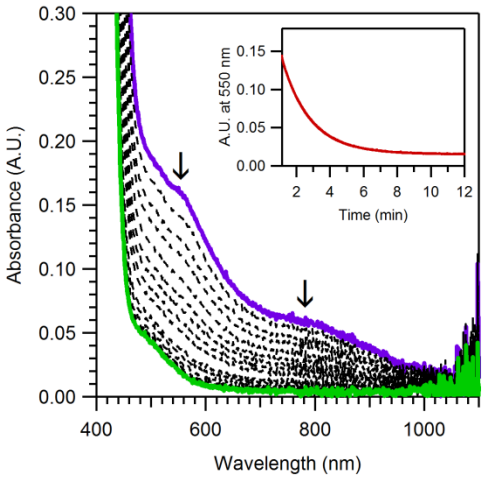

Figure 5.4. Electronic absorption spectra of 1.25 mM $[Mn^{III}(OMe)(dpaq)]^+$ upon the addition of 100 equiv. TEMPOH at 25 ºC in MeCN under argon. Inset: Decay of the 550 nm absorption signal from data collected every 0.3 s. The electronic absorption bands of $[Mn^{III}(OMe)(dpaq)]^+$ are broadened in MeCN as compared to data collected for a sample in MeOH (see Fig. 5.2)

The PCET reactivity of $[Mn^{III}(OMe)(dpaq)]^+$ was investigated using TEMPOH as the substrate to permit comparison with other Mn^{III}–OR oxidants.[25,29] Treatment of $[Mn^{III}(OMe)(dpaq)]^+$ with 100 equiv. of TEMPOH under an argon atmosphere in MeCN at 25 ºC lead to the rapid disappearance of the electronic absorption bands of $[Mn^{III}(OMe)(dpaq)]^+$ (Figure 5.4). The final electronic absorption spectrum appears essentially identical to that of $[Mn^{II}(dpaq)](OTf)$ dissolved in MeCN, showing a very weak band at 510 nm. Using the intensity and the extinction coefficient of this band, the final yield of $[Mn^{II}(dpaq)]^+$ was calculated to be over 99%. The X-band EPR spectrum (perpendicular-mode) of the final reaction mixture at 5 K shows an intense feature centered at g = 2.04 that is characteristic of the TEMPO radical (Figure A4.3). Together these data demonstrate that the reaction between TEMPOH and $[Mn^{III}(OMe)(dpaq)]^+$ approaches completion under these conditions, generating TEMPO radical and $[Mn^{II}(MeOH)(dpaq)]^+$.

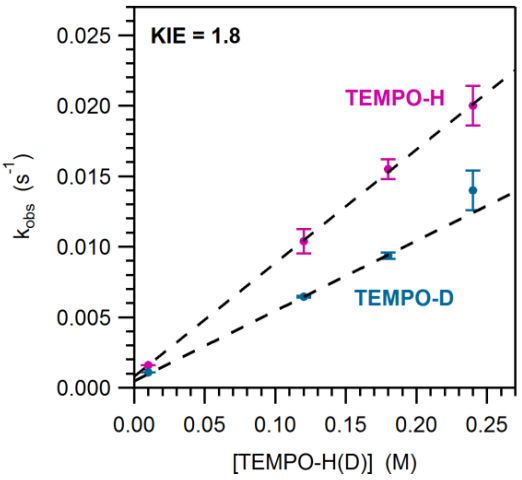

Figure 5.5. Pseudo-first order rate constants, k_{obs} (s^{-1}) versus TEMPOH and TEMPOD concentration for a 1.25 mM solution of $[Mn^{III}(OMe)(dpaq)]^+$ at 25 ºC. The second-order rate constant, k_2 ($M^{-1}s^{-1}$), was calculated from the linear correlation of the observed rate constant and substrate concentration.

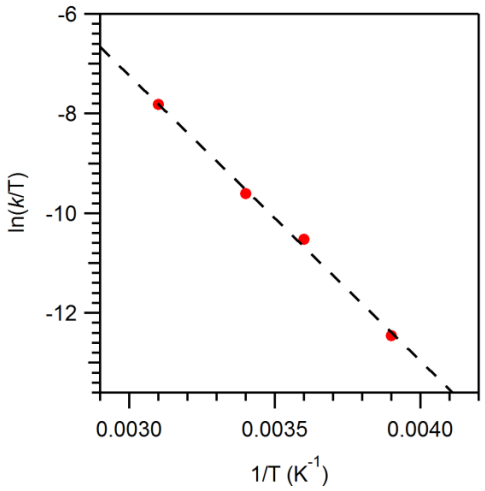

Figure 5.6. Eyring plot showing ln(k/T) versus 1/T (K^{-1}) for the reaction of 1.25 mM $[Mn^{III}(OMe)(dpaq)]^+$ with TEMPOH from -15 to 50 ºC (258 to 323 K).

The reaction of $[Mn^{III}(OMe)(dpaq)]^+$ and TEMPOH was studied over a range of TEMPOH concentrations (10 – 200 equiv. with respect to initial $[Mn^{III}(OMe)(dpaq)]^+$ concentration), and the pseudo-first-order rate constants were observed to increase linearly with

the concentration of TEMPOH (Figure 5.5). In all cases, the disappearance of $[Mn^{III}(OMe)(dpaq)]^+$ showed pseudo-first-order behavior up to at least five half-lives. A second-order rate constant of 8.0(1) × 10^{-2} M^{-1} s^{-1} was calculated based on these data, which is slightly lower than the rate observed for TEMPOH oxidation by $[Mn^{III}(OH)(dpaq)]^+$ (1.3(1) × 10^{-1} M^{-1} s^{-1}). Using the deuterated substrate, TEMPOD, a KIE of 1.8 was calculated for this PCET process, which suggests a rate-limiting O–H/D bond breaking step. Given the exceptionally high pK_a of TEMPOH in MeCN (pK_a = 41),[7] and the highly negative reduction potential of $[Mn^{III}(OMe)(dpaq)]^+$, these results are consistent with a rate-limiting CPET reaction. An Eyring analysis of the reaction between $[Mn^{III}(OMe)(dpaq)]^+$ and TEMPOH from -15 to 50 ºC (258 to 323 K) yielded activation parameters $\Delta H^{\neq}$ and $\Delta S^{\neq}$ of 11.4(5) kcal/mol and -27(2) cal/mol K, respectively (Figure 5.6).

5.3.4. Reactivity of $[Mn^{III}(OMe)(dpaq)]^+$ with Phenols. $[Mn^{III}(OMe)(dpaq)]^+$ also reacted with 2,4,6-tri-*t*-butylphenol ($^{4\text{-}t\text{-butyl}}$ArOH) in MeCN at 50 ºC. The formation of the corresponding phenoxyl radical (λ_{max} = 628 nm; ϵ = 400(10) M^{-1} cm^{-1} in MeCN[38] at 25 ºC; see Figure 5.7) and the decay of $[Mn^{III}(OMe)(dpaq)]^+$ were concomitant, which suggests the absence of secondary reactions involving $[Mn^{III}(OMe)(dpaq)]^+$ and the radical. The phenoxyl radical was formed in ~75% yield relative to the initial $[Mn^{III}(OMe)(dpaq)]^+$ concentration, a yield similar to that previously reported for the reaction of $^{4\text{-}t\text{-butyl}}$ArOH with $[Mn^{III}(OH)(dpaq)]^+$.[29] The perpendicular-mode X-band EPR spectrum of the final products of $^{4\text{-}t\text{-butyl}}$ArOH oxidation provide evidence for the formation of the phenoxyl radical (Figure A4.3). The ~75% yield of the phenoxyl radical was observed regardless of the initial $[Mn^{III}(OMe)(dpaq)]^+$: $^{4\text{-}t\text{-butyl}}$ArOH ratio (Table A4.3).

When $[Mn^{III}(OMe)(dpaq)]^+$ was treated with an excess of $^{4\text{-}t\text{-butyl}}$ArOH (10 – 125 equiv.) in MeCN, the decay of $[Mn^{III}(OMe)(dpaq)]^+$ and the formation of $^{4\text{-}t\text{-butyl}}ArO^\bullet$ followed pseudo-first-order kinetics up to at least three half-lives. $[Mn^{III}(OMe)(dpaq)]^+$ exhibited linear dependence of the rate of the reaction (k_{obs}) on phenol concentration up to 0.15 M $^{4\text{-}t\text{-butyl}}$ArOH (Figure 5.8). The second order rate constant found from these data is $5.2(1) \times 10^{-3}$ M^{-1} s^{-1}. The y-intercept of the linear fit of k_{obs} versus [$^{4\text{-}t\text{-butyl}}$ArOH] corresponds to a self-decay rate of $3.3(1) \times 10^{-5}$ s^{-1}, which is in good agreement with the observed self-decay rate of $[Mn^{III}(OMe)(dpaq)]^+$ of 2.5×10^{-5} s^{-1} in MeCN at 50ºC (*vide supra*).

The lack of rate saturation at high phenol concentrations is suggestive of a single-step reaction with no accumulating intermediates from a pre-equilibrium step. In addition, oxidation of $^{4\text{-}t\text{-butyl}}$ArOH by $[Mn^{III}(OMe)(dpaq)]^+$ in MeOH, instead of MeCN, at 50 ºC shows a linear correlation between k_{obs} and [$^{4\text{-}t\text{-butyl}}$ArOH] as well, with a second order rate constant of $3.7(1) \times 10^{-3}$ M^{-1} s^{-1} (Figure A4.4). The observation of similar rates in both protic and non-protic solvents for oxidation of the same substrate suggests the absence of charged intermediates during the course of the reaction.[27] Thus, the similar rates in MeOH and MeCN are supportive of a single step CPET process rather than a stepwise PCET, where the proton and electron transfer occur in separate kinetic steps.

To further investigate the mechanism of phenol oxidation, we explored the reactivity of $[Mn^{III}(OMe)(dpaq)]^+$ with other phenolic substrates, including 4-methoxy-2,6-di-*t*-butylphenol ($^{4\text{-MeO}}$ArOH), 4-methyl-2,6-di-*t*-butylphenol ($^{4\text{-Me}}$ArOH), 2,6-di-*t*-butylphenol ($^{4\text{-H}}$ArOH), and 4-cyano-2,6-di-*t*-butylphenol ($^{4\text{-CN}}$ArOH). A linear dependence between the oxidation rate and the O–H bond strength would provide stronger evidence for a CPET process for phenolic O–H oxidation by $[Mn^{III}(OMe)(dpaq)]^+$. With the exception of $^{4\text{-CN}}$ArOH, all of the phenols reacted

with $[Mn^{III}(OMe)(dpaq)]^+$ to give phenoxyl radicals and Mn^{II} species, and in each case, a linear dependence between the rate of the reaction and the substrate concentration was observed (Figure A4.5). The second order rate constants calculated from these kinetic data are collected in Table 5.2. In the reaction of $[Mn^{III}(OMe)(dpaq)]^+$ with $^{4\text{-CN}}$ArOH (BDFE = 79 kcal/mol), the reaction did not approach completion, implying that the thermodynamic limit of the O–H bond oxidation by $[Mn^{III}(OMe)(dpaq)]^+$ lies around 79 kcal/mol.

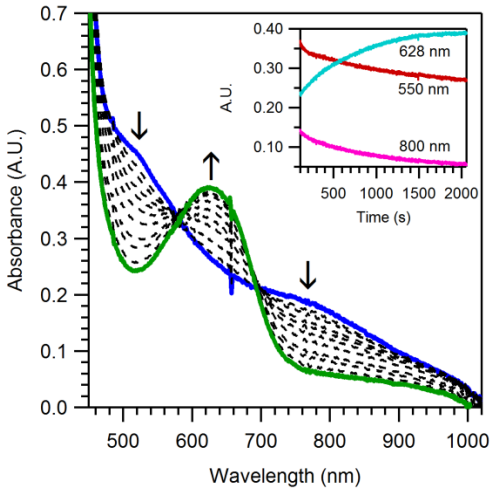

Figure 5.7. Electronic absorption spectra of 1.25 mM $[Mn^{III}(OMe)(dpaq)]^+$ upon the addition of 100 equiv. 2,4,6-tri-*t*-butylphenol ($^{4\text{-}t\text{-butyl}}$ArOH) at 50 ºC in MeCN under argon. Inset: Time evolution of single-wavelength traces at 628, 550, and 800 nm.

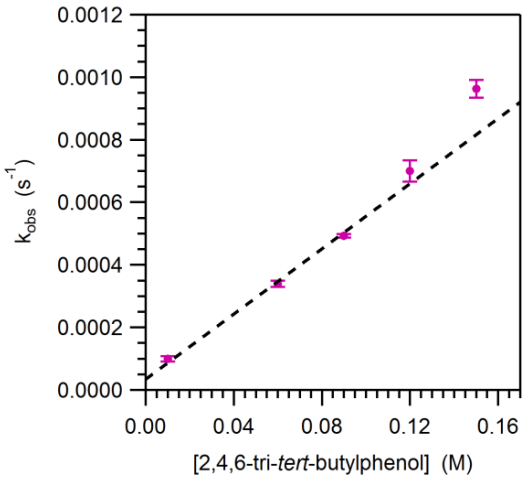

Figure 5.8. Observed pseudo-first-order rate constants (k_{obs}) as a function of $^{4\text{-}t\text{-butyl}}$ArOH concentration for $[Mn^{III}(OMe)(dpaq)]^{+}$.

Table 5.2. Rate Constants from Kinetic Experiments between $[Mn^{III}(OMe)(dpaq)]^{+}$ and O–H Bond Substrates in MeCN, and Substrate $BDFE_{O-H}$ Values.

substrate	k_2 (M^{-1} s^{-1})	$BDFE_{O-H}$ [a]
TEMPOH	$8.0(1) \times 10^{-2}$	66.5(1)
$^{4\text{-MeO}}$ArOH	1.1(1)	73.9(1)
$^{4\text{-Me}}$ArOH	$8.2(1) \times 10^{-3}$	76.0(1)
$^{4\text{-}t\text{-butyl}}$ArOH	$5.2(1) \times 10^{-3}$	77.1(1)
$^{4\text{-}t\text{-butyl}}$ArOH (MeOH) [b]	$3.7(1) \times 10^{-3}$	77.1(1)
$^{4\text{-H}}$ArOH	$1.4(1) \times 10^{-3}$	78.5(1)
$^{4\text{-CN}}$ArOH	[c]	79.0(1)

[a] kcal/mol; from Warren *et al*. (ref. 7) or determined following Waidmann *et al.* (ref. 14). [b] MeOH was used as the solvent for this reaction. [c] The reaction of $[Mn^{III}(OMe)(dpaq)]^{+}$ with $^{4\text{-CN}}$ArOH did not go to completion.

An Evans-Polanyi plot generated using second-order rate constants of O–H bond oxidation reactions mediated by $[Mn^{III}(OMe)(dpaq)]^{+}$ is shown in Figure 5.9. This set of substrates comprise a reasonable range of substrate BDFEs (66 – 78.5 kcal/mol in MeCN),[39] and a linear dependence between the log of reaction rate versus BDFE of the substrate is observed with a slope of -0.2. In this analysis, the oxidation of $^{4\text{-MeO}}$ArOH displays a much faster rate than expected on the basis of its bond strength, and is a clear outlier (Figure 5.9). Importantly, the

Polanyi slope obtained by excluding the data point for $^{4\text{-MeO}}$ArOH is still -0.2; thus, the deviation in the oxidation rate of $^{4\text{-MeO}}$ArOH does not affect the Polanyi slope. The slope seen for this series is smaller than expected from Marcus theory for a reaction with a small thermodynamic driving force (-0.5). Such small slopes have been seen for most mid-valent Mn and Fe oxidants (*vide infra*).[26-29]

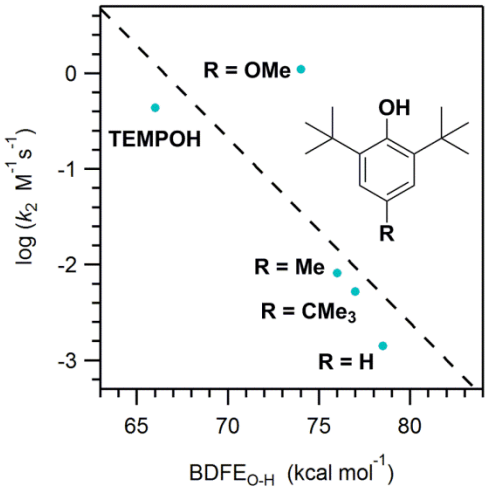

Figure 5.9. Evans-Polanyi plot of log of PCET rate (k_2) versus the BDFE of the substrate.

The C–H bond oxidation capability of [Mn^{III}(OMe)(dpaq)](OTf) was also investigated using xanthene, which has a C–H BDFE of 73.3 kcal/mol in dimethysulfoxide. Treatment of a MeCN solution of [Mn^{III}(OMe)(dpaq)](OTf) with xanthene at 50 ºC led to an observed decay rate of the Mn^{III}–OMe complex indistinguishable to the self-decay rate at this temperature (Figure A4.6).[40] Thus, unlike the corresponding Mn^{III}–OH complex,[29] [Mn^{III}(OMe)(dpaq)]$^+$ does not appear to be capable of xanthene oxidation.

5.4. Discussion

Mn-dependent enzymes catalyze a range of biological processes, during which PCET reactions play a vital role.[1] Active sites in a number of these enzymes are known to contain mid-valent Mn oxidants.[41-45] Specifically, the active-site of Mn-lipoxygenase is presumed to contain a Mn^{III}–OH unit that initiates fatty acid oxidation by a PCET step.[27,45,46] Support for this proposal comes from the H/D KIE of ~20 at 50 ºC.[46] Notably, this KIE is significantly smaller than that of Fe-lipoxygenase (~56 at 30 ºC),[47,48] and, unlike that of Fe-lipoxyganese, the Mn-lipoxygenase H/D KIE is temperature-dependent, increasing to ~38 at 8 ºC.[46] The basis for the different KIE behaviors of Fe- and Mn-lipoxygenases is currently unknown. In light of this and other biological examples, there have been several investigations of model complexes containing M^{III}–OR units (M = Mn or Fe).[25-29] Only a few of the synthetic M^{III}–OR complexes are known to mediate PCET reactions, but these studies have revealed interesting differences between mid-valent M^{III}–OR complexes and high-valent $M^{IV/V}$=O adducts.[25-29,49] Most obviously, high-valent oxidants are capable of activating significantly stronger substrate bonds (up to 100 kcal/mol) than mid-valent oxidants (up to 80 kcal/mol). Although substrate oxidations of high-valent oxidants have been the subject of numerous detailed studies, understanding of PCET reactivity mediated by low-valent oxidants is still in its infancy.[49]

This present work describes the formation and PCET reactivity of the new Mn^{III}–OMe complex, $[Mn^{III}(OMe)(dpaq)]^+$. This complex is formed in quantitative yields by the reaction of $[Mn^{II}(dpaq)]^+$ with dioxygen in methanol. Previously reported $[Mn^{II}(dpaq)]^+$ represents a rare example of a monomeric Mn^{II} complex that can activate dioxygen in solution under ambient conditions to form a single product.[29] The mechanism of O_2 activation by $[Mn^{II}(dpaq)]^+$ is currently under investigation. Although synthetic Mn^{II} complexes that can activate dioxygen are

unusual, the presence of an amido ligand, as in $[Mn^{II}(dpaq)]^+$, is known to significantly alter the electronic properties of the metal center.[50-55] $[Mn^{III}(OMe)(dpaq)]^+$ is remarkably stable in solution with a half-life of ~26 days in MeCN at 25 °C. In addition, a distinct property of this system is that $[Mn^{III}(OMe)(dpaq)]^+$ can be stoichiometrically generated by dissolving the previously reported $[Mn^{III}(OH)(dpaq)]^+$ complex in MeOH, and this reaction can be completely reversed when $[Mn^{III}(OMe)(dpaq)]^+$ is placed in water (Figure A4.1).

Table 5.3. Thermodynamic and Kinetic Parameters Related to PCET reactivity of Mn^{III}–OH and Mn^{III}–OMe Oxidants with TEMPOH in MeCN at 25 ^oC.

	[a]$[Mn^{III}(OH)(dpaq)]^+$	$[Mn^{III}(OMe)(dpaq)]^+$	[b]$[Mn^{III}(OH)(S^{Me2}N_4(tren))]^+$	[b]$[Mn^{III}(OMe)(S^{Me2}N_4(tren))]^+$
k_2 (M^{-1} s^{-1})	1.3×10^{-1}	8.0×10^{-2}	2.1×10^{3}	3.6×10^{2}
conc. (mM)	1.25	1.25	0.5	0.5
E (M^{III}/M^{II})	-0.6 [d]	-0.88 [e]	-0.6 [d]	-0.45 [d]
pK_a M^{II}-O(H)R	NA[c]	NA[c]	21.2	≥16.2
BDFE M^{II}-O(H)R [f,g]	NA[c]	NA[c]	70.1	≥64.4
$\Delta H^{\ddagger}$ [g]	9.9(9)	11.4(5)	8.2	8.3
$\Delta S^{\ddagger}$ [h]	-35(3)	-27(2)	-25.5	-29
$\Delta G^{\ddagger}$ [g,i]	20.3(1.8)	19.5(1.1)	15.8	16.9

[a] Data taken from reference 29. [b] Data taken from reference 25. [c] Not available. [d] Reduction potential ($E_{1/2}$) and [e] cathodic peak potential ($E_{p,c}$) vs Fc^+/Fc in volts at 25 ^oC in MeCN. [f] in MeCN. [g] in kcal/mol. [h] in cal/mol K. [i] at 25 ^oC.

5.4.1. PCET Mechanism of $[Mn^{III}(OMe)(dpaq)]^+$. $[Mn^{III}(OMe)(dpaq)]^+$ is capable of oxidizing substrate O–H bonds of BDFEs less than 79 kcal/mol. To date, this is the only Mn^{III}–OMe species reported to activate phenolic O–H bonds. Using this complex, we have performed the oxidation of a series of *para*-substitued-2,6-di-*tert*-butylphenols ($^{4\text{-}R}$ArOH) and TEMPOH (Table 5.2), which encompasses a reasonable range of substrate O–H BDFEs (66.5 – 78.5 kcal/mol). The Evans-Polanyi plot for O–H bond oxidation of these substrates by $[Mn^{III}(OMe)(dpaq)]^+$ shows a linear dependence of the log of O–H bond oxidation rates on the BDFE of the substrate O–H bond (Figure 5.9). This is suggestive of a CPET mechanism for O–H oxidation by $[Mn^{III}(OMe)(dpaq)]^+$. Furthermore, $[Mn^{III}(OMe)(dpaq)]^+$ reacts with TEMPOH, a substrate that is most likely to undergo CPET due to its remarkably high pK_a (41 in MeCN) and reduction potential (+0.71 V vs. Fc^+/Fc in MeCN).[7] The H/D KIE observed for this oxidation is 1.8, which is suggestive of a rate-limiting CPET. In addition, we carried out the oxidation of $^{4\text{-}t\text{-butyl}}$ArOH in both MeCN and MeOH, and these reactions proceeded with similar second-order rates of 5.2(1) × 10^{-3} M^{-1} s^{-1} and 3.7(1) × 10^{-3} M^{-1} s^{-1} respectively (Figure A4.4). Such similar rates in both protic and non-protic solvents have been previously attributed to the absence of charged intermediates during the reaction, which suggests that sequential proton- and electron-transfer steps do not occur.[27] Finally, given the low $E_{p,c}$ for $[Mn^{III}(OMe)(dpaq)]^+$ (-0.88 V vs Fc^+/Fc in MeCN at 25 °C) and the potential for the $PhO^{\bullet}/PhO^-$ couple of $^{4\text{-}t\text{-butyl}}$ArOH (-0.70 V vs Fc^+/Fc in MeCN at 25 °C),[7] a stepwise PCET involving initial electron transfer between $[Mn^{III}(OMe)(dpaq)]^+$ and $^{4\text{-}t\text{-butyl}}$ArOH is energetically up-hill by at least 0.18 V. Taken together, these cumulative observations strongly support a CPET process for $[Mn^{III}(OMe)(dpaq)]^+$-mediated O–H bond oxidation. The thermodynamic driving force for these CPET processes is defined as the difference in O–H BDFE of the reduced-protonated form of the oxidant

(M^{II}–O(H)R in Scheme 5.1; M = Mn or Fe) and that of the substrate being oxidized. When both the pK_a of the M^{II}–O(H)R species and E^o of the M^{III}/M^{II} couple are known, the BDFE of the metal oxidant can be calculated using the Bordwell relationship (*vide supra*). Although we were able to obtain an $E_{p,c}$ of -0.88 V (vs Fc^+/Fc) for the Mn^{III}/Mn^{II} couple of $[Mn^{III}(OMe)(dpaq)]^+$ (Figure A4.2), all attempts in determining the pK_a of the M^{III}–O(H)R form of this oxidant were unsuccessful.[56] We have encountered similar difficulties in determining the pK_a for $[Mn^{II}(OH_2)(dpaq)]^+$. Consequently, the BDFEs of $[Mn^{II}(MeOH)(dpaq)]^+$ and $[Mn^{II}(OH_2)(dpaq)]^+$ are not known.

In contrast, the thermodynamic driving forces for PCET reactions by other Mn^{III}–OR adducts have been determined using experimental BDFEs of the M^{II}–O(H)R species.[25-28] For example, the BDFE of $[Mn^{II}(OH_2)(S^{Me2}N_4(tren))]^+$ was determined using a modified Bordwell relationship,[25] and was found to be 70.1 kcal/mol in MeCN (74.0 kcal/mol in H_2O). In that study, $[Mn^{III}(OH)(S^{Me2}N_4(tren))]^+$ exhibited a E^o of -0.60 V (vs Fc^+/Fc), and the corresponding Mn^{II}–OH_2 species had a pK_a of 21.2 (Table 5.3). The related Mn^{III}–OMe complex exhibited a E^o of -0.45 V (vs Fc^+/Fc), but the pK_a of the Mn^{III}–O(H)Me form could not be precisely defined (a lower limit of 16.2 was estimated). Based on these values, the M^{II}–OH_2 complex has a stronger O–H bond by at most 5.6 kcal/mol compared to the M^{II}–O(H)Me species (Table 5.3).[25] As a consequence of these weak BDFEs, $[Mn^{III}(OH)(S^{Me2}N_4(tren))]^+$ and $[Mn^{III}(OMe)(S^{Me2}N_4(tren))]^+$ were only able to oxidize TEMPOH. In contrast, Stack and Goldsmith reported a BDFE of 82 kcal/mol in MeCN for the $[Mn^{II}(OH_2)(PY5)]^{2+}$ complex, and, as a result, the $[Mn^{III}(OH)(PY5)]^{2+}$ oxidant was capable of oxidizing moderately strong C–H bonds, including that of toluene (C–H BDFE of 87 kcal/mol in MeCN),[7] with a second-order rate constant of $2.2(5) \times 10^{-3}$ M^{-1} s^{-1}.[26] Therefore, the current examples of Mn^{III}–OH complexes reveal that, even with the same metal

and –OR ligand, the BDFE of the metal oxidant can vary considerably (17 kcal/mol) as a function of the supporting ligand. Although the BDFEs are not known for the reduced, protonated forms of $[Mn^{III}(OMe)(dpaq)]^+$ and $[Mn^{III}(OH)(dpaq)]^+$, these complexes show reactivity intermediate between the $S^{Me2}N_4$(tren)- and PY5-supported systems. That is, unlike the $[Mn^{III}(OR)(S^{Me2}N_4(tren))]^+$ complexes, the $[Mn^{III}(OR)(dpaq)]^+$ oxidants can oxidize phenolic O–H bonds, but cannot oxidize the stronger C–H bonds that the $[Mn^{III}(OH)(PY5)]^+$ complex readily attacks.

Table 5.4. Comparison of H/D KIEs and Polanyi slopes for O–H Activation by Mid-valent vs High-valent Oxidants.

Oxidant	Solvent	Polanyi slope	H/D KIE	*T* (°C)	Ref.
mid-valent oxidants					
$[Mn^{III}(OMe)(dpaq)]^+$	MeCN	-0.2	1.8 [a]	25	This work
$[Mn^{III}(OH)(dpaq)]^+$	MeCN	-0.07	1.8 [a], 1.4 [b]	25, 50	29
$[Mn^{III}(OMe)(S^{Me2}N_4(tren))]^+$	MeCN	NR [d]	2.1 [a]	25	25
$[Mn^{III}(OH)(S^{Me2}N_4(tren))]^+$	MeCN	NR [d]	3.1 [a]	25	25
$[Fe^{III}(OMe)(PY5)]^+$	MeCN	NR [d]	2.0 [b]	25	27
high-valent oxidants					
$[(TBP_8Cz)Mn^{V}(O)]$	DCM	-0.39	5.9 [b]	23	23
$[Mn^{IV}(salen)(OH)]$	DCM	-0.59 [e]	9.5 [c]	-70	57
$[Fe^{IV}(O)(TMC)(N_3)]^-$	MeCN	-0.36	NR [d]	25	20
$[Fe^{IV}(O)(TMC)(OOCCF_3)]^-$	MeCN	-0.42	NR [d]	25	20
$[Fe^{IV}(O)(TMC)(NCCH_3)]^-$	MeCN	-0.55	NR [d]	25	20
$[Fe^{IV}(\beta\text{-BPMCN})(OO^tBu)(OH)]^{2+}$	PrCN	-0.4 [e]	2.0 [b]	-70	59

H/D KIE was studied using [a] TEMPOH, [b] 4-*t*-butylArOH, and [c] 4-HArOH as the O–H bond substrate. [d] Not reported. [e] Polanyi slopes were not reported; we calculated the slope using the reported kinetic data in refs. 57 and 59.

5.4.2. Rates and Activation Parameters for O–H Bond Oxidation by Mid-valent Mn Oxidants. TEMPOH is commonly used as a weak O–H bond substrate (BDFE = 66.5 kcal/mol in MeCN) in metal-mediated PCET processes and provides a good point of comparison for the reactivity of Mn^{III}–OR oxidants (Table 5.3). $[Mn^{III}(OMe)(dpaq)]^+$ oxidizes TEMPOH at a second-order rate of 8.0×10^{-2} M^{-1} s^{-1} in MeCN at 25 °C, which is very similar to that of $[Mn^{III}(OH)(dpaq)]^+$ (1.3×10^{-1} M^{-1} s^{-1}). The enthalpy of activation ($\Delta H^{\ddagger}$) for TEMPOH oxidation by $[Mn^{III}(OMe)(dpaq)]^+$ is 11.4(5) kcal/mol, marginally higher than that observed for $[Mn^{III}(OH)(dpaq)]^+$ (9.9(9) kcal/mol). In contrast, $[Mn^{III}(OMe)(dpaq)]^+$ shows a smaller entropic barrier to TEMPOH oxidation when compared to $[Mn^{III}(OH)(dpaq)]^+$ ($T\Delta S^{\ddagger}$ = 8.0(6) and 10.4(9) kcal/mol at 25 °C, respectively). As a net result of these changes in $\Delta H^{\ddagger}$ and $T\Delta S^{\ddagger}$, $[Mn^{III}(OMe)(dpaq)]^+$ and $[Mn^{III}(OH)(dpaq)]^+$ have similar free energies of activation ($\Delta G^{\ddagger}$) for TEMPOH oxidation at 25 °C (19.5(1.1) and 20.3(1.8) kcal/mol respectively). This is consistent with the very similar second-order rate constants at this temperature (Table 5.3).

On the other hand, the $\Delta G^{\ddagger}$ (25 °C) for TEMPOH oxidation by $[Mn^{III}(OMe)(S^{Me2}N_4(tren))]^+$ and $[Mn^{III}(OH)(S^{Me2}N_4(tren))]^+$ were found to be 16.9 and 15.8 kcal/mol respectively, substantially lower than those of the $[Mn^{III}(OR)(dpaq)]^+$ complexes. This is in line with the 10^4-greater rate of TEMPOH oxidation by the $S^{Me2}N_4$(tren)-supported complexes (Table 5.3). The 1.1 kcal/mol difference between the $\Delta G^{\ddagger}$ values of $[Mn^{III}(OMe)(S^{Me2}N_4(tren))]^+$ and $[Mn^{III}(OH)(S^{Me2}N_4(tren))]^+$ results in the Mn^{III}–OMe complex having a rate of TEMPOH oxidation an order of magnitude slower than that of the Mn^{III}–OH complex (3.6×10^2 and 2.1×10^3 $M^{-1}s^{-1}$, respectively).[25] Notably, the enthalpic ($\Delta H^{\ddagger}$) contribution to the $\Delta G^{\ddagger}$ values of $[Mn^{III}(OMe)(S^{Me2}N_4(tren))]^+$ and $[Mn^{III}(OH)(S^{Me2}N_4(tren))]^+$ are virtually identical (Table 5.3). Thus, the more sluggish reactivity of

$[Mn^{III}(OMe)(S^{Me2}N_4(tren))]^+$ is due to the larger entropy of activation (Table 5.3). However, the smaller $\Delta G^{\ddagger}$ for TEMPOH oxidation by $[Mn^{III}(OR)(S^{Me2}N_4(tren))]^+$ complexes in comparison with $[Mn^{III}(OR)(dpaq)]^+$ oxidants is intriguing, given that it solely reflects differences between the dpaq and $S^{Me2}N_4$(tren) supporting ligands (Figure 5.1).

When comparing the phenol oxidation behavior of $[Mn^{III}(OMe)(dpaq)]^+$ and $[Mn^{III}(OH)(dpaq)]^+$, the most significant difference is that the former complex lacks the rate saturation behavior at high phenol concentrations.[29] The saturation behavior of $[Mn^{III}(OH)(dpaq)]^+$ was proposed to be due to the equilibrium formation of a precursor complex prior to the rate-determining CPET step. This precursor complex was proposed to be a hydrogen-bonded adduct between the phenolic substrate and the Mn^{III}–OH unit of $[Mn^{III}(OH)(dpaq)]^+$. The formation of a similar adduct might be disfavored for $[Mn^{III}(OMe)(dpaq)]^+$ due to steric clash between the methyl moiety and the bulky phenol substrates. For most of the phenols, the K_{eq} for precursor complex formation with $[Mn^{III}(OH)(dpaq)]^+$ was ~20, which corresponds to a small free energy of reaction of ~2 kcal/mol. Thus, a subtle steric or electronic effect in the $[Mn^{III}(OMe)(dpaq)]^+$ system could be expected to impact the equilibrium position such that the pre-equilibrium step is no longer observed.

5.4.3. KIEs and Polanyi Slopes of Mid-valent Oxidants. In comparison with high-valent oxidants, the H/D KIEs and the Polanyi slopes for O–H bond oxidations by mid-valent oxidants display notable differences, as summarized in Table 5.4. The KIEs for O–H bond oxidation reactions of mid-valent M–OR oxidants are smaller (~2 – 3)[25,29] than those of high-valent oxo and hydroxo oxidants (~5 – 10),[23,57,58] with the exception of the $[Fe^{IV}(\beta$-BPMCN)(OO^{t}Bu)(OH)$]^{2+}$ oxidant.[59] For example, the H/D KIE observed for $^{4\text{-}t\text{-butyl}}$ArOH oxidation by $[Mn^{III}(OH)(dpaq)]^+$ is remarkably small (1.4),[29] while the high-valent $Mn^V{\equiv}O$

complex, [(TBP_8Cz)Mn^V(O)], has been shown to carry out the same substrate oxidation at a similar temperature with a larger KIE of 5.9.[23]

Moreover, according to Marcus theory, a Polanyi slope of -0.5 is expected for a process with a small thermodynamic driving force and a transition state position mid-way between reactants and products.[60] The Polanyi slopes observed for O–H oxidation reactions of mid-valent oxidants range between -0.07[29] and -0.2,[61] which is significantly smaller than the expected value. Albeit, at present, only a limited number of data sets are available.[61] This is in contrast with high-valent oxidants that oxidize substrate O–H bonds with a Polanyi slope of -0.4 to -0.6.[20,23,57-59] Each Polanyi study listed in Table 5.4 is based on *para*-substitued-2,6-di-*tert*-butylphenols as O–H substrates. Irrespective of the identity of the metal (Mn or Fe), high-valent oxidants show slopes closer to the expected value of -0.5. Generally, a Polanyi slope of <0.5 indicates an early transition state that resembles the reactants,[60] with a rate less sensitive to the driving force of the reaction. It is an open question therefore, whether the lower sensitivity of PCET rates to the driving force of the reaction is a characteristic property of these mid-valent oxidants, and if they go through an early transition state regardless of the identity of the substrate. The small KIE values observed for these oxidants could also be a consequence of this phenomenon.

5.5. Conclusions and Outlook

Designing metal oxidants with well-tuned properties for rapid, selective PCET is a desirable goal in synthetic chemistry, as such oxidants could be of significant benefit in industry, as well as in biomimetic studies. Among other metal oxidants, mid-valent M–OR adducts exhibit the potential for good tunability in their PCET reactivities, as both E^o and pK_a can be controlled by changing the R group in the M–OR unit, or through modification of the supporting ligand.

For example, the variation in Mn^{III}/Mn^{II} potentials with respect to the properties of the supporting ligands is observed in the series of Mn^{III}–OH complexes supported by neutral PY5 (+0.17 V vs Fc^{+}/Fc), monoanionic $S^{Me2}N_4$(tren) and dpaq (-0.60 V vs Fc^{+}/Fc for both), and trianionic H_31^{3-} (H_31^{3-} = [[tris(*N*'-*tert*-butylureaylato)*N*-ethyl]aminato]) ligands (-1.51 V vs Fc^{+}/Fc).[25,26,62] Also, the pK_a of the oxidant can be altered utilizing supporting ligands and –OR ligand properties, as seen in the $[Mn^{III}(OR)(S^{Me2}N_4(tren))]^{+}$ series of complexes (Table 5.3).[25] As a result of these differences, a range of O–H BDFEs is observed for M^{II}–OH_2 species derived from M^{III}–OH oxidants (17 kcal/mol), along with large differences in substrate oxidation rates (10^4-fold for TEMPOH as substrate; see Table 5.3). Additional work on mid-valent oxidants is warranted to gain further insight into the specific geometric and electronic factors governing their PCET reactivities.

5.6. References

1. Mayer, J. M.; Rhile, I. J., *Biochim. Biophys. Acta, Bioenerg.* **2004,** *1655*, 51-58.
2. (a)Y. Umena, K. Kawakami, J.-R. Shen and N. Kamiya, *Nature*, 2011, **473**, 55–60. (b) C. Kupitz, S. Basu, I. Grotjohann, R. Fromme, N. A. Zatsepin, K. N. Rendek, M. S. Hunter, R. L. Shoeman, T. A. White, D. Wang, D. James, J.-H. Yang, D. E. Cobb, B. Reeder, R. G. Sierra, H. Liu, A. Barty, A. L. Aquila, D. Deponte, R. A. Kirian, S. Bari, J. J. Bergkamp, K. R. Beyerlein, M. J. Bogan, C. Caleman, T.-C. Chao, C. E. Conrad, K. M. Davis, H. Fleckenstein, L. Galli, S. P. Hau-Riege, S. Kassemeyer, H. Laksmono, M. Liang, L. Lomb, S. Marchesini, A. V. Martin, M. Messerschmidt, D. Milathianaki, K. Nass, A. Ros, S. Roy-Chowdhury, K. Schmidt, M. Seibert, J. Steinbrener, F. Stellato, L. Yan, C. Yoon, T. A. Moore, A. L. Moore, Y. Pushkar, G. J. Williams, S. Boutet, R. B. Doak, U. Weierstall, M. Frank, H. N. Chapman, J. C. H. Spence and P. Fromme, *Nature*, 2014, **513**, 261-265.
3. Tommos, C.; Babcock, G. T., *Acc. Chem. Res.* **1998,** *31*, 18-25.
4. Westphal, K. L.; Tommos, C.; Cukier, R. I.; Babcock, G. T., *Current Opinion in Plant Biology* **2000,** *3*, 236-242.
5. Kim, S.; Liang, J.; Barry, B. A., *Proc. Natl. Acad. Sci. U. S. A.* **1997,** *94*, 14406-14411.
6. Babcock, G. T. In *The oxygen-evolving complex in photosystem II as a metallo-radical enzyme*, 1995; Kluwer: 1995; pp 209-215.

7. Warren, J. J.; Tronic, T. A.; Mayer, J. M., *Chem. Rev.* **2010,** *110*, 6961-7001.
8. Huynh, M. H. V.; Meyer, T. J., *Chem. Rev.* **2007,** *107*, 5004-5064.
9. Mader, E. A.; Davidson, E. R.; Mayer, J. M., *J. Am. Chem. Soc.* **2007,** *129*, 5153-5166.
10. Mader, E. A.; Manner, V. W.; Markle, T. F.; Wu, A.; Franz, J. A.; Mayer, J. M., *J. Am. Chem. Soc.* **2009,** *131*, 4335-4345.
11. Mader, E. A.; Mayer, J. M., *Inorg. Chem.* **2010,** *49*, 3685-3687.
12. Manner, V. W.; Mayer, J. M., *J. Am. Chem. Soc.* **2009,** *131*, 9874-9875.
13. Mayer, J. M., *Acc. Chem. Res.* **2010,** *44*, 36-46.
14. Waidmann, C. R.; Zhou, X.; Tsai, E. A.; Kaminsky, W.; Hrovat, D. A.; Borden, W. T.; Mayer, J. M., *J. Am. Chem. Soc.* **2009,** *131*, 4729-4743.
15. (a) J. J. Warren and J. M. Mayer, *J. Am. Chem. Soc*., 2008, **130**, 2774–2776.(b) J. J. Warren and J. M. Mayer, *J. Am. Chem. Soc*., 2011, **133**, 8544–8551.
16. D. R. Weinberg, C. J. Gagliardi, J. F. Hull, C. F. Murphy, C. A. Kent, B. C. Westlake, A. Paul, D. H. Ess, D. G. McCafferty and T. J. Meyer, *Chem. Rev.* 2012, **112**, 4016-4093, and references therein.
17. Warren, J. J.; Menzeleev, A. R.; Kretchmer, J. S.; Miller, T. F.; Gray, H. B.; Mayer, J. M., *J. Phys. Chem. Lett.* **2013,** *4*, 519-523.
18. Layfield, J. P.; Hammes-Schiffer, S., *Chem. Rev.* **2013,** *114*, 3466-3494.
19. Alternatively, HAT and CPET have respectively been attributed to electronically adiabatic and nonadiabatic proton transfer, as described by Hammes-Schiffer and co-workers (see reference 18).
20. Sastri, C. V.; Lee, J.; Oh, K.; Lee, Y. J.; Lee, J.; Jackson, T. A.; Hirao, H.; Que, L., Jr.; Shaik, S.; Nam, W., *Proc. Natl. Acad. Sci. U. S. A.* **2007,** *104*, 19181-19186.
21. Leto, D. F.; Ingram, R.; Day, V. W.; Jackson, T. A., *Chem. Commun.* **2013,** *49*, 5378-5380.
22. Krebs, C.; Galonić Fujimori, D.; Walsh, C. T.; Bollinger, J. M., *Acc. Chem. Res.* **2007,** *40*, 484-492.
23. Lansky, D. E.; Goldberg, D. P., *Inorg. Chem.* **2006,** *45*, 5119-5125.
24. Wang, D.; Zhang, M.; Bühlmann, P.; Que, L., Jr., *J. Am. Chem. Soc.* **2010,** *132*, 7638-7644.
25. Coggins, M. K.; Brines, L. M.; Kovacs, J. A., *Inorg. Chem.* **2013,** *52*, 12383-12393.
26. Goldsmith, C. R.; Cole, A. P.; Stack, T. D. P., *J. Am. Chem. Soc.* **2005,** *127*, 9904-9912.
27. Goldsmith, C. R.; Jonas, R. T.; Stack, T. D. P., *J. Am. Chem. Soc.* **2001,** *124*, 83-96.
28. Goldsmith, C. R.; Stack, T. D. P., *Inorg. Chem.* **2006,** *45*, 6048-6055.
29. Wijeratne, G. B.; Corzine, B.; Day, V. W.; Jackson, T. A., *Inorg. Chem.* **2014,** *53*, 7622-7634.
30. Bordwell, F. G.; Cheng, J.; Ji, G. Z.; Satish, A. V.; Zhang, X., *J. Am. Chem. Soc.* **1991,** *113*, 9790-9795.
31. Hitomi, Y.; Arakawa, K.; Funabiki, T.; Kodera, M., *Angew. Chem., Int. Ed.* **2012,** *51*, 3448-3452.
32. Wu, A.; Mader, E. A.; Datta, A.; Hrovat, D. A.; Borden, W. T.; Mayer, J. M., *J. Am. Chem. Soc.* **2009,** *131*, 11985-11997.

33. International Tables for Crystallography, V. A., 4th ed., Kluwer: Boston (1996).
34. Data Collection: SMART Software in APEX2 v2010.3-0 Suite. Bruker-AXS, E. C. P., Madison, WI 53711-5373 USA.
35. Data Reduction: SAINT Software in APEX2 v2010.3-0 Suite. Bruker-AXS, E. C. P., Madison, WI 53711-5373 USA
36. Refinement: SHELXTL v2010.3-0. Bruker-AXS, E. C. P., Madison, WI 53711-5373 USA.
37. Ghachtouli, S. E.; Guillot, R.; Aukauloo, A.; Dorlet, P.; Anxolabéhère-Mallart, E.; Costentin, C., *Inorg. Chem.* **2012,** *51*, 3603-3612.
38. Manner, V. W.; Markle, T. F.; Freudenthal, J. H.; Roth, J. P.; Mayer, J. M., *Chem. Commun.* **2008**, 256-258.
39. To investigate if the mixed solvent system used for phenol oxidation reactions significantly impacts the kinetic data, a set of kinetic experiments were performed where the oxidation of TEMPOD was studied in 20:1 MeCN:DCM solvent mixture (same solvent composition used in phenol oxidation). These experiments resulted in similar oxidation rates as observed in pure MeCN ($6.53(4) \times 10^{-3}$ s^{-1} and $6.45(7) \times 10^{-3}$ s^{-1}, respectively, for 100 equiv. of TEMPOD).
40. Upon the addition of 250 equiv. of xanthene at 50 ºC, the electronic absorption features of $[Mn^{III}(OMe)(dpaq)]^+$ in MeCN slowly decays over several hours. At the end of 25 hours, 10% of the $[Mn^{III}(OMe)(dpaq)]^+$ complex had been consumed (Figure A4.6). However, the observed decay rate (4.7×10^{-5} s^{-1}, determined using the initial rate method), was very similar the self-decay rate under these conditions (2.5×10^{-5} s^{-1}).
41. McEvoy, J. P.; Brudvig, G. W., *Chem. Rev.* **2006,** *106*, 4455-4483.
42. Miller, A.-F., *Curr. Opin. Chem. Biol.* **2004,** *8*, 162-168.
43. Grove, L. E.; Brunold, T. C., *Comments Inorg. Chem.* **2008,** *29*, 134-168.
44. Su, C.; Oliw, E. H., *J. Biol. Chem.* **1998,** *273*, 13072-13079.
45. Su, C.; Sahlin, M.; Oliw, E. H., *J. Biol. Chem.* **2000,** *275*, 18830-18835.
46. Wennman, A.; Karkehabadi, S.; Oliw, E. H., *Arch. Biochem. Biophys.* **2014,** *555–556*, 9-15.
47. Glickman, M. H.; Klinman, J. P., *Biochemistry* **1995,** *34*, 14077-14092.
48. Segraves, E. N.; Holman, T. R., *Biochemistry* **2003,** *42*, 5236-5243.
49. Porter, T. R.; Mayer, J. M., *Chem. Sci.* **2014,** *5*, 372-380.
50. Young, K. J.; Takase, M. K.; Brudvig, G. W., *Inorg. Chem.* **2013,** *52*, 7615-7622.
51. Hitomi, Y.; Arakawa, K.; Kodera, M., *Chem. Commun.* **2014,** *50*, 7485-7487.
52. Eroy-Reveles, A. A.; Leung, Y.; Beavers, C. M.; Olmstead, M. M.; Mascharak, P. K., *J. Am. Chem. Soc.* **2008,** *130*, 4447-4458.
53. Gupta, R.; MacBeth, C. E.; Young, V. G.; Borovik, A. S., *J. Am. Chem. Soc.* **2002,** *124*, 1136-1137.
54. MacBeth, C. E.; Gupta, R.; Mitchell-Koch, K. R.; Young, V. G.; Lushington, G. H.; Thompson, W. H.; Hendrich, M. P.; Borovik, A. S., *J. Am. Chem. Soc.* **2004,** *126*, 2556-2567.
55. Shirin, Z.; S. Borovik, A.; G. Young Jr, V., *Chem. Commun.* **1997**, 1967-1968.
56. The determination of pK_a by titrating $[Mn^{III}(OMe)(dpaq)]^+$ with various acids (HCl and $HClO_4$) was attempted in MeCN. Unfortunately, $[Mn^{III}(OMe)(dpaq)]^+$ reacts rapidly with acids to generate a Mn^{II} species, which has been verified by EPR

spectroscopy. This could be reflective of the impaired stability of $[Mn^{III}(MeOH)(dpaq)]^{+}$, which prevents its accumulation in solution. Therefore, the determination of the pK_a of $[Mn^{II}(MeOH)(dpaq)]^{+}$ was not feasible by titrating $[Mn^{III}(OMe)(dpaq)]^{+}$ with acids.

57. Kurahashi, T.; Kikuchi, A.; Shiro, Y.; Hada, M.; Fujii, H., *Inorg. Chem.* **2010,** *49*, 6664-6672.
58. Yiu, D. T. Y.; Lee, M. F. W.; Lam, W. W. Y.; Lau, T.-C., *Inorg. Chem.* **2003,** *42*, 1225-1232.
59. Fiedler, A. T.; Que, L., Jr., *Inorg. Chem.* **2009,** *48*, 11038-11047.
60. Mayer, J. M., Thermodynamic Influences on C–H Bond Oxidation. In *Biomimetic Oxidations Catalyzed by Transition Metal Complexes* Meunier, B., Ed. Imperial College Press, London: 2000; pp 1-43.
61. The only examples for Polanyi studies of O–H bond oxidation by mid-valent oxidants are found in our work on $[Mn^{III}(OH)(dpaq)]^{+}$ and $[Mn^{III}(OMe)(dpaq)]^{+}$. Thus, it should be noted that this range of Polanyi slopes comes from a limited set of oxidants. However, for C–H oxidation reactions of Mn and Fe mid-valent oxidants of Stack and co-workers, small Polanyi slopes were observed that ranged between -0.1 and -0.2 (see references 26, 27 and 28).
62. Gupta, R.; Borovik, A. S., *J. Am. Chem. Soc.* **2003,** *125*, 13234-13242.
63. O'Neill, M. K.; Trappey, A. F.; Battle, P.; Boswell, C. L.; Blauch, D. N., *Dalton Trans.* **2009**, 3391-3394.
64. Ottaviani, M. F.; Garcia-Garibay, M.; Turro, N. J., *Colloids and Surfaces A: Physicochemical and Engineering Aspects* **1993,** *72*, 321-332.

CHAPTER 6

Mechanistic Investigations into Dioxygen Activation Pathways of Monomeric Manganese(II) Complexes

X-ray absorption spectroscopic data collection and analysis for [Mn^{II}(dpaq)](OTf) was performed by Derek B. Rice. X-ray diffraction data collection and analysis were carried out by Dr. Victor W. Day.

6.1. Introduction

Mn-dependent enzymes that utilize dioxygen as the oxidant for the dioxygenation of catechols,[1,2] and oxidation[3,4] and decarboxylation[5,6] of oxalates are ubiquitous in nature. Similar manganese catalysts that can activate dioxygen are of great significance, since both the catalyst and the oxidant are environmentally benign and less expensive, compared to most precious metal industrial catalysts currently used.[7] Furthermore, these catalysts are presumed to be of immense potential, both in organic synthesis and alternate energy applications such as fuel cells. Synthetic manganese(II) complexes that are capable of reducing dioxygen are rare, predominantly due to the inherently high reduction potential of the Mn^{III}/Mn^{II} redox couple (1.51 V vs. NHE in H_2O).[8] Thus, dioxygen activation by Mn^{II} centers is virtually impractical, unless the metal center is supported by an electron rich supporting ligand that could significantly alter its redox potential.[9] Accordingly, all synthetic examples of dioxygen activating Mn^{II} complexes are supported by either mono-, di-, or trianionic supporting ligands (*vide infra*), and a handful of these complexes are also capable of catalytic O_2 reduction.[10-12] Some Mn^{II} systems have been successfully utilized as synthetic oxidation catalysts for organic transformations, where olefin epoxidation and alkane oxidation are the most common processes.[13-18] In addition, some reports include structural and/or spectroscopic characterization of key intermediates formed during Mn-dependent O_2 activation, which provides useful mechanistic details.[9,10,19,20]

6.1.1. Synthetic applications of Mn^{II}-catalyzed dioxygen reduction. In 1986, Fontecave and coworkers reported both catalytic olefin epoxidation and alkane oxidation using $[Mn^{III}(TPP)(Cl)]$ (TPP = tetraphenylporphyrin; Figure 6.1) catalyst and dioxygen (Scheme 6.1).[13] It was shown that the catalytic efficiency of this system is superior to other porphyrin-based synthetic catalysts previously reported for these chemical processes.[21-25] Along with

[Mn^{III}(TPP)(Cl)] and O_2, this system required Zn powder as the reducing agent (presumably to reduce staring Mn^{III} to Mn^{II} in order to initiate catalysis, as seen in other systems[19]), acetic acid (AcOH) as the proton source, and 1-methylimidazole co-catalyst for optimum activity. The optimized molar ratios for Mn: 1-methylimidazole: AcOH: Zn: substrate were 1: 100: 150: 150: 3850, where all reactions were performed under excess O_2 in MeCN at 20 ^oC. Both cyclic (cyclooctene) and acyclic (2-methylhept-2-ene and non-1-ene) olefins were successfully converted to the corresponding epoxides in moderate yields (~50 %) with up to 75 turnovers for cyclooctene epoxidation.[13] Alkane oxidation yielded the corresponding alcohol or the ketone depending on the extent of oxidation, as commonly observed for Mn-mediated substrate oxidation reactions. Previous work, where hydride donor reagents such as $NaBH_4$, NBu_4BH_4, and H_2 has been used along with ascorbate[21-23] in place of Zn and AcOH, displayed lower yields of the hydroxylated products compared to this system. Although higher yields of epoxidation and oxidation were obtained using O_2, mechanistic details of these conversions that presumably include Mn-dependent O_2 activation are currently unknown.

Electrocatalytic olefin epoxidation was later reported by Horwitz, Murray and coworkers using $[Mn^{III}(salen)]^+$ (salen = 2,2'-Ethylenebis(nitrilomethylidene)diphenol; Figure 6.1), along with dioxygen, 1-methylimidazole and benzoic anhydride (Scheme 6.1).[14] A detailed cyclic voltammetric and rotating-disk-electrode electrochemical analysis provided useful insights into the reactive intermediates involved. It was observed that initial electrochemical reduction of Mn^{III} to Mn^{II} facilitated dioxygen activation, to generate the corresponding η^2-peroxomanganese(III) adduct. As observed previously for $[Mn^{III}(O_2)(TPP)]^-$,[25] this peroxomanganese(III) complex then reacts with benzoic anhydride to generate the $Mn^V{\equiv}O$ adduct, which mediates epoxidation, regenerating the Mn^{III} starting compound. In addition to

epoxidation, allylic hydroxylation was also observed when cyclohexene was used as the substrate. This work represents one of the earliest reports where a Mn-dependent dioxygen activation mechanism was supported by detailed characterization of reaction intermediates.

Furthermore, there are numerous other examples where Mn^{II} mediated dioxygen activation has been successfully coupled with organic substrate oxidation to generate synthetically desirable targets. Christoffers showed that α-hydroxylation of cyclic β-keto esters can be achieved with $Mn(OAc)_2 \cdot 4\ H_2O$ and dioxygen under ambient conditions in dichloromethane (Scheme 6.1).[16] Prolonged reaction times produced further oxidized products, providing useful insights into the mechanism of the reaction. It was proposed that a high-valent $Mn^{V}{\equiv}O$ species performs epoxidative reactivity that leads to the final hydroxylated products. Lastly, Nishida and coworkers have reported a unique system where dioxygen reduction has been observed by Mn^{II} centers supported by pentadentate supporting ligands in the presence of aliphatic aldehyde additives such as cyclohexanecarboxyaldehyde (Scheme 6.1).[17] In this electrochemical study, dioxygen was proposed to weakly interact with Mn^{II} as it H-bonds with secondary amine functionalities of the supporting ligand. Then, dioxygen is electrochemically activated without a change in the manganese oxidation state, where the activated dioxygen reacts with *trans*-stilbene to generate stilbene oxide. Although the proposed mechanism disfavored the formation of peroxomanganese(III) adducts, the possibility of such an intermediate could not be completely discounted.

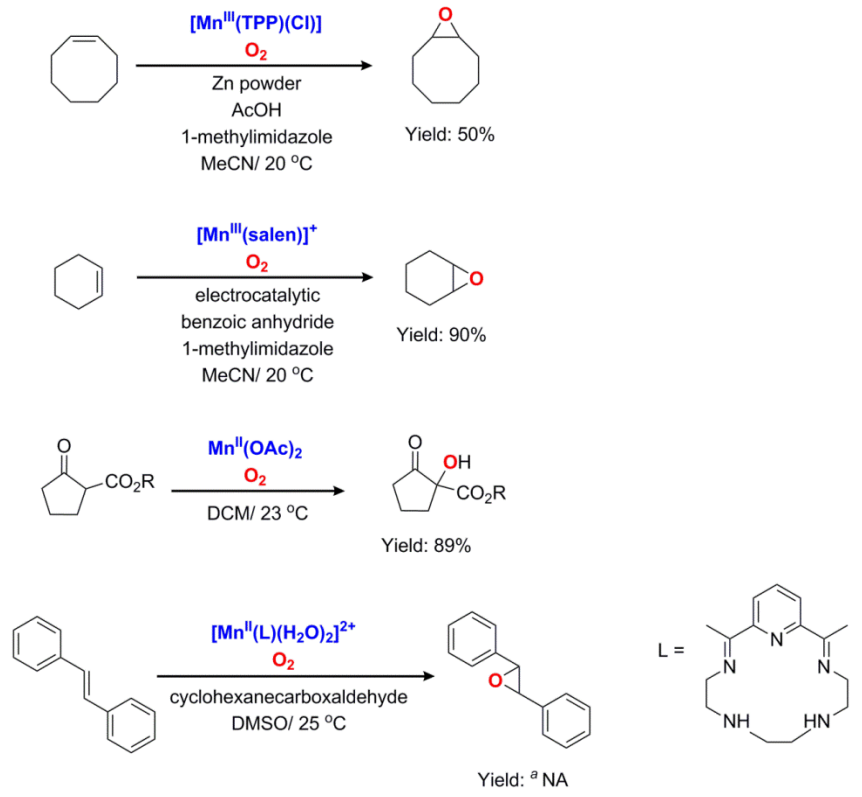

Scheme 6.1. Several synthetic applications of Mn^{II} mediated dioxygen activation. [a]Not available.

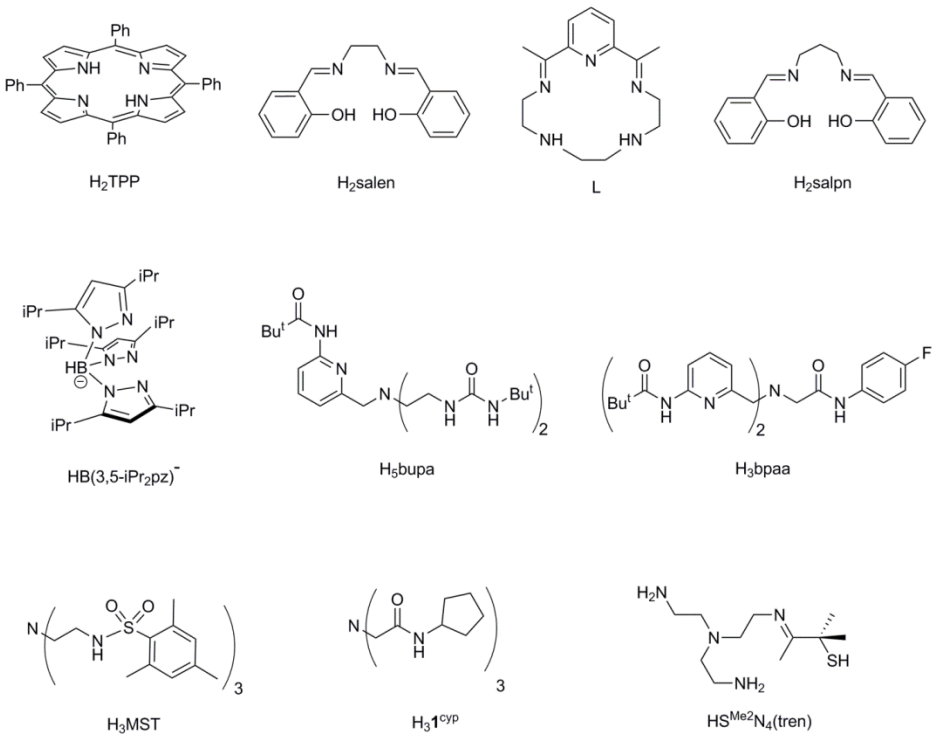

Figure 6.1. Ligands used to support Mn^{II} complexes that mediate the activation of dioxygen.

6.1.2. Dioxygen activation by bio-inspired Mn^{II} centers. Designing Mn^{II} model complexes that are capable of dioxygen activation has long been a challenging goal for synthetic inorganic chemists. Especially, Mn^{II} systems that generate a clean single end product from dioxygen activation are rare.[9] Taylor, Horwitz, Kitajima and their coworkers have reported several such systems where dioxygen activation has been observed, and the end product has often been characterized as a dimeric Mn species. In 1986, Taylor and coworkers reported a dioxygen activating Mn^{II} system, [Mn^{II}(salpn)] (salpn = 2,2'-((1*E*,1'*E*)-(propane-1,3-diylbis(azanylylidene))bis(methanylylidene))diphenol; Figure 6.1), where they proposed the initial formation of a superoxomanganese(III) species, which goes through a trans-μ-1,2-peroxo-bridged dimanganese(III,III) species to generate a final bis(μ-oxo)dimanganese(IV,IV) complex.[26,27] Alternatively, electrochemical studies of this system later revealed the involvement of a η^2-peroxomanganese(IV) species that reacts with a second equivalent of [Mn^{II}(salpn)] to generate the final bis(μ-oxo)dimanganese(IV,IV) species. The final bis(μ-oxo)dimanganese(IV,IV) species has been characterized by cyclic voltammetry, electron paramagnetic resonance (EPR) and infrared spectroscopies.[14,19,28] In addition, dioxygen activation product of [Mn^{II}(TPP)] has also been detected by EPR, which was also suggestive of a dimeric manganese species. However, the exact identity of this product is not established to date, but is debated to be either a monooxo-bridged dimanganese(II,III) species or a trans-μ-1,2-peroxo-bridged dimanganese(II,III) species.[29] Furthermore, Kitajima has observed that the bis(μ-hydroxo)dimanganese(II,II) complex, [Mn^{II}(HB(3,5-iPr_2pz)$_3$)(μ-OH)]$_2$ (HB(3,5-iPr_2pz^- = tris(3,5-diisopropyl-1H-pyrazol-1-yl)hydroborate; Figure 6.1), reacts with dioxygen to generate the structurally characterized bis(μ-oxo)dimanganese(III,III) (50% yield) and monooxo-bridged dimanganese(III,III) (40% yield) species. In the latter species, one iPr group of each ligand was

oxidized to an alkoxo group, which was observed to coordinate to the Mn center in the X-ray crystal structure.[30]

Dioxygen activation by Mn^{II} complexes to generate monomeric Mn products is much less common. Borovik and coworkers have reported several such systems, where the metal complexes consist of unique anionic ligand architectures with substantial steric bulk and H-bonding cavities around the site of O_2 binding. These ligand systems utilize secondary coordination sphere non-covalent interactions in directing the reactivity of the metal center, as well as stabilizing reactive intermediates. In addition, their steric bulk aids in preventing the formation of undesired dimeric metal adducts.[31] Dimeric metal species are often of high thermodynamic stability, and thus, do not function as active oxidants or catalytic intermediates. The Borovik group has reported two dioxygen activating Mn^{II} systems, $[Mn^{II}(Hbpaa)]$[31] and $[Mn^{II}(H_2bupa)]^-$,[10,32] which function under ambient conditions. In the presence of the weak N–H bond substrate 1,2-diphenylhradrazine (DPH), the final product of $[Mn^{II}(Hbpaa)]$-dependent O_2 activation was spectroscopically characterized as the corresponding η^2-peroxomanganese(III) complex, $[Mn^{III}(O_2)(Hbpaa)]^-$. Similarly, $[Mn^{II}(H_2bupa)]^-$ forms $[Mn^{III}(O_2)(H_3bupa)]^-$ when treated with excess dioxygen in the presence of DPH, where it exhibits a cleaner conversion to the peroxo species compared to $[Mn^{II}(Hbpaa)]$ (the yield of the peroxo complex increased from 50% to 80%).[32] In these processes, DPH plays the role of an $H^\bullet$ ($H^\bullet = H^+ + e^-$) atom donor, where the electron assisted in the reduction of dioxygen to peroxide (in conjugation with the metal), and the proton was used up for protonation of the carboxamido functionality of the supporting ligand. In a later report, the $[Mn^{II}(H_2bupa)]^-$ system was also utilized in catalytic reduction of dioxygen to water, where the O–O bond cleavage of $[Mn^{III}(O_2)(H_3bupa)]^-$ was observed over 5 hours to generate the crystallographically characterized Mn^{III}-oxo/ Mn^{III}-

hydroxo hybrid complex.[10] This species reacts further with DPH to afford the $[Mn^{II}(H_2bupa)]^-$ starting complex and water. Thus, for each equivalent of consumed dioxygen, two equivalents of DPH were also consumed, and two equivalents of water were produced. The protons of the produced water molecules were derived from DPH, while the DPH-derived electrons were consumed in O_2 reduction. These mechanistic proposals were confirmed by quantifying azobenzene (product of DPH oxidation) by ^{1}H NMR spectroscopy, and water content by Karl Fischer titrations. The major characteristic feature of this system that enabled this unique chemistry was highlighted as the proton scavenging capability of the carboxamido functionality of the supporting ligand.[10]

Furthermore, redox-inactive group 2 metal ions have been observed to have profound effects on dioxygen activation by Mn^{II}. It has been observed by Borovik and coworkers that the $[Mn^{II}(MST)]^-$ complex reacts at a very slow rate with dioxygen, but the rate increased several orders of magnitude in the presence of Ca^{2+} or Ba^{2+}.[33] This increase in rate was also observed to be dependent on the Lewis acidity of the group 2 metals, where Ba^{2+} induced a much larger rate enhancement. The final product of this reactivity was isolated, and structurally characterized as $[15\text{-crown-5}\supset M^{II}\text{–}(\mu\text{-OH})\text{–}Mn^{III}(MST)]^+$ where $M^{II} = Ca^{2+}$ or Ba^{2+} (15-crown-5 was essential to solubilize $Ca(OTf)_2$ and $Ba(OTf)_2$ in dichloromethane). The rate increment of a factor of ~35 for dioxygen activation by this system in the presence of group 2 metal ions complement the similar effects reported by Fukuzumi and coworkers for the dioxygen activation reactivity of $[Co^{II}(TPP)]$.[34] Although mechanistic details of the involvement of redox inactive metals in Mn-dependent dioxygen reduction are still unclear, it was proposed for this system that prior coordination of the group 2 metal ions to the sulfonamide groups of the supporting ligand would facilitate the coordination of dioxygen on the Mn^{II} center, which undergoes an intramolecular

electron transfer to generate the Mn^{III}-superoxo adduct.[33] The formation of this adduct is likely facilitated by the presence of group 2 cations, since they may aid in accommodating the charge build-up on the dioxygen moiety. This proposal is consistent with the dependence of rate enhancements on the Lewis acidity of the group 2 metals. Subsequently, this proposed Mn^{III}-superoxo adduct would react further to generate the observed [15-crown-5⊃M^{II}–(μ-OH)–Mn^{III}(MST)]$^+$ product.

There have been a couple reports where Mn^{III}-OH complexes have been generated from Mn^{II} precursors using O_2 as the oxidant. Borovik has proposed a mechanism for the formation of [Mn^{III}(OH)(**1**^{cyp})]$^-$, which involves the formation of an initial peroxo-bridged dimanganese(III,III) dimeric species that undergoes homolytic O–O bond cleavage to generate a Mn^{IV}=O adduct.[35] This abstracts a $H^{\bullet}$ from the solvent to generate [Mn^{III}(OH)(**1**^{cyp})]$^-$ (Scheme 6.2). The evidence for this mechanism stem from manometric measurements, $^{18}O_2$-labeling experiments, and substrate oxidation by the putative Mn^{IV}=O adduct. In contrast, Kovacs and coworkers have reported the formation of a mono-oxo bridged dimanganese(III,III) dimeric species from O_2 activation, with the intermediacy of a structurally characterized trans-μ-1,2-peroxo-bridged dimanganese(III,III) dimeric complex.[20,36] They propose the homolytic O–O bond cleavage of the trans-μ-1,2-peroxo-bridged dimanganese(III,III) adduct to generate a high-valent Mn^{IV}=O species, which reacts with a second equivalent of Mn^{II} to generate the observed mono-oxo bridged dimanganese(III,III) dimer. In a related system, a Mn^{III}-OH complex was generated by the hydrolysis of a similar mono-oxo bridged dimanganese(III,III) dimeric species (Scheme 6.2).[11] This mechanism was supported by spectroscopic, kinetic and computational evidence, as well as $^{18}O_2$-labeling experiments. The major difference between these two

mechanisms (Scheme 6.2) is the Mn:O stoichiometry, which is 2:1 and 4:1 for the Borovik and Kovacs systems, respectively.

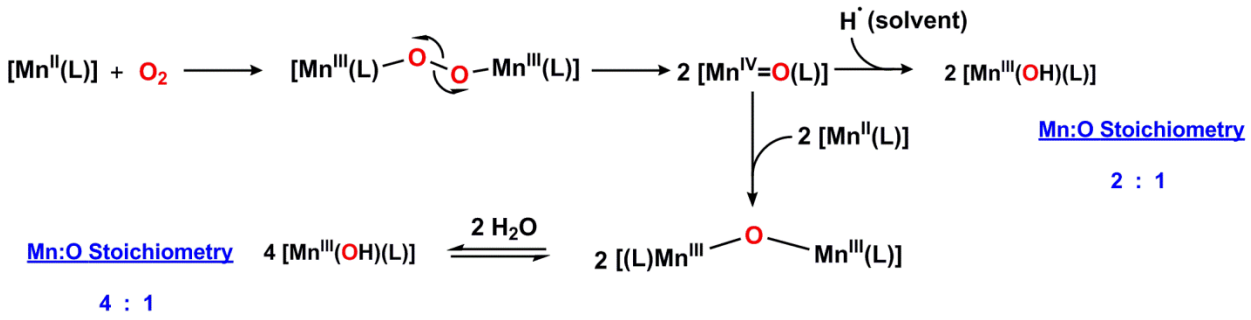

Scheme 6.2. Combined schematic representation of proposed dioxygen activation mechanisms to generate monomeric Mn^{III}-OH complexes from Mn^{II} precursors.

In light of this work, we were interested in investigating the mechanistic details of the dioxygen activation reactivity of $[Mn^{II}(dpaq)](OTf)$ to generate $[Mn^{III}(OH)dpaq)](OTf)$. Accordingly, we have performed O_2 titrations, EPR studies of reaction intermediates, and X-ray absorption experiments along with O_2 reactivity studies in the presence of organic substrates and Lewis acids. The results of these experiments are suggestive of a mechanism similar to the Kovacs system, where the Mn:O stoichiometry is 4:1. In addition, we have designed, synthesized, and characterized new supporting ligands with variable steric and electronic properties, which could also provide useful insights into the mechanism of dioxygen activation by $[Mn^{II}(dpaq)](OTf)$.

6.2. Experimental Methods

6.2.1. Materials and Instrumentation. All chemicals and solvents were obtained from commercial vendors at ACS grade or better and were used without further purification. Acetonitrile, methanol and ether were dried and degassed using a Pure Solv (2010) solvent purification system. These solvents were degassed in air-tight solvent reservoirs (4 L), by passing Ar gas at room temperature for 20 min. Acetonitrile and ether were dried using air-tight alumina columns, and methanol was dried using a drierite column. Anhydrous dichloromethane and deuterated acetonitrile (MeCN-d_3) was purchased from Acros Organics, and were degassed by four freeze-pump-thaw cycles using Schlenk techniques. All dried, degassed solvents were immediately taken into an argon-filled glove box, and were stored in tightly-sealed Schlenk glassware. All experimental procedures were carried out under an argon atmosphere unless otherwise stated. The purity of O_2 gas used was >99% and was further purified using a gas purifier column packed with drierite and 5 Å molecular sieves prior to use. [Mn^{II}(dpaq)](OTf) and [Mn^{III}(OH)(dpaq)](OTf) were prepared following previously reported methods,[12] and were stored under an inert atmosphere. Triphenylphosphine (PPh_3), 9,10-dihydroanthracene (DHA) were purchased from commercial vendors, and were recrystallized according to literature procedures prior to use.[37] All ^{1}H NMR spectra were collected on a Bruker DRZ 400 MHz spectrometer and a Bruker DPX 300 MHz spectrometer with an ONP probe. These experiments were performed at room temperature in $CDCl_3$ (δ = 7.24 ppm) unless stated otherwise. Mass spectrometry experiments were performed using an LCT Primers MicroMass electrospray time-of-flight instrument. Electronic absorption spectra were obtained on a Varian Cary 50 Bio spectrophotometer interfaced with a Unisoku cryostat (USP-203-A) capable of maintaining temperatures between 150 and 373 K.

6.2.2. Generation of [Mn^{III}(OH)(dpaq)](OTf) in the presence of PPh_3 or DHA. [Mn^{III}(OH)(dpaq)](OTf) was synthesized using [Mn^{II}(dpaq)](OTf) and O_2 in the presence of organic substrates such PPh_3 and DHA, which are known to be highly reactive towards high-valent oxidants such as Mn^{IV}=O adducts.[38,39] The oxidation of PPh_3 and DHA would provide indirect evidence for the formation of such an intermediate during the formation of [Mn^{III}(OH)(dpaq)](OTf).[35] A representative procedure is as follows. A 2.5 mM [Mn^{II}(dpaq)](OTf) solution (2.9 mg in 2 mL of MeCN) was prepared under an inert atmosphere along with 100 equiv. of either PPh_3 or DHA, and transferred to a gas-tight cuvette sealed with a pierceable septum. An excess of O_2 gas was then delivered to the solution by means of a syringe, and the formation of [Mn^{III}(OH)(dpaq)](OTf) was monitored by electronic absorption spectroscopy. The formation was complete in ~40 min and the resulting dark gold solution was analyzed by mass spectrometry for the presence of triphenylphosphine oxide or anthracene.

6.2.3. Generation of [Mn^{III}(OH)(dpaq)](OTf) in MeCN-d_3. [Mn^{III}(OH)(dpaq)](OTf) was generated in MeCN-d_3 in order to clarify if the hydrogen atom of the hydroxyl group of [Mn^{III}(OH)(dpaq)](OTf) is derived from the solvent, as observed in other reports.[35] A representative synthetic procedure is as follows. A 2.5 mM [Mn^{II}(dpaq)](OTf) solution (2.9 mg in 2 mL of MeCN-d_3) was prepared under an inert atmosphere, and transferred to a gas-tight cuvette sealed with a pierceable septum. An excess of O_2 gas was then delivered to the solution by means of a syringe, and the formation of [Mn^{III}(OH)(dpaq)](OTf) was monitored by electronic absorption spectroscopy. The formation was complete in ~40 min and the resulting dark gold solution was analyzed by mass spectrometry for the presence of $[Mn^{III}(OD)(dpaq)]^+$.

6.2.4. EPR analysis of intermediates formed during the formation of [Mn^{III}(OH)(dpaq)](OTf). [Mn^{III}(OH)(dpaq)](OTf) was generated using a 2.5 mM [Mn^{II}(dpaq)](OTf) solution (2.9 mg in 2 mL of MeCN) according to literature producers,[12] and was monitored by electronic absorption spectroscopy. Aliquots of this solution were taken out at 25%, 50%, and 75% yields of [Mn^{III}(OH)(dpaq)](OTf) (as monitored optically), and EPR samples were prepared at room temperature. These samples were flash-frozen in liquid nitrogen, and were analyzed by X-band EPR spectroscopy at 5 K.

6.2.5. Reactivity of [Mn^{II}(dpaq)](OTf) with iodosobenzene (PhIO). A 2.5 mM [Mn^{II}(dpaq)](OTf) solution (2.9 mg in 2 mL of 2,2,2-trifluoroethanol (TFE)) was prepared under an inert atmosphere, and transferred to a gas-tight cuvette sealed with a pierceable septum. Then, 2.5 equiv. of PhIO was added in TFE at room temperature, and the reaction was monitored by electronic absorption. The final solution was analyzed by mass spectrometry.

6.2.6. Reactivity of [Mn^{II}(dpaq)](OTf) with O_2 in the presence of $Sc(OTf)_3$. A 2.5 mM [Mn^{II}(dpaq)](OTf) solution (2.9 mg in 2 mL of MeCN) containing 1 equiv. of $Sc(OTf)_3$ was prepared under an inert atmosphere, and transferred to a gas-tight cuvette sealed with a pierceable septum. An excess of O_2 gas was then delivered to the solution by means of a syringe, and the solution was monitored by electronic absorption spectroscopy at room temperature.

6.2.7. Dioxygen titrations of [Mn^{II}(dpaq)](OTf). [Mn^{II}(dpaq)](OTf) solutions of 2.5 mM concentration were titrated with variable quantities of dioxygen, and the yield of [Mn^{III}(OH)(dpaq)](OTf) was quantified using its molar absorption coefficients.[12] A representative experimental procedure is as follows. A 2.5 mM [Mn^{II}(dpaq)](OTf) solution (2.9 mg in 2 mL of MeCN) was prepared under an inert atmosphere, and transferred to a gas-tight cuvette sealed with a pierceable septum. A known amount of O_2 was then delivered to the

[Mn^{II}(dpaq)](OTf) solution by means of a gas-tight syringe, and the solution was monitored by electronic absorption spectroscopy at room temperature. The cuvette was maintained under a nitrogen atmosphere for the duration of the experiment, and the pseudo-first-order rates of formation of [Mn^{III}(OH)(dpaq)](OTf) for each dioxygen concentration were calculated using the time evolution of the 550 nm absorption feature.

6.2.8. Mn *K*-edge X-ray absorption sample preparation, data collection and data analysis of [Mn^{III}(OH)(dpaq)](OTf) and [Mn^{III}(OMe)(dpaq)](OTf). Samples of [Mn^{III}(OH)(dpaq)](OTf) for Mn *K*-edge X-ray absorption spectroscopic (XAS) analysis were prepared from 15 mM solutions in MeCN and H_2O. [Mn^{III}(OMe)(dpaq)](OTf) samples were prepared with 15 mM solutions in MeOH. Approximately 400 μL of the solution was transferred to a sample holder covered with Kapton tape, and was frozen in liquid nitrogen. XAS data were collected on beamline X3B at the National Synchrotron Light Source (NSLS), Brookhaven National Laboratory (storage ring conditions, 2.8 GeV, 100-300 mA). The sample was maintained at 25 K with a helium displex closed-cycle cryostat over the energy rage 6.4-7.4 keV (Si(111) monochromator). A solid-state 13-element germanium detector was used to obtain data as fluorescence excitation spectra. Contamination of higher harmonics radiation was minimized by using a harmonic rejection mirror. Background signals were minimized using a 6 μm Cr filter. A Mn foil spectrum was recorded simultaneously as an internal energy calibration, and the inflection point of the *K*-edge energy was assigned to 6539.0 eV. The spectra were measured with 5 eV steps below the edge, 0.3 eV steps in the edge region, and steps equivalent to 0.05 $Å^{-1}$ increments above the edge (region borders were 6354, 6529, and 6554 eV). XAS data reduction and averaging were fully performed using the program EXAFSPAK. Pre-edge background intensity was removed by fitting a Gaussian function to the pre-edge background and subtracting

this function from the whole spectrum. Then, the spectrum was fit with a three-segment spline function with fourth-order polynomial components to remove low-frequency background. The *k*-space window utilized for analysis of all samples was $k = 2 – 12$ Å^{-1}.

6.2.9. Synthesis of Hdpaq$^{2\text{-Me}}$ ligand. 2-methylquinolin-8-amine (1.00 g, 6.32 mmol) and 2-bromoacetyl bromide (0.725 mL, 8.32 mmol) were combined in acetonitrile (20 mL) along with excess Na_2CO_3 (1.03g, 9.70 mmol) under an inert atmosphere, and the resulting solution was stirred for 30 min at 0 ^{o}C. The solution was then allowed to warm up to room temperature, and was filtered through celite, and evaporated to dryness under reduced pressure. The solid product was combined with di-picolyl amine (1.5 mL, 8.33 mmol) and Na_2CO_3 (1.03g, 9.70 mmol) in acetonitrile (40 mL), and was stirred overnight at 0 ^{o}C under an inert atmosphere. The final reaction mixture was filtered through celite, and evaporated to dryness. The crude product was purified by flash chromatography on a silica column using MeOH/DCM. The pure ligand (Hdpaq$^{2\text{-Me}}$; Figure 6.2) was isolated in good yield (77%) as a brown oil, and was characterized by ^{1}H NMR and ESI-MS (Figures A5.1 and A5.2). ^{1}H NMR data (400 MHz) for Hdpaq$^{2\text{-Me}}$ ($CDCl_3$, δ) = 11.52 (s, 1H), 8.70 (dd, J = 6.4, 2.7 Hz, 1H), 8.50 – 8.40 (m, 2H), 8.02 (d, J = 8.3 Hz, 1H), 7.92 (d, J = 7.8 Hz, 2H), 7.54 (td, J = 7.6, 1.9 Hz, 2H), 7.46 – 7.28 (m, 3H), 7.15 – 7.02 (m, 2H), 3.93 (s, 4H), 3.45 (s, 2H), 2.82 (d, J = 4.3 Hz, 3H). ESI-MS: {[Hdpaq$^{2\text{-Me}}$ + Na]$^{+}$} *m/z* = 420.1766 (calc. = 420.1800).

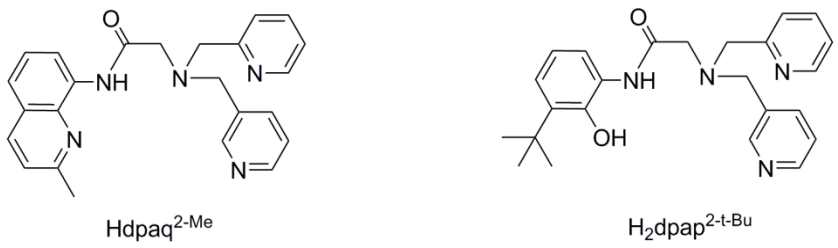

Figure 6.2. Novel ligands included in this study as modifications to the dpaq platform.

6.2.10. Synthesis of $H_2dpap^{2\text{-t-Bu}}$ ligand. 2-amino-6-*tert*-butylphenol (250 mg, 1.51 mmol) and 2-bromoacetyl bromide (0.157 mL, 1.80 mmol) were combined in acetonitrile (10 mL) along with excess Na_2CO_3 (223.4 mg, 2.11 mmol) under an inert atmosphere, and the resulting solution was stirred for 30 min at 0 ^oC. The solution was then allowed to warm up to room temperature, and was filtered through celite, and evaporated to dryness under reduced pressure. The solid product was combined with di-picolyl amine (0.324 mL, 1.80 mmol) and Na_2CO_3 (223.4 mg, 2.11 mmol) in acetonitrile (20 mL), and was stirred overnight at 0 ^oC under an inert atmosphere. The final reaction mixture was filtered through celite, and evaporated to dryness. The crude product was then purified by flash chromatography on a silica column using MeOH/DCM. The pure ligand ($H_2dpap^{2\text{-t-Bu}}$; Figure 6.2) was isolated in moderate yield (45%) as a dark brown oil, and was characterized by ^1H NMR and ESI-MS (Figures A5.3 and A5.4). ^1H NMR data (400 MHz) for $H_2dpap^{2\text{-t-Bu}}$ ($CDCl_3$, δ) = 10.97 (s, 1H), 8.88 – 8.43 (m, 2H), 7.74 – 7.57 (m, 2H), 7.50 – 7.37 (m, 1H), 7.29 (d, J = 7.9 Hz, 2H), 7.24 (ddd, J = 7.6, 4.9, 1.3 Hz, 2H), 7.17 (s, 1H), 6.91 – 6.83 (m, 1H), 3.98 (s, 4H), 3.57 (s, 2H), 1.48 (d, J = 1.5 Hz, 9H). ESI-MS: $\{[H_2dpap^{2\text{-t-Bu}} + Na]^+\}$ m/z = 427.2045 (calc. = 427.2110).

6.2.11. Preparation of $[Mn^{II}(dpaq^{2\text{-Me}})](OTf)$. To a stirred solution of 103 mg (0.26 mmol) of H-$dpaq^{2\text{-Me}}$ in 2 mL of MeOH was added 92 mg (0.26 mmol) of $Mn^{II}(OTf)_2$ in 2 mL of MeOH, followed by 25 mg (0.26 mmol) of NaO^tBu in 2 mL of MeOH under an inert atmosphere. The $Mn^{II}(OTf)_2$ salt was generated using a previously reported method.[40] The orange colored resultant solution was stirred overnight, and then filtered and evaporated to dryness under vacuum. The solid product was recrystallized using MeOH/ Et_2O to yield yellow crystals of $[Mn^{II}(H\text{-}dpaq^{2\text{-Me}})](OTf)$. Crystals for X-ray diffraction analysis were obtained by subsequent recrystallization of the final solid product in the MeOH/ Et_2O solvent system.

[Mn^{II}(dpaq$^{2\text{-Me}}$)](OTf) was further characterized by ESI-MS (Figure A5.5). {[Mn^{II}(H-dpaq$^{2\text{-Me}}$)]$^{+}$} *m/z* = 451.1177 (calc. 451.1205).

6.2.12. X-ray Diffraction Data Collection and Analysis for [Mn^{II}(dpaq$^{2\text{-Me}}$)](OTf). A yellow colored single-domain crystal of [Mn^{II}(dpaq$^{2\text{-Me}}$)](OTf) was suspended with Paratone N oil on a MiteGen MicroMount and placed on a goniometer head in a cold nitrogen stream at 100 K for a single-crystal X-ray structure determination. Monochromatic X-rays were provided by a Bruker diffractometer equipped with Helios high-brilliance multilayer optics, a Platinum 135 CCD detector and a Bruker MicroStar microfocus rotating anode X-ray source operating at 45 kV and 60 mA. Intensity data (6590 0.5°-wide ω- or φ-scan frames with counting times of 4-6 seconds each) were collected with the Bruker program SMART[41] and diffracted intensities were measured with the Bruker program SAINT[42]. The space group[43] and crystallographic data are summarized in Table A5.1. The Bruker software package SHELXTL was used to solve the structure and locate all nonhydrogen atoms with "direct methods" techniques. Each methyl group was incorporated into the structural model as a fixed rigid group (using idealized sp^3-hybridized geometry and a C–H bond length of 0.98 Å) with idealized "staggered" geometry. The remaining hydrogen atoms were included in the structural model as idealized atoms (assuming sp^2- or sp^3-hybridization of the carbon and C–H bond lengths of 0.95 - 0.99 Å). The isotropic thermal parameters of all idealized hydrogen atoms were fixed at values 1.2 (nonmethyl) or 1.5 (methyl) times the equivalent isotropic thermal parameter of the carbon atom to which they are covalently bonded.

All three triflate anions are 50:50 disordered over two closely separated sites in the unit cell. The first and third triflates are disordered about crystallographic inversion centers at (½, 0, 0) and (½, 0, ½), respectively. The bond lengths and angles of the triflates were mildly

restrained to have similar values. All stages of weighted full-matrix least-squares refinement were conducted using Fo^2 data with the SHELXTL XLMP v2013/4 software package.[44] The final structural model incorporated anisotropic thermal parameters for all non-hydrogen atoms and isotropic thermal parameters for all hydrogen atoms.

6.2.13. Preparation of [Mn^{III}(OH)($dpaq^{2\text{-}Me}$)](OTf). A 2.5 mM [Mn^{II}($dpaq^{2\text{-}Me}$)](OTf) solution (3.0 mg in 2 mL of MeCN) was prepared under an inert atmosphere and transferred to a gas-tight cuvette sealed with a pierceable septum. An excess of O_2 gas was then delivered to the solution by means of a syringe, and the formation of [Mn^{III}(OH)($dpaq^{2\text{-}Me}$)](OTf) was monitored by electronic absorption spectroscopy. The formation was complete in ~250 min and the resulting dark red solution was evaporated to dryness under reduced pressure. The solid residue was then recrystallized using MeCN/ Et_2O. (3.2 mg/ 98% yield). Synthesis of [Mn^{III}(OH)($dpaq^{2\text{-}Me}$)](OTf) on a larger scale was undertaken to obtain suitable material for X-ray crystallographic analysis. In this procedure, O_2 gas was passed through an acetonitrile solution (20 mg in 5 mL) of [Mn^{II}($dpaq^{2\text{-}Me}$)](OTf), and the completion of the formation of [Mn^{III}(OH)($dpaq^{2\text{-}Me}$)](OTf) was confirmed by ESI-MS and electronic absorption spectroscopy. The resulting solution was evaporated to dryness under reduced pressure, and the solid residue was recrystallized using MeCN/ Et_2O. Dark red [Mn^{III}(OH)($dpaq^{2\text{-}Me}$)](OTf) crystals of X-ray crystallographic quality were obtained by repetitive recrystallization, and were further characterized by ESI-MS (Figure A5.6). ESI-MS: {[Mn^{III}(OH)($dpaq^{2\text{-}Me}$)]$^+$} *m/z* = 468.1204 (calc. 468.1232).

6.2.14. X-ray Diffraction Data Collection and Analysis for [Mn^{III}(OH)($dpaq^{2\text{-}Me}$)](OTf). A deep red single-domain crystal of [Mn^{III}(OH)($dpaq^{2\text{-}Me}$)](OTf) was suspended with Paratone N oil on a MiteGen MicroMount and placed on a goniometer head in a cold nitrogen stream at 100 K for a single-crystal X-ray structure determination. Monochromatic X-rays were

provided by a Bruker diffractometer equipped with Helios high-brilliance multilayer optics, a Platinum 135 CCD detector and a Bruker MicroStar microfocus rotating anode X-ray source operating at 45 kV and 60 mA. Intensity data (4431 0.5°-wide ω- or φ-scan frames with counting times of 5-10 seconds each) were collected with the Bruker program SMART[41] and diffracted intensities were measured with the Bruker program SAINT.[42] The space group[43] and crystallographic data are summarized in Table A5.2. The Bruker software package SHELXTL was used to solve the structure and locate all nonhydrogen atoms with "direct methods" techniques. Hydrogen atoms were located from a difference Fourier and initially included in the structural model as independent isotropic atoms whose parameters were allowed to vary in least-squares refinement cycles. In the final least-squares refinement cycles, the acetonitrile methyl group was included in the structural model as an idealized sp^3-hybridized rigid rotor (with C–H bond lengths of 0.98 Å) that was allowed to rotate freely about its C–C bond and the isotropic thermal parameter of H(11a) was fixed at a value 1.2 times the equivalent isotropic thermal parameter of carbon atom C(11). The triflate CF_3 group is 88:12 rotationally disordered about the C–S bond and the three minor-occupancy fluorine sites were incorporated in the structural model with isotropic thermal parameters. All stages of weighted full-matrix least-squares refinement were conducted using F_o^2 data with the SHELXTL XLMP v2013/4 software package.[44] The final structural model incorporated anisotropic thermal parameters for all full- and major-occupancy non-hydrogen atoms and isotropic thermal parameters for all hydrogen atoms and the three minor-occupancy fluorine atoms.

6.2.15. Preparation of [$Mn^{II}(H_2dpap^{2\text{-}t\text{-}Bu})$]. To a stirred solution of 105 mg (0.26 mmol) of $H_2dpap^{2\text{-}t\text{-}Bu}$ in 2 mL of MeOH was added 92 mg (0.26 mmol) of $Mn^{II}(OTf)_2$ in 2 mL of MeOH, followed by 50 mg (0.52 mmol) of NaO^tBu in 2 mL of MeOH under an inert

atmosphere. The $Mn^{II}(OTf)_2$ salt was generated using a previously reported method.[40] The red colored resultant solution was stirred overnight and then filtered and evaporated to dryness under vacuum. The solid product was recrystallized using MeOH/ Et_2O. Note: The metalation reaction of $H_2dpap^{2\text{-t-Bu}}$ generated excessive amounts of white insoluble solid, and the yield of the final crystalline solid was observed to be lower (~40%) than the typically expected yield for a metalation procedure.

6.3. Results and Analysis

6.3.1. Generation of $[Mn^{III}(OH)(dpaq)](OTf)$ in the presence of PPh_3, DHA, and MeCN-d_3.

High-valent Mn^{IV}=O oxidants are known to rapidly oxidize substrates with weak C–H bonds, such as DHA (BDFE = 76 kcal/mol in DMSO[45]), via proton-coupled electron transfer (PCET) reactions to generate substrate based radicals. In the case of DHA, a subsequent PCET process with a second equivalent of the oxidant generates anthracene as the major organic product (Note: anthraquinone may also form due to O_2 quenching of the substrate based radical, or hydroxyl rebound).[38] Thus, if such a high-valent intermediate is formed during dioxygen activation by $[Mn^{II}(dpaq)](OTf)$, it is expected to rapidly oxidize DHA to anthracene (or anthraquinone), which is detectable by ESI-MS, electronic absorption spectroscopy and GC-MS. However, under these conditions, we did not observe the formation of any anthracene in solution. Similarly, when dioxygen was reduced by $[Mn^{II}(dpaq)](OTf)$ in the presence of an excess of PPh_3, ESI-MS of the final solution did not provide evidence for the formation of $P(O)Ph_3$ as a result of an oxo-atom transfer (OAT) reactivity. Furthermore, the rates of formation of $[Mn^{III}(OH)(dpaq)](OTf)$ in the presence of these substrates were comparable to those without any organic substrate. These observations could either indicate the absence of a high-valent

Mn^{IV}=O oxidant that forms during the reaction, or the extremely rapid reactivity of such an intermediate towards Mn^{II} starting complex in solution (as previously observed[36]), making it challenging to intercept it with an external organic substrate. In fact, there have been reports where some Mn^{IV}=O oxidants have oxidized DHA at rates much slower than expected, regardless of the weak C–H bond strength of this substrate.[46] In such a scenario, rather than oxidizing DHA, the proposed Mn^{IV}=O adduct would rapidly react with [Mn^{II}(dpaq)](OTf) leading to the formation of a monooxo-bridged dimanganese(III,III) dimer, which could then hydrolyze to generate [Mn^{III}(OH)(dpaq)](OTf). Furthermore, when [Mn^{II}(dpaq)](OTf) was oxygenated in MeCN-d_3, the sole product observed (by ESI-MS) was [Mn^{III}(OH)(dpaq)](OTf), not [Mn^{III}(OD)(dpaq)](OTf). This result reveals that the hydrogen atom of the hydroxyl group of [Mn^{III}(OH)(dpaq)](OTf) is not MeCN derived. This stands in contrast to the Mn^{III}-OH adduct reported by Borovik and coworkers, where the –OH proton is solvent-derived.[35]

6.3.2. EPR analysis of intermediates generated during the formation of [Mn^{III}(OH)(dpaq)](OTf). The perpendicular mode X-band EPR spectra corresponding to frozen acetonitrile solutions (at 5 K) of 25%, 50%, and 75% yields of [Mn^{III}(OH)(dpaq)](OTf) with respect to the starting Mn^{II} concentration are shown in Figure 6.3. At 25% formation of [Mn^{III}(OH)(dpaq)](OTf), a prominent derivative-shaped signal is observed at 350 mT, which is indicative of the large excess of unreacted [Mn^{II}(dpaq)](OTf) in solution.[12] When 50% [Mn^{III}(OH)(dpaq)](OTf) is formed, the solution EPR spectrum displays a unique 14-line signal, although the derivative shape of the Mn^{II} signal is still evident. Such multi-line EPR spectra are generally indicative of dimeric metal species such as bis(μ-oxo)dimanganese complexes.[9,47-50] This multi-line EPR feature could also result from resolving the hyperfine splitting due to nitrogen nuclei of the supporting ligand, although the observed splitting constant of ~10 mT is

most consistent with a dimeric Mn species.[47] The EPR spectra of such species often display multi-line signals due to the hyperfine splitting induced by the two Mn centers. Although the source of this multi-line EPR signal is currently unclear, the evidence of potential formation of a dimeric Mn species en route to [Mn^{III}(OH)(dpaq)](OTf) is intriguing. At 75% formation, the multi-line EPR signal is reduced in intensity. The final EPR spectrum is featureless,[12] due to the >99% yield of [Mn^{III}(OH)(dpaq)](OTf). Furthermore, the parallel mode EPR spectra of these samples were observed to be featureless under the same conditions.

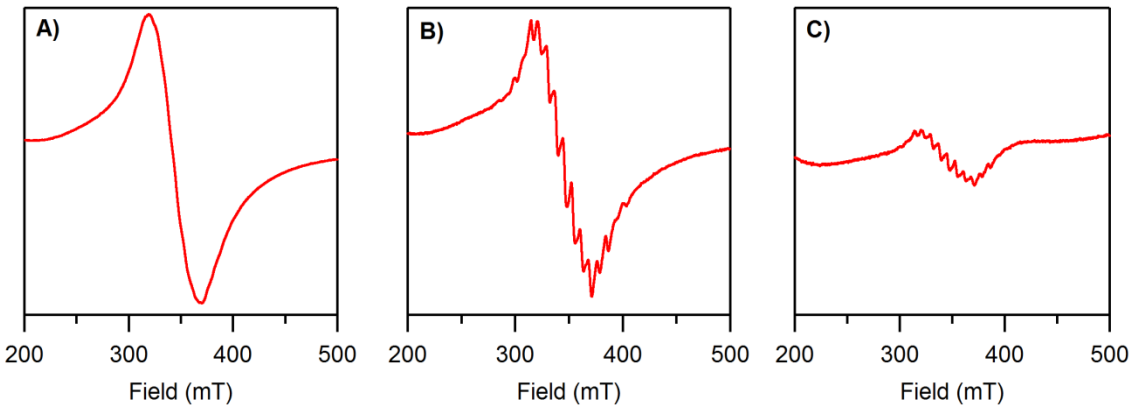

Figure 6.3. Perpendicular mode X-band EPR spectra for A) 25% B) 50% and C) 75% formation of [Mn^{III}(OH)(dpaq)](OTf) from [Mn^{II}(dpaq)](OTf) and O_2 collected in frozen MeCN solutions at 5 K.

6.3.3. Reactivity of [Mn^{II}(dpaq)](OTf) with iodosobenzene (PhIO). PhIO is commonly used as a two-electron oxidant and an oxo-atom transfer reagent to generate Mn^{IV}=O species from Mn^{II} precursors.[38,51] Furthermore, a majority of non-porphyrinoid Mn^{IV}=O adducts exhibit enhanced stabilities in TFE,[38,51] the reasons for which are not fully understood. In light of this work, we attempted the generation of [Mn^{IV}(O)(dpaq)]$^+$ by treating [Mn^{II}(dpaq)](OTf) with 2.5 equiv. of PhIO in TFE at room temperature. [Mn^{II}(dpaq)](OTf) reacted rapidly with PhIO, generating absorption features with striking similarities to those of [Mn^{III}(OH)(dpaq)](OTf)[12]

(Figure 6.4). A mass spectrometric analysis of the final reaction indicated the clean conversion of $[Mn^{II}(dpaq)](OTf)$ to $[Mn^{III}(OCH_2CF_3)(dpaq)]^+$ (Figure A5.7). ESI-MS: $\{[Mn^{III}(OCH_2CF_3)(dpaq)]^+\}$ *m/z* = 536.1119 (calc. = 536.1106). Stack and coworkers have also observed the oxidation of the $[Mn^{II}(PY5)]^{2+}$ complex to generate $[Mn^{III}(OH)(PY5)]^+$ when treated with 1 equiv. of PhIO in MeCN under ambient conditions.[52] These results could be suggestive of an initial generation of a highly reactive Mn^{IV}=O species in solution, which reacts further to generate the final Mn^{III}-OH species. However, if the proposed Mn^{IV}=O species reacts with solvent in a PCET process to generate the final Mn^{III} species, one would expect to observe its rapid reactivity with the much weaker C–H bonds of DHA. Thus, these results collectively suggest that $[Mn^{IV}(O)(dpaq)]^+$ could most likely react with excess Mn^{II} in solution for the generation of $[Mn^{III}(OH)(dpaq)](OTf)$, as previously proposed by Kovacs and coworkers for the $[Mn^{III}(OH)(S^{Me2}N_4(tren))]^+$ system.[36]

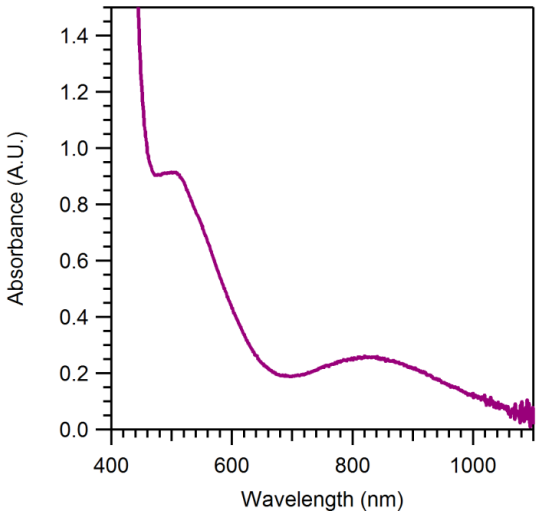

Figure 6.4. The final absorption spectrum of the reaction between a 2.5 mM solution of $[Mn^{II}(dpaq)](OTf)$ and 2.5 equiv. of PhIO in TFE at 25 °C.

6.3.4. Reactivity of [Mn^{II}(dpaq)](OTf) with O_2 in the presence of $Sc(OTf)_3$. When 1 equiv. of $Sc(OTf)_3$ was added into a 2.5 mM solution of [Mn^{II}(dpaq)](OTf), it changed color from light yellow to colorless. Furthermore, the weak absorption feature of [Mn^{II}(dpaq)](OTf) centered at 540 nm[12] could not be observed anymore (Figure 6.5). Most importantly, this solution did not react with dioxygen in air even under prolonged exposure times (up to 5 days). These observations reveal that the strong Lewis acid Sc^{3+} has modified the electronic properties of the Mn^{II} center, shutting down its dioxygen activation capabilities. We propose strong interactions of Sc^{3+} with the carbonyl group of the axial amide functionality of the dpaq ligand increases the Mn^{III}/Mn^{II} reduction potential, deactivating the dioxygen activating pathway of [Mn^{II}(dpaq)](OTf). This proposal can be interrogated by carrying out cyclic voltammetric experiments of [Mn^{II}(dpaq)](OTf) in the presence of Sc^{3+} to gain insight into the modified Mn^{III}/Mn^{II} reduction potential. Our observations of the effects of $Sc(OTf)_3$ on O_2 reduction is in contrast to what has been observed by Borovik and coworkers,[33] where the dioxygen activation rates of $[Mn^{II}(MST)]^-$ were enhanced in the presence of redox-inactive Lewis acids. In those systems, Lewis acids were thought to facilitate the manganese-mediated dioxygen reduction, which leads to the observed rate enhancement. Studies attempting structural characterization of the [Mn^{II}(dpaq)](OTf)•••Sc^{3+} adduct are currently underway. In addition, the reactivity of [Mn^{II}(dpaq)](OTf) with other oxidants, specifically PhIO, in the presence of Sc^{3+} will be performed by others.

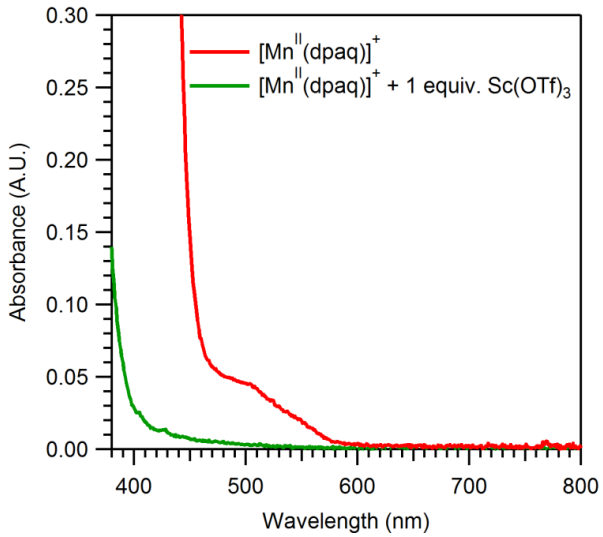

Figure 6.5. Changes observed in the electronic absorption spectrum of [Mn^{II}(dpaq)](OTf) when treated with 1 equiv. of $Sc(OTf)_3$ in MeCN at 25 ^{o}C.

6.3.5. Dioxygen titrations of [Mn^{II}(dpaq)](OTf). Dioxygen titrations were performed by the addition of variable volumes of dioxygen (0.1 – 10 equiv. with respect to initial Mn^{II} concentration) by means of a gas-tight syringe into a cuvette containing a 2.5 mM solution of [Mn^{II}(dpaq)](OTf). As seen in Figure 6.6A, the final yield of [Mn^{III}(OH)(dpaq)](OTf) varied as a function of [O_2]. The experimental yields of [Mn^{III}(OH)(dpaq)](OTf) for 0.1 – 1 equiv. of O_2 are summarized in Table 6.3. A comparison of those yields with the expected yields for Mn:O stoichiometries of 2:1 and 4:1 reveal that the current experimental results are inconclusive of the actual Mn:O stoichiometry. However, the experimentally observed [Mn^{III}(OH)(dpaq)](OTf) yields at 0.1 and 0.18 equiv. of O_2 are higher than what is expected for a Mn:O stoichiometry of 2:1, which could be suggestive of a 4:1 stoichiometry. Furthermore, when samples with less than a 100% yield were exposed to the atmosphere following the experiment, the yield of [Mn^{III}(OH)(dpaq)](OTf) started increasing further, ultimately leveling off at 100%. This observation provided evidence that our experimental setup was reliable for carrying out air-free O_2 titrations of [Mn^{II}(dpaq)](OTf). It should also be noted that during these experiments, O_2

would partition between gas phase and solution phase in order to dissolve in MeCN, prior to reacting with [Mn^{II}(dpaq)](OTf). Thus, due to the considerable head space inside the cuvette, only a fraction of added O_2 will react with [Mn^{II}(dpaq)](OTf) during a given trial. Manometric experiments would potentially aid in minimizing similar issues, as the direct uptake of O_2 due to reacting with [Mn^{II}(dpaq)](OTf) will be measured in terms of pressure differences in the head-space of the reaction vessel. Future work will involve such manometric and $^{18}O_2$-labeling experiments, which will potentially yield a clearer insight into the Mn:O stoichiometry of this reaction. Furthermore, the pseudo-first-order rate constants of formation of [Mn^{III}(OH)(dpaq)](OTf) in these experiments display a linear dependence on the [O_2] (Figure 6.6B) with a second-order rate constant (k_2) of 3.3(1) × 10^{-5} M^{-1} s^{-1}. This reveals that dioxygen is involved in the overall rate-limiting step in the formation of [Mn^{III}(OH)(dpaq)](OTf).

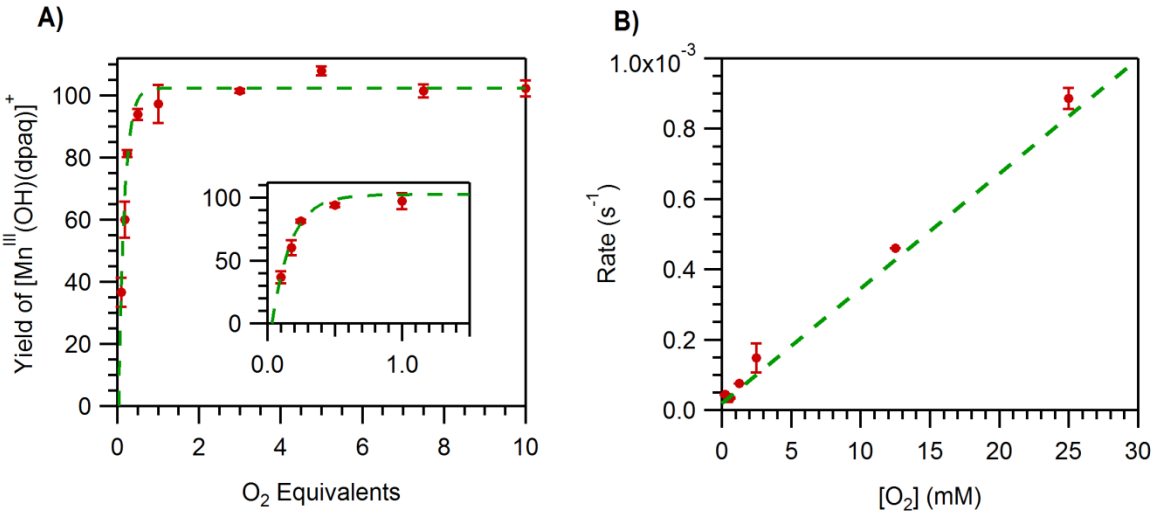

Figure 6.6. A) The yields of [Mn^{III}(OH)(dpaq)](OTf) when [Mn^{II}(dpaq)](OTf) was treated with 0.1 – 10 equiv. of gaseous O_2 in MeCN at 25 ^oC. Inset shows the expanded region from 0.1 – 1 equiv. of gaseous O_2. B) Pseudo-first-order rate constants for the formation of [Mn^{III}(OH)(dpaq)](OTf) versus [O_2] calculated for a 2.5 mM solution of [Mn^{II}(dpaq)](OTf) in MeCN at 25 ^oC. The second order rate constant k_2 was calculated from the linear correlation of the pseudo-first-order rate constants and O_2 concentrations.

Table 6.3. The variation of experimental yields of [Mn^{III}(OH)(dpaq)](OTf) as a function of added O_2 equivalents (calculated at 25 ^oC in MeCN), and the expected yields for the previously proposed Mn:O stoichiometries.

[a] O_2 equiv.	Exp. Yields %	Mn : O 4 : 1 Expected %	Mn : O 2 : 1 Expected %
0.1	37(4)	40	20
0.18	60(5)	72	36
0.25	82(1)	100	50
0.5	94(1)	100	100
1	97(6)	100	100

[a] O_2 equiv. are calculated with respect to initial [Mn^{II}(dpaq)](OTf) concentration.

6.3.6. Mn *K*-edge X-ray absorption characterization of [Mn^{III}(OH)(dpaq)](OTf). Mn *K*-edge X-ray absorption spectroscopic data collected for 15 mM solutions of [Mn^{II}(dpaq)](OTf) in MeCN, [Mn^{III}(OH)(dpaq)](OTf) in MeCN and H_2O, and [Mn^{III}(OMe)(dpaq)](OTf) in MeOH reveal interesting trends. The EXAFS data for [Mn^{II}(dpaq)](OTf) display intense features at ~1.7 and 2.5 Å in its Fourier transform (Figure 6.7), which compare well with the Mn–N distances and Mn–C distances observed in its X-ray crystal structure (Note: the actual distances between Mn and the scattering atoms that result from the Fourier transform is R' + ≈0.4 Å following the phase shift, and thus, these distances correspond to Mn–N and Mn–C distances of ~2.1 Å and ~2.9 Å respectively). Thus, the [Mn^{II}(dpaq)](OTf) EXAFS data are representative of a typical monomeric metal species, where the Fourier transform is dominated by an intense feature corresponding to its primary coordination sphere. In contrast, the EXAFS data for [Mn^{III}(OH)(dpaq)](OTf) in MeCN exhibits several strong features up to ~3.4 Å in its Fourier transform (Figure 6.7), which is most reminiscent of dimeric Mn species rather than a monomeric complex.[47] Typically, dimeric metal species exhibit long-range scattering with low signal-to-noise due to the presence of the second metal center, which result in intense Fourier

transform features up to longer distances. Thus, we propose that in solution, [Mn^{III}(OH)(dpaq)](OTf) is in equilibrium with its monooxo-bridged dimanganese(III,III) dimer, [(Mn^{III}(dpaq))$_2$(μ-O)]$^{2+}$ (Scheme 6.3), which becomes the dominant form in solution at extremely low temperatures. Accordingly, in H_2O, the equilibrium is biased in the reverse direction, and the monomeric [Mn^{III}(OH)(dpaq)](OTf) form dominates over the dimeric species. This proposal is further supported by the EXAFS and Fourier transform data for [Mn^{III}(OH)(dpaq)](OTf) collected in H_2O (Figure 6.7), where the data are indicative of a predominant monomeric metal species (compare the yellow, red, and green spectra in Figure 6.7). Moreover, the X-ray absorption near edge spectra (XANES) for both MeCN and H_2O samples of [Mn^{III}(OH)(dpaq)](OTf) exhibit identical edge energies (fit to the first inflection point) at ~6541 eV (Figure 6.8). In spite of the dissimilarities in their EXAFS data, this indicates that both MeCN and H_2O samples contain Mn species with same oxidation state, implying that the Mn^{III} oxidation state is preserved during the dimerization of [Mn^{III}(OH)(dpaq)](OTf). Furthermore, the Fourier transform of the [Mn^{III}(OH)(dpaq)](OTf) data collected in MeCN exhibits the most intense feature at ~3.3 Å, which corresponds to a Mn–Mn distances of ~3.7 Å with the phase shift. This is slightly longer than the often observed Mn–Mn distance for other monooxo-bridged dimanganese(III,III) dimers found in literature (~3.5 Å).[11,53,54] To further support this proposal, [Mn^{III}(OMe)(dpaq)](OTf) complex does not display any dimerization in frozen MeOH solution (Figure 6.7). Unfortunately, obtaining high-quality fits for these data sets using the structural parameters of the proposed species has been unsuccessful thus far. It is noteworthy that the presence of multiple metal species in solution could contribute significantly to the difficulties involved with fitting, as the data represents an average signal with contributions from all Mn centers present in the sample.

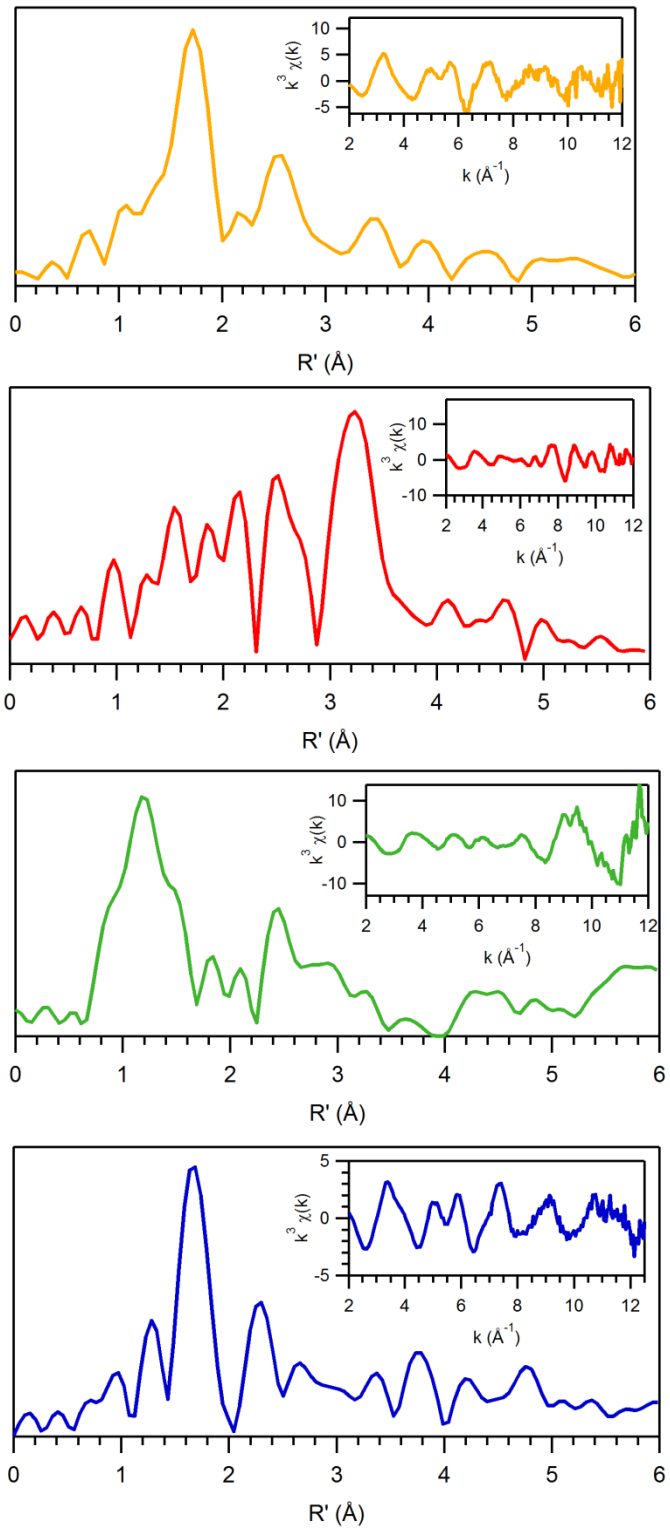

Figure 6.7. Fourier transforms of Mn *K*-edge EXAFS data [$k^3\chi(k)$] and raw EXAFS spectra (insets) for 15 mM [Mn^{II}(dpaq)](OTf) (yellow), [Mn^{III}(OH)(dpaq)](OTf) in MeCN (red) and H_2O (green), and [Mn^{III}(OMe)(dpaq)](OTf) in MeOH (blue).

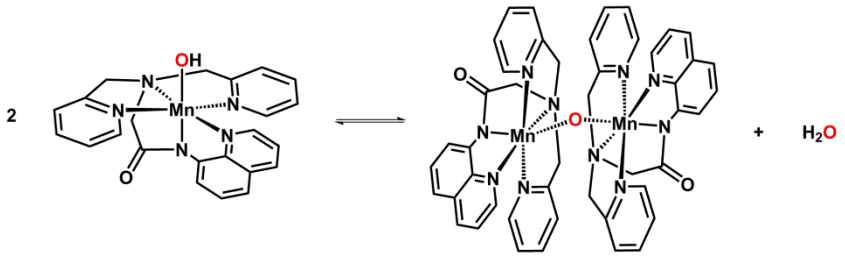

Scheme 6.3. The proposed dimerization of [Mn^{III}(OH)(dpaq)](OTf) in solution forming the monooxo-bridged dimanganese(III,III) species.

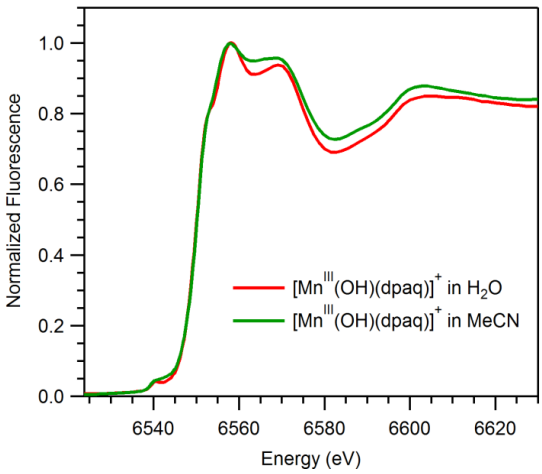

Figure 6.8. Normalized Mn *K*-edge XANES spectra for 15 mM [Mn^{III}(OH)(dpaq)](OTf) in MeCN (green) and H_2O (red) collected at 20 K.

6.3.7. Structural properties of [Mn^{II}(dpaq$^{2\text{-Me}}$)](OTf). To further investigate the proposal of the involvement of dimeric metal species during the formation of [Mn^{III}(OH)(dpaq)](OTf), we have designed and synthesized a derivative of the dpaq ligand, dpaq$^{2\text{-Me}}$. This ligand contains extra steric bulk (a methyl group) close to the proposed site of dioxygen activation, which should narrow down the feasibility of dimeric species formation due to interligand steric clash induced by the methyl groups. The X-ray diffraction structure of the corresponding Mn^{II} complex, [Mn^{II}(dpaq$^{2\text{-Me}}$)](OTf), shows two [Mn^{II}(dpaq$^{2\text{-Me}}$)](OTf) molecules in the smallest asymmetric unit. Although these two molecules do show slight differences in bond lengths and angles, each consists of a Mn^{II} center in a highly distorted

octahedral geometry (Figure 6.9), with two pyridine ligands (N4, N5), the quinoline ligand (N1) and the tertiary amine (N3) in the equatorial plane, and the amide nitrogen (N2) at an axial position. The other axial site is occupied by the amide oxygen atom (O1) of a second $[Mn^{II}(dpaq^{2\text{-}Me})](OTf)$ molecule, forming an overall polymeric structure. Table 6.4 summarizes the structural properties for the two cations of $[Mn^{II}(dpaq^{2\text{-}Me})]^{+}$ in the asymmetric unit. For the two cations, the angle between the axial ligands (O1–Mn–N2) is ~170° and the angles between the equatorial ligands vary from ~75° to ~110°, indicating large deviations from idealized octahedral geometry. Three triflate ions and two acetonitrile molecules are also present in the crystal structure but do not interact with the Mn^{II} centers (Mn–O and Mn–N distances of ~5.6 Å and ~5.0 Å respectively). All Mn^{II}–ligand distances are in the range of 2.2 to 2.3 Å, which is typical for a high-spin Mn^{II} center.[55,56] Notably, the C10–O1 distance of the amide ranges from 1.255 to 1.259 Å, which is typical of a C=O double bond. Thus, the Mn–O1 interaction is likely weak, and presumably the polymeric structure observed in the crystal structure reverts to separate monomeric entities in solution as observed in $[Mn^{II}(dpaq)](OTf)$.[12] The structure of $[Mn^{II}(dpaq^{2\text{-}Me})](OTf)$ also compares well with the recently reported $[Mn(dpaq)(NO)](ClO_4)$ complex.[57] The shorter bond lengths in that complex are expected given the formulation of that complex as a low-spin Mn^{II} center antiferromagnetically coupled to an NO radical.

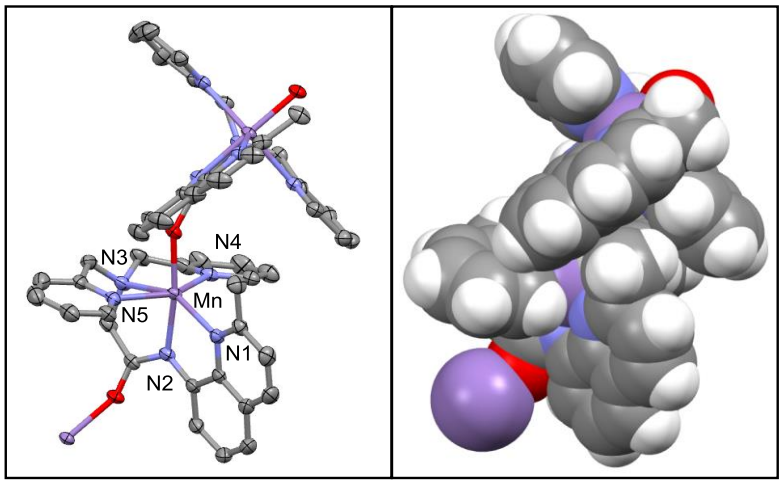

Figure 6.9. ORTEP (left) and space-filling (right) diagrams showing the two cations in the asymmetric unit of the X-ray crystal structure of $[Mn^{II}(dpaq^{2\text{-}Me})]^{+}$. ORTEP diagram shows 50% probability thermal ellipsoids. Hydrogen atoms, non-coordinating solvent molecules and triflate counter anions are excluded for clarity.

Table 6.4. Selected bond lengths (Å) and angles (deg) for $[Mn^{II}(dpaq^{2\text{-}Me})](OTf)$ (two cations in the asymmetric unit denoted as A and B), and $[Mn^{III}(OH)(dpaq^{2\text{-}Me})](OTf)$.

$[Mn^{II}(dpaq^{2\text{-}Me})]^{+}$ (A)			
Mn–O1C	2.094(2)	O1C–Mn–N2A	169.50(9)
Mn–N2A	2.181(2)	N4A–Mn–N5A	149.73(9)
Mn–N1A	2.265(2)	N1A–Mn–N3A	150.76(9)
Mn–N3A	2.304(2)	N4A–Mn–N2A	89.97(9)
Mn–N4A	2.272(3)	N1A–Mn–N2A	74.50(9)
Mn–N5A	2.292(3)	N3A–Mn–N2A	77.42(9)
$[Mn^{II}(dpaq^{2\text{-}Me})]^{+}$ (B)			
Mn–O1A	2.116(2)	O1A–Mn–N2B	170.36(9)
Mn–N2B	2.173(3)	N4B–Mn–N5B	149.05(10)
Mn–N1B	2.268(3)	N1B–Mn–N3B	150.55(9)
Mn–N3B	2.316(3)	N4B–Mn–N2B	87.33(9)
Mn–N4B	2.275(3)	N1B–Mn–N2B	4.59(9)
Mn–N5B	2.286(3)	N3B–Mn–N2B	76.40(10)
$[Mn^{III}(OH)(dpaq^{2\text{-}Me})]^{+}$			
Mn–O1	1.819(3)	O2–Mn–N2	174.44(12)
Mn–N2	1.980(3)	N4–Mn–N5	155.19(12)
Mn–N1	2.186(3)	N1–Mn–N3	160.79(11)
Mn–N3	2.203(3)	N4–Mn–N2	91.69(12)
Mn–N4	2.149(3)	N1–Mn–N2	79.51(12)
Mn–N5	2.159(3)	N3–Mn–N2	81.55(12)

6.3.8. Formation of [Mn^{III}(OH)($dpaq^{2\text{-}Me}$)](OTf). The absorption spectrum of [Mn^{II}($dpaq^{2\text{-}Me}$)](OTf) in acetonitrile shows a very weak band at 500 nm (ε = 24 M^{-1} cm^{-1}), similar to that of [Mn^{II}(dpaq)](OTf).[12] When treated with excess O_2 gas at 25 ºC, the light yellow colored [Mn^{II}($dpaq^{2\text{-}Me}$)](OTf) solution slowly changed its color to deep red, as new absorption features grew in at 515 (ε = 228 M^{-1} cm^{-1}) and 770 nm (ε = 100 M^{-1} cm^{-1}) (Figure 6.10; the extinction coefficients were obtained using recrystallized [Mn^{III}(OH)($dpaq^{2\text{-}Me}$)](OTf)). Formation of these new electronic absorption features is consistent with the oxidation of Mn^{II} upon reacting with O_2. The final product, [Mn^{III}(OH)($dpaq^{2\text{-}Me}$)](OTf), was isolated in an essentially quantitative yield of greater than 98%. These electronic absorption spectral signatures are very similar to those of the related hydroxomanganese(III) species, [Mn^{III}(OH)(dpaq)](OTf).[12] However, the reaction times for 2.5 mM solutions of [Mn^{II}(dpaq)](OTf) and [Mn^{II}($dpaq^{2\text{-}Me}$)](OTf) with O_2 are remarkably different, with the latter reacting ~5 times slower. Since the only difference between these complexes is the added steric bulk on [Mn^{II}($dpaq^{2\text{-}Me}$)](OTf), this could be suggestive of the formation of a dimeric or polymeric Mn species during dioxygen activation, which has been observed for other similar systems.[19,35,36]

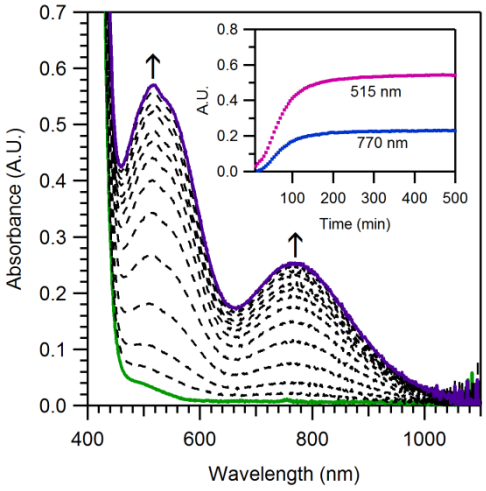

Figure 6.10 Electronic absorption spectra of [Mn^{II}($dpaq^{2\text{-}Me}$)](OTf) (solid green trace) upon addition of excess O_2 in MeCN at 25 ^{o}C under argon. Inset: time evolution of the absorption features at 515 nm and 770 nm.

6.3.9. Properties of [Mn^{III}(OH)(dpaq)](OTf). The X-ray structure of [Mn^{III}(OH)($dpaq^{2\text{-}Me}$)](OTf) contains a six-coordinate Mn^{III} center with a distorted octahedral geometry (Figure 6.11). Coordination of the $dpaq^{2\text{-}Me}$ ligand is the same as in [Mn^{II}($dpaq^{2\text{-}Me}$)](OTf), with the exception that all Mn–N bonds are shorter in [Mn^{III}(OH)($dpaq^{2\text{-}Me}$)](OTf) by 0.079 to 0.201 Å (Table 6.4). The hydroxide group in [Mn^{III}(OH)($dpaq^{2\text{-}Me}$)](OTf) is axial to the amide nitrogen, with a Mn–O2 distance of 1.819(3) Å. Inspection of the extended structure of [Mn^{III}(OH)($dpaq^{2\text{-}Me}$)]$^{+}$ reveals that the hydrogen atom of the hydroxo ligand is involved in a hydrogen-bonding interaction with the amide oxygen of an adjacent [Mn^{III}(OH)($dpaq^{2\text{-}Me}$)]$^{+}$ molecule (O···O and H···O separations of 2.787 and 1.982 Å, respectively). Such intermolecular H-bonding is not at all unusual for Mn^{III}-OH adducts, since five of the nine known X-ray structures show second-sphere hydrogen-bonding interactions in the solid-state structures.[11,12,35,52,58] A free triflate ion, an acetonitrile molecule, and an ether molecule are also observed within the asymmetric unit, but are not associated with the metal center (Mn–O and Mn–N distances of ~5.9, ~5.6 and ~7.1 Å

for triflate oxygen, ether oxygen, and acetonitrile nitrogen, respectively). There have been several X-ray structures of mononuclear Mn^{III}-OH complexes, including the closely related $[Mn^{III}(OH)(dpaq)](OTf)$ complex.[10-12,35,52,58-61] These have revealed Mn–O(H) distances within the range of 1.81 Å – 1.86 Å. Thus, the Mn–O(H) distance of $[Mn^{III}(OH)(dpaq^{2\text{-}Me})](OTf)$ falls toward the lower end of this range. The O2–Mn–N2 axis, which includes the hydroxide oxygen and amide nitrogen ligands, represents the compressed pseudo-Jahn-Teller axis of this species.

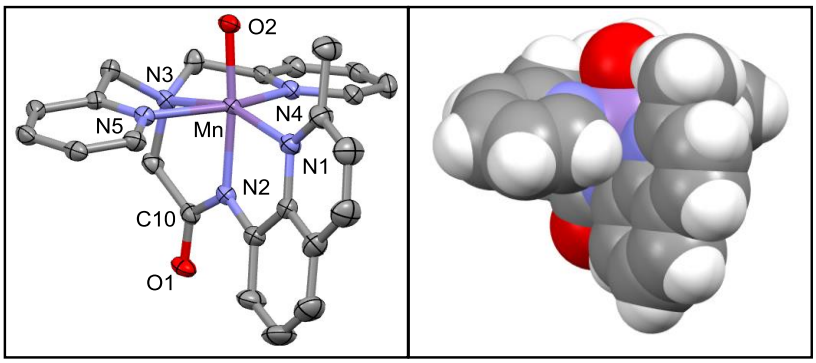

Figure 6.11. ORTEP (left) and space-filling (right) diagrams showing the X-ray crystal structure of $[Mn^{III}(OH)(dpaq^{2\text{-}Me})]^{+}$. ORTEP diagram shows 50% probability thermal ellipsoids. Hydrogen atoms, non-coordinating solvent molecules and triflate counter anions are excluded for clarity.

6.3.10. Synthesis and purification of $[Mn^{II}(dpap^{2\text{-}t\text{-}Bu})]$. When the phenolate-containing pentadentate ligand $H_2dpap^{2\text{-}t\text{-}Bu}$ was metalated with $Mn^{II}(OTf)_2$, a large quantity of white insoluble solid was formed. It should be noted that hydroxyl moieties are known to act as excellent bridging ligands,[33,54,62-69] and thus, this white solid could be a polymerized metal adduct via the phenolate functionality of $dpap^{2\text{-}t\text{-}Bu}$. However, its full characterization is still underway. Moreover, since $[Mn^{II}(dpap^{2\text{-}t\text{-}Bu})]$ is neutral in charge, it makes it challenging to analyze its purity by mass spectrometry. In fact, an air-free mass spectrum of $[Mn^{II}(dpap^{2\text{-}t\text{-}Bu})]$ in

MeCN is dominated by a single mass peak at m/z = 457.1406, which corresponds to the $[Mn^{III}(dpap^{2\text{-}t\text{-}Bu})]^{+}$ ion (calc. 457.1436; Figure A5.8). Thus, the presence of Mn^{III} is evident, although its origin is currently unknown. Due to these complications, we have not been successful in generating $[Mn^{II}(dpap^{2\text{-}t\text{-}Bu})]$ crystals that are of appropriate quality for X-ray crystallographic analysis so far. Current work involves the further purification of $[Mn^{II}(dpap^{2\text{-}t\text{-}Bu})]$, and the characterization of the insoluble white solid that forms during the metalation reaction. The magnetic susceptibility, and electronic absorption and EPR spectroscopies will provide useful insights into the oxidation state of the final metal product of the metalation of $H_2dpap^{2\text{-}t\text{-}Bu}$.

6.4. Discussion

Dioxygen activation with the aid of a catalytically active metal center is a common feature of a number of metalloenzymes in biology,[1-6] where the involvement of metal-superoxo, -peroxo and/or -oxo type intermediates are known to significantly lower the activation barrier, achieving oxygenated products at a low energy cost. Although this is a seemingly trivial chemical process, achieving synthetic examples of efficient dioxygen activating metal centers has been a continuing challenge. To this end, dioxygen activation and their applications involving environmentally benign, cheaper metals are even more intriguing, when compared to the currently used precious metal catalysts with large environmental impacts. Thus, dioxygen activation by Mn^{II} centers holds great significance, both in synthetic and alternative energy applications warranting enhanced understanding of the mechanistic details. Although several Mn^{II} systems with synthetic application have been reported,[13-18] mechanisms of dioxygen activation by a majority of these systems are not fully understood. Biological systems of similar reactivity patterns could provide important insights into some such systems, and a detailed

understanding of the mechanism will enable the fine-tuning of ligand properties, in order to design superior dioxygen activating Mn^{II} systems.

Herein, we report the dioxygen activation mechanistic studies we have carried out on $[Mn^{II}(dpaq)](OTf)$, which rapidly reacts with O_2 to generate the corresponding Mn^{III}-OH complex, $[Mn^{III}(OH)(dpaq)](OTf)$.[12] We have carried out spectroscopic analysis of accumulating intermediates, X-ray absorption studies on low-temperature solution samples, dioxygen titrations, and reactivity studies which provide useful insights into the potential mechanism involved. The negative results of experiments involving DHA, PPh_3, and MeCN-d_3 (*vide supra*) are reflective of several important details. Firstly, the absence of anthracene and $P(O)Ph_3$ are either suggestive of the absence of a Mn^{IV}=O type intermediate, or the very rapid reactivity of such an intermediate with the large excess of $[Mn^{II}(dpaq)](OTf)$ in solution. Such a rapid reactivity of the corresponding Mn^{IV}=O is also supported by the observation of $[Mn^{III}(OH)(dpaq)](OTf)$ as the final product when $[Mn^{II}(dpaq)](OTf)$ is treated with PhIO (*vide supra*). Secondly, the absence of $[Mn^{III}(OD)(dpaq)](OTf)$ when $[Mn^{II}(dpaq)](OTf)$ was oxygenated in MeCN-d_3 implies that the hydrogen atom of the Mn^{III}-OH adduct is not solvent derived. We cannot rule out the possibility that trace amounts of H_2O in MeCN could have rapidly exchanged with DO^- if $[Mn^{III}(OD)(dpaq)](OTf)$ was formed. Therefore, future work will involve the oxygenation of $[Mn^{II}(dpaq)](OTf)$ in ultra-dry MeCN, which will provide more insight into the involvement of H_2O in the mechanism. Thirdly, although dioxygen titration experiments are complicated by its partitioning between solution and gaseous phases, the overall yields of $[Mn^{III}(OH)(dpaq)](OTf)$ are suggestive of a Mn:O stoichiometry of 4:1. Furthermore, kinetic analysis of the rates of these titration experiments reveals that dioxygen is involved in the overall rate-determining step for $[Mn^{III}(OH)(dpaq)](OTf)$ formation. In combination, these data

are supportive of the dioxygen activation mechanism of [Mn^{II}(dpaq)](OTf) involving a mono-oxo bridged dimanganese(III,III) dimeric species, as seen in the systems of Kovacs and coworkers.[36,70] Evidence for the feasibility of formation of such a dimeric species between two [Mn^{III}(OH)(dpaq)](OTf) molecules can be seen in X-ray absorption data collected in frozen MeCN (*vide supra*). In addition, the related [Mn^{III}(OMe)(dpaq)](OTf) complex shows no evidence of dimerization in MeOH under the same conditions. Finally, the ~5 times slower oxidation rate of [Mn^{II}($dpaq^{2\text{-}Me}$)](OTf) compared to [Mn^{II}(dpaq)](OTf) is suggestive of the involvement of a dimeric intermediate species during O_2 activation. Therefore, the proposed dioxygen activation mechanism for [Mn^{II}(dpaq)](OTf) would involve the initial formation of a trans-μ-1,2-peroxo-bridged dimanganese(III,III) species, which undergoes homolytic O–O bond cleavage to generate the corresponding Mn^{IV}=O species, $[Mn^{IV}(O)(dpaq)]^{+}$ (Scheme 6.4). This highly unstable intermediate is rapidly trapped by excess [Mn^{II}(dpaq)](OTf) in solution giving rise to the proposed monooxo-bridged dimanganese(III,III) dimer. Ultimately, this adduct is hydrolyzed to form the monomeric Mn^{III}-OH species in solution.

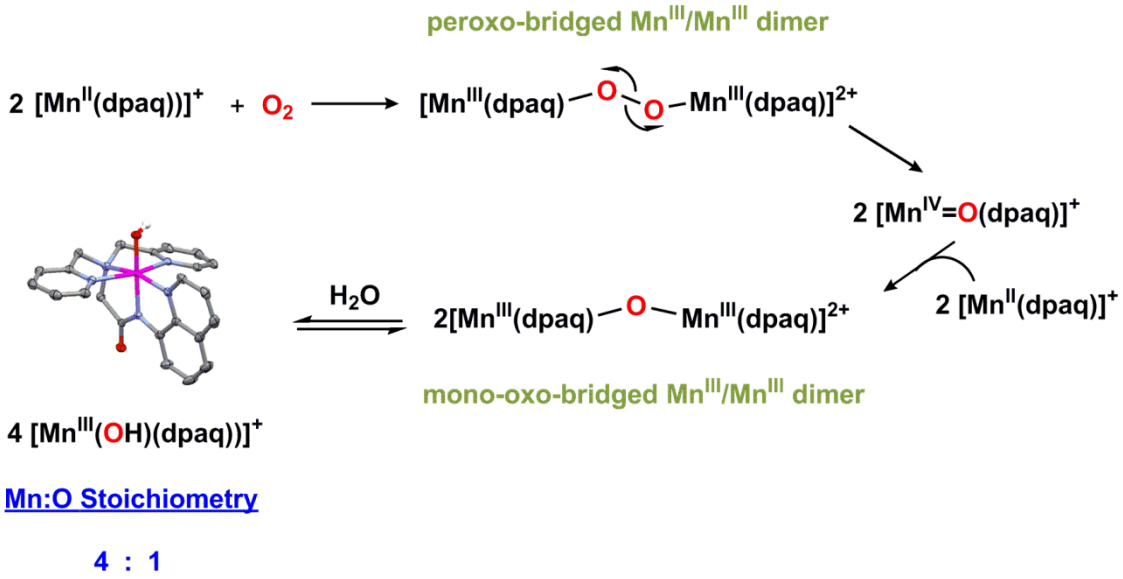

Scheme 6.4. Proposed dioxygen activation mechanism for [Mn^{II}(dpaq)](OTf).

However, further analysis of this system is warranted to test this mechanism. Most importantly, manometric measurements of O_2 uptake by a given concentration of [Mn^{II}(dpaq)](OTf) in MeCN will directly reveal the Mn:O stoichiometry. This can be achieved by measuring the pressure change in the head-space of the reaction vessel using a manometric apparatus, as a known concentration of [Mn^{II}(dpaq)](OTf) reacts with excess O_2. In addition, the oxygenation of [Mn^{II}(dpaq)](OTf) with $^{18}O_2$ would also provide important insights into the dioxygen activation mechanism, based on the distribution patterns of the ^{18}O label. That is, the Mn:O stoichiometry will be reflected by the ratios between [Mn^{III}(^{18}OH)(dpaq)](OTf) and [Mn^{III}(^{16}OH)(dpaq)](OTf) produced. In addition to these proposed experiments, organic substrate oxidation by O_2 in the presence of [Mn^{II}(dpaq)](OTf) could also provide useful insights into the mechanistic details of [Mn^{II}(dpaq)](OTf)/O_2 interactions. Analysis of organic product distribution of a given reaction will aid in quantifying the generated metal based oxidizing equivalents reflecting the mechanism of dioxygen activation. Furthermore, ^{18}O label distribution

among organic products of an oxidation reaction would also provide useful mechanistic insights. A major challenge involved with utilizing [Mn^{II}(dpaq)](OTf) as an aerobic oxidation catalyst is the mild oxidation capabilities of [Mn^{III}(OH)(dpaq)](OTf). For this reason, target substrates are required to consist of a weak C–H, O–H or N–H bonds that are activated during catalysis. Thus, those substrates also possess high tendency to get oxidized by O_2 even in the absence of the metal complex.

Moreover, geometric and electronic properties of the supporting ligand could also be fine-tuned to enhance the oxidizing capabilities of this system, which will improve the substrate scope and efficiency related to organic oxidation reactions. Furthermore, systematic ligand modifications will also facilitate the generation of related Mn^{II} complexes with varied ligand properties, which will offer mechanistic insights into dioxygen activation. Future work will involve the generation of a series of such ligands where electronic properties of the dpaq ligand platform is varied in terms of quinolone ring substituents.[71,72] These ligands will enable variations in electronic properties related to axial amide ligation, which will directly affect the dioxygen activation site of [Mn^{II}(dpaq)](OTf). Mn^{II} complexes of these ligand derivatives could also aid in stabilizing key intermediates of dioxygen activation, including the proposed high-valent Mn^{IV}=O adduct.

In conclusion, we have carried out mechanistic investigations into the dioxygen activation reactivity of [Mn^{II}(dpaq)](OTf), where a mechanistic proposal is offered based on our experimental evidence. However, further studies are warranted in order to a gain better understanding of the proposed intermediates. Furthermore, future work will also involve the synthesis of a series of dpaq ligand derivatives, which will serve as useful tools for dioxygen activation mechanics studies. Enhanced knowledge of dioxygen activation by Mn^{II} centers will

facilitate the development of environmentally friendly, less expensive aerobic oxidation catalysts, which are of high significance both in understanding biological pathways as well as in synthetic catalysis and alternate energy applications.

6.5. References

1. Koehntop, K. D.; Emerson, J. P.; Que, L., Jr., *J. Biol. Inorg. Chem.* **2005,** *10*, 87-93.
2. Gunderson, W. A.; Zatsman, A. I.; Emerson, J. P.; Farquhar, E. R.; Que, L.; Lipscomb, J. D.; Hendrich, M. P., *J. Am. Chem. Soc.* **2008,** *130*, 14465-14467.
3. Opaleye, O.; Rose, R.-S.; Whittaker, M. M.; Woo, E.-J.; Whittaker, J. W.; Pickersgill, R. W., *J. Biol. Chem.* **2006,** *281*, 6428-6433.
4. Borowski, T.; Bassan, A.; Richards, N. G. J.; Siegbahn, P. E. M., *J. Chem. Theory Comput.* **2005,** *1*, 686-693.
5. Tanner, A.; Bowater, L.; Fairhurst, S. A.; Bornemann, S., *J. Biol. Chem.* **2001,** *276*, 43627-43634.
6. Tabares, L. C.; Gätjens, J.; Hureau, C.; Burrell, M. R.; Bowater, L.; Pecoraro, V. L.; Bornemann, S.; Un, S., *J. Phys. Chem. B* **2009,** *113*, 9016-9025.
7. Saisaha, P.; de Boer, J. W.; Browne, W. R., *Chem. Soc. Rev.* **2013,** *42*, 2059-2074.
8. Rybak-Akimova, E. V., In *Mechanisms of Oxygen Binding and Activation at Transition Metal Centers. In Physical Inorganic Chemistry*, Bakac, A., Ed. John Wiley & Sons, Inc.: Hoboken, NJ: 2010; pp 109-188.
9. Pecoraro, V. L.; Baldwin, M. J.; Gelasco, A., *Chem. Rev.* **1994,** *94*, 807-826.
10. Shook, R. L.; Peterson, S. M.; Greaves, J.; Moore, C.; Rheingold, A. L.; Borovik, A. S., *J. Am. Chem. Soc.* **2011,** *133*, 5810-5817.
11. Coggins, M. K.; Brines, L. M.; Kovacs, J. A., *Inorg. Chem.* **2013,** *52*, 12383-12393.
12. Wijeratne, G. B.; Corzine, B.; Day, V. W.; Jackson, T. A., *Inorg. Chem.* **2014,** *53*, 7622-7634.
13. Battioni, P.; Bartoli, J. F.; Leduc, P.; Fontecave, M.; Mansuy, D., *J. Chem. Soc., Chem. Commun.* **1987**, 791-792.
14. Horwitz, C. P.; Creager, S. E.; Murray, R. W., *Inorg. Chem.* **1990,** *29*, 1006-1011.
15. Zhang, C.; Xu, Z.; Shen, T.; Wu, G.; Zhang, L.; Jiao, N., *Org. Lett.* **2012,** *14*, 2362-2365.
16. Christoffers, J., *J. Org. Chem.* **1999,** *64*, 7668-7669.
17. Nishida, Y.; Tanaka, N.; Yamazaki, A.; Tokii, T.; Hashimoto, N.; Ide, K.; Iwasawa, K., *Inorg. Chem.* **1995,** *34*, 3616-3620.
18. Komatsuzaki, H.; Nagasu, Y.; Suzuki, K.; Shibasaki, T.; Satoh, M.; Ebina, F.; Hikichi, S.; Akita, M.; Moro-oka, Y., *J. Chem. Soc., Dalton Trans.* **1998**, 511-512.
19. Horwitz, C. P.; Dailey, G. C., *Comments Inorg. Chem.* **1993,** *14*, 283-319.
20. Coggins, M. K.; Sun, X.; Kwak, Y.; Solomon, E. I.; Rybak-Akimova, E.; Kovacs, J. A., *J. Am. Chem. Soc.* **2013,** *135*, 5631-5640.
21. Mansuy, D.; Leclaire, J.; Fontecave, M.; Dansette, P., *Tetrahedron* **1984,** *40*, 2847-2857.
22. Tabushi, I.; Kodera, M.; Yokoyama, M., *J. Am. Chem. Soc.* **1985,** *107*, 4466-4473.
23. Perree-Fauvet, M.; Gaudemer, A., *J. Chem. Soc., Chem. Commun.* **1981**, 874-875.

24. Tabushi, I.; Yazaki, A., *J. Am. Chem. Soc.* **1981,** *103*, 7371-7373.
25. Creager, S. E.; Raybuck, S. A.; Murray, R. W., *J. Am. Chem. Soc.* **1986,** *108*, 4225-4227.
26. Coleman, W. M.; Taylor, L. T., *Coord. Chem. Rev.* **1980,** *32*, 1-31.
27. Frederick, F. C.; Taylor, L. T., *Polyhedron* **1986,** *5*, 887-893.
28. Horwitz, C. P.; Winslow, P. J.; Warden, J. T.; Lisek, C. A., *Inorg. Chem.* **1993,** *32*, 82-88.
29. Dismukes, G. C.; Sheats, J. E.; Smegal, J. A., *J. Am. Chem. Soc.* **1987,** *109*, 7202-7203.
30. Kitajima, N.; Singh, U. P.; Amagai, H.; Osawa, M.; Morooka, Y., *J. Am. Chem. Soc.* **1991,** *113*, 7757-7758.
31. Shook, R. L.; Borovik, A. S., *Inorg. Chem.* **2010,** *49*, 3646-3660.
32. Shook, R. L.; Gunderson, W. A.; Greaves, J.; Ziller, J. W.; Hendrich, M. P.; Borovik, A. S., *J. Am. Chem. Soc.* **2008,** *130*, 8888-8889.
33. Park, Y. J.; Ziller, J. W.; Borovik, A. S., *J. Am. Chem. Soc.* **2011,** *133*, 9258-9261.
34. Fukuzumi, S.; Ohkubo, K., *Chem. Eur. J.* **2000,** *6*, 4532-4535.
35. Shirin, Z.; S. Borovik, A.; G. Young Jr, V., *Chem. Commun.* **1997**, 1967-1968.
36. Coggins, M. K.; Toledo, S.; Shaffer, E.; Kaminsky, W.; Shearer, J.; Kovacs, J. A., *Inorg. Chem.* **2012,** *51*, 6633-6644.
37. Copyright. In *Purification of Laboratory Chemicals (Sixth Edition)*, Chai, W. L. F. A. L. L., Ed. Butterworth-Heinemann: Oxford, 2009; p iv.
38. Leto, D. F.; Ingram, R.; Day, V. W.; Jackson, T. A., *Chem. Commun.* **2013,** *49*, 5378-5380.
39. Parsell, T. H.; Behan, R. K.; Green, M. T.; Hendrich, M. P.; Borovik, A. S., *J. Am. Chem. Soc.* **2006,** *128*, 8728-8729.
40. Seo, M. S.; Kim, J. Y.; Annaraj, J.; Kim, Y.; Lee, Y.-M.; Kim, S.-J.; Kim, J.; Nam, W., *Angew. Chem., Int. Ed.* **2007,** *46*, 377-380.
41. Data Collection: SMART Software in APEX2 v2010.3-0 Suite. Bruker-AXS, E. C. P., Madison, WI 53711-5373 USA.
42. Data Reduction: SAINT Software in APEX2 v2010.3-0 Suite. Bruker-AXS, E. C. P., Madison, WI 53711-5373 USA
43. International Tables for Crystallography, V. A., 4th ed., Kluwer: Boston (1996).
44. Refinement: SHELXTL v2010.3-0. Bruker-AXS, E. C. P., Madison, WI 53711-5373 USA.
45. Warren, J. J.; Tronic, T. A.; Mayer, J. M., *Chem. Rev.* **2010,** *110*, 6961-7001.
46. Chen, Z.; Yin, G., *Chem. Soc. Rev.* **2015,** *44*, 1083-1100.
47. Leto, D. F.; Chattopadhyay, S.; Day, V. W.; Jackson, T. A., *Dalton Trans.* **2013,** *42*, 13014-13025.
48. Lessa, J. A.; Horn, A.; Bull, É. S.; Rocha, M. R.; Benassi, M.; Catharino, R. R.; Eberlin, M. N.; Casellato, A.; Noble, C. J.; Hanson, G. R.; Schenk, G.; Silva, G. C.; Antunes, O. A. C.; Fernandes, C., *Inorg. Chem.* **2009,** *48*, 4569-4579.
49. Wu, A. J.; Penner-Hahn, J. E.; Pecoraro, V. L., *Chem. Rev.* **2004,** *104*, 903-938.
50. Hureau, C.; Blondin, G.; Charlot, M.-F.; Philouze, C.; Nierlich, M.; Césario, M.; Anxolabéhère-Mallart, E., *Inorg. Chem.* **2005,** *44*, 3669-3683.
51. Wu, X.; Seo, M. S.; Davis, K. M.; Lee, Y.-M.; Chen, J.; Cho, K.-B.; Pushkar, Y. N.; Nam, W., *J. Am. Chem. Soc.* **2011,** *133*, 20088-20091.
52. Goldsmith, C. R.; Cole, A. P.; Stack, T. D. P., *J. Am. Chem. Soc.* **2005,** *127*, 9904-9912.

53. Horner, O.; Anxolabéhère-Mallart, E.; Charlot, M.-F.; Tchertanov, L.; Guilhem, J.; Mattioli, T. A.; Boussac, A.; Girerd, J.-J., *Inorg. Chem.* **1999,** *38*, 1222-1232.
54. Mukhopadhyay, S.; Mandal, S. K.; Bhaduri, S.; Armstrong, W. H., *Chem. Rev.* **2004,** *104*, 3981-4026.
55. Geiger, R. A.; Chattopadhyay, S.; Day, V. W.; Jackson, T. A., *J. Am. Chem. Soc.* **2010,** *132*, 2821-2831.
56. Geiger, R. A.; Wijeratne, G.; Day, V. W.; Jackson, T. A., *Eur. J. Inorg. Chem.* **2012**, 1598-1608.
57. Coggins, M. K.; Zhang, M.-T.; Vannucci, A. K.; Dares, C. J.; Meyer, T. J., *J. Am. Chem. Soc.* **2014,** *136*, 5531-5534.
58. El Ghachtouli, S.; Lassalle-Kaiser, B.; Dorlet, P.; Guillot, R.; Anxolabehere-Mallart, E.; Costentin, C.; Aukauloo, A., *Energy Environ. Sci.* **2011,** *4*, 2041-2044.
59. Eroy-Reveles, A. A.; Leung, Y.; Beavers, C. M.; Olmstead, M. M.; Mascharak, P. K., *J. Am. Chem. Soc.* **2008,** *130*, 4447-4458.
60. Eichhorn, D. M.; Armstrong, W. H., *J. Chem. Soc., Chem. Commun.* **1992**, 85-87.
61. Hubin, T. J.; McCormick, J. M.; Alcock, N. W.; Busch, D. H., *Inorg. Chem.* **2001,** *40*, 435-444.
62. Baldwin, M. J.; Pecoraro, V. L., *J. Am. Chem. Soc.* **1996,** *118*, 11325-11326.
63. Wang, K.; Mayer, J. M., *J. Am. Chem. Soc.* **1997,** *119*, 1470-1471.
64. Larsen, A. S.; Wang, K.; Lockwood, M. A.; Rice, G. L.; Won, T.-J.; Lovell, S.; Sadílek, M.; Tureček, F.; Mayer, J. M., *J. Am. Chem. Soc.* **2002,** *124*, 10112-10123.
65. Sano, Y.; Weitz, A. C.; Ziller, J. W.; Hendrich, M. P.; Borovik, A. S., *Inorg. Chem.* **2013,** *52*, 10229-10231.
66. Baldwin, M. J.; Law, N. A.; Stemmler, T. L.; Kampf, J. W.; Penner-Hahn, J. E.; Pecoraro, V. L., *Inorg. Chem.* **1999,** *38*, 4801-4809.
67. Baldwin, M. J.; Stemmler, T. L.; Riggs-Gelasco, P. J.; Kirk, M. L.; Penner-Hahn, J. E.; Pecoraro, V. L., *J. Am. Chem. Soc.* **1994,** *116*, 11349-56.
68. Zhou, H.-B.; Wang, H.-S.; Chen, Y.; Xu, Y.-L.; Song, X.-J.; Song, Y.; Zhang, Y.-Q.; You, X.-Z., *Dalton Trans.* **2011,** *40*, 5999-6006.
69. Cheng, B.; Fries, P. H.; Marchon, J.-C.; Scheidt, W. R., *Inorg. Chem.* **1996,** *35*, 1024-1032.
70. Coggins, M. K.; Sun, X.; Kwak, Y.; Solomon, E. I.; Rybak-Akimova, E. V.; Kovacs, J. A., *J. Am. Chem. Soc.* **2013,** *135*, 5631-5640.
71. Hitomi, Y.; Arakawa, K.; Funabiki, T.; Kodera, M., *Angew. Chem., Int. Ed.* **2012,** *51*, 3448-3452.
72. Hitomi, Y.; Iwamoto, Y.; Kodera, M., *Dalton Trans.* **2014,** *43*, 2161-2167.

APPENDIX A1.

A1.1. Solid-State Single-Crystal X-ray Structure Determinations for [Mn(L^7iso-q_2)$(OTf)_2$] ·CH_3COCH_3 (*1*) and [Mn($L^7py_2^{4\text{-}Cl}$)$(OTf)_2$] (*2*). Crystals for the acetone solvate of [Mn(L^7iso-q_2)$(OTf)_2$] (*1*) are, at 100(2) K, monoclinic, space group $P2_1/n$ [an alternate setting of $P2_1/c$ – C_{2h}^5 (No. 14)] [S1] with a = 12.2501(3) Å, b = 16.4994(4) Å, c = 18.0034(4) Å, β = 109.500°(1) , V = 3430.1(1) $Å^3$ and Z = 4 formula units {d_{calcd} = 1.537 g/cm^3; μ_a(CuKα) = 5.022 mm^{-1}}. Crystals of [Mn($L^7py_2^{4\text{-}Cl}$)$(OTf)_2$] (*2*) are, at 100(2) K, monoclinic, space group $P2_1$ – C_2^2 (No. 4)] [S1] with a = 14.2345(5) Å, b = 9.0034(3) Å, c = 42.186(1) Å, β = 97.843(1)°, V = 5356.0(3) $Å^3$ and Z = 8 molecules {d_{calcd} = 1.747 g/cm^3; μ_a(CuKα) = 8.102 mm^{-1}}. Complete sets of unique diffracted intensities [6399 (*1*) and 4015(*2*) frames with an ω- or ϕ-scan width of 0.50° and frame counting times of 1-8 sec] were measured[S2] for specimens of *1* and *2* using monochromated CuKα radiation (λ= 1.54178 Å) on a Bruker Single Crystal Diffraction System equipped with Helios multilayer x-ray optics, an APEX II CCD detector and a Bruker MicroSTAR microfocus rotating anode x-ray source operated at 45kV and 60mA. Lattice constants were determined with the Bruker SAINT software package using peak centers for 9811 (*1*) and 9786 (*2*) reflections. Totals of 30270 (*1*) and 35226 (*2*) integrated reflection intensities having 2θ(CuKα)< 138.63° (*1*) or 138.59° (*2*) were produced using the Bruker program SAINT[S3]; 6101 (*1*) and 16487 (*2*) of these were unique and gave R_{int} = 0.085 (*1*) and 0.043 (*2*) with coverages which were 95.1% (*1*) and 96.1% (*2*) complete. The data were corrected empirically for variable absorption effects using equivalent reflections; the relative transmission factors ranged from 0.761 (*1*) and 0.681 (*2*) to 1.000. The Bruker software package SHELXTL was used to solve both structures using "direct methods" techniques. All stages of weighted full-matrix least-squares refinement were conducted using F_o^2 data with the SHELXTL Version 6.10 software package[S4].

The final structural model for ***1*** incorporated anisotropic thermal parameters for all

nonhydrogen atoms and isotropic thermal parameters for all hydrogen atoms. The two methyl groups for the acetone solvent molecule of crystallization were incorporated into the structural model as rigid groups (using idealized sp^3-hybridized geometry and a C-H bond length of 0.98 Å) which were allowed to rotate about their C-C bonds in least-squares refinement cycles. All remaining hydrogen atoms were included in the structural model at idealized positions (sp^2- or sp^3-hybridized geometry and C-H bond lengths of 0.95 – 0.99 Å). All hydrogen atoms were assigned isotropic thermal parameters that were fixed at values 1.20 (nonmethyl) times or 1.5 (methyl) times the equivalent isotropic thermal parameter of the carbon atom to which they were covalently bonded. A total of 453 parameters were refined using no restraints, 6101 data and weights of $w = 1/ [\sigma^2(F^2) + (0.0764\ P)^2 + (8.7438\ P)]$, where $P = [F_O^2 + 2F_C^2] / 3$. Final agreement factors at convergence were: R_1(unweighted, based on F) = 0.059 for 6038 independent absorption-corrected "observed" reflections having $2\theta(CuK\alpha) < 136.63°$ and $I > 2\sigma(I)$; R_1(unweighted, based on F) = 0.059 and wR_2(weighted, based on F^2) = 0.152 for all 6101 independent absorption-corrected reflections having $2\theta(CuK\alpha) < 136.63°$. The largest shift/s.u. was 0.000 in the final refinement cycle. The final difference map had maxima and minima of 1.24 and -0.70 $e^-/Å^3$, respectively.

The structure of **2** was initially solved and refined in the centrosymmetric monoclinic space group $P2_1/c - C_{2h}^5$ (No. 14) with two crystallographically-independent molecules in the asymmetric unit. These two independent molecules were related by non-crystallographic symmetry and their nonhydrogen atoms were modeled with anisotropic thermal parameters and their idealized hydrogen atoms were modeled with isotropic thermal parameters. This structural model converged to : R_1(unweighted, based on F) = 0.111 for 9300 independent absorption-corrected "observed" reflections having $2\theta(CuK\alpha) < 138.59°$ and $I > 2\sigma(I)$ in space group $P2_1/c$.

An examination of the intensity statistics for reflections of **2** that were supposed to be

systematically absent in space group $P2_1/c$ revealed that all screw axis extinctions were indeed missing and had $I<3\sigma(I)$. However, 9.1% of the glide extinctions had weak intensities with $I>3\sigma(I)$. The structure was therefore solved and refined again in the noncentrosymmetric space groups Pc and $P2_1$ which are both maximal non-isomorphic subgroups of the original centrosymmetric space group $P2_1/c$. The asymmetric unit with both of these space groups contained 4 crystallographically-independent molecules.

The structure solution and refinement of **2** as a racemic twin with anisotropic nonhydrogen atoms and isotropic hydrogen atoms in space group $Pc\text{-}C_s^2$ (No. 7) converged to: R_1(unweighted, based on F) = 0.093 for the independent absorption-corrected "observed" reflections having $2\theta(CuK\alpha)<$ 138.59° and $I>2\sigma(I)$. Sixteen nonhydrogen atoms had non-positive-definite anisotropic thermal parameters at convergence.

The structure solution and refinement of **2** as a 51/49 racemic twin with anisotropic nonhydrogen atoms and isotropic hydrogen atoms in space group $P2_1$ converged to: R_1(unweighted, based on F) = 0.088 for the "observed" reflections having $2\theta(CuK\alpha)<$ 138.59° and $I>2\sigma(I)$; Six nonhydrogen atoms initially had non-positive-definite anisotropic thermal parameters. Mild restraints were applied to the anisotropic thermal parameters of these six nonhydrogen atoms and seven others that had positive-definite, but somewhat unreasonable, thermal parameters.

Although crystals of **2** clearly mimic (at least) the centrosymmetric space group $P2_1/c$, the more consistent intensity statistics for systematic absences, slightly lower R_1 value and smaller number of non-positive-definite nonhydrogen atoms at initial convergence were used as criteria for choosing $P2_1 - C_2^2$ (No. 4) as the final space group for describing the crystal structure of **2** All hydrogen atoms were included in the structural model for **2** at idealized positions (sp^2- or sp^3-hybridized geometry with C-H bond lengths of 0.95 – 0.99 Å) and with isotropic thermal

parameters that were fixed at values 1.20 times the equivalent isotropic thermal parameter of the carbon atom to which they were covalently bonded. A total of 1442 parameters were refined using 79 restraints, 16487 data and weights of $w = 1/ [\sigma^2(F^2) + (0.0993\ P)^2 + (39.1753\ P)]$, where $P = [F_o^2 + 2F_c^2] / 3$. Final agreement factors at convergence in space group $P2_1$ were: R_1(unweighted, based on F) = 0.088 for 15217 independent absorption-corrected "observed" reflections having $2\theta(CuK\alpha) < 138.59°$ and $I > 2\sigma(I)$; R_1(unweighted, based on F) = 0.093 and wR_2(weighted, based on F^2) = 0.220 for all 16487 independent absorption-corrected reflections having $2\theta(CuK\alpha) < 138.59°$. The largest shift/s.u. was 0.001 in the final refinement cycle. The final difference map had maxima and minima of 3.07 and -1.25 $e^-/Å^3$, respectively.

References

[S1] International Tables for Crystallography, Vol A, 4th ed., Kluwer: Boston (1996).

[S2] Data Collection: SMART Software in APEX2 v2010.3-0 Suite. Bruker-AXS, 5465 E. Cheryl Parkway, Madison, WI 53711-5373 USA.

[S3] Data Reduction: SAINT Software in APEX2 v2010.3-0 Suite. Bruker-AXS, 5465 E. Cheryl Parkway, Madison, WI 53711-5373 USA.

[S4] Refinement: SHELXTL v2010.3-0. Bruker-AXS, 5465 E. Cheryl Parkway, Madison, WI 53711-5373 USA.

Table A1.1. Crystal Data and Structure Refinement for $[Mn(C_{25}H_{26}N_4)(O_3SCF_3)_2]$ ($[Mn(L^7iso\text{-}q_2)(OTf)_2]\cdot CH_3COCH_3$).

Identification code	q07b	
Empirical formula	$C_{30}H_{32}F_6MnN_4O_7S_2$	
Formula weight	793.66	
Temperature	100(2) K	
Wavelength	1.54178 Å	
Crystal system	Monoclinic	
Space group	P2(1)/n	
Unit cell dimensions	a = 12.2501(3) Å	α= 90°.
	b = 16.4994(4) Å	β= 109.5000(10)°.
	c = 18.0034(4) Å	γ = 90°.
Volume	3430.12(14) $Å^3$	
Z	4	
Density (calculated)	1.537 Mg/m^3	
Absorption coefficient	5.022 mm^{-1}	
F(000)	1628	
Crystal size	0.33 x 0.18 x 0.15 mm^3	
Theta range for data collection	3.84 to 69.32°.	
Index ranges	-14<=h<=14, -17<=k<=20, -21<=l<=21	
Reflections collected	30270	
Independent reflections	6101 [R(int) = 0.0851]	
Completeness to theta = 69.32°	95.1 %	
Absorption correction	Multi-scan	
Max. and min. transmission	1.000 and 0.761	
Refinement method	Full-matrix least-squares on F^2	
Data / restraints / parameters	6101 / 0 / 453	
Goodness-of-fit on F^2	1.050	
Final R indices [I>2sigma(I)]	R1 = 0.0585, wR2 = 0.1521	
R indices (all data)	R1 = 0.0589, wR2 = 0.1523	
Largest diff. peak and hole	1.236 and -0.702 $e.Å^{-3}$	

Table A1.2. Atomic coordinates ($\times 10^4$) and equivalent isotropic displacement parameters ($Å^2 \times 10^3$) for $[Mn(C_{25}H_{26}N_4)(O_3SCF_3)_2]$ ($[Mn(L^7iso\text{-}q_2)(OTf)_2] \cdot CH_3COCH_3$). U(eq) is defined as one third of the trace of the orthogonalized U^{ij} tensor.

	x	y	z	U(eq)
Mn	827(1)	2454(1)	2640(1)	16(1)
N(1)	165(2)	3657(2)	2116(2)	21(1)
N(2)	1587(2)	2648(2)	1658(1)	14(1)
N(3)	1019(2)	1239(2)	2132(1)	15(1)
N(4)	1028(2)	1544(2)	3605(2)	18(1)
C(1)	-643(3)	4088(2)	2325(2)	26(1)
C(2)	-946(3)	4860(2)	2086(2)	24(1)
C(3)	-413(3)	5252(2)	1592(2)	20(1)
C(4)	413(2)	4808(2)	1361(2)	16(1)
C(5)	666(2)	3998(2)	1646(2)	16(1)
C(6)	1590(3)	3515(2)	1463(2)	18(1)
C(7)	2794(3)	2346(2)	1814(2)	22(1)
C(8)	2868(3)	1432(2)	1822(2)	23(1)
C(9)	2273(3)	1033(2)	2334(2)	20(1)
C(11)	1379(3)	1723(2)	4392(2)	23(1)
C(12)	1562(3)	1147(2)	4962(2)	24(1)
C(13)	1335(3)	327(2)	4742(2)	21(1)
C(14)	932(3)	134(2)	3924(2)	19(1)
C(15)	827(3)	777(2)	3380(2)	18(1)
C(16)	469(3)	633(2)	2493(2)	20(1)
C(17)	446(3)	1351(2)	1275(2)	22(1)
C(18)	741(3)	2202(2)	998(2)	19(1)
C(21)	-669(3)	6063(2)	1335(2)	25(1)
C(22)	-116(3)	6420(2)	873(2)	26(1)
C(23)	709(3)	5979(2)	644(2)	24(1)
C(24)	961(3)	5192(2)	872(2)	18(1)
C(25)	1490(3)	-303(2)	5303(2)	28(1)
C(26)	1245(3)	-1085(2)	5063(2)	32(1)
C(27)	815(3)	-1273(2)	4260(2)	29(1)
C(28)	662(3)	-687(2)	3695(2)	24(1)
S(1)	3160(1)	3601(1)	3846(1)	25(1)
F(11)	3278(3)	4880(1)	4715(2)	51(1)
F(21)	2266(3)	3923(2)	4942(2)	59(1)
F(31)	1593(2)	4659(2)	3882(2)	60(1)
O(11)	2247(3)	3021(2)	3533(2)	41(1)
O(21)	3392(3)	4081(2)	3254(2)	40(1)
O(31)	4154(3)	3287(2)	4443(2)	52(1)
C(1A)	2540(4)	4300(2)	4375(2)	35(1)
S(2)	-1905(1)	1973(1)	2617(1)	29(1)
F(12)	-4147(2)	2135(3)	2107(3)	104(2)
F(22)	-3203(2)	3149(2)	1838(2)	62(1)
F(32)	-3416(3)	2056(3)	1183(2)	79(1)
O(12)	-1064(2)	2188(2)	2244(1)	25(1)
O(22)	-2044(3)	1134(2)	2705(2)	59(1)
O(32)	-1791(4)	2446(2)	3313(2)	60(1)
C(2A)	-3228(4)	2336(4)	1906(3)	53(1)
O(1S)	-2399(4)	3023(2)	4922(2)	66(1)
C(1S)	-3269(5)	3867(4)	3830(3)	61(1)
C(2S)	-2274(4)	3546(3)	4487(2)	45(1)
C(3S)	-1129(6)	3902(5)	4593(4)	79(2)

Table A1.3. Crystal Data and Structure Refinement for $[Mn(C_{17}H_{20}Cl_2N_4)(O_3SCF_3)_2]$ ($[Mn(L^7py_2^{4-Cl})(OTf)_2]$).

Identification code	q64a	
Empirical formula	$C_{19}H_{20}Cl_2F_6MnN_4O_6S_2$	
Formula weight	704.35	
Temperature	100(2) K	
Wavelength	1.54178 Å	
Crystal system	Monoclinic	
Space group	P2(1)	
Unit cell dimensions	a = 14.2345(5) Å	α= 90°.
	b = 9.0034(3) Å	β= 97.8430(10)°.
	c = 42.1864(14) Å	γ = 90°.
Volume	5356.0(3) $Å^3$	
Z	8	
Density (calculated)	1.747 Mg/m^3	
Absorption coefficient	8.102 mm^{-1}	
F(000)	2840	
Crystal size	0.14 x 0.13 x 0.04 mm^3	
Theta range for data collection	1.06 to 69.29°.	
Index ranges	-17<=h<=16, -10<=k<=10, -50<=l<=43	
Reflections collected	35226	
Independent reflections	16487 [R(int) = 0.0430]	
Completeness to theta = 69.29°	96.1 %	
Absorption correction	Multi-scan	
Max. and min. transmission	1.000 and 0.681	
Refinement method	Full-matrix least-squares on F^2	
Data / restraints / parameters	16487 / 79 / 1442	
Goodness-of-fit on F^2	1.051	
Final R indices [I>2sigma(I)]	R1 = 0.0884, wR2 = 0.2158	
R indices (all data)	R1 = 0.0931, wR2 = 0.2199	
Absolute structure parameter	0.0(4)	
Largest diff. peak and hole	3.069 and -1.250 $e.Å^{-3}$	

Table A1.4. Atomic coordinates ($\times 10^4$) and equivalent isotropic displacement parameters ($Å^2 \times 10^3$) for $[Mn(C_{17}H_{20}Cl_2N_4)(O_3SCF_3)_2]$ ($[Mn(L^7py_2{}^{4\text{-}Cl})(OTf)_2]$). U(eq) is defined as one third of the trace of the orthogonalized U^{ij} tensor.

	x	y	z	U(eq)
Mn(1)	7919(1)	3306(2)	3796(1)	15(1)
Cl(1A)	5157(2)	7173(4)	2658(1)	41(1)
Cl(2A)	8554(2)	-1680(3)	5010(1)	30(1)
N(1A)	6942(5)	4546(10)	3420(2)	18(2)
N(2A)	8859(5)	5007(11)	3580(2)	23(2)
N(3A)	9121(6)	3959(10)	4169(2)	23(2)
N(4A)	8187(5)	1473(10)	4175(2)	21(2)
C(1A)	5987(6)	4317(13)	3367(2)	27(2)
C(2A)	5398(6)	5180(11)	3141(2)	19(2)
C(3A)	5832(7)	6170(13)	2949(2)	27(2)
C(4A)	6776(8)	6361(13)	2997(2)	34(3)
C(5A)	7355(7)	5514(11)	3227(2)	20(2)
C(6A)	8411(6)	5537(10)	3266(2)	16(2)
C(7A)	9847(6)	4526(15)	3556(3)	35(3)
C(8A)	10115(6)	3187(12)	3775(2)	27(2)
C(9A)	10065(6)	3360(12)	4117(2)	24(2)
C(11A)	7833(6)	73(13)	4151(2)	22(2)
C(12A)	7937(6)	-918(11)	4396(2)	23(2)
C(13A)	8398(6)	-505(13)	4681(2)	22(2)
C(14A)	8745(6)	979(12)	4728(2)	22(2)
C(15A)	8600(5)	1909(10)	4468(2)	13(2)
C(16A)	8934(6)	3541(13)	4488(2)	22(2)
C(17A)	9199(7)	5662(12)	4161(2)	26(2)
C(18A)	8791(7)	6203(13)	3816(2)	29(2)
S(1A)	7960(2)	762(3)	3226(1)	29(1)
F(11A)	7176(5)	244(9)	2645(1)	44(2)
F(12A)	6883(5)	2411(9)	2815(1)	43(2)
F(13A)	6203(5)	492(11)	2983(2)	53(2)
O(11A)	7569(4)	1432(8)	3486(2)	24(1)
O(12A)	8109(5)	-836(9)	3266(2)	28(2)
O(13A)	8753(4)	1582(9)	3126(1)	30(2)
C(20A)	7011(7)	981(13)	2900(2)	30(2)
S(2A)	6170(2)	5042(3)	4166(1)	18(1)
F(21A)	5596(5)	6015(9)	4692(2)	44(2)
F(22A)	7078(4)	5460(9)	4740(1)	40(2)
F(23A)	6043(6)	3707(11)	4707(2)	62(3)
O(21A)	6883(4)	3893(9)	4118(2)	26(2)
O(22A)	5200(5)	4639(9)	4065(2)	26(2)
O(23A)	6432(4)	6541(8)	4091(2)	23(1)
C(21A)	6258(7)	5094(13)	4608(3)	29(2)
Mn(2)	2910(1)	750(2)	3712(1)	20(1)
Cl(1B)	28(2)	-3382(5)	2662(1)	49(1)
Cl(2B)	3542(2)	5752(4)	4926(1)	35(1)
N(1B)	1910(6)	-408(10)	3347(2)	25(2)
N(2B)	3827(5)	-1025(10)	3501(2)	23(2)
N(3B)	4147(5)	-14(10)	4101(2)	21(2)
N(4B)	3120(5)	2605(9)	4089(2)	17(2)
C(1B)	959(8)	-290(14)	3290(3)	35(3)
C(2B)	356(6)	-1059(13)	3083(2)	25(2)
C(3B)	767(7)	-2171(13)	2920(2)	27(2)
C(4B)	1736(7)	-2397(14)	2968(2)	27(2)
C(5B)	2248(7)	-1542(15)	3167(2)	29(2)

C(6B)	3327(6)	-1600(14)	3189(2)	27(2)
C(7B)	4784(7)	-432(12)	3451(2)	31(2)
C(8B)	5443(6)	-236(11)	3738(2)	22(2)
C(9B)	5038(7)	686(13)	4009(2)	28(2)
C(11B)	2757(7)	4010(12)	4066(3)	25(2)
C(12B)	2865(6)	4997(13)	4328(2)	25(2)
C(13B)	3373(6)	4551(14)	4599(2)	28(2)
C(14B)	3774(6)	3134(15)	4636(2)	30(2)
C(15B)	3594(6)	2182(14)	4375(3)	29(2)
C(16B)	3952(7)	624(12)	4399(2)	22(2)
C(17B)	4128(8)	-1698(14)	4076(3)	34(2)
C(18B)	3908(7)	-2223(12)	3742(2)	22(2)
S(1B)	2720(2)	3416(3)	3218(1)	27(1)
F(11B)	1991(6)	3781(9)	2621(1)	48(2)
F(12B)	2249(6)	1499(10)	2752(2)	56(2)
F(13B)	3424(6)	3073(15)	2689(2)	85(4)
O(11B)	3401(5)	2302(8)	3369(1)	25(1)
O(12B)	3086(5)	4845(9)	3222(2)	32(2)
O(13B)	1780(5)	3229(9)	3307(2)	33(2)
C(20B)	2615(7)	2956(10)	2795(2)	22(2)
S(2B)	1146(2)	-986(3)	4099(1)	21(1)
F(21B)	552(4)	-1789(8)	4631(1)	32(1)
F(22B)	2077(4)	-1516(9)	4670(1)	39(2)
F(23B)	1143(5)	440(7)	4643(1)	38(2)
O(21B)	1918(5)	36(9)	4041(2)	28(2)
O(22B)	203(5)	-442(9)	3993(1)	26(2)
O(23B)	1339(5)	-2491(9)	4022(2)	28(2)
C(21B)	1255(7)	-947(13)	4535(2)	25(2)
Mn(3)	-2909(1)	-2693(2)	1287(1)	35(1)
Cl(1C)	-18(2)	1385(5)	2344(1)	52(1)
Cl(2C)	-3537(2)	-7663(5)	70(1)	60(1)
N(1C)	-1882(6)	-1524(14)	1662(2)	36(2)
N(2C)	-3816(6)	-939(14)	1505(2)	40(2)
N(3C)	-4109(8)	-1982(12)	921(3)	43(3)
N(4C)	-3101(7)	-4497(15)	904(2)	48(3)
C(1C)	-935(7)	-1719(16)	1703(2)	36(3)
C(2C)	-350(8)	-730(20)	1912(3)	53(4)
C(3C)	-731(8)	287(19)	2075(3)	53(4)
C(4C)	-1680(8)	491(16)	2043(3)	39(3)
C(5C)	-2281(7)	-529(12)	1825(3)	28(2)
C(6C)	-3339(8)	-509(14)	1807(3)	36(3)
C(7C)	-4772(7)	-1449(19)	1557(4)	57(4)
C(8C)	-5353(11)	-1920(20)	1241(4)	76(5)
C(9C)	-5015(8)	-2570(20)	989(4)	64(5)
C(11C)	-2745(8)	-5888(16)	922(3)	39(3)
C(12C)	-2837(8)	-6891(16)	687(3)	41(3)
C(13C)	-3382(8)	-6446(15)	394(3)	39(3)
C(14C)	-3734(8)	-5087(18)	367(3)	42(3)
C(15C)	-3617(8)	-4133(16)	627(3)	37(3)
C(16C)	-3923(10)	-2450(20)	597(3)	64(5)
C(17C)	-4144(8)	-356(18)	905(3)	43(3)
C(18C)	-3831(9)	299(17)	1270(3)	51(3)
S(1C)	-2732(2)	-5382(4)	1784(1)	39(1)
F(11C)	-1953(7)	-5719(14)	2376(2)	86(3)
F(12C)	-2339(6)	-3493(10)	2254(2)	52(2)
F(13C)	-3410(6)	-5044(11)	2316(2)	64(2)
O(11C)	-3333(8)	-4323(15)	1658(3)	79(4)
O(12C)	-3104(7)	-6886(11)	1771(2)	51(2)
O(13C)	-1807(9)	-5190(20)	1690(3)	109(6)

C(20C)	-2476(17)	-4790(30)	2214(5)	99(7)
S(2C)	-1153(2)	-930(4)	902(1)	39(1)
F(21C)	-563(5)	-115(15)	359(2)	79(3)
F(22C)	-2053(5)	-450(11)	324(2)	53(2)
F(23C)	-1123(7)	-2259(12)	354(2)	75(3)
O(21C)	-1881(6)	-1901(15)	952(2)	61(3)
O(22C)	-211(5)	-1398(14)	994(2)	58(3)
O(23C)	-1331(7)	602(15)	953(2)	61(3)
C(21C)	-1204(10)	-972(19)	459(3)	52(4)
Mn(4)	2081(1)	4789(3)	1209(1)	38(1)
Cl(1D)	4851(2)	892(5)	2338(1)	51(1)
Cl(2D)	1445(2)	9781(5)	0(1)	60(1)
N(1D)	3069(7)	3574(16)	1591(2)	48(3)
N(2D)	1143(6)	3026(14)	1427(2)	41(3)
N(3D)	840(6)	3920(12)	813(2)	32(2)
N(4D)	1839(6)	6579(12)	827(2)	33(2)
C(1D)	4015(8)	3633(16)	1635(2)	39(3)
C(2D)	4585(9)	3020(20)	1874(3)	68(5)
C(3D)	4161(8)	1952(16)	2044(2)	40(3)
C(4D)	3172(7)	1763(15)	2004(2)	34(3)
C(5D)	2684(7)	2652(16)	1772(3)	38(3)
C(6D)	1613(8)	2680(20)	1758(3)	55(4)
C(7D)	142(8)	3424(18)	1430(3)	46(3)
C(8D)	-192(10)	4730(20)	1230(3)	61(4)
C(9D)	-48(8)	4689(17)	884(3)	49(4)
C(11D)	2126(8)	7982(16)	861(3)	41(3)
C(12D)	2077(7)	9063(19)	604(2)	48(4)
C(13D)	1577(8)	8468(18)	308(3)	44(3)
C(14D)	1236(8)	7168(18)	284(3)	46(4)
C(15D)	1359(8)	6146(18)	547(3)	45(3)
C(16D)	1097(9)	4594(17)	505(3)	45(3)
C(17D)	855(10)	2329(15)	848(3)	44(3)
C(18D)	1181(8)	1829(16)	1185(3)	39(3)
S(1D)	2038(3)	7322(5)	1770(1)	51(1)
F(11D)	2814(6)	7949(15)	2362(2)	81(4)
F(12D)	3078(8)	5728(13)	2196(2)	85(4)
F(13D)	3789(5)	7692(13)	2025(2)	62(3)
O(11D)	2387(10)	6543(14)	1513(2)	86(4)
O(12D)	2005(8)	8790(14)	1753(2)	72(4)
O(13D)	1282(8)	6420(20)	1863(5)	153(8)
C(20D)	2983(11)	7130(30)	2115(3)	76(6)
S(2D)	3825(2)	3006(4)	838(1)	41(1)
F(21D)	4411(5)	2130(15)	314(2)	80(4)
F(22D)	2912(5)	2538(13)	255(2)	61(2)
F(23D)	3900(6)	4355(11)	288(2)	58(2)
O(21D)	3139(6)	4093(12)	888(2)	48(2)
O(22D)	4771(6)	3503(15)	952(2)	55(3)
O(23D)	3546(7)	1550(13)	914(2)	62(3)
C(21D)	3795(9)	3100(20)	405(3)	61(5)

Table A1.5. Selected Bond Lengths (Å) and Angles (º) for the Four Independent [$Mn^{II}(L^{7}py_2^{4-Cl})(OTf)_2$] Molecules Found in the Asymmetric Unit.

	A	B	C	D	Average	Standard Deviation
Mn(1)-N(1)	2.256(7)	2.212(9)	2.262(10)	2.269(11)	2.250	0.026
Mn(1)-N(2)	2.304(8)	2.316(9)	2.307(11)	2.342(11)	2.317	0.017
Mn(1)-N(3)	2.239(8)	2.339(8)	2.236(10)	2.392(8)	2.302	0.077
Mn(1)-N(4)	2.292(8)	2.298(9)	2.282(11)	2.273(10)	2.286	0.011
Mn(1)-O(11)	2.151(7)	2.193(6)	2.286(14)	2.042(11)	2.168	0.101
Mn(1)-O(21)	2.199(6)	2.207(7)	2.284(9)	2.249(9)	2.235	0.039
N(1)-Mn(1)-N(4)	150.9(3)	146.7(3)	146.1(4)	149.8(4)	148.4	2.3
N(2)-Mn(1)-N(3)	71.0(3)	70.0(3)	70.3(4)	69.3(3)	70.2	0.7
O(11)-Mn(1)-O(21)	116.4(3)	152.8(3)	151.2(4)	119.4(5)	135.0	19.7

Table A1.6. Cartesian coordinates for DFT-optimized model of $[Mn^{III}(O_2)(L^7iso\text{-}q_2)]^+$ Optimized Using the BP86 Functional.

Atom	x	y	z
Mn	1.794354	2.035194	4.038406
O	3.116850	2.560432	2.833478
O	1.798920	2.880611	2.352309
N	0.766041	0.211111	3.077138
N	-0.260978	2.185233	4.810929
N	1.680337	3.880055	5.396980
N	3.220002	1.653641	5.581945
C	1.258842	-0.511516	2.008512
C	0.383727	-1.297095	1.170976
C	-1.008705	-1.287897	1.469356
C	-1.474359	-0.549315	2.546306
C	-0.546785	0.184973	3.333714
C	-0.997569	0.909839	4.583543
C	-0.886761	3.302678	4.004620
C	-0.460482	4.715213	4.441662
C	1.044187	4.972703	4.616471
C	3.775316	0.429015	5.910141
C	4.969880	0.350070	6.714022
C	5.543945	1.567644	7.176601
C	4.937925	2.774941	6.866917
C	3.771459	2.784864	6.058104
C	3.103523	4.099659	5.692595
C	0.894451	3.531719	6.607437
C	-0.234232	2.519633	6.268400
C	2.655198	-0.498405	1.728423
C	3.163061	-1.236280	0.664447
C	2.303000	-2.011605	-0.163387
C	0.936348	-2.040262	0.085004
C	3.160806	-0.772903	5.462966
C	3.716861	-2.006465	5.786593
C	4.904450	-2.088890	6.565412
C	5.519054	-0.930060	7.022554
H	-1.704667	-1.866540	0.839594
H	-2.545189	-0.524188	2.801404
H	-2.097242	1.083608	4.567301
H	-0.785750	0.241463	5.446342
H	-0.645922	3.114000	2.937253
H	-1.994299	3.231348	4.117172
H	-0.993275	4.978948	5.380672
H	-0.845800	5.424583	3.677529
H	1.560336	5.022024	3.635748
H	1.183461	5.952434	5.137028
H	6.458544	1.539026	7.791204
H	5.345520	3.728567	7.235499
H	3.262373	4.845727	6.508099
H	3.585029	4.506064	4.775689
H	1.582677	3.066819	7.339899
H	0.491341	4.453116	7.084434
H	-0.051826	1.572148	6.812040
H	-1.232377	2.894875	6.588871
H	3.318332	0.115744	2.357002
H	4.246030	-1.218264	0.457352
H	2.726296	-2.586072	-1.003547
H	0.259320	-2.634019	-0.551607
H	2.235858	-0.712279	4.867470
H	3.229081	-2.930972	5.438192
H	5.330471	-3.075341	6.808452
H	6.436076	-0.979703	7.631989

Table A1.7. Cartesian coordinates for DFT-optimized model of $[Mn^{III}(O_2)(L^7py_2{}^{4\text{-}Cl})]^+$ Optimized Using the BP86 Functional

Atom	x	y	z
Mn	-0.161960	2.341567	15.729564
O	-0.027933	3.636949	17.066531
O	-1.180242	3.830047	16.222084
N	0.728029	3.389578	13.989738
N	-1.322193	1.459750	14.071871
N	1.323574	1.079874	16.529135
N	-1.330313	0.575730	16.578420
Cl	0.828395	6.552382	10.745826
Cl	4.301023	-1.333123	18.928468
C	0.894850	0.286381	17.550304
C	3.161080	-0.405835	18.004987
C	1.516453	4.480536	14.112350
C	1.596994	5.479979	13.136858
C	-0.037291	4.214931	11.851835
C	-0.035529	3.257176	12.876277
C	0.796539	5.337281	11.990350
C	1.790436	-0.477831	18.308699
C	-1.259671	-0.548427	15.611061
C	-0.813785	1.963029	12.757470
C	-0.599336	0.293388	17.826897
C	-2.741798	1.925044	14.306884
C	-1.223355	-0.032344	14.144646
C	-2.726516	1.049563	16.786745
C	-3.466832	1.190535	15.447700
C	2.643398	1.130918	16.237454
C	3.604538	0.406985	16.947025
H	2.104012	4.557644	15.041631
H	2.258543	6.347433	13.276338
H	-0.673613	4.086481	10.963425
H	1.422400	-1.120156	19.122448
H	-2.103881	-1.255175	15.777295
H	-0.327828	-1.111843	15.812666
H	-1.642646	2.065932	12.023144
H	-0.114856	1.201437	12.349148
H	-0.912825	-0.665674	18.303012
H	-0.829226	1.110885	18.546391
H	-3.323133	1.755812	13.370099
H	-2.704504	3.020912	14.480632
H	-0.254415	-0.312105	13.686855
H	-2.026086	-0.497417	13.528772
H	-3.285468	0.327535	17.430861
H	-2.670066	2.020562	17.321424
H	-4.416889	1.736120	15.636437
H	-3.775919	0.185243	15.090261
H	2.935784	1.778840	15.396239
H	4.667390	0.475824	16.674075

Table A1.8. Cartesian coordinates for DFT-optimized model of $[Mn^{III}(O_2)(L^7py_2{}^{4\text{-}Cl})]^+$ Optimized Using the B3LYP Functional

Atom	x	y	z
Mn	-0.176819	2.372877	15.759508
O	-0.065904	3.665605	17.118578
O	-1.212792	3.861458	16.303506
N	0.671203	3.453057	13.996492
N	-1.342217	1.481355	14.074377
N	1.343303	1.099168	16.567371
N	-1.319719	0.570590	16.579148
Cl	0.957994	6.444527	10.626621
Cl	4.290103	-1.397785	18.895513
C	0.906438	0.279706	17.550237
C	3.154809	-0.429533	17.994078
C	1.468216	4.528672	14.104832
C	1.605134	5.474863	13.093007
C	0.012360	4.179622	11.808750
C	-0.046136	3.275149	12.872464
C	0.853815	5.286713	11.929846
C	1.790677	-0.507503	18.286624
C	-1.241504	-0.535411	15.596160
C	-0.851639	1.996863	12.765789
C	-0.588192	0.270837	17.818858
C	-2.759164	1.927536	14.328309
C	-1.222618	-0.005022	14.138125
C	-2.718207	1.020463	16.798050
C	-3.468524	1.178319	15.467977
C	2.656249	1.158928	16.288621
C	3.607517	0.412265	16.975307
H	2.012519	4.641133	15.046524
H	2.266872	6.333285	13.220318
H	-0.585835	4.019709	10.909765
H	1.416920	-1.170577	19.068958
H	-2.070853	-1.247066	15.756073
H	-0.310402	-1.089401	15.779427
H	-1.686606	2.128892	12.057383
H	-0.183916	1.237778	12.325714
H	-0.891106	-0.694222	18.266379
H	-0.822263	1.062387	18.552606
H	-3.346467	1.762516	13.405372
H	-2.735595	3.013066	14.513292
H	-0.261046	-0.270079	13.677406
H	-2.017383	-0.475263	13.531515
H	-3.261155	0.283867	17.423164
H	-2.678064	1.973304	17.348454
H	-4.409975	1.716738	15.671996
H	-3.775826	0.184142	15.104229
H	2.957089	1.830646	15.480332
H	4.664041	0.488177	16.713276

Table A1.9. Cartesian coordinates for DFT-optimized model of $[Mn^{III}(O_2)(L^7py_2{}^{6\text{-}Me})]^+$ Optimized Using the B3LYP Functional

Atom	x	y	z
Mn	-0.025435	-0.035712	0.350498
O	-0.423498	-0.135008	2.356419
O	0.653937	-0.322817	3.123754
N	-2.080787	-0.813860	-0.199306
N	-0.912933	1.660655	-0.906340
N	1.386493	1.779880	0.422991
N	1.954015	-0.877681	-0.178570
C	-2.706362	-1.859072	0.393223
C	-4.069876	-2.097690	0.171293
C	-4.797482	-1.236104	-0.647561
C	-4.143092	-0.156367	-1.244314
C	-2.779616	0.015196	-1.007354
C	-1.996367	1.091816	-1.729262
C	-1.454122	2.630810	0.099436
C	-0.384432	3.522472	0.740400
C	0.832712	2.810590	1.339761
C	-1.912791	-2.746515	1.312649
C	2.205318	-2.050339	-0.805574
C	3.519771	-2.488385	-1.010251
C	4.582826	-1.701617	-0.571655
C	4.311308	-0.481984	0.052108
C	2.983463	-0.098934	0.235385
C	2.641509	1.204354	0.933436
C	1.521561	2.292404	-0.961691
C	0.168806	2.253568	-1.728928
C	1.038562	-2.882152	-1.261828
H	-4.549386	-2.955671	0.647540
H	-5.864268	-1.404307	-0.821986
H	-4.677863	0.541316	-1.893417
H	-1.534752	0.625493	-2.615668
H	-2.682204	1.877165	-2.099099
H	-1.998275	2.053027	0.866943
H	-2.193844	3.287884	-0.398434
H	-0.051445	4.274405	0.005420
H	-0.873762	4.095282	1.546278
H	0.570737	2.307575	2.283743
H	1.609266	3.567937	1.565755
H	-0.886786	-2.900971	0.941199
H	-2.395833	-3.730747	1.420419
H	-1.835160	-2.288907	2.315331
H	3.697378	-3.438574	-1.518515
H	5.615164	-2.027129	-0.728415
H	5.118328	0.173287	0.387861
H	3.487157	1.912552	0.841855
H	2.494016	0.996645	2.007515
H	2.245280	1.653272	-1.486563
H	1.944530	3.313690	-0.950311
H	-0.118270	3.259569	-2.082912
H	0.282298	1.620647	-2.620493
H	0.739077	-3.596685	-0.472531
H	1.302860	-3.473971	-2.152974
H	0.163793	-2.257154	-1.511080

Table A1.10. Cartesian coordinates for DFT-optimized model of $[Mn^{III}(O_2)(L^7py_2^H)]^+$ Optimized Using the B3LYP Functional

Atom	x	y	z
Mn	-0.073032	0.050029	0.691644
O	0.133200	-0.409912	2.509674
O	-0.817994	0.631590	2.322936
N	-1.864437	-1.027821	-0.045134
N	-0.932514	1.525446	-0.764831
N	1.555870	1.578983	0.208826
N	1.575041	-1.123290	-0.030817
C	-2.278030	-2.209558	0.451328
C	-3.562891	-2.701256	0.245857
C	-4.460912	-1.920060	-0.491067
C	-4.035440	-0.690795	-0.993816
C	-2.719711	-0.273679	-0.755119
C	-2.205512	1.020187	-1.356512
C	-1.185816	2.777168	0.033347
C	0.074390	3.575396	0.397614
C	1.259185	2.804818	0.991772
C	1.504733	-2.390207	-0.475469
C	2.638988	-3.140953	-0.773108
C	3.892509	-2.545867	-0.606293
C	3.963614	-1.225344	-0.155630
C	2.783450	-0.536725	0.129491
C	2.780661	0.890518	0.642170
C	1.534234	1.836440	-1.249773
C	0.095398	1.747369	-1.823845
H	-1.545638	-2.770916	1.038934
H	-3.852693	-3.669551	0.659646
H	-5.483851	-2.263505	-0.668492
H	-4.713632	-0.052764	-1.566949
H	-2.053694	0.845027	-2.434978
H	-2.990823	1.790851	-1.286226
H	-1.746959	2.482373	0.933744
H	-1.837850	3.443844	-0.560582
H	0.412552	4.135814	-0.490024
H	-0.231912	4.343976	1.128704
H	1.055181	2.496672	2.029541
H	2.143238	3.473664	0.999402
H	0.502699	-2.808245	-0.599250
H	2.533670	-4.166240	-1.133490
H	4.807109	-3.099993	-0.834401
H	4.926867	-0.724615	-0.031516
H	3.697328	1.416754	0.315596
H	2.784417	0.875797	1.746448
H	2.155838	1.075861	-1.741854
H	1.997688	2.813959	-1.471781
H	-0.155320	2.650448	-2.410238
H	0.037743	0.887913	-2.506457

Table A1.11. Cartesian coordinates for DFT-optimized model of $[Mn^{III}(O_2)(L^7iso\text{-}q_2)]^+$ Optimized Using the B3LYP Functional

Atom	x	y	z
Mn	0.031550	4.716896	4.246492
O	-0.928833	4.026118	2.781708
O	-0.723479	5.430802	2.677011
N	2.121655	4.009735	3.818414
N	0.501422	6.672619	5.146401
N	-1.346893	4.949037	6.059204
N	0.213217	2.875613	5.479247
C	2.464494	2.846656	4.354819
C	4.295641	4.252157	2.821951
C	3.775960	2.293417	4.196630
C	3.016032	4.693636	3.042974
C	4.177915	1.050289	4.766227
C	6.395710	1.312111	3.803361
C	4.723167	3.031571	3.412017
C	5.459763	0.573678	4.572283
C	6.035823	2.517170	3.233512
C	-0.465223	8.620574	6.198394
C	1.630030	7.392658	4.870436
C	0.713144	9.376554	5.889917
C	1.773223	8.711101	5.218877
C	-1.449151	10.603748	7.211646
C	-0.503425	7.247195	5.803338
C	0.783150	10.746167	6.262805
C	-1.543278	9.270004	6.868022
C	-0.278075	11.346454	6.910703
C	-1.705379	6.372517	6.101277
C	-1.038325	2.047553	5.379701
C	0.441023	3.378406	6.863424
C	1.360247	2.054817	5.026669
C	-2.552846	4.090617	5.905619
C	-0.517805	4.545405	7.224669
C	-2.238844	2.613576	6.140319
H	-2.150272	6.635689	7.077650
H	-2.480066	6.552037	5.334693
H	-1.264986	1.941252	4.307087
H	-0.824725	1.038946	5.779300
H	1.482188	3.732546	6.907400
H	0.347605	2.546902	7.584948
H	0.987398	1.338799	4.273152
H	1.741448	1.454438	5.868527
H	-2.947140	4.255117	4.889205
H	-3.331964	4.406644	6.627724
H	-1.164045	4.286886	8.081590
H	0.081224	5.412720	7.531317
H	-2.114830	2.425708	7.219305
H	-3.122680	2.026032	5.838898
H	4.976622	4.832131	2.193723
H	2.647132	5.614660	2.587171
H	3.477357	0.460780	5.360757
H	7.406969	0.920123	3.660645
H	5.757390	-0.381318	5.013994
H	6.751564	3.089466	2.636229
H	2.428668	6.857188	4.357931
H	2.696729	9.242629	4.976974
H	-2.284293	11.093254	7.721052
H	1.687907	11.313532	6.025897
H	-2.456479	8.722125	7.107388
H	-0.219796	12.400911	7.196256

Table A1.12. Cartesian coordinates for DFT-optimized model of $[Mn^{III}(O_2)(L^7q_2)]^+$ Optimized Using the B3LYP Functional

Atom	x	y	z
Mn	1.786069	2.057035	4.017534
O	3.116123	2.630164	2.809234
O	1.821325	2.945057	2.330178
N	0.738922	0.247447	3.043561
N	-0.301114	2.223591	4.775932
N	1.674259	3.872043	5.421472
N	3.226211	1.638238	5.592399
C	1.246878	-0.508793	2.011683
C	0.394657	-1.345960	1.219474
C	-0.992503	-1.353339	1.520108
C	-1.470370	-0.578493	2.552971
C	-0.561294	0.209944	3.302081
C	-1.051224	0.971453	4.514019
C	-0.890662	3.367023	3.989443
C	-0.441693	4.760791	4.457636
C	1.061668	4.988607	4.663088
C	3.793026	0.418694	5.895050
C	4.986853	0.338488	6.682067
C	5.547718	1.550503	7.161799
C	4.929022	2.748404	6.881872
C	3.761134	2.757518	6.082108
C	3.089146	4.077561	5.746143
C	0.868070	3.505370	6.608398
C	-0.274525	2.525139	6.235634
C	2.636626	-0.474253	1.723313
C	3.154664	-1.243853	0.698511
C	2.313832	-2.075342	-0.085064
C	0.957987	-2.123720	0.170093
C	3.189846	-0.780059	5.436754
C	3.760027	-2.004814	5.731560
C	4.953357	-2.086631	6.492717
C	5.553721	-0.935263	6.961378
H	-1.670595	-1.972811	0.925062
H	-2.533318	-0.562654	2.805125
H	-2.134050	1.171210	4.430739
H	-0.916418	0.306044	5.383279
H	-0.644651	3.200652	2.928848
H	-1.991853	3.321255	4.087041
H	-0.980203	5.016551	5.385332
H	-0.796234	5.484813	3.704273
H	1.587438	5.063416	3.699072
H	1.203156	5.943310	5.208919
H	6.461210	1.521359	7.762920
H	5.325318	3.692772	7.261143
H	3.229590	4.790055	6.582046
H	3.584810	4.510562	4.860637
H	1.530299	3.013084	7.333135
H	0.476156	4.413992	7.098157
H	-0.112695	1.572104	6.758176
H	-1.257244	2.911571	6.559462
H	3.286789	0.177305	2.311040
H	4.227424	-1.207626	0.485400
H	2.745403	-2.672935	-0.893287
H	0.297424	-2.757151	-0.430130
H	2.263318	-0.727747	4.860628
H	3.282800	-2.922389	5.376382
H	5.390760	-3.064650	6.711376
H	6.470675	-0.982992	7.555734

Table A1.13. Cartesian coordinates for DFT-optimized model of $[Mn^{III}(O_2)(L^7py_2{}^{4\text{-Me}})]^+$ Optimized Using the B3LYP Functional

Atom	x	y	z
Mn	-0.415321	2.854771	1.107033
O	-0.783211	4.647694	0.667084
O	-0.701313	4.449152	2.074463
N	-2.427252	2.039162	0.678454
N	-0.134158	1.962495	-0.936974
N	1.833131	2.585904	0.768107
N	0.247955	1.669914	2.770100
C	-3.494165	2.220235	1.478462
C	-4.799869	2.010384	1.052526
C	-5.036543	1.604094	-0.271944
C	-3.914480	1.431106	-1.094994
C	-2.630080	1.656046	-0.593619
C	-1.419333	1.433729	-1.480610
C	-6.428342	1.375434	-0.797550
H	-3.283849	2.557482	2.497461
H	-5.626732	2.172901	1.748469
H	-4.036867	1.122232	-2.137255
H	-1.318986	0.349209	-1.654659
H	-1.617653	1.876450	-2.469488
H	-6.530422	0.352135	-1.201486
H	-6.649533	2.073363	-1.625975
H	-7.187024	1.517497	-0.011070
C	0.384982	3.071781	-1.814690
C	1.850710	3.455750	-1.568736
C	2.289925	3.685156	-0.118284
C	1.253576	0.154444	2.040532
C	0.868934	0.867206	-0.787746
H	0.299880	2.753123	-2.870314
H	-0.283367	3.934899	-1.675381
H	2.039635	4.385983	-2.132106
H	2.503328	2.697191	-2.031944
H	1.877671	4.625939	0.279350
H	3.395722	3.758484	-0.092421
H	2.097995	0.511601	0.962341
H	3.009820	1.223556	-0.373758
H	1.244076	0.561486	-1.781195
H	0.336791	0.005199	-0.360882
C	-0.529223	0.923561	3.576147
C	-0.042655	0.295663	4.715711
C	1.314336	0.430639	5.056249
C	2.113452	1.201492	4.197530
C	1.558183	1.810394	3.073177
C	2.381607	2.667479	2.130004
C	1.880287	-0.217645	6.289726
H	-1.578497	0.825358	3.287353
H	-0.721299	-0.301670	5.329999
H	3.181229	1.325784	4.398212
H	2.320671	3.721483	2.454468
H	3.447317	2.372262	2.172303
H	2.979950	-0.281852	6.245605
H	1.467185	-1.230598	6.432438
H	1.609079	0.373041	7.185192

Table A1.14. Electronic transition energies (cm^{-1}) and bandwidths (fwhm; cm^{-1}) from Gaussian deconvolutions of 2K, 7 T MCD data of $[Mn^{III}(O_2)(L^7\text{iso-}q_2)]^+$.

Band	Energy	fwhm
1	15 500	2000
2	not observed	
3	21 560	1200
4	24 120	1660
5	26 730	1750
6	not observed	

Table A1.15. Electronic transition energies (cm^{-1}) and bandwidths (fwhm; cm^{-1}) from Gaussian deconvolutions of 2K, 7 T MCD data of $[Mn^{III}(O_2)(L^7q_2)]^+$.

Band	Energy	fwhm
1	14 450	1400
2	19 150	1400
3	21 650	1600
4	23 760	1500
5	26000	1500
6	27 950	1550

Table A1.16. Electronic transition energies (cm^{-1}) and bandwidths (fwhm; cm^{-1}) from Gaussian deconvolutions of 2K, 7 T MCD data of $[Mn^{III}(O_2)(L^7py_2^{4\text{-Me}})]^+$.

Band	Energy	fwhm
1	16 400	2300
2	19 090	1000
3	21 325	1300
4	23 000	1600
5	24 500	1700
6	27 110	2030

Table A1.17. Electronic transition energies (cm^{-1}) and bandwidths (fwhm; cm^{-1}) from Gaussian deconvolutions of 2K, 7 T MCD data of $[Mn^{III}(O_2)(L^7py_2^{4\text{-Cl}})]^+$.

Band	Energy	fwhm
1	16 630	1500
2	19 180	1100
3	21 510	1200
4	23 340	1500
5	24 750	1500
6	26 980	2000

Table A1.18. Metal-Ligand Bond Lengths (Å) for Peroxomanganese(III) Complexes Based on DFT Geometry Optimizations Using the B3LYP Functional.

	$[Mn^{III}(O_2)(L)]^+$					
L =	$L^7iso\text{-}q_2$	L^7q_2	$L^7py_2^{4\text{-}Me}$	$L^7py_2^{4\text{-}Cl}$	$L^7py_2^{H}$	$L^7py_2^{6\text{-}Me}$
Mn-O(1)	1.883	1.907	1.887	1.893	1.887	1.908
Mn-O(2)	1.883	1.886	1.882	1.879	1.885	1.887
O(1)-O(2)	1.423	1.416	1.424	1.421	1.423	1.416
Mn-N(1)	2.204	2.175	2.213	2.141	2.217	2.350
Mn-N(2)	2.289	2.297	2.248	2.286	2.244	2.224
Mn-N(3)	2.223	2.227	2.290	2.234	2.286	2.308
Mn-N(4)	2.248	2.306	2.147	2.235	2.148	2.169

Table A1.19. Experimental and TD-DFT Computed Energies (cm^{-1}) of the Mn $d_z^2 \rightarrow d_{xy}$ Electronic Transition (Band 1).

	$[Mn^{III}(O_2)(L)]^+$					
L =	$L^7iso\text{-}q_2$	L^7q_2	$L^7py_2^{4\text{-}Me}$	$L^7py_2^{4\text{-}Cl}$	$L^7py_2^{H}$	$L^7py_2^{6\text{-}Me}$
Experimental	15 500	14 450	16 400	16 630	16 300	13 650
TD-DFT B3LYP	18 550	17 622	17 493	17 619	17 636	16 280
TD-DFT PBE0	20 681	19 463	19 554	19 508	19 532	18 047

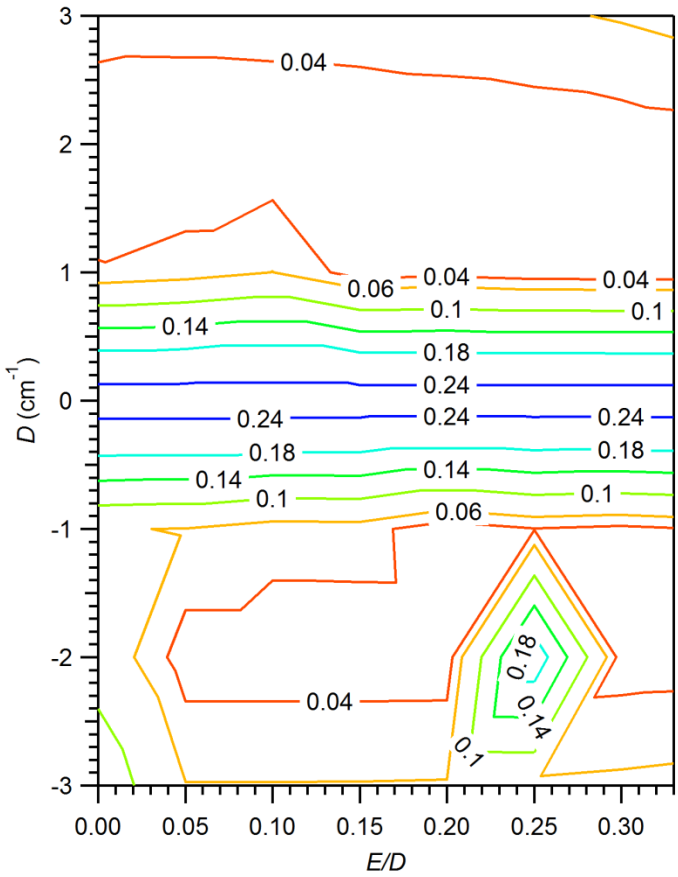

Figure A1.1. Contour plot of χ^2 as a function of *D* and *E/D* for fits of VTVH MCD data collected for $[Mn^{III}(O_2)(L^7iso\text{-}q_2)]^+$ at 21 600 cm^{-1}.

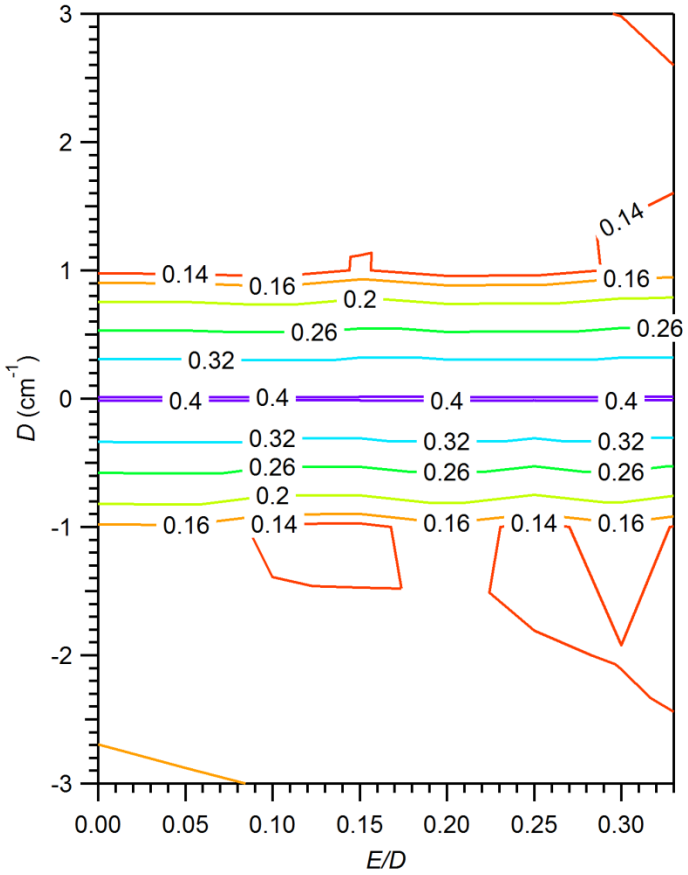

Figure A1.2. Contour plot of χ^2 as a function of *D* and *E/D* for fits of VTVH MCD data collected for $[Mn^{III}(O_2)(L^7py_2^{4\text{-}Me})]^+$ at 21 350 cm^{-1}.

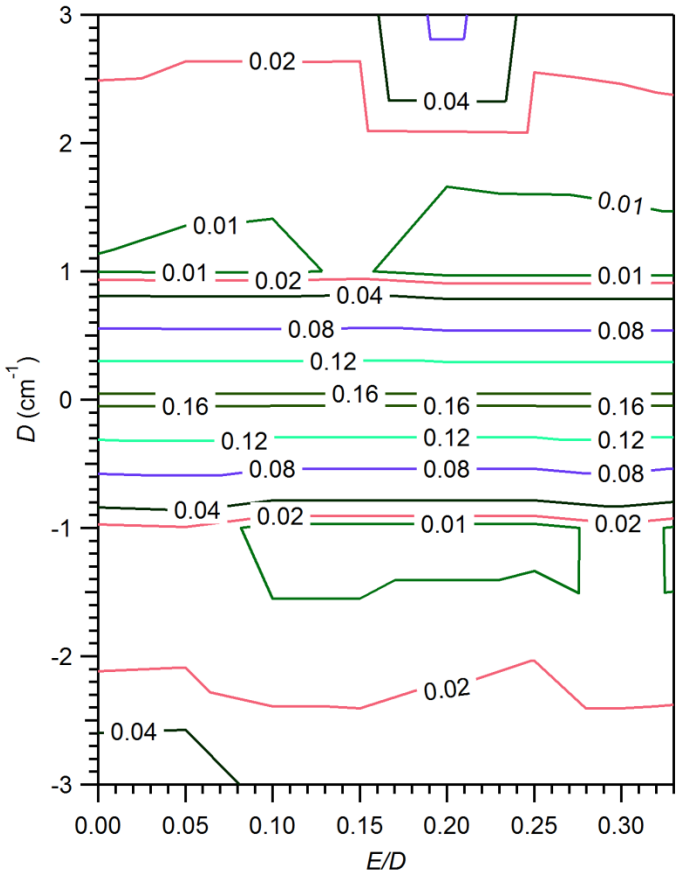

Figure A1.3. Plot of the DFT-computed Mn−O(1) distance as a function of the energy of band 1 determined by MCD spectroscopy.

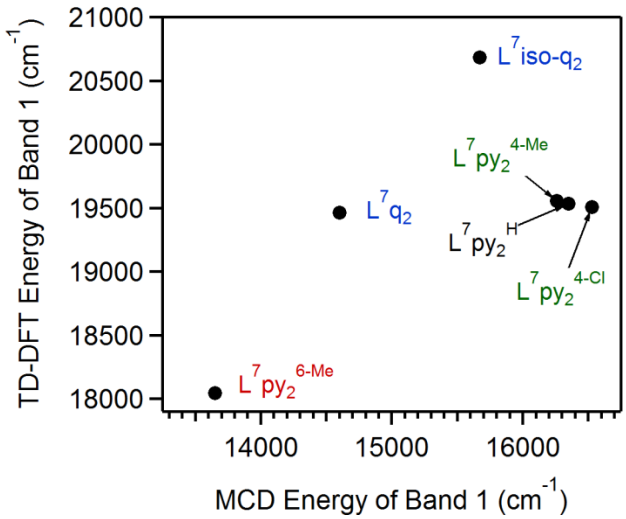

Figure A1.4. Plot of experimental and TD-DFT (PBE0) computed energies of band 1.

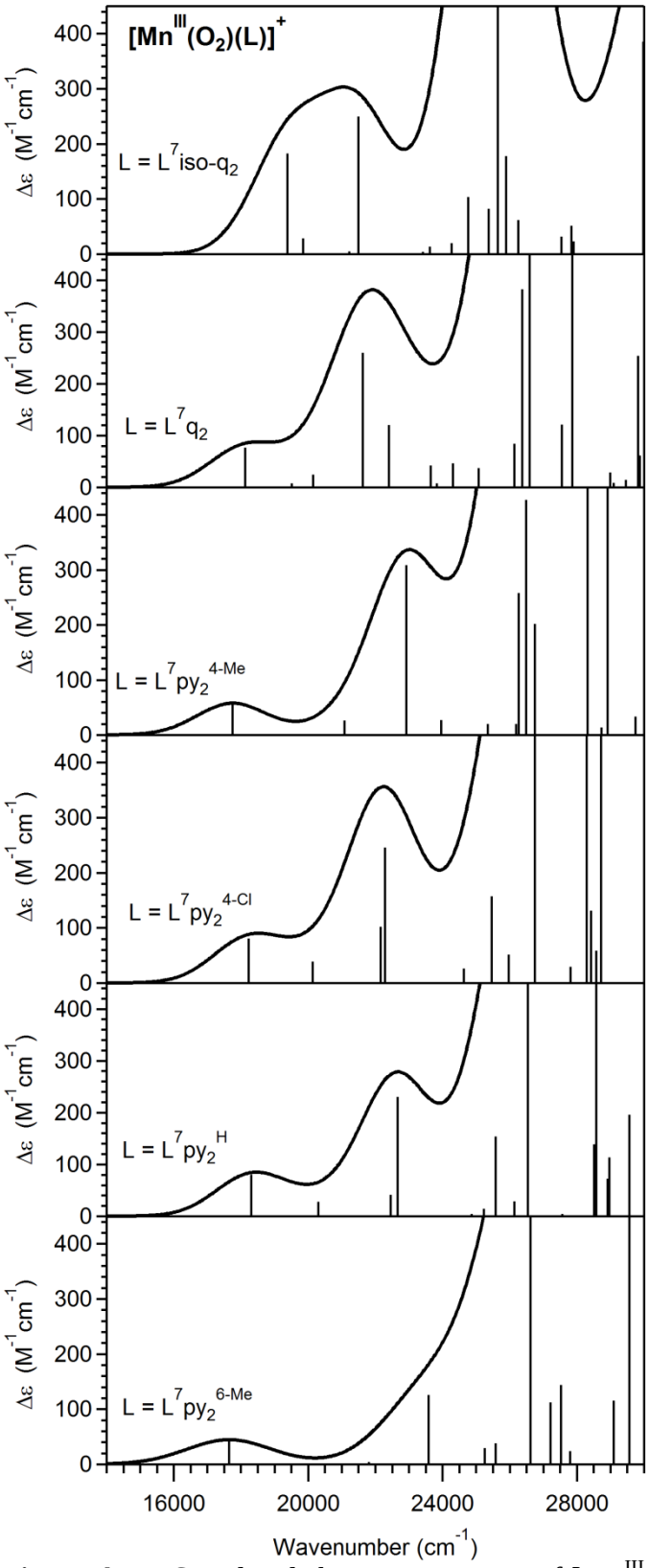

Figure A1.5. Simulated absorption spectra of $[Mn^{III}(O_2)(L)]^+$ (L = L^7q_2, $L^7iso\text{-}q_2$, $L^7py_2^{4\text{-}Me}$, $L^7py_2^{4\text{-}Cl}$, $L^7py_2^{H}$, $L^7py_2^{6\text{-}Me}$) based on TD-DFT computations employing the B3LYP functional.

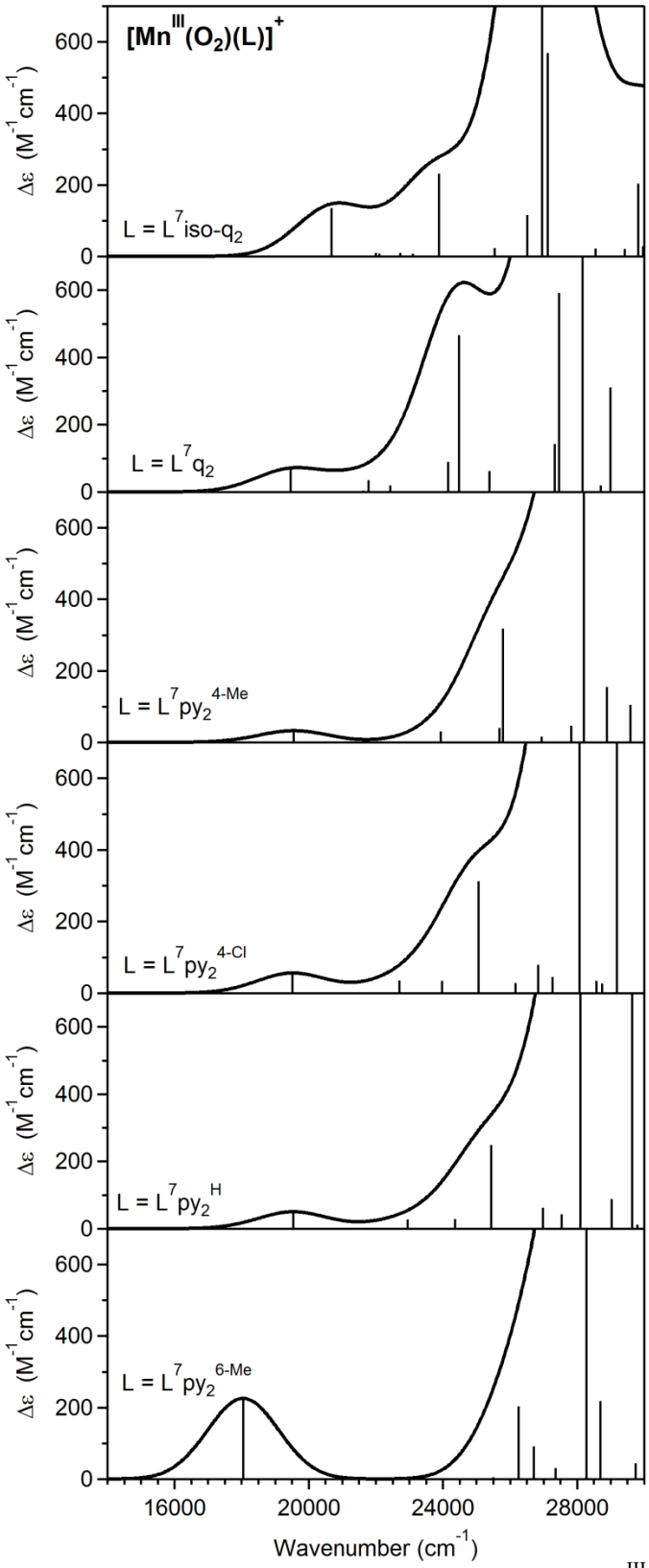

Figure A1.6. Simulated absorption spectra of $[Mn^{III}(O_2)(L)]^+$ (L = L^7q_2, $L^7iso\text{-}q_2$, $L^7py_2^{4\text{-}Me}$, $L^7py_2^{4\text{-}Cl}$, $L^7py_2^{H}$, $L^7py_2^{6\text{-}Me}$) based on TD-DFT computations employing the PBE0 functional.

APPENDIX A2.

Table A2.1. Crystal Data and Structure Refinement for $[Mn^{II}(L^{7}BQ)](OTf)$.

Empirical formula	$C_{27}H_{25}F_6MnN_5O_6S_2$	
Formula weight	748.58	
Temperature	100(2) K	
Wavelength	1.54178 Å	
Crystal system	Monoclinic	
Space group	P2(1)/n	
Unit cell dimensions	a = 13.8379(4) Å	a= 90°.
	b = 14.1652(4) Å	b= 105.2110(10)°.
	c = 16.3768(4) Å	g = 90°.
Volume	3097.66(15) $Å^3$	
Z	4	
Density (calculated)	1.605 Mg/m^3	
Absorption coefficient	5.509 mm^{-1}	
F(000)	1524	
Crystal size	0.24 x 0.18 x 0.10 mm^3	
Theta range for data collection	3.73 to 69.49°.	
Index ranges	-15<=h<=16, -17<=k<=17, -13<=l<=19	
Reflections collected	26589	
Independent reflections	5484 [R(int) = 0.0310]	
Completeness to theta = 66.00°	97.0 %	
Absorption correction	Multi-scan	
Max. and min. transmission	1.000 and 0.787	
Refinement method	Full-matrix least-squares on F^2	
Data / restraints / parameters	5484 / 0 / 525	
Goodness-of-fit on F^2	1.039	
Final R indices [I>2sigma(I)]	R1 = 0.0293, wR2 = 0.0748	
R indices (all data)	R1 = 0.0295, wR2 = 0.0750	
Extinction coefficient	0.00022(5)	
Largest diff. peak and hole	0.404 and -0.336 $e.Å^{-3}$	

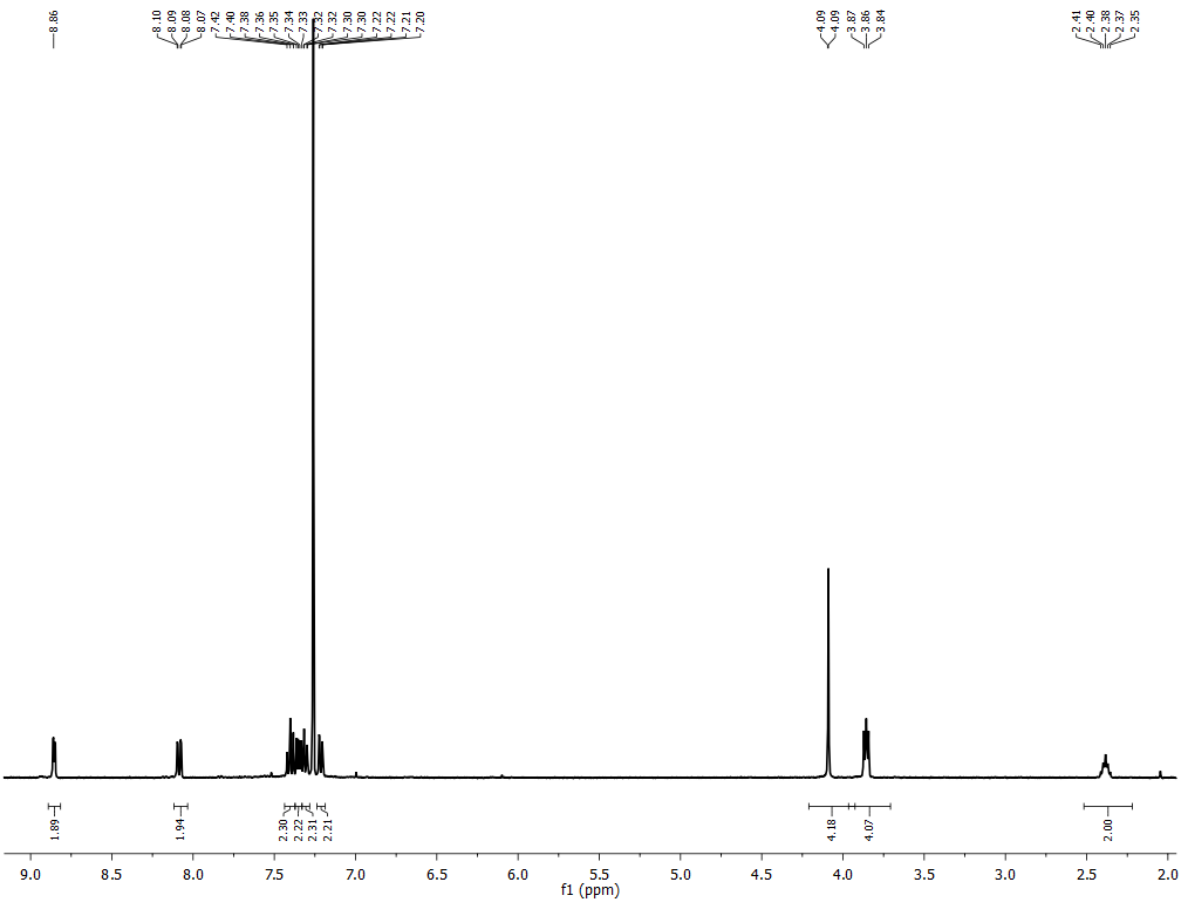

Figure A2.1. ^{1}H NMR spectrum of the $L^{7}BQ$ ligand collected in $CDCl_3$ under ambient conditions.

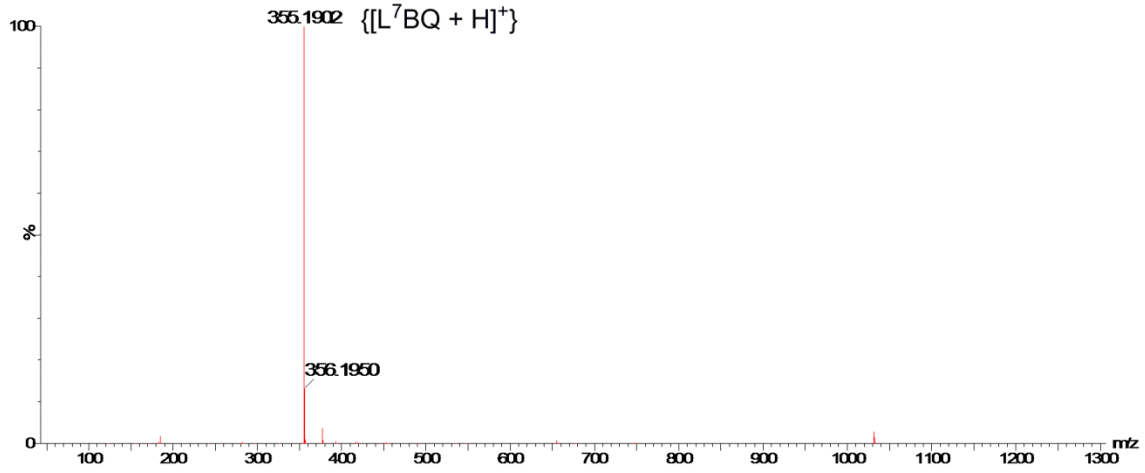

Figure A2.2. ESI-MS data showing the purified $L^{7}BQ$ ligand.

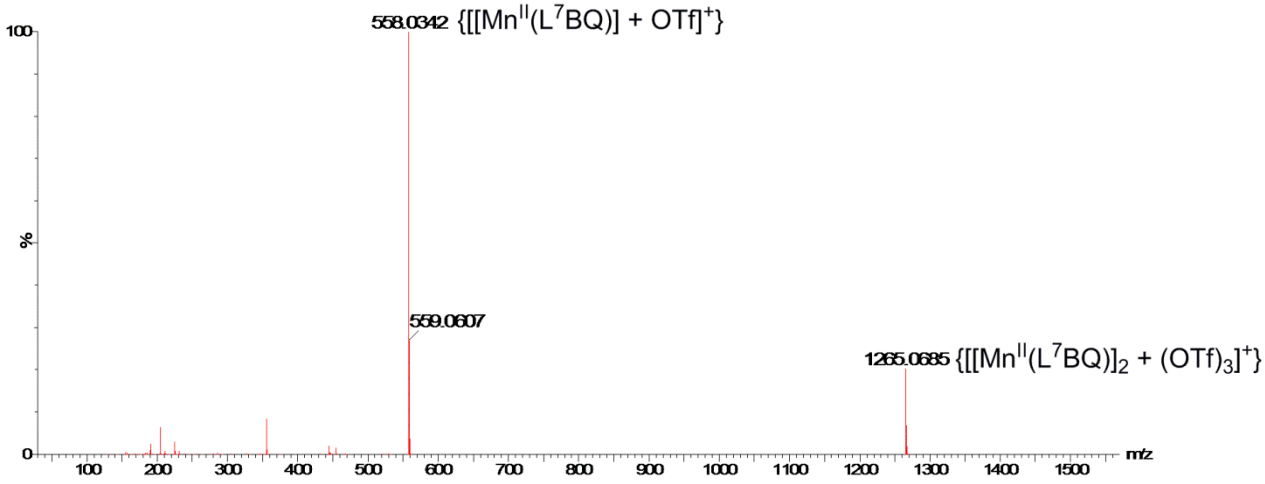

Figure A2.3. ESI-MS spectrum of $[Mn^{II}(L^7BQ)(OTf)_2]$.

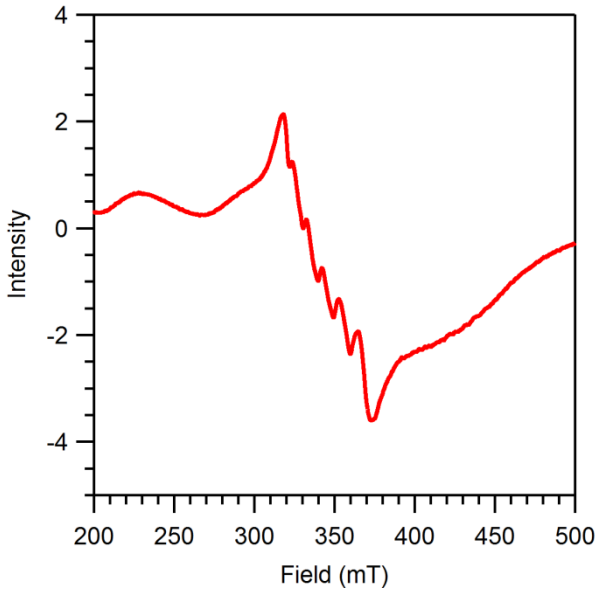

Figure A2.4. Perpendicular mode X-band EPR spectrum of a 2 mM frozen acetonitrile solution of $[Mn^{II}(L^7BQ)(OTf)_2]$.

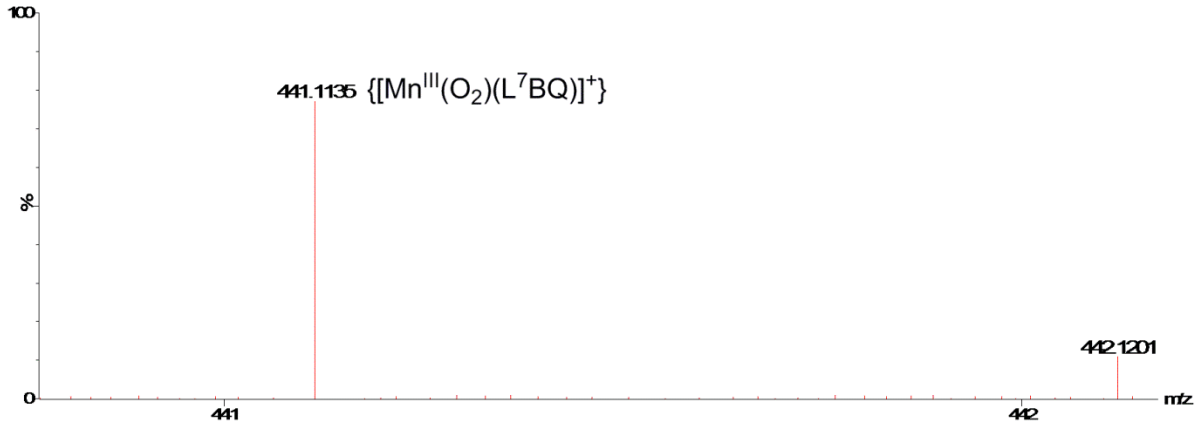

Figure A2.5. Low-temperature ESI-MS spectrum of $[Mn^{III}(O_2)L^7BQ)]^+$.

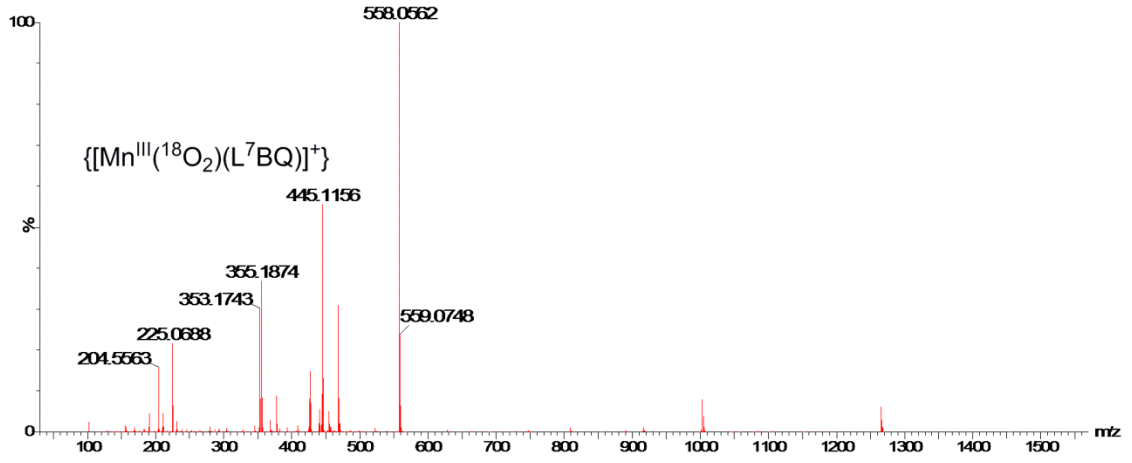

Figure A2.6. Low-temperature ESI-MS spectrum of $[Mn^{III}(^{18}O_2)L^7BQ)]^+$.

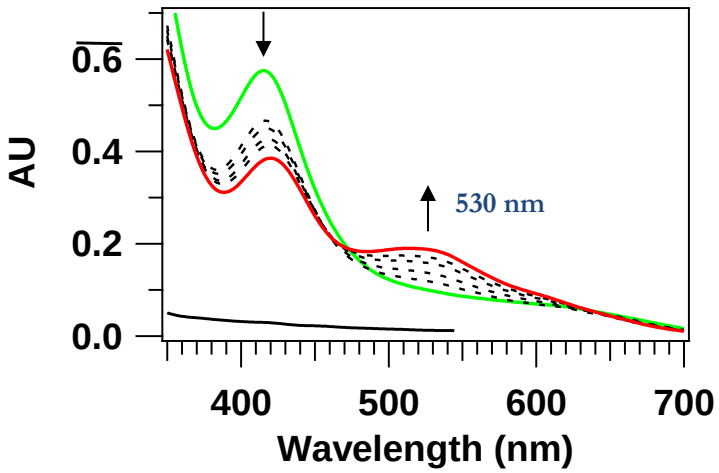

Figure A2.7. Changes in electronic absorption occurred after the addition of 1 equiv. of $HClO_4$ into a solution of $[Mn^{III}(O_2)(L^7py_2^{6\text{-}Me})]^+$ in MeCN at -40 ^oC.

APPENDIX A3.

Table A3.1. Crystal Data and Structure Refinement for [Mn^{II}(dpaq)](OTf).

Empirical formula	$C_{72}H_{57}F_9Mn_3N_{15}O_{12}S_3$	
Formula weight	1756.33	
Temperature	100(2) K	
Wavelength	1.54178 Å	
Crystal system	Monoclinic	
Space group	Cc	
Unit cell dimensions	a = 28.6094(9) Å	α = 90°.
	b = 9.2197(3) Å	β = 100.5500(10)°.
	c = 28.5260(9) Å	γ = 90°.
Volume	7397.1(4) $Å^3$	
Z	4	
Density (calculated)	1.577 Mg/m^3	
Absorption coefficient	5.729 mm^{-1}	
F(000)	3576	
Crystal size	0.15 x 0.10 x 0.10 mm^3	
Theta range for data collection	3.14 to 69.79°.	
Index ranges	-34<=h<=34, -11<=k<=8, -34<=l<=31	
Reflections collected	30828	
Independent reflections	9683 [R(int) = 0.0370]	
Completeness to theta = 66.00°	99.2 %	
Absorption correction	Multi-scan	
Max. and min. transmission	1.000 and 0.836	
Refinement method	Full-matrix least-squares on F^2	
Data / restraints / parameters	9683 / 2 / 1028	
Goodness-of-fit on F^2	1.018	
Final R indices [I>2sigma(I)]	R1 = 0.0370, wR2 = 0.0958	
R indices (all data)	R1 = 0.0372, wR2 = 0.0960	
Absolute structure parameter	0.022(3)	
Extinction coefficient	0.000086(15)	
Largest diff. peak and hole	1.303 and -0.520 $e.Å^{-3}$	

$R_1 = \Sigma \, ||F_O| - |F_C|| \, / \, \Sigma \, |F_O|$

$wR_2 = \{ \, \Sigma \, [w(F_O^{\,2} - F_C^{\,2})^2] \, / \, \Sigma \, [w(F_O^{\,2})^2] \, \}^{1/2}$

Table A3.2. Crystal Data and Structure Refinement for $[Mn^{III}(OH)(dpaq)](OTf)$.

Empirical formula	$C_{26}H_{24}F_3MnN_6O_5S$	
Formula weight	644.51	
Temperature	100(2) K	
Wavelength	1.54178 Å	
Crystal system	Monoclinic	
Space group	P2(1)/n	
Unit cell dimensions	a = 9.2406(3) Å	α = 90°.
	b = 24.7263(8) Å	β = 97.2570(10)°.
	c = 12.2658(4) Å	γ = 90°.
Volume	2780.11(16) $Å^3$	
Z	4	
Density (calculated)	1.540 Mg/m^3	
Absorption coefficient	5.176 mm^{-1}	
F(000)	1320	
Crystal size	0.27 x 0.10 x 0.03 mm^3	
Theta range for data collection	3.57 to 69.82°.	
Index ranges	-10<=h<=10, -29<=k<=30, -10<=l<=14	
Reflections collected	25663	
Independent reflections	5017 [R(int) = 0.0388]	
Completeness to theta = 66.00°	98.4 %	
Absorption correction	Multi-scan	
Max. and min. transmission	1.000 and 0.689	
Refinement method	Full-matrix least-squares on F^2	
Data / restraints / parameters	5017 / 19 / 509	
Goodness-of-fit on F^2	1.035	
Final R indices [I>2sigma(I)]	R1 = 0.0311, wR2 = 0.0782	
R indices (all data)	R1 = 0.0314, wR2 = 0.0785	
Extinction coefficient	0.00037(7)	
Largest diff. peak and hole	0.491 and -0.583 $e.Å^{-3}$	

$R_1 = \Sigma \, ||F_O| - |F_C|| \, / \, \Sigma \, |F_O|$

$wR_2 = \{ \, \Sigma \, [w(F_O^{\,2} - F_C^{\,2})^2] \, / \, \Sigma \, [w(F_O^{\,2})^2] \, \}^{1/2}$

Table A3.3. Selected Bond Lengths (Å) and Angles (deg) for Two of the Three $[Mn^{II}(dpaq)]^+$ Cations in the X-ray Diffraction Structure of $[Mn^{II}(dpaq)](OTf)$.

$[Mn^{II}(dpaq)]^+$ (A)			
Mn–O1A	2.075(2)	O1A–Mn–N2A	168.99(10)
Mn–N2A	2.177(3)	N4A–Mn–N5A	147.70(11)
Mn–N1A	2.247(3)	N1A–Mn–N3A	149.36(10)
Mn–N3A	2.329(3)	N4A–Mn–N2A	88.95(10)
Mn–N4A	2.325(3)	N1A–Mn–N2A	74.42(10)
Mn–N5A	2.278(3)	N3A–Mn–N2A	77.74(10)
$[Mn^{II}(dpaq)]^+$ (C)			
Mn–O1C	2.084(2)	O1C–Mn–N2C	168.01(10)
Mn–N2C	2.174(3)	N4C–Mn–N5C	148.46(11)
Mn–N1C	2.221(3)	N1C–Mn–N3C	151.53(10)
Mn–N3C	2.313(3)	N4C–Mn–N2C	91.11(10)
Mn–N4C	2.279(3)	N1C–Mn–N2C	74.76(10)
Mn–N5C	2.263(3)	N3C–Mn–N2C	78.21(10)

Table A3.4. Yields of $^{4\text{-}t\text{-butyl}}ArO\cdot$ from the Oxidation of $^{4\text{-}t\text{-butyl}}ArOH$ by $[Mn^{III}(OH)(dpaq)]^+$ at 50 ºC in MeCN at Variable Concentrations of the Phenol.

$[Mn^{III}(OH)(dpaq)]^+_0$ (mM)[a]	$[^{4\text{-}t\text{-butyl}}ArOH]_0$ (mM)[a]	AU_{628} (final)	$[^{4\text{-}t\text{-butyl}}ArO\cdot]_f$ (mM)[b]	Percent conversion[c]
1.25	12.5	0.38	0.95	76%
1.25	25.0	0.39	0.98	80%
1.25	37.5	0.38	0.95	76%
1.25	50.0	0.37	0.93	74%
1.25	65.5	0.38	0.95	76%
1.25	93.8	0.38	0.95	76%
1.25	125	0.39	0.98	80%
1.25	156	0.37	0.93	74%
0.63	156	0.18	0.45	72%

[a] Initial concentration at t = 0 s. [b] Final concentration of phenoxyl radical determined using the extinction coefficient of $^{4\text{-}t\text{-butyl}}ArO\cdot$ at 25 ºC in MeCN.[1] [c]Percent conversion of phenoxyl radical relative to initial concentration of $[Mn^{III}(OH)(dpaq)]^+$.

A)

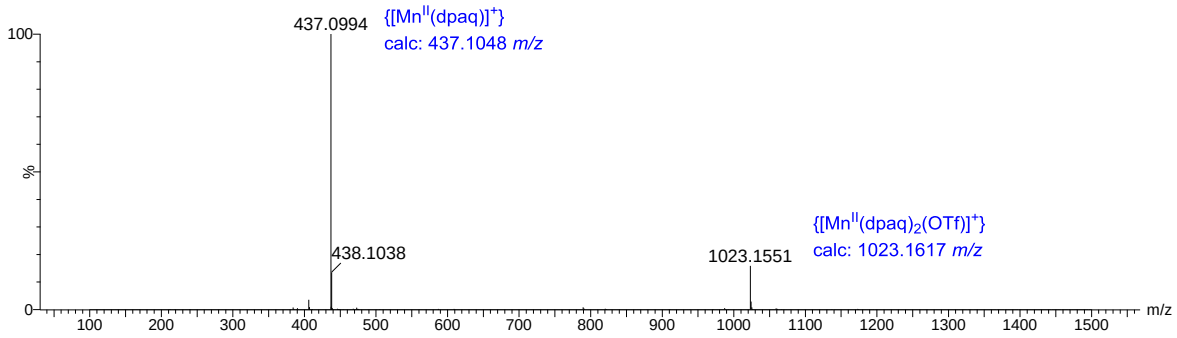

B)

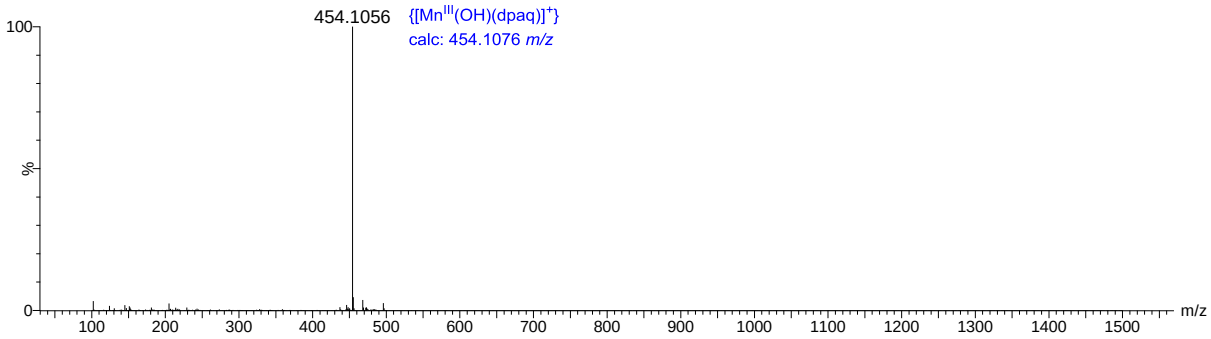

Figure A3.1. ESI mass spectra of A) $[Mn^{II}(dpaq)]^+$ and B) $[Mn^{III}(OH)(dpaq)]^+$.

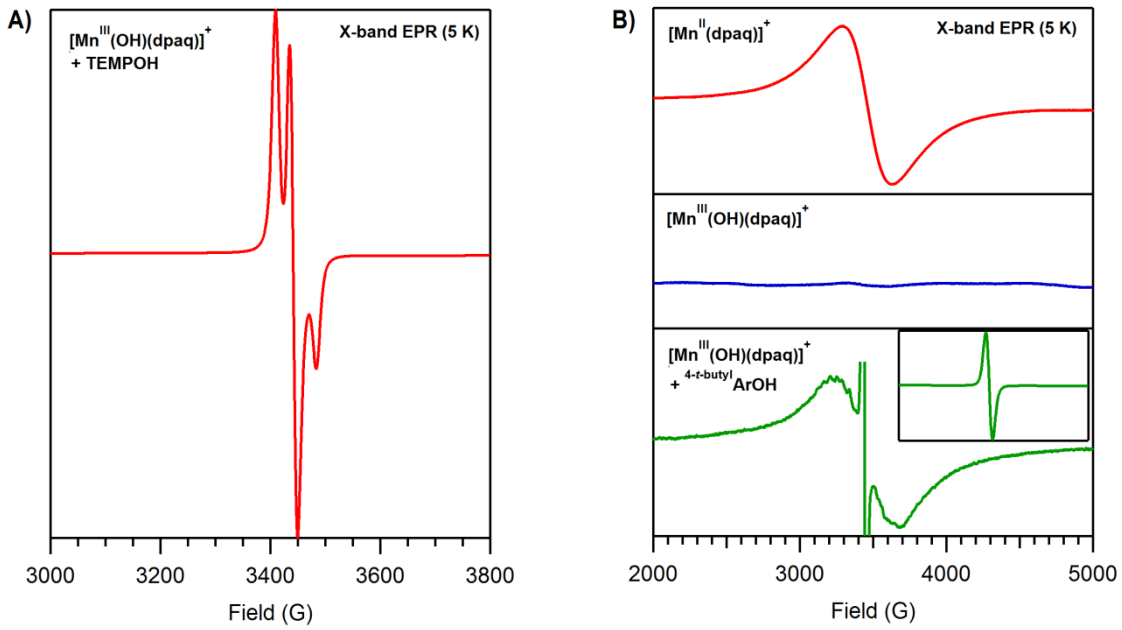

Figure A3.2. A) 5 K EPR spectrum of the final products of TEMPOH oxidation by $[Mn^{III}(OH)(dpaq)]^+$ in MeCN. The intense features centered at g = 2.04 has been previously observed for TEMPO radical.[2] B) A comparison of perpendicular-mode 5 K X-band EPR spectra of $[Mn^{II}(dpaq)]^+$ (red), $[Mn^{III}(OH)(dpaq)]^+$ (blue), and the final reaction mixture of $[Mn^{III}(OH)(dpaq)]^+$ and $^{4\text{-}t\text{-butyl}}$ArOH (green) in MeCN. Inset: Full EPR spectrum of the final reaction mixture showing the intense signal resulting from the $^{4\text{-}t\text{-butyl}}$ArO· centered at g = 2.04.[3] We note the absence of any signals in parallel-mode EPR spectra collected for all samples described above.

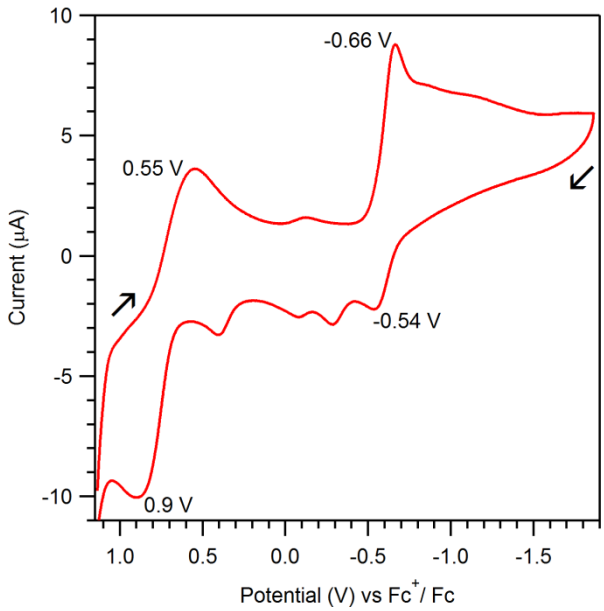

Figure A3.3. Cyclic voltammogram of $[Mn^{III}(OH)(dpaq)]^{+}$ under an argon atmosphere in acetonitrile (12.89 mg in 10 ml) at 298 K (Scan rate = 100 mV s^{-1}; starting potential = 1.13 V). Glassy carbon working electrode, a platinum auxiliary electrode, and a AgCl/Ag reference electrode were utilized along with a 0.1 M acetonitrile solution of $Bu_4N(PF_6)$ as the supporting electrolyte.

NOTE: The partially reversible redox event at $E_{1/2}$ = -0.6 V (ΔE_p = 120 mV) is attributed to the Mn^{II}/Mn^{III} couple. The three oxidation events observed between $E_{p,a}$ = +0.5 and -0.4 V could correspond to oxidation of the 8-aminoquinolinyl moiety of the supporting ligand, as previously observed for ruthenium(II) complexes supported by 8-aminoquinoline.[4] In that study, the 8-aminoquinoline ligands exhibited three oxidation waves between $E_{p,a}$ = +0.5 and -0.3 V vs Fc^{+}/Fc (reported $E_{p,a}$ values between +0.1 and +0.9 V vs AgCl/Ag). In the present system, the intense, partially reversible redox process at $E_{1/2}$ = +0.73 V (ΔE_p = 350 mV) could be due to the Mn^{IV}/Mn^{III} couple, but further investigations are warranted to support this conclusion.

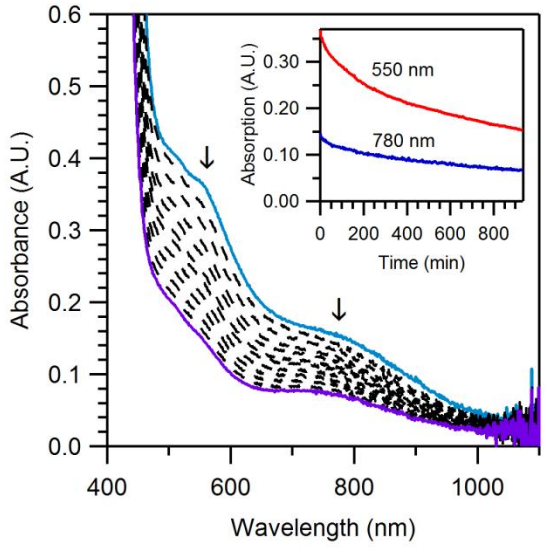

Figure A3.4. Electronic absorption spectra of 1.25 mM $[Mn^{III}(OH)(dpaq)]^{+}$ upon the addition of 250 equiv. xanthene at 50 ºC in MeCN under argon. Inset: Time evolution of absorption signals at 550 and 780 nm. The pseudo-first order rate constant for this reaction was determined using the method of initial rates.

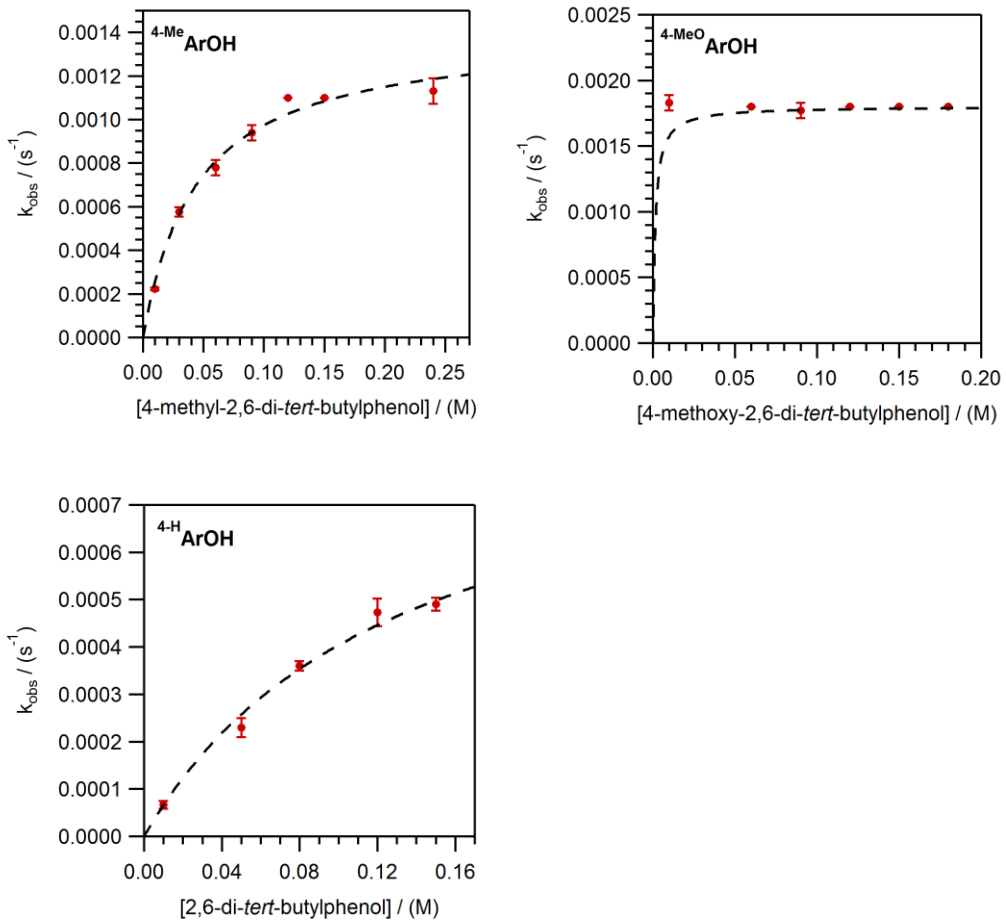

Figure A3.5. Observed pseudo-first order rate constants (k_{obs}) as a function of phenol concentration for reactions of $^{4\text{-Me}}$ArOH, $^{4\text{-MeO}}$ArOH, and $^{4\text{-H}}$ArOH with $[Mn^{III}(OH)(dpaq)]^{+}$ in MeCN at 50 ºC.

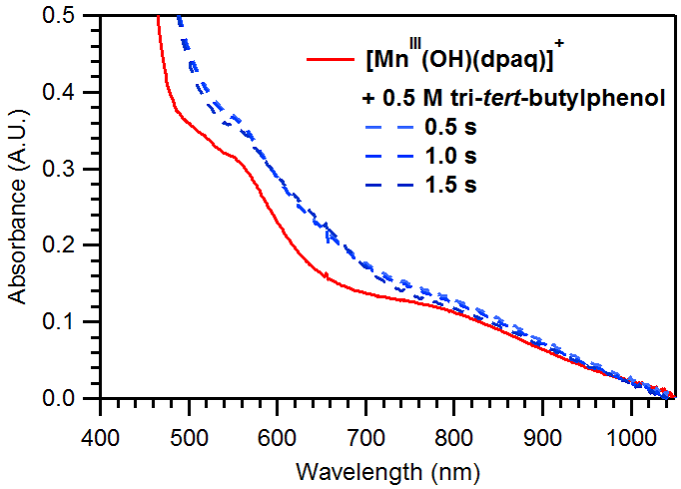

Figure A3.6. Electronic absorption spectrum of 1.25 mM $[Mn^{III}(OH)(dpaq)]^+$ in MeCN at 50 ºC before (solid red trace) and spectra collected immediately following the addition of 0.5 M tri-*tert*-butylphenol (dashed blue traces).

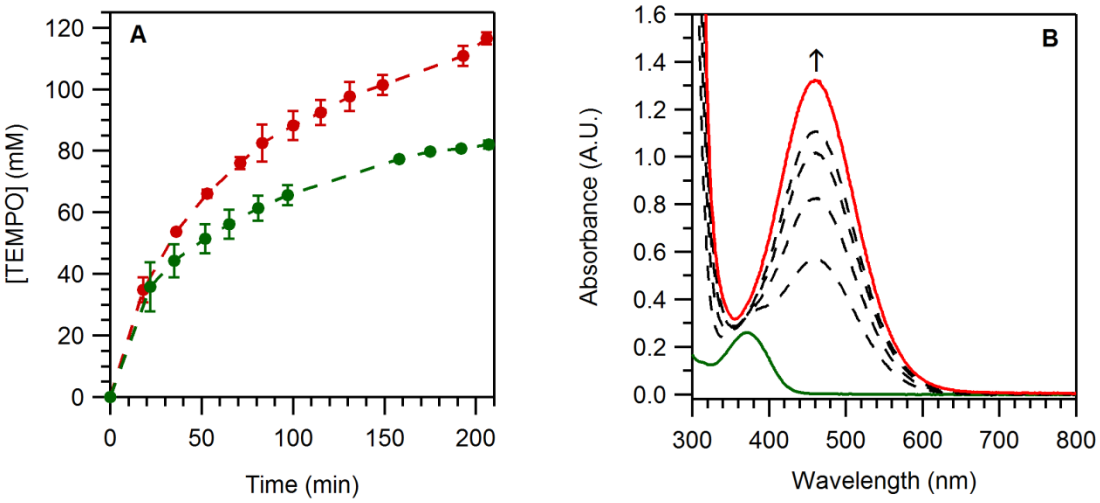

Figure A3.7. A) Formation of TEMPO as a function of time in the presence (red; concentration of $[Mn^{III}(OH)(dpaq)]^+$ = 0.031 mM) and absence (green) of $[Mn^{III}(OH)(dpaq)]^+$ in MeCN at 25 ºC. At each data point, the concentration of TEMPO was calculated using the extinction coefficient at 464 nm in acetonitrile.[5] B) Changes observed in electronic absorption spectrum as TEMPOH is oxidized to TEMPO.

References

(1) Manner, V. W.; Markle, T. F.; Freudenthal, J. H.; Roth, J. P.; Mayer, J. M. *Chem. Commun.* **2008**, 256-258.
(2) Ottaviani, M. F.; Garcia-Garibay, M.; Turro, N. J. *Colloids and Surfaces A: Physicochemical and Engineering Aspects* **1993**, *72*, 321-332.
(3) Fiedler, A. T.; Que, L. *Inorg. Chem.* **2009**, *48*, 11038-11047.
(4) O'Neill, M. K.; Trappey, A. F.; Battle, P.; Boswell, C. L.; Blauch, D. N. *Dalton Trans.* **2009**, 3391-3394.
(5) Chateauneuf, J.; Lusztyk, J.; Ingold, K. U. *J. Org. Chem.* **1990**, *55*, 1061-1065.

APPENDIX A4.

Table A4.1. Crystal Data and Structure Refinement for $[Mn^{III}(OMe)(dpaq)](OTf)$.

Empirical formula	$C_{50}H_{46}F_6Mn_2N_{10}O_{10.73}S_2$	
Formula weight	1246.73	
Temperature	100(2) K	
Wavelength	1.54178 Å	
Crystal system	Orthorhombic	
Space group	Pna2(1)	
Unit cell dimensions	a = 13.6388(4) Å	a= 90°.
	b = 26.1547(7) Å	b= 90°.
	c = 15.1412(4) Å	g = 90°.
Volume	5401.1(3) $Å^3$	
Z	4	
Density (calculated)	1.533 Mg/m^3	
Absorption coefficient	5.306 mm^{-1}	
F(000)	2552	
Crystal size	0.20 x 0.09 x 0.06 mm^3	
Theta range for data collection	3.37 to 70.01°.	
Index ranges	-16<=h<=16, -30<=k<=29, -15<=l<=17	
Reflections collected	50470	
Independent reflections	8511 [R(int) = 0.0247]	
Completeness to theta = 66.00°	97.7 %	
Absorption correction	Multi-scan	
Max. and min. transmission	1.000 and 0.715	
Refinement method	Full-matrix least-squares on F^2	
Data / restraints / parameters	8511 / 211 / 826	
Goodness-of-fit on F^2	1.051	
Final R indices [I>2sigma(I)]	R1 = 0.0748, wR2 = 0.2117	
R indices (all data)	R1 = 0.0757, wR2 = 0.2131	
Absolute structure parameter	0(3)	
Largest diff. peak and hole	1.177 and -0.773 $e.Å^{-3}$	

$R_1 = \Sigma \, ||F_O| - |F_C|| \, / \, \Sigma \, |F_O|$

$wR_2 = \{ \, \Sigma \, [w(F_O^2 - F_C^2)^2] \, / \, \Sigma \, [w(F_O^2)^2] \, \}^{1/2}$

A)

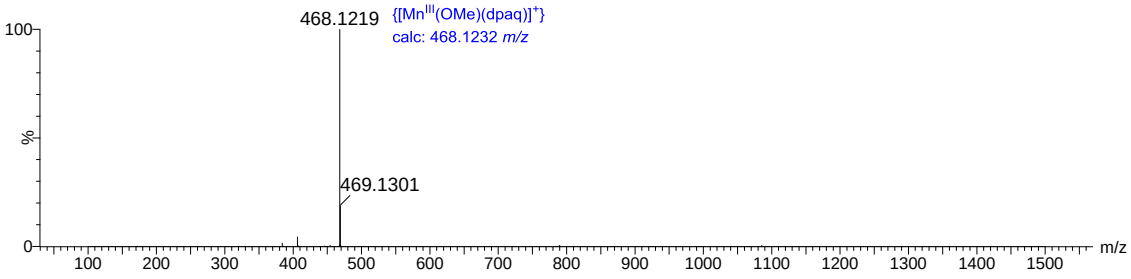

B)

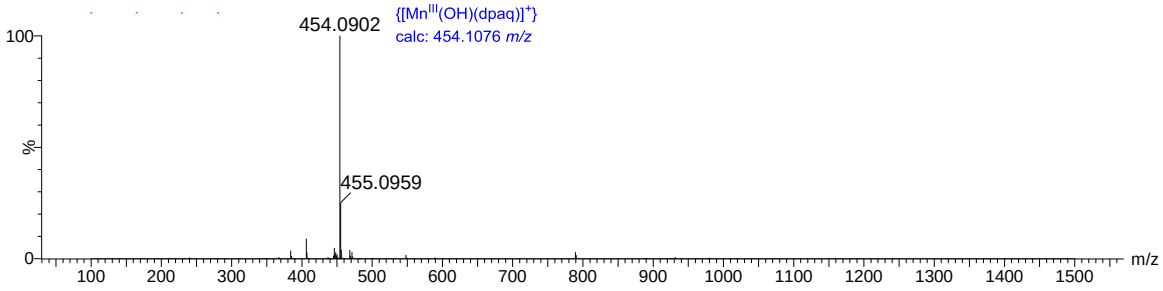

Figure A4.1. ESI mass spectra of A) $[Mn^{III}(OMe)(dpaq)]^+$ in MeOH and B) $[Mn^{III}(OMe)(dpaq)]^+$ dissolved in H_2O, showing full conversion to $[Mn^{III}(OH)(dpaq)]^+$.

Table A4.2. Selected Bond Lengths (Å) and Angles (deg) for One of the Two $[Mn^{III}(OMe)(dpaq)]^+$ Cations in the X-ray Diffraction Structure of $[Mn^{III}(OMe)(dpaq)]^+$.

$[Mn^{III}(OMe)(dpaq)]^+$ (B)			
Mn–O2	1.814(5)	O2–Mn–N2	178.0(3)
Mn–N2	1.982(6)	N4–Mn–N5	153.8(2)
Mn–N1	2.086(11)	N1–Mn–N3	156.5(4)
Mn–N3	2.169(6)	N4–Mn–N2	86.8(2)
Mn–N4	2.154(7)	N1–Mn–N2	74.5(2)
Mn–N5	2.195(6)	N3–Mn–N2	82.1(3)

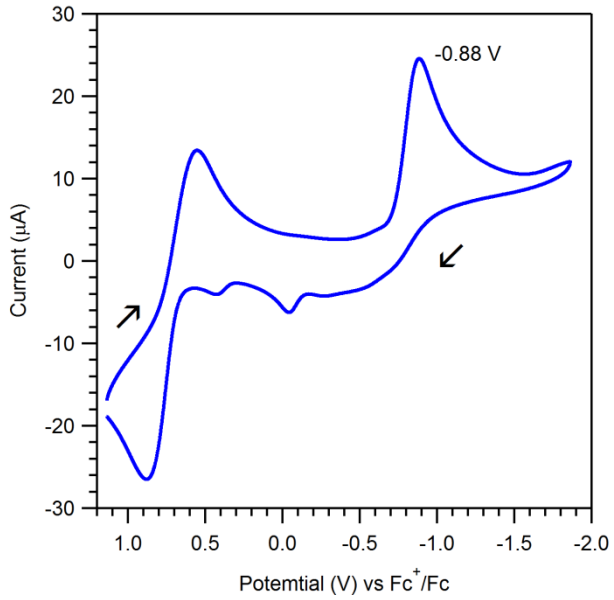

Figure A4.2. Cyclic voltammogram of $[Mn^{III}(OMe)(dpaq)]^+$ in acetonitrile (12.89 mg in 10 ml) at 298 K (Scan rate = 100 mV s^{-1}; starting potential = 1.13 V) under an argon atmosphere. The electrochemical cell consisted of a glassy carbon working electrode, a platinum auxiliary electrode, and a AgCl/Ag reference electrode along with a 0.1 M acetonitrile solution of $Bu_4N(PF_6)$ as the supporting electrolyte.

NOTE: The irreversible redox event at $E_{p,c}$ = -0.88 V is attributed to the Mn^{III}/Mn^{II} couple which is 0.22 V lower than that of $[Mn^{III}(OH)(dpaq)]^+$ (-0.6 V vs Fc^+/Fc).[1] The multiple oxidation events between E_{pa} = +0.5 and -0.4 V are possibly due to the redox activity of the 8-aminoquinolinyl moiety of the supporting ligand, as previously observed for ruthenium(II) complexes supported by 8-aminoquinoline.[2]

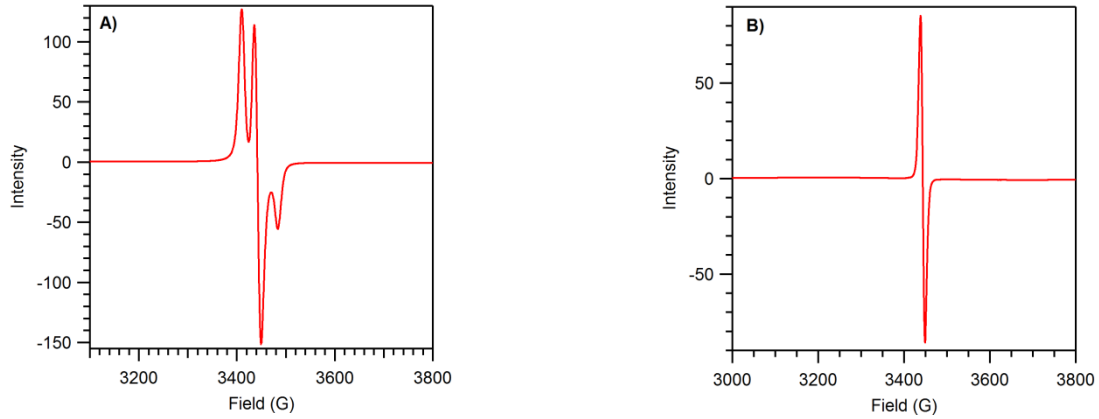

Figure A4.3. A) 5 K EPR spectra of the final products of A) TEMPOH and B) $^{4\text{-}t\text{-butyl}}$ArOH oxidation by $[Mn^{III}(OMe)(dpaq)]^{+}$ in MeCN. The intense features centered at g = 2.04 has been previously observed for both TEMPO and $^{4\text{-}t\text{-butyl}}$ArO· radicals.[3, 4] Parallel-mode EPR experiments were performed on both of these samples, but no features were observed.

Table A4.3. Yields of $^{4\text{-}t\text{-butyl}}ArO^{\bullet}$ from the Oxidation of $^{4\text{-}t\text{-butyl}}$ArOH by $[Mn^{III}(OMe)(dpaq)]^{+}$ at 50 ºC in MeCN at Variable Concentrations of the Phenol.

$[Mn^{III}(OMe)(dpaq)]^{+}_0$ (mM) [a]	$[^{4\text{-}t\text{-butyl}}ArOH]_0$ (mM) [a]	AU_{628} (final)	$[^{4\text{-}t\text{-butyl}}ArO\cdot]_f$ (mM) [b]	Percent conversion [c]
1.25	12.5	0.36	0.90	72%
1.25	62.5	0.38	0.95	76%
1.25	93.8	0.36	0.90	72%
1.25	125	0.38	0.95	76%
1.25	156	0.39	0.98	79%

[a] Initial concentration at t = 0 s. [b] Final concentration of phenoxyl radical determined using the extinction coefficient of $^{4\text{-}t\text{-butyl}}$ArO· at 25 ºC in MeCN.[5] [c] Percent conversion of phenoxyl radical relative to initial concentration of $[Mn^{III}(OMe)(dpaq)]^{+}$.

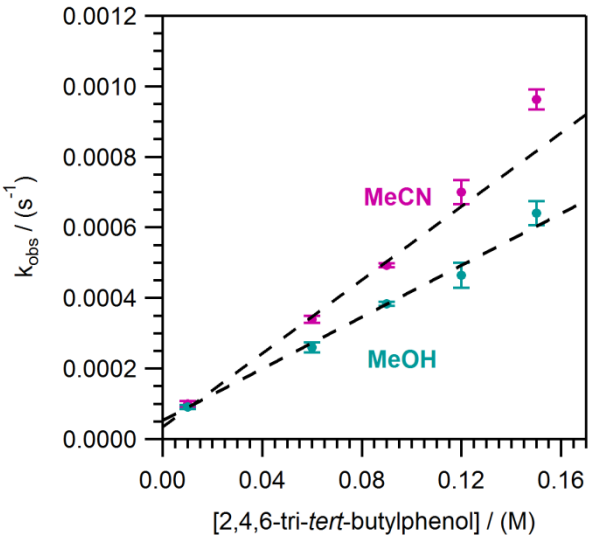

Figure A4.4. Observed pseudo-first order rate constants (k_{obs}) as a function of substrate concentration for the oxidation of $^{4\text{-}t\text{-butyl}}$ArOH by $[Mn^{III}(OMe)(dpaq)]^{+}$ in MeCN and in MeOH at 50 ºC.

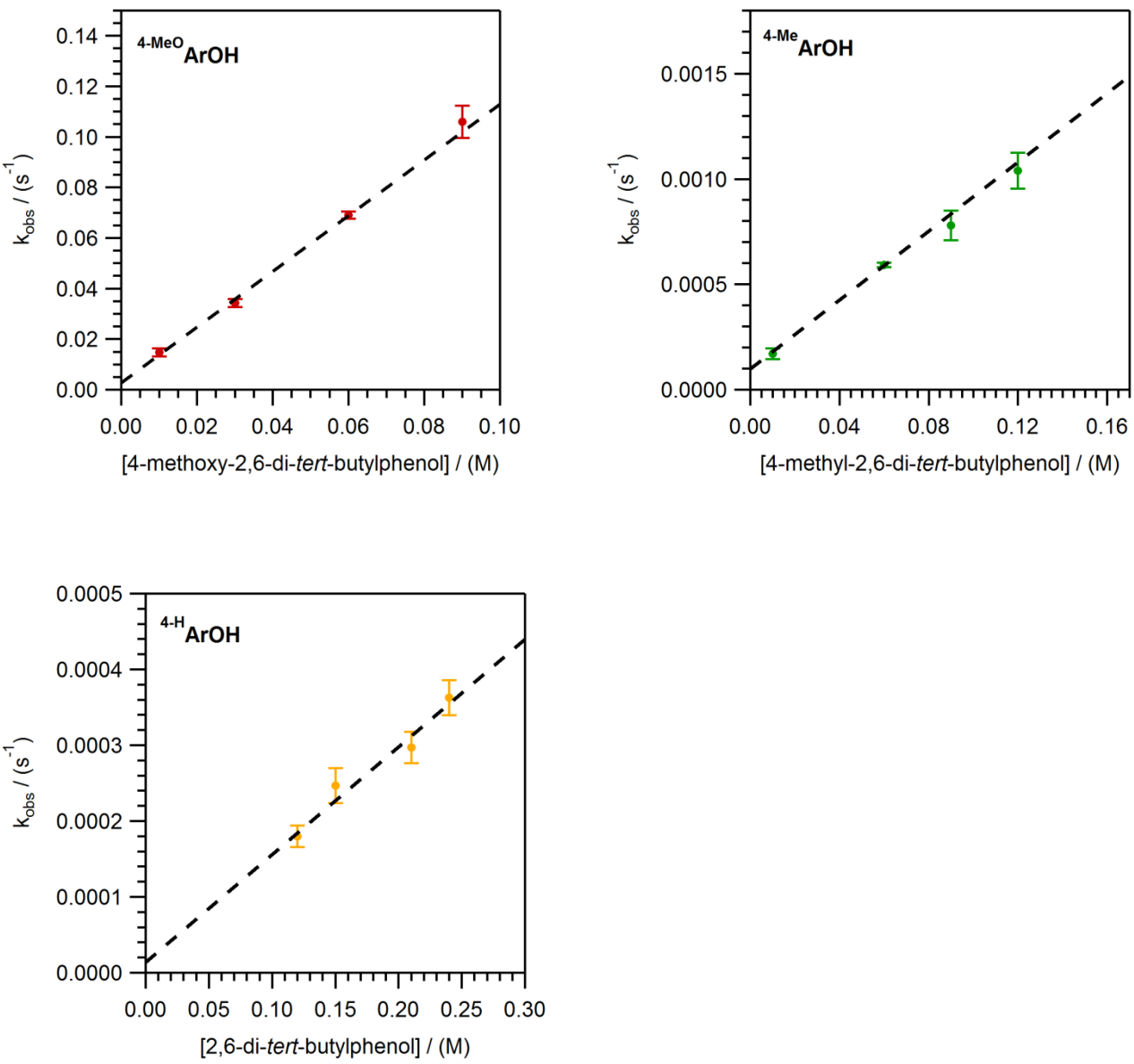

Figure A4.5. Observed pseudo-first order rate constants (k_{obs}) as a function of phenol concentration for reactions of $^{4\text{-OMe}}$ArOH, $^{4\text{-Me}}$ArOH, and $^{4\text{-H}}$ArOH with $[Mn^{III}(OMe)(dpaq)]^{+}$ in MeCN at 50 ºC.

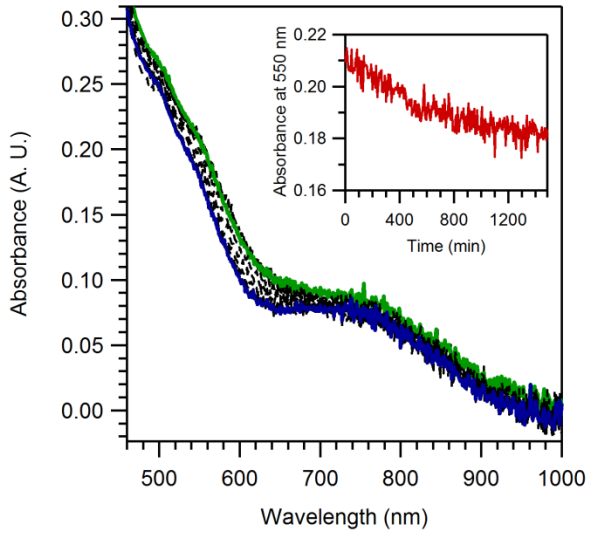

Figure A4.6. The decay of electronic absorption features of a 1.25 mM MeCN solution of $[Mn^{III}(OMe)(dpaq)]^{+}$ upon the addition of 250 equiv. xanthene at 50 ºC under argon. Inset: Time evolution of the absorption signal at 550 nm. The pseudo-first order rate constant for this reaction was determined using the method of initial rates.

References

1. G. B. Wijeratne, B. Corzine, V. W. Day and T. A. Jackson, *Inorg. Chem.*, 2014, **53**, 7622-7634.
2. M. K. O'Neill, A. F. Trappey, P. Battle, C. L. Boswell and D. N. Blauch, *Dalton Trans.*, 2009, 3391-3394.
3. M. F. Ottaviani, M. Garcia-Garibay and N. J. Turro, *Colloids and Surfaces A: Physicochemical and Engineering Aspects*, 1993, **72**, 321-332.
4. A. T. Fiedler and L. Que, *Inorg. Chem.*, 2009, **48**, 11038-11047.
5. V. W. Manner, T. F. Markle, J. H. Freudenthal, J. P. Roth and J. M. Mayer, *Chem. Commun.* 2008, 256-258.

APPENDIX A5.

Table A5.1. Crystal data and structure refinement for $[Mn^{II}(dpaq^{2\text{-}Me})](OTf)$.

Empirical formula	$C_{27}H_{25}F_3MnN_6O_4S$	
Formula weight	641.53	
Temperature	100(2) K	
Wavelength	1.54178 Å	
Crystal system	Triclinic	
Space group	P -1	
Unit cell dimensions	a = 11.9552(16) Å	a= 107.482(4)°.
	b = 14.164(2) Å	b= 90.366(4)°.
	c = 18.528(3) Å	g = 109.556(4)°.
Volume	2799.9(7) $Å^3$	
Z	4	
Density (calculated)	1.522 Mg/m^3	
Absorption coefficient	5.109 mm^{-1}	
F(000)	1316	
Crystal size	0.270 x 0.210 x 0.065 mm^3	
Theta range for data collection	2.518 to 67.864°.	
Index ranges	-9<=h<=14, -16<=k<=16, -21<=l<=21	
Reflections collected	24462	
Independent reflections	9690 [R(int) = 0.0361]	
Completeness to theta = 66.000°	97.3 %	
Absorption correction	Multi-scan	
Max. and min. transmission	1.000 and 0.665	
Refinement method	Full-matrix least-squares on F^2	
Data / restraints / parameters	9690 / 114 / 902	
Goodness-of-fit on F^2	1.051	
Final R indices [I>2sigma(I)]	R1 = 0.0523, wR2 = 0.1480	
R indices (all data)	R1 = 0.0543, wR2 = 0.1498	
Extinction coefficient	n/a	
Largest diff. peak and hole	1.014 and -0.430 $e.Å^{-3}$	

Table A5.2. Crystal data and structure refinement for $[Mn^{III}(OH)(dpaq^{2\text{-}Me})](OTf)$.

Empirical formula	$C_{31}H_{36}F_3MnN_6O_6S$	
Formula weight	732.66	
Temperature	100(2) K	
Wavelength	1.54178 Å	
Crystal system	Monoclinic	
Space group	P 21/c	
Unit cell dimensions	a = 8.4929(5) Å	a= 90°.
	b = 14.2757(8) Å	b= 96.229(3)°.
	c = 27.9728(16) Å	g = 90°.
Volume	3371.5(3) $Å^3$	
Z	4	
Density (calculated)	1.443 Mg/m^3	
Absorption coefficient	4.359 mm^{-1}	
F(000)	1520	
Crystal size	0.350 x 0.330 x 0.050 mm^3	
Theta range for data collection	3.178 to 67.952°.	
Index ranges	-9<=h<=10, -10<=k<=17, -28<=l<=33	
Reflections collected	17082	
Independent reflections	5876 [R(int) = 0.0438]	
Completeness to theta = 66.000°	98.0 %	
Absorption correction	Multi-scan	
Max. and min. transmission	1.000 and 0.645	
Refinement method	Full-matrix least-squares on F^2	
Data / restraints / parameters	5876 / 0 / 581	
Goodness-of-fit on F^2	1.043	
Final R indices [I>2sigma(I)]	R1 = 0.0615, wR2 = 0.1692	
R indices (all data)	R1 = 0.0678, wR2 = 0.1741	
Extinction coefficient	n/a	
Largest diff. peak and hole	0.961 and -0.621 $e.Å^{-3}$	

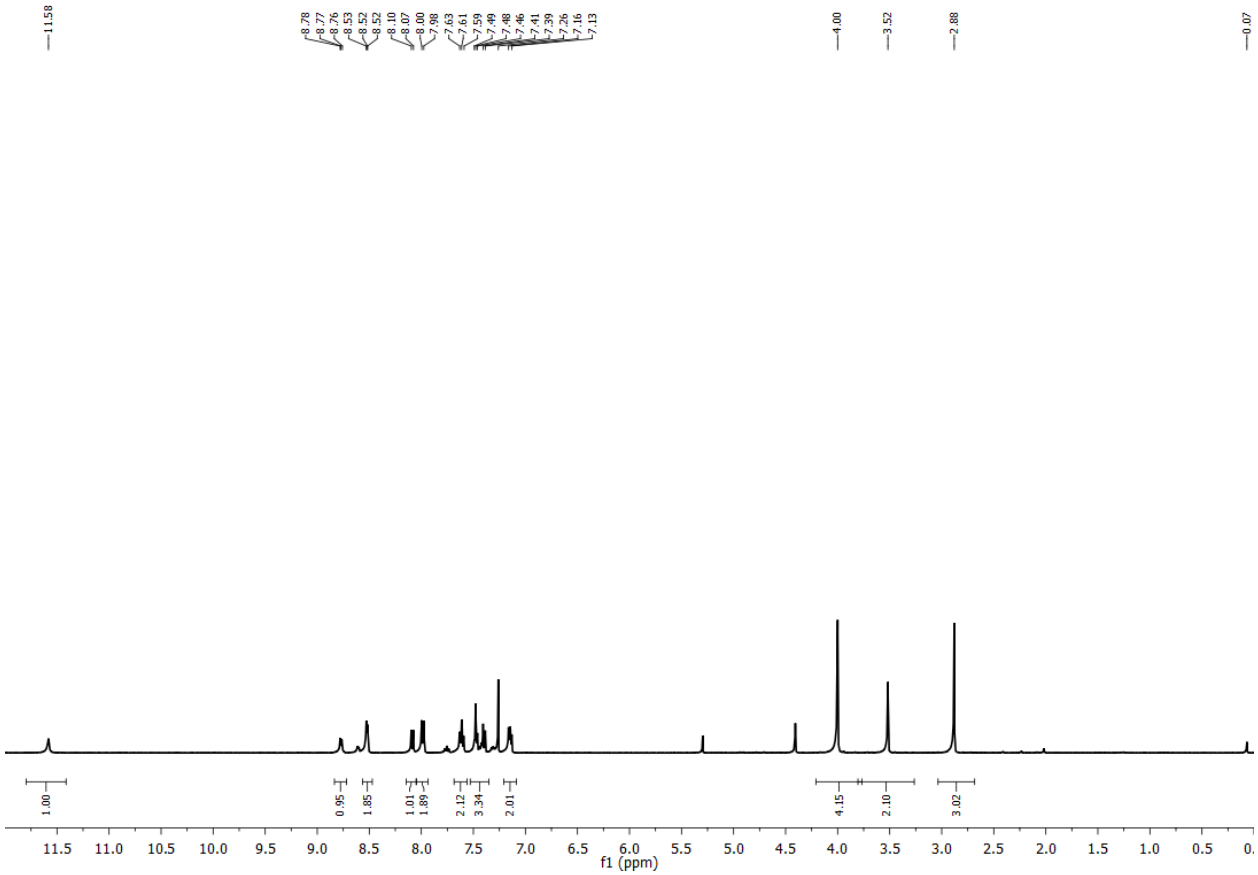

Figure A5.1. ^{1}H NMR spectrum of Hdpaq$^{2\text{-Me}}$ ligand collected in $CDCl_3$ at under ambient conditions.

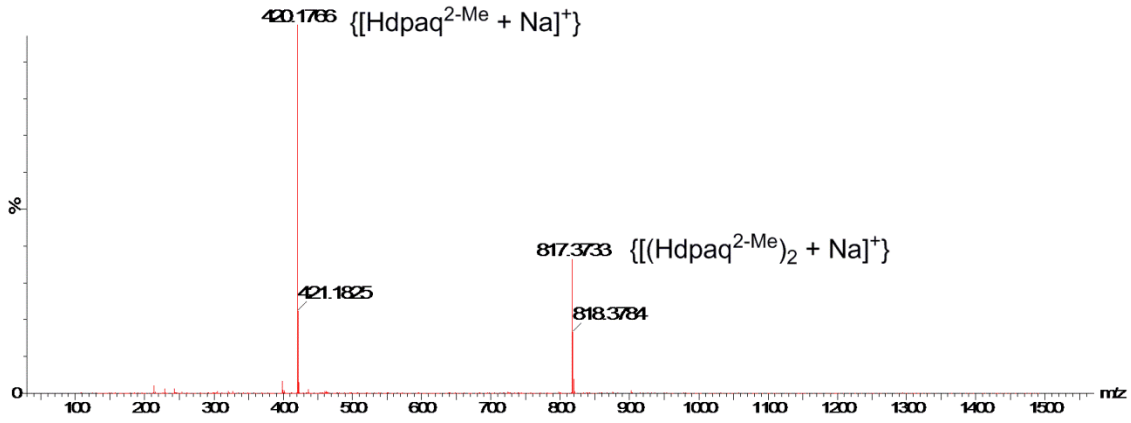

Figure A5.2. ESI-MS spectrum of the purified Hdpaq$^{2\text{-Me}}$ ligand.

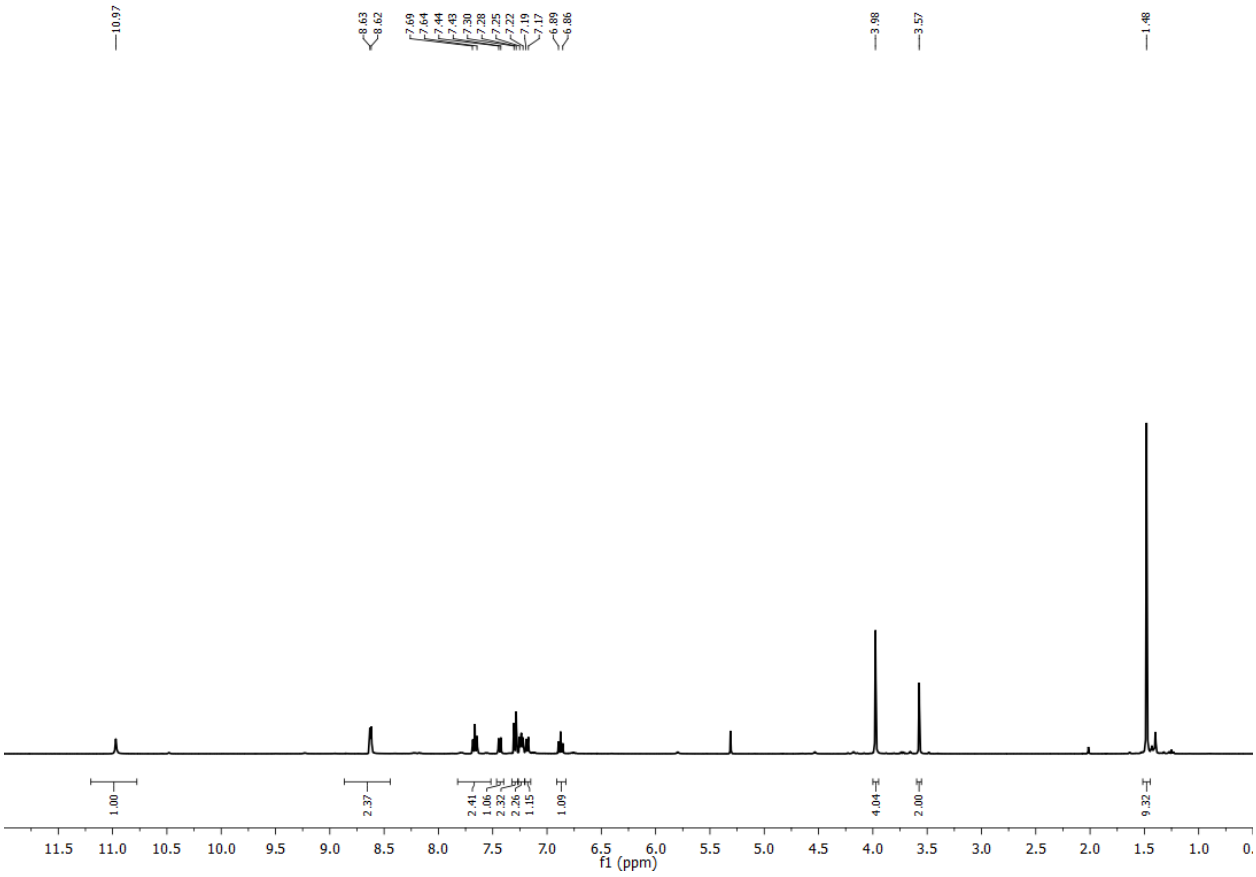

Figure A5.3. ^{1}H NMR spectrum of H_2dpap$^{2\text{-t-Bu}}$ ligand collected in $CDCl_3$ at under ambient conditions.

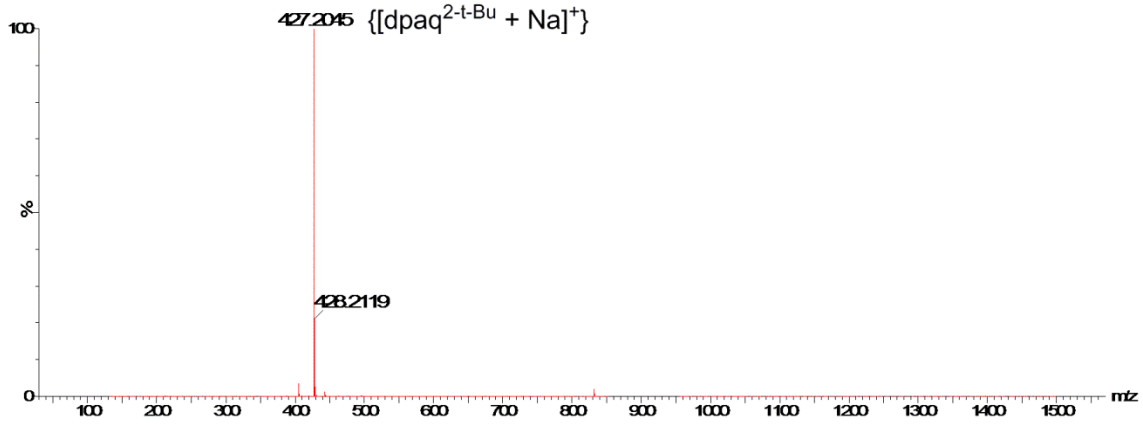

Figure A5.4. ESI-MS spectrum of the purified H_2dpap$^{2\text{-t-Bu}}$ ligand.

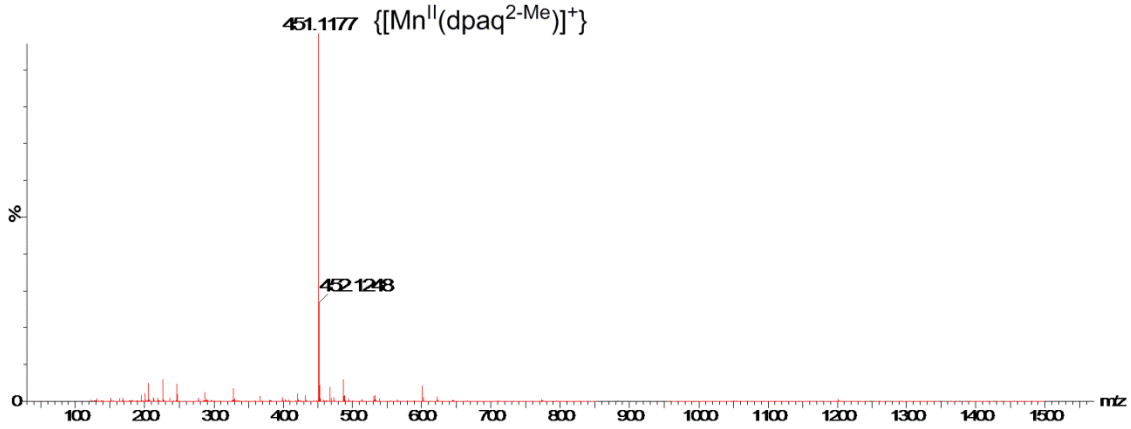

Figure A5.5. ESI-MS spectrum of $[Mn^{II}(H\text{-}dpaq^{2\text{-}Me})]^{+}$.

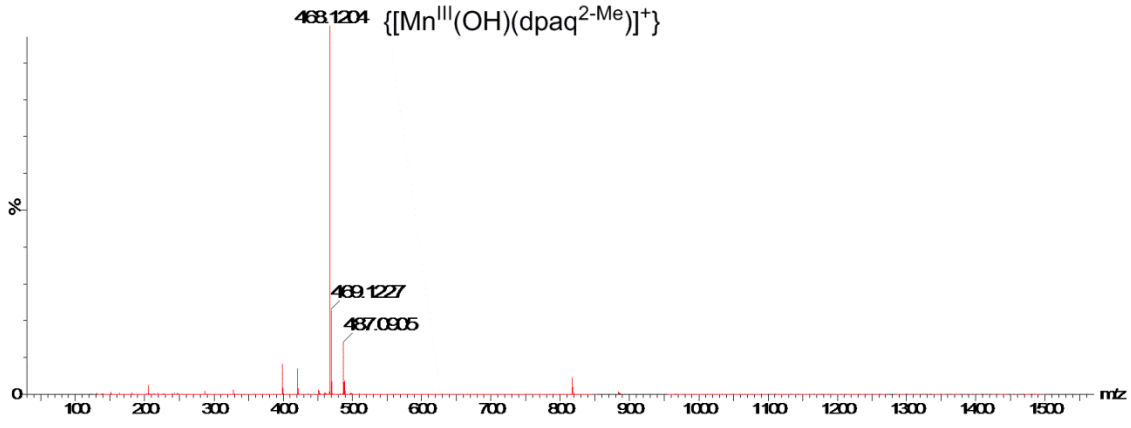

Figure A5.6. ESI-MS spectrum of $[Mn^{III}(OH)(dpaq^{2\text{-}Me})]^{+}$.

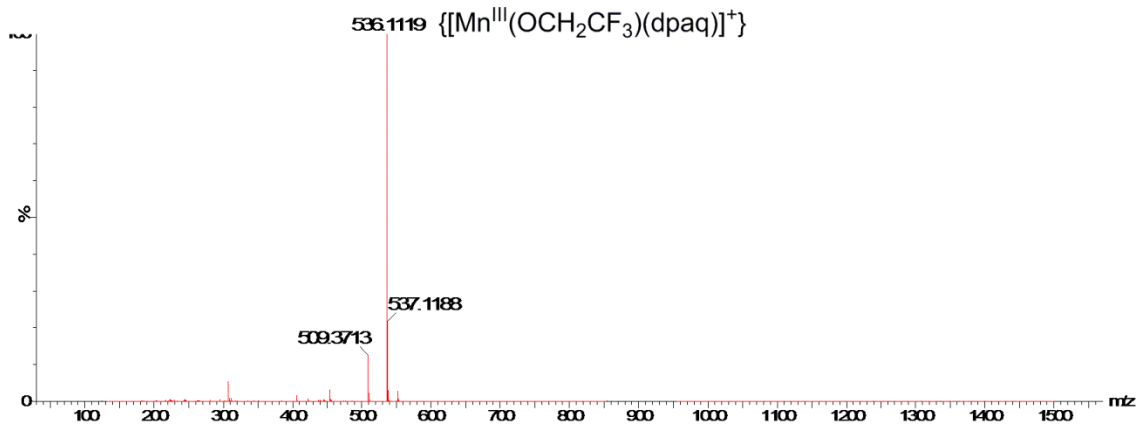

Figure A5.7. ESI-MS spectrum of the final solution resulted from the reaction between $[Mn^{II}(dpaq)](OTf)$ and PhIO in TFE at room temperature.

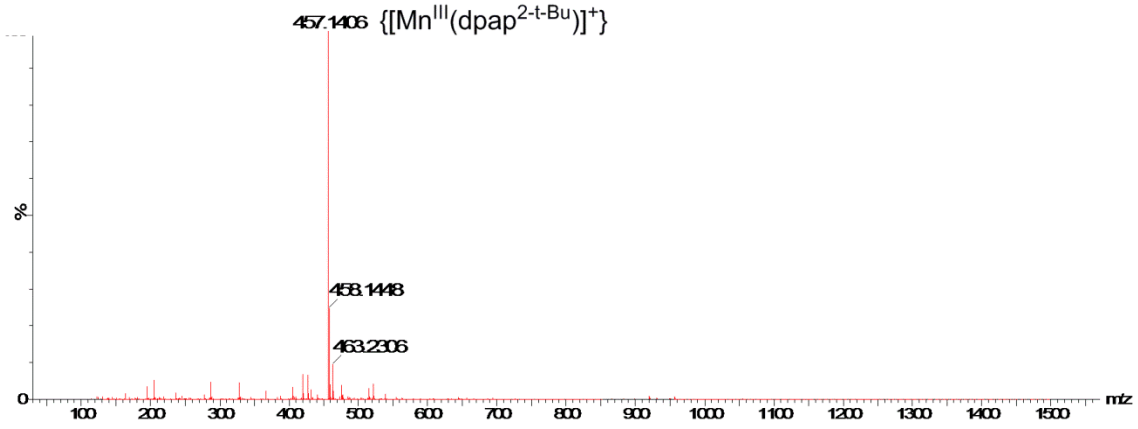

Figure A5.8. ESI-MS spectrum of the final solid resulted from the metalation of $H_2dpap^{2\text{-t-Bu}}$.